UNIVERSITAT POLITÈCNICA DE CATALUNYA
BARCELONATECH
Departament de Teoria del Senyal
i Comunicacions

Analysis and design of an edge-technique-based Doppler wind lidar. Practical assessment of a laboratory prototype

Ph.D. Thesis dissertation
Submitted in partial fulfilment of the requirements for the degree of

DOCTOR IN PHILOSOPHY

Submitted by

Constantino Muñoz-Porcar

Thesis advisors:

Dr. Adolfo Comerón Tejero and Dr. Alejandro Rodríguez Gómez

Doctorate Program in Signal Theory and Communications

Barcelona, December de 2012

Analysis and design of an edge-technique-based Doppler wind lidar. Practical assessment of a laboratory prototype

Remote Sensing Laboratory
Departament de Teoria del Senyal i Comunicacions
Universitat Politècnica de Catalunya – BARCELONA**TECH**

Barcelona, 2012

A mis hijos

A Sonia

A mis padres

Abstract

This thesis is the initial stage in the development of a range-resolving, aerosol-return-based Doppler wind lidar. Such instruments measure the speed of the wind by detecting the Doppler frequency shift undergone by the light that is scattered by aerosols, which are taken as wind tracers, when they are illuminated by pulsed laser radiation. The detection technique considered in this work is the so-called 'edge-technique', where the slope of the frequency response of an optical filter is used as frequency discriminator.

The thesis is divided in two parts. In the first one, the optimal configuration of the optical filter is calculated and a complete analysis of the system performance is carried out. The second part is devoted to the design, implementation and assessment of a laboratory prototype. The objective of this development is to assess the implementation of the detection technique and to characterize and adjust the operation of some of the critical elements and subsystems that will be part of the Doppler wind lidar.

Keywords: Lidar, Doppler, aerosol, laser, Fabry-Perot, interferometer, velocimeter.

Agraïments

Vull agraïr, en primer lloc, l'ajuda i el recolzament que, al llarg d'aquests anys, en tot moment he rebut dels meus amics i directors de tesi, Adolfo Comerón i Alejandro Rodríguez.

És obligatori també un reconeixement a les persones que dintre del grup de recerca i el departament han contribuït, d'una forma o altra, als resultats que es presentaran aquí: Michaël Sicard, Francesc Rocadenbosch, David Garcia, Federico Dios, Miguel Ángel López, Sergio Tomás, Diego Lange, Òscar Batet, Dhiraj Kumar, Nadzri Reba, Joaquim Giner, Carles Diaz, Josep Maria Haro, Ruben Tardío, Jordi Guillem, Josep Pastor, Albert Martón i Alfredo Cano.

Tampoc puc oblidar als estudiants de Projecte Final de Carrera que han participat de forma directa en diferents etapes d'aquest treball: Alberto Muriel, Xavier Alfonso, Elena Jiménez, Maria Freixes, Joan Mercadal, Daniel Pérez, Sergi Manuel, Miguel Ángel Leo i Daniel Ballesta.

Finalment, per suposat, també ha estat important els suport –i en moltes ocasions també les aportacions i els consells– dels meus companys en tasques docents, tant a la Escola Politècnica Superior d'Enginyeria de Vilanova i la Geltrú com a la Escola d'Enginyeria de Telecomunicacions i Aeroespacial de Castelldefels. Entre tots ells, que han estat molts, no vull deixar de mecionar a Vicent Sales, Antoni Barlabé, Ramon Guzman, Joan Castell, Josep Segarra i Eduard Úbeda.

Acknowledgements

The following institutions are gratefully acknowledged for their contributions to this work:

- MCYT (Ministerio de Ciencia y Tecnología), MICINN (Ministerio de Ciencia e Innovación) and ERDF (European Regional Development Fund) under the R&D projects REN2003-09753-C02-C02/CLI, TEC2006-07850/TCM and TEC2009-09106 funding the RSLAB (Remote Sensing Laboratory) - lidar.

- European Commission under the ACTRIS (Aerosols, Clouds, and Trace gases Research InfraStructure Network) FP7 Grant Agreement no. 262254, the EARLINET-ASOS (European Aerosol Research Lidar Network-Advanced Sustainable Observation System) FP6 contract no. RICA-025991 and the EARLINET (A European Aerosol Research Network to Establish an Aerosol Climatology) FP5 contract no. EVR1-CT-1999-40003 funding the European Lidar Network EARLINET.

- CDTI (Centro para el Desarrollo Tecnológico Industrial) under the R&D project ATLAS (Desarrollo de un instrumento de ayuda a la navegación aérea en condiciones meteorológicas desfavorables. Aplicación de Técnicas LIDAR en el sector Aeronáutico para el incremento de la Seguridad aérea) Ref. SAE-20081054 funding the RSLAB (Remote Sensing Laboratory) - lidar.

- CIRIT (Comissió Interdepartamental de Recerca i Innovació Tecnològica), DURSI/DMA (Departament d'Universitats, Recerca i Societat de la Informació / Departament de Medi Ambient) under de R&D project IMMPACTE (Integració metodològica i de models per a la previsió i l'anàlisi de la contaminació i el temps i dels seus efectes) funding the RSLAB (Remote Sensing Laboratory) - lidar.

- AGAUR (Agencia de Gestió d'Ajuts Universitaris i de Recerca. Departament d'Economia i Conneixement. Generalitat de Catalunya) funding the Grup Consolidat de Fotònica of the Universitat Politècnica de Catalunya (UPC).

Contents

List of figures

List of Tables

1 Introduction

1.1 Introduction to lidars

Lidars, also known as laser-radars, are optical remote sensing systems, that is, they explore distant objects using light as vehicle for the information. Remote sensing using light is not of course a modern invention. Seeing is something that many animals do since they are born to acquire information about the surrounding world. Since the appearance of intelligence, however, humans have used technology to enhance this natural capability. As probably the first example, as soon as men were able to light a fire, they surely used it to illuminate objects in the dark. This was, actually, an active technique for improving their visual capability: they emitted the light that, after being scattered by objects, was detected by their eyes and permitted, in naturally adverse conditions for vision such as night time or inside dark caves, obtaining information about them. In essence, what lidars do is not much different; the source of light in the case of lidars, however, is a laser (instead of a torch), the detector is formed by a telescope and an optoelectronic receiver (instead of the human visual system) and, according to their respective characteristics, the type of information that lidars help to become 'visible' is usually as well different.

Lidar systems, nevertheless, are not so old. The origins and basis of the lidar techniques can be actually found, in first instance, in the development of radar systems during the interwar period. Radars, an application of radio communications technology in the field of remote sensing, use echo localization in the radio frequency range to obtain information about targets. Later, already in the decade of 60s of the 20th century, the invention of lasers and the

development of optoelectronics provided the technologies required for efficiently adapting these techniques to the optical frequencies. In fact, both denominations: laser-radar and lidar –which is an acronym of **Li**ght **D**etection **A**nd **R**anging (as an optical version of the one first used for radars: **Ra**dio **D**etection **A**nd **R**anging)–, reveal eloquently this inheritance.

The range of wavelengths used by laser-radars, occupying in most of applications near-ultraviolet, visible and near-infrared frequency bands, determines some of their unique features as remote sensing instruments. At these frequencies, the electromagnetic radiation interacts –in some cases strongly– with the atmospheric constituents. Lidars, taking advantage of this interaction, can be used for deriving range-resolved information of the atmosphere state. Atmospheric science has indeed stood out as one of the main fields of application of lidar technologies. A manifold of atmospheric variables such as temperature, pressure, speed of the wind or content of aerosol particles, water vapour and trace gases, whose knowledge is important for understanding and modelling the complex processes that govern the atmospheric dynamics, have been successfully profiled using lidar instruments. Their main advantages with respect to the traditional in situ techniques, applied from sounding rockets or balloons for atmospheric profiling, are higher spatial and temporal resolution and the possibility of continuous monitoring. Radars are also used in atmospheric research and their capabilities are a good complement of lidar ones. While lidars, which need clean-air conditions to operate, are capable to measure gases and aerosols, radars rely on the scattering from atmospheric hydrometeors and are therefore better suited for rainfall monitoring, thunderstorm tracking or cloud profiling.

1.2 Background

Lidar activities started in the *Universitat Politècnica de Catalunya* (*UPC*) in 1993. Since then, three lidar systems, dedicated mainly to measure and monitor atmospheric aerosol particles have been developed by the Lidar Group of the *UPC* and have been exploited in the frame of different national and international projects. This thesis is related to the aim of the *UPC* lidar group to extend its activity scope developing a Doppler wind lidar.

Doppler wind lidars measure the speed of the wind by detecting the Doppler frequency shift undergone by the light that is scattered by aerosols and air molecules, which are taken as wind tracers, when they are illuminated by laser radiation. Different methods can be used to measure frequency shifts between two optical signals. The choice of the technique, however, determines the characteristics on the main subsystems of the instrument. In this sense, the laser transmitter is one of the critical elements to be taken in account. The *UPC* group counts on an injection-seeded Q-switched pulsed Nd:Yag laser, emitting 10 ns duration, 1 J pulses with repetition frequency (*PRF*) of 10 Hz, at a wavelength of 1064 nm and, actually, these characteristics became the starting point of the selection process of the detection technique.

In the first place, the pulses emitted by this laser are too short for using coherent detection methods, whose precision depends directly on the spectral width of the transmitted pulses and is, therefore, strongly conditioned by their duration (commonly, above several hundreds of ns) [1]. Direct-detection techniques, which use frequency discriminators in the optical range and whose precision is not so significantly determined by the pulse duration, have, thus, to be employed. The edge technique (single [2] or double [3]) and the fringe-imaging technique [4] are the main direct-detection methods that can be used by lidar systems to measure winds. Both of them can be implemented with the same type of frequency discriminator, but the former needs much simpler photodetectors. For this reason, the edge-technique has been the method chosen to be used in the UPC Doppler lidar. Systems using this technique discriminate frequencies by

comparing the transmittance of optical filters. There exist, however, two variations of this method: the single-edge-technique or simply edge-technique, which uses only one filter, and the double-edge-technique, a more sophisticated and sensitive version using two filters. The edge-technique is the version that, for simplicity issues, will be implemented as a first step.

Edge-technique wind lidars can be in turn designed to rely either on aerosol (Mie) [5] or on molecular (Rayleigh) backscatter [2]. The proposed Doppler wind lidar will be in principle a ground-based station that will be housed in the *UPC* facilities in Barcelona, an urban area at sea level, where the mixing boundary layer is usually heavily aerosol-loaded. Aerosol-based systems are under these conditions better suited for wind measurements than the ones relying on molecular return. They are as well technologically less demanding as they are inherently more sensitive. In conclusion, the Doppler wind lidar that the *UPC* group has finally decided to develop will use the edge-technique and will operate relying on aerosol scattering. The work presented in this Ph. D. thesis has been therefore carried out in the frame of the general objective of developing a system with such characteristics.

1.3 Objectives

The first part of this thesis has been devoted to carry out the performance analysis and the optimization of the detection unit of an edge-technique-based Doppler wind lidar. The performance of the detection system is first analyzed in terms of precision (uncertainty) in the velocity measurements as a function of the configuration of the frequency discriminator, the incident optical power and the proportion of interfering Rayleigh component in the return signal. The results of this analysis permit to optimize the configuration of the proposed optical frequency discriminator (a Fabry-Perot interferometer). Power budgets for the planned *UPC* system in different measuring scenarios are then calculated. Precision parameters (uncertainty and range-time resolution) are calculated and are compared with standard reference examples. The effect of Rayleigh contamination both on the precision and on the accuracy (bias) of the measurements has been also studied in detail. Partial milestones of this part have been:

- Derivation of the expressions necessary for analyzing the precision and the accuracy of the measurements for an edge-technique-based Doppler lidar.
- Analysis of the precision (uncertainty) of the measuring system as a function of the configuration parameters of the frequency discriminator, the incident power and the Rayleigh contamination.
- Definition and application of an objective criterion for optimizing the configuration of the frequency discriminator of the Doppler receiver.
- Calculation of the power budgets of the *UPC* system under different measuring scenarios using the optimal configuration of the frequency discriminator.
- Analysis of the precision of the *UPC* system under different measuring scenarios. Comparison with reference examples.
- Analysis of the harmful effects of the molecular scattering on the accuracy (bias) of the aerosol-based wind measurements and demonstration of a possible solution.

As second objective of this thesis, a laboratory prototype has been designed and built in order to assess the implementation of the edge-technique as method to measure velocities and the performance of the critical subsystems of the instrument. Doppler wind lidars emit pulsed

radiation in order to achieve both range resolution and high-peak-power transmitted light pulses, which are indispensable for atmospheric sounding. However, dealing with pulsed atmospheric lidar signals is demanding: they are neither constant nor predictable and their duration is very short. Furthermore, it is difficult to validate the measurements since the true measured velocity is a priori unknown and is not easily measurable by independent means. For assessing the detection technique in controlled and convenient conditions, avoiding these difficulties, the laboratory set-up uses continuous-wave radiation and measures the velocity of hard targets. The performance analysis and the optimization of the Doppler receiver in such a version of the edge-technique-based Doppler lidar have been also carried out and are included in the first part of this work along with the study of the pulsed atmospheric case. Milestones of this part are:

- Design and implementation of the continuous-wave, hard-target laboratory prototype.
- Design and implementation of the calibration, control and measurement procedures and routines.
- Design and implementation of a tuning control loop for stabilizing the frequency discriminator with respect to the transmitted beam.
- Assessment and characterization of the Fabry-Perot interferometer as frequency discriminator.
- Assessment and characterization of the tuning control loop.
- Analysis of practical velocity measurements in terms of uncertainty (statistical noise) and bias error.
- Comparison with the expected performance.

1.4 Organization of the thesis

Chapters 2 and 3 treat fundamental introductory subjects. **Chapter 2** is dedicated to explain the basis of Doppler wind lidars. First, their main characteristics and applications and a brief history are described. Afterwards, the different techniques that can be used for detecting the Doppler frequency shift in the return signal are classified and their respective principles, applications and main characteristics are revised.

The main characteristics of the lidar signal (the one collected by the telescope after being scattered by the atmosphere) are reviewed in **Chapter 3**. The spectral width and the wavelength dependence are important for determining some system parameters. The lidar equation, derived after a complete temporal analysis, is indispensable for calculating power budgets and quality parameters of the velocity measurements.

In **Chapter 4**, the edge technique is presented and analyzed. Its principle is described, some quality parameters concerning the precision of the velocity measurements, such as the sensitivity to velocity changes, the signal-to-noise ratio and the uncertainty are defined and the expressions for calculating them are derived. The effect of Rayleigh component on the accuracy of the aerosol-based measurements is analyzed in detail too.

Chapter 5 is dedicated to analyze the performance of the measuring system and to calculate, using the uncertainty in the velocity determination as quality parameter, the optimal configuration of the frequency discriminator. These studies are carried out for two types of edge-technique-based Doppler lidars: first, a continuous-wave velocimeter like the one that

has been built to assess the measuring technique and secondly, a pulsed atmospheric wind lidar. In both cases, results are obtained as a function of the incident power, independently of the power budget of the system. Power budgets, quality parameters trade-offs and calculations about the effect of molecular contamination of the aerosol signals are included as well in this chapter.

In **Chapter 6**, a complete description of the laboratory continuous-wave prototype is presented. The expressions used to retrieve the velocity of the target from the detected voltages are derived. The measuring procedures and the schemes of the different routines that have been programmed and used for the velocity measurements are also described in detail.

Experimental results obtained with the laboratory prototype are reported in **Chapter 7**. Several practical measurements, whose objective is the validation of the implementation of the edge-technique as method to detect the velocity, have been made and are reported and analyzed in this chapter. Firstly, however, the performance of the frequency discriminator and the tuning control loop have been tested and carefully characterized.

A **final Chapter** including the main conclusions that can be derived from this thesis and a proposal of future lines of work related with them ends this dissertation.

2 Doppler wind lidars

2.1 Introduction to Doppler wind lidars

Remote spatially-resolved wind-speed measurements are required in many fields. Ground-based [6] and space-borne [7], [8] wind measurements can provide valuable insight in atmospheric dynamics with applications in meteorology and climate science. Global atmospheric wind profiles, from ground to 120 km, have special importance for the improvement of atmospheric analysis, being useful for climate research, numerical weather forecast, modelling of stratospheric transport and, in geophysical research, for improving gravity wave parameterization in models [7], [8], [9]. In the field of air-traffic safety, typical applications include detection and tracking of air turbulence, wind shear, gust fronts or aircraft wake vortices and true air speed (TAS) indicators [1], [7], [10], [11]. In the area of electrical power generation, the installation of wind farms has experienced an important growth in the last years. Large wind turbines are installed often in complex terrains, offshore, in forests, etc. Thus, flexible and accurate wind measurements become indispensable for site testing and operation optimization [12], [13]. In all these areas and others, the research community has been looking for wind velocity measurements with higher resolution, both in space and time, than that provided by the traditional techniques such as rawinsondes, jimspheres, or anemometers in ground stations, buoys, ships and aircrafts.

Lidars, which take advantage of the –in general terms– strong interaction between electromagnetic radiation at optical wavelengths and the atmosphere constituents to derive range-resolved information on the atmosphere state, offer a choice technique for wind velocity measurements. Capability for clear weather and long range operation permit lidars overcoming limitations of other systems, like radars operating in the microwave frequency range, which rely on the presence of precipitation or at least droplets to measure wind velocity, and sodars, whose range is typically limited to several hundred meters. Other

advantages of lidars are smaller dimensions –which makes them better suited for mobile platforms– and narrower transmitted beams –which provides higher spatial resolution in wind profiling–. On the other hand, their inability to operate under adverse weather conditions stands out as their main drawback. Regarding the basic measurement used to obtain the wind speed, wind lidar techniques can be classified into two basic categories: Doppler techniques and aerosol-inhomogeneity-tracking (direct motion detection) techniques. Doppler techniques measure the motion of the major constituent molecules of the atmosphere, N_2 and O_2, hence of the wind, or of particles suspended in the atmosphere (aerosols), which are taken as wind tracers, by determining the Doppler shift undergone by the backscattered radiation. According to the Doppler effect, the frequency shift of the backscattered light (f_D) is directly related to the wind speed in the line-of-sight direction (v_r):

$$f_D = -\frac{2}{\lambda_0} v_r \tag{1}$$

Where λ_0 is the emitted wavelength and the speed is counted positive when the wind is moving away from the instrument. Aerosol-inhomogeneity-tracking techniques rely on the existence of aerosol spatial inhomogeneities –a common situation in the mixing layer– whose motion is tracked by processing the direct-detected backscatter lidar profiles along one or several line of sights.

Doppler techniques can be in turn broadly classified into two groups: coherent and direct-detection techniques. Coherent systems measure the Doppler shift using heterodyne techniques that extrapolate to the optical domain radio-frequency radar techniques. Their operation is based on mixing the return signal with a frequency-stable local oscillator (a laser beam) on a wideband optical detector; the resulting intermediate-frequency signal is processed for estimating its spectral peak. This technique offers enhanced photoreceiver sensitivity and high precision, but technological constraints limit its operation to the infrared region, where molecular return is weak and, as a result, its applicability is restricted to regions with high aerosol content, basically within the planetary boundary layer. Direct-detection-based Doppler wind lidars use optical frequency discriminators to spectrally resolve, prior to detection, the return optical signal. In this case, no technological restrictions prevent their operation in the ultraviolet region, where molecular return is strong. Wind measurements in aerosol-free conditions are thus possible, making currently this technique the preferred one for wind profiling in the mid and upper troposphere and in the stratosphere.

2.2 History of Doppler wind lidars

The origin of Doppler wind lidars is traced back to the success of laser Doppler velocimetry using coherent techniques for measuring flows in wind tunnels and high speed jets in mid sixties [14]-[16]. In 1967, Jelalian and Huffaker [17] applied this technique for the first short-range atmospheric wind velocity measurements using a continuous-wave CO_2 laser operating at 10.6 μm. Later development of successive generations of coherent lidars has been related to advances on laser technology. The appearance of CO_2 pulsed lasers based on the master oscillator / power amplifier architecture (MOPA) in the early seventies, made possible longer range observations and better range resolution [18], [19] and the transverse excited atmospheric technology (TEA) permitted, in the early eighties, CO_2 lasers increasing the pulse energy above 1 J and perform long-range wind speed measurements of atmospheric winds [1]. In 1985, the first lidar using a solid-state Nd:YAG laser at 1.06 μm and a MOPA configuration was built [20]. This technology, in spite of several drawbacks like noneye

safety and stricter optical requirements for coherent detection associated to shorter wavelengths, provided smaller size, long life operation and higher backscatter coefficients and velocity resolution. Eye safety and higher atmospheric transmission encouraged in the first nineties the development of coherent lidars using solid-state transmitters operating at wavelengths close to 2 μm (e.g. Tm,Ho:YAG at 2.09 μm [21] or Tm:YAG at 2.01 μm [22]). Successive improvements have since been achieved in measurement capabilities of the 2 μm solid-state systems, reducing their size and power requirements and increasing their reliability. Finally, a great deal of effort has recently been addressed to the development of systems based on fiber lasers at 1550 nm, with MOPA architecture, which offer evident advantages of availability and reliability [23].

Concerning direct-detection techniques the first measurements of atmospheric wind velocity were reported by Benedetti-Michelangeli and co-workers in 1972 [24]. However, the lack of a suitable reliable high-power-pulse laser limited these measurements to distances of only several hundreds of meters. The availability of single-mode high-power solid-state transmitters in the mid eighties was the starting point for developing systems that, operating in the visible and ultraviolet regions, and using direct-detection techniques, were able to measure wind velocities relying on molecular return. Different techniques were proposed, analyzed and implemented since the late eighties, and several systems have been operated from ground-based or mobile stations for wind profiling of the atmosphere [3], [25], [26], [27], [28]. Demonstrated clean-air measuring capabilities made direct-detection techniques candidates to be flown in space-borne platforms for measuring global scale wind fields. In 2000, the European Space Agency started the technical development of the Atmospheric Dynamics Mission (ADM-Aeolus), whose launch is scheduled for 2013 and includes a Doppler wind lidar instrument based on direct-detection techniques for space-borne global observations [29]. The objective of a joint NASA, NOAA and US Department of Defense mission is to field by 2022 the Hybrid Doppler Wind Lidar (HDWL) on a research satellite. The system will use both coherent detection for accurate observations when sufficient aerosols or clouds exist and molecular direct-detection techniques above 2 km [30].

2.3 Types of Doppler wind lidars

2.3.1 Coherent Doppler wind lidars

Coherent Doppler wind lidars adapt to optical frequencies classical radio-frequency heterodyne detection techniques to measure the Doppler shift in the return signal backscattered by particles that are suspended in the air and dragged by the wind. Fig. 1 shows the basic layout of a lidar using coherent detection. A frequency stable, narrowband, continuous-wave (CW) reference laser is used both to transfer its spectral purity to the transmitter and as the local oscillator needed for heterodyne detection. High spectral purity is required both in the transmitter and in the reference laser since it determines the resolution of the Doppler shift detection. Frequency stability is also important to achieve accuracy in the measurements. The optical mix between the collected return signal and the reference laser beam is usually achieved by superposing the wave fronts on the active surface of a photodetector, such as a photodiode or a photomultiplier. If the frequencies are close enough, the detected beat signal can be electrically amplified, low-pass filtered and processed. A frequency shifter is normally used to perform heterodyne instead of homodyne detection, which is necessary to detect the sign of the detected velocity.

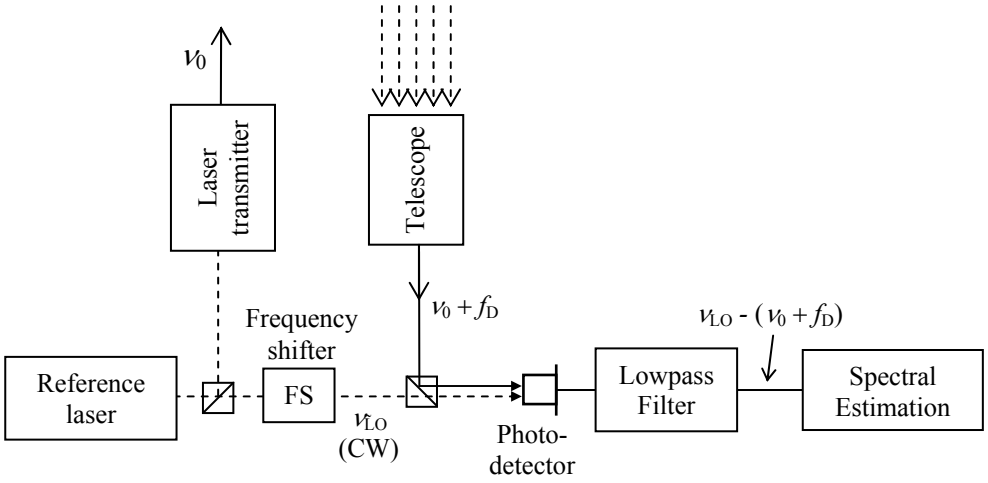

Fig. 1. *Scheme of a coherent Doppler lidar detector.*

Enhanced sensitivity is one of the features of coherent optical detection. The combination on the optical detector of a weak optical signal (the received one) with the strong local oscillator laser results in a beat signal whose power is proportional to the power of both. If the power of the local oscillator is big enough, the total noise is also proportional to it and, as a consequence, the signal-to-noise ratio only depends on the signal power. In this situation, the signal-to-noise ratio is limited by the quantum noise in the signal detection and is the maximum possible (quantum-limit) [31], [32], [33].

Also, optical background noise is typically not a problem in coherent lidars for two reasons: it is not phase coherent and therefore does not mix efficiently with the local oscillator on the photodetector and most of the background photons that do produce a heterodyne beat fall outside the electronic pass band of the receiver [32].

On the other hand, the main drawback of coherent detection is its difficulty to deal with zones with low aerosol content. In these regions, which include large zones of the southern hemisphere, the central regions of the oceans and practically the whole atmosphere above the boundary layer, molecular return must be used. The dependence with the operating wavelength of the corresponding Rayleigh backscatter coefficient is proportional to λ^{-4} and as a result, short, ultraviolet wavelengths are the optimal for wind molecular measurements. Optical heterodyne detection suffers from important technological restrictions at short wavelengths. First, the requirements on the alignment and on the optical surface quality of the telescope are stricter than at longer wavelengths. Also, the wavefront degradation effects due to atmospheric refractive turbulence are more harmful, affecting to the spatial coherence of the backscattered light and, as a consequence, to the heterodyne detection efficiency [18], [34]. Moreover the large spectral width of the beat signal arising from the molecular scattering (see section 3.1.1) would require large bandwidths in the electrical part of the photoreceiver and put heavy constraints in the acquisition system and data processing. These technological issues limit the operation of coherent Doppler Wind Lidars to the infrared region, roughly between 1 and 10 μm, where aerosol return is dominant.

The coherent detection is therefore an extremely sensitive technique that has been widely used in wind Doppler lidar and is the preferred one for measurements in most of the continental regions in the lower troposphere, where the concentration of aerosols is high.

2.3.2 Direct-detection Doppler wind lidars

Unlike coherent systems, direct-detection Doppler wind lidars do not use optical heterodyne mixing, previous to frequency analysis, for measuring the Doppler shift in the return signal. Instead, the collected light is spectrally analyzed prior to detection by using optical frequency discriminators [2], [4], [24]. Two basic types of frequency discriminator are used in direct-detection systems. The first group is formed by high resolution optical filters, like Fabry-Perot interferometers or filters based on molecular absorption lines, in which their frequency response is used to convert frequency shifts into changes of the detected optical intensity. This technique is usually called 'Edge Technique' or 'Double-Edge Technique' if the system uses two filters to discriminate frequencies. Fig. 2 shows this principle for both variants of the technique.

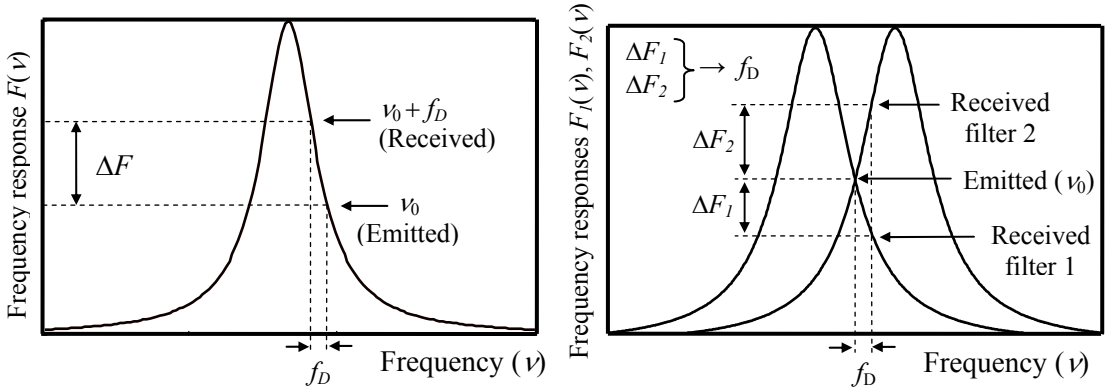

Fig. 2. *Principle of operation of direct-detection techniques based on frequency to intensity conversion. Edge technique (left) and double-edge technique (right).* ν_0 *is the emitted frequency,* f_D *is the Doppler frequency shift between received and emitted signals,* $F(\nu)$, $F_1(\nu)$ *and* $F_2(\nu)$ *are the frequency responses of the optical filters used to perform the frequency to intensity conversion (in this case Fabry-Perot interferometers) and* ΔF, ΔF_1 *and* ΔF_2 *are the changes in the filters transmission, due to frequency changes, to be detected.*

A second group of direct-detection receivers use fringe pattern imaging instruments as frequency discriminators. Systems using this technique resolve the backscattered Doppler shift by projecting the interference pattern from an optical interferometer onto a multichannel detector. In the case of using a Fabry-Perot interferometer, only angles fulfilling the resonance condition into the cavity ($2d\cos\theta = m\lambda$, where θ is the incidence angle onto the etalon, d is the cavity length and m is an integer number [35]) will be completely transmitted and, as a result, the output of the interferometer, properly imaged, will be a collection of concentric rings. The transmitted angles, and consequently the position of the rings, depend on the incident wavelength. The Doppler shift is obtained measuring the angular displacement of the fringe locations (Fig. 3).

Direct-detection Doppler wind lidars are suited to operate in the ultraviolet region and therefore can measure in aerosol-free conditions. This stands out as their main advantage with respect to lidars based in coherent detection and makes them a good choice for measuring global-scale wind fields from space-borne stations and for stratospheric wind profiling. However, although current interest on non-coherent systems is mainly due to their capability for measuring winds in aerosol-free conditions, and particularly to their suitability for space-borne applications, all direct-detection techniques can be also applied for aerosol (Mie) return. Although their performance is, in aerosol-loaded regions, worse than the one of coherent systems, some advantages like their flexibility to be easily adapted to molecular

measurements and the possibility of using shorter pulses make them an interesting option in some cases. In such conditions, however, some of the main design parameters of the receiver and the performance of the measuring system are different from those of molecular-return-based systems.

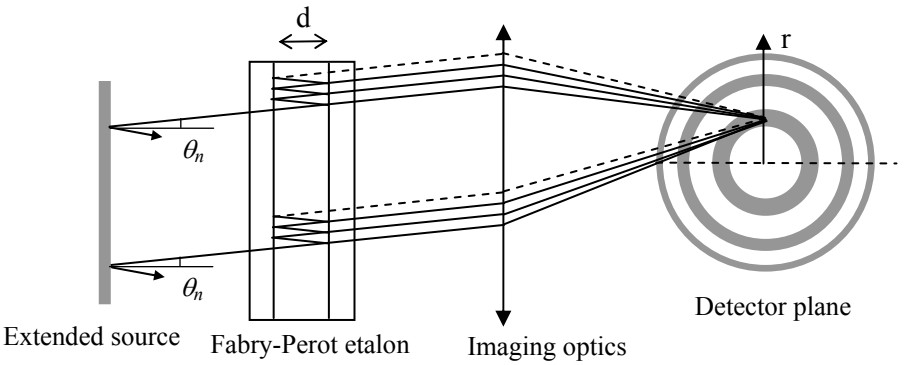

Fig. 3. *Principle of operation of a lidar based on the fringe-imaging technique, in this case using a Fabry-Perot interferometer as frequency discriminator.*

Typical accuracy requirements, often better than few meters per second, and measurement ranges, usually from ground to tens of kilometres, oblige direct-detection Doppler wind lidars to use single-frequency, high peak-power pulsed lasers as optical sources. Although other technologies were initially considered [24], [36], as soon as they were available in the mid 80s, injection-seeded, high-pulse-energy, single-longitudinal mode Nd:YAG lasers have been universally used in Direct-Detection instruments due to their spectral stability, reliability, high efficiency, long lifetime and commercial availability. Due to the λ^{-4} dependence of the Rayleigh scattering, systems relying on aerosol return usually operate using the fundamental wavelength (1064 nm) in order to minimize the molecular background contamination (section 3.1.3). On the other hand, the use of non-linear elements in the transmitter permits the systems based on molecular return to operate at doubled (wavelength 532 nm) and tripled (355 nm) frequencies of the fundamental wavelength to enhance the available backscattered Rayleigh return. Typical pulse duration varies from 5 to 30 ns. Unlike for coherent systems, longer pulses do not improve significantly the precision of the instrument [2]. In aerosol systems, although longer pulses result directly in a spectrally narrower return, the precision is limited by the resolving power of the frequency discriminator. In molecular systems, the spectral width of the return is basically determined by the spectral broadening suffered by the scattered light due to Brownian motions of the molecules (section 3.1.1), being only residually dependent on the spectral width of the emitted pulse.

3 Elastic scattering of light in the atmosphere

Lidar systems retrieve information of the state of the atmosphere by analyzing the electromagnetic energy that is scattered when it is illuminated with a laser beam. Different contributions to the overall scattered energy can be identified and classified depending on the characteristics of the physical phenomenon responsible of it. A first classification is established between elastic and non-elastic scattering processes. By elastic scattering it is understood that one in which the energy of the incident photons, and therefore their frequency, is conserved and only their direction changes. Elastic scattering can be, in turn, classified in Mie and Rayleigh scattering. Mie scattering refers to elastic scattering in aerosol particles whose size is comparable or larger than the wavelength of the incident radiation, while Rayleigh scattering is produced in particles whose size is much smaller than the incident wavelength, including the molecules of the constituents of the atmosphere. Doppler wind lidars measure the wind speed by detecting the frequency shift, due to Doppler effect, that is undergone by the radiation that is elastically scattered either by the air molecules or by the suspended particles. An accurate analysis and the design of any Doppler wind lidar require taking in account the main characteristics of the return signal due to elastic scattering. In this chapter, these characteristics will be discussed and several analytical expressions will be derived in terms of transmitter, receiver and atmospheric parameters.

3.1 Frequency features of the return signal

Lidars employed to profile atmospheric variables emit highly energetic laser pulses. As they propagate, they encounter an atmosphere composed of gas molecules and suspended particles that scatter part of the energy of the travelling wave. Part of this scattered radiation propagates backwards, towards the lidar system, and is collected by the telescope of the system. At any time, the incident field includes the contribution of a big amount of scatterers (all those within the volume limited by the laser beam and a slice of the atmosphere located at

a distance proportional to the time elapsed since the emission and with a thickness that depends on the pulse duration [37]). If all the scatterers within this volume were stationary with respect to each other, the Doppler shift would be common to all the contributions. In a real situation, nevertheless, the atmosphere constituents and suspended particulates are subject to random motion due to collisions –thermal (Brownian) motion– and turbulence. This motion is superimposed on the possible drift (advection) velocity that the particles may have. The collection of radial velocities within the scattered volume results in a collection of different Doppler shifts in the return signal and, as a consequence, in a broadening of the spectrum of the backscattered radiation with respect to that of the transmitted one. Doppler wind lidars, in fact, measure the average velocity of the individual scatterers contributing to the incident field at any time, i.e. the wind speed, by detecting the average Doppler shift in the broadened return spectrum. The thermal-motion-induced broadening is negligible for the scattering produced by particles (aerosols or droplets) [38], but cannot be ignored in the scattering arising from the air constituent molecules. As a result, there exist big differences in the spectral characteristics of the return signal depending on the size of the scatterers with respect to the wavelength of the incident wave and these differences strongly condition the requirements imposed to the receivers. As mentioned in the introduction of this chapter, according to this critera, elastic scattering can be broadly classified in two types: Mie and Rayleigh scattering.

3.1.1 Rayleigh scattering

The scattering of electromagnetic radiation by particles that have a radius much smaller than the wavelength, including the molecules of the air, is known as Rayleigh scattering. However, in the context of lidar, Rayleigh scattering is always used as synonym of molecular scattering in the atmosphere. The standard mixture of gaseous species in the atmosphere contains mainly nitrogen (N_2, 78%) and oxygen (O_2, 21%). In spite of existing other permanent and non-permanent species, it can be assumed that they are the responsible of the Rayleigh return in a lidar system [39].

The effect of thermal motion on the broadening of the backscattered radiation is very well modelled by considering the atmosphere as formed by fictitious "air molecules" of mass equal to the weighted (according to their respective proportions) average of the masses of the N_2 and O_2 molecules. The resulting "air molecule" mass turns out to be approximately $m_{am} = 4.8 \times 10^{-26}$ kg. According to the Maxwell-Boltzmann's law for the velocity distribution of the molecules of a gas at temperature *T*, the probability density function of a given component v_u of the "air molecule" velocity will correspond to that of a normal law,

$$f\left(v_u\right) = \sqrt{\frac{m_{am}}{2\pi k\, T}} \times \exp\left(-\frac{m_{am} v_u^2}{2\, k\, T}\right), \tag{2}$$

where $k = 1.38 \times 10^{-23}\ \mathrm{J\,K^{-1}}$ is the Boltzmann's constant. In conditions in which the mean free-path length between collisions of the molecules is much longer than the incident radiation wavelength, the broadening of the spectrum of the backscattered radiation can be calculated directly from Eq. (2) and taking in account the Doppler effect (Eq. (1)) for translating velocities to frequencies. Assuming a monochromatic radiation of frequency $\nu_0 = c/\lambda_0$ illuminating a volume of air with radial component of the draft velocity v_r, the Rayleigh-backscattered radiation would in these conditions have a Gaussian spectrum centered at

$$\nu = \left(1 - 2\frac{v_r}{c}\right)\nu_0 , \tag{3}$$

with a full width at $1/\sqrt{e}$ of its maximum given by

$$\Delta\nu_R = \frac{4}{\lambda_0}\sqrt{\frac{kT}{m_{am}}} ; \tag{4}$$

as an example, for $\lambda_0 = 355$ nm (the wavelength corresponding to the third harmonic of the Nd:YAG laser fundamental wavelength) and T = 290 K the widening would be $\Delta\nu_R$ = 3.24 GHz. However, these conditions only occur at altitudes large enough for the pressure to be low and the mean path between collisions large. If the mean free path between collisions of the air molecules becomes comparable to, or shorter than, the electromagnetic radiation wavelength, the interaction of the electromagnetic wave with sound waves must be taken into account in the scattering (Rayleigh-Brillouin scattering [40], [41]). Fig. 4 (left) shows the mean free path given by the US Standard Atmosphere 1976 model up to an altitude of 20 km. In Fig. 4 (right) the expected backscatter spectra around the central Doppler-shifted backscatter for an incident wave at 355 nm wavelength are represented assuming the US Standard Atmosphere conditions at sea level and at 5000 m altitude using the Pan s7 model [42]; the Gaussian backscatter spectrum of purely temperature-broadened Rayleigh scattering for 5000 m conditions is also represented [43].

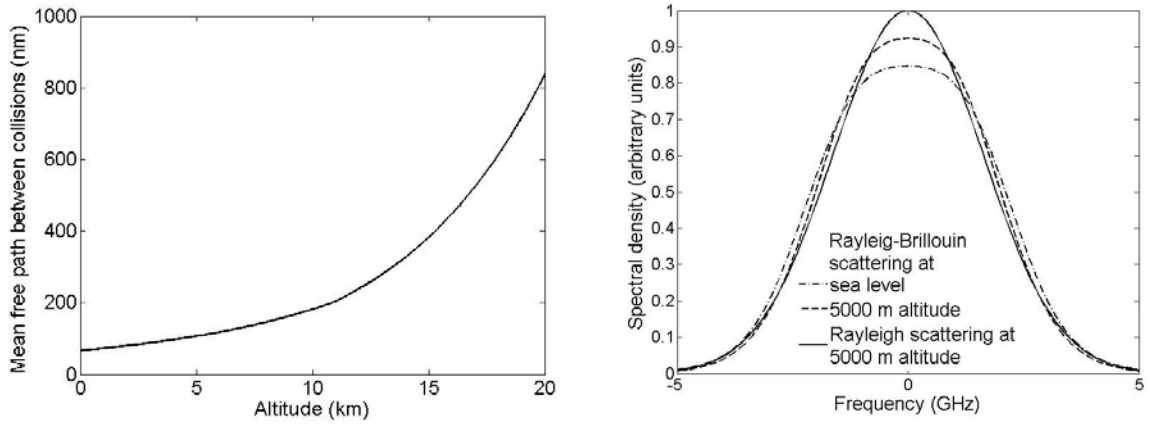

Fig. 4. *Effect of collisions of air molecules on the spectrum of the backscattered radiation. Mean free path between collisions after the US Standard Atmosphere Model, 1976 (left); Rayleigh-Brillouin normalized backscatter spectra at 355 nm around the central backscatter frequency at sea level (dash-dotted curve) and 5000 m (dashed curve) calculated using the Pan s7 model* [42]*; the continuous curve represents the ideal Rayleigh scattering at 5000 m (right)* [43].

The Rayleigh atmospheric volume backscatter coefficient, indicating the strength of atmospheric scattering in air molecules, turns out to depend on density, pressure and temperature and, as a consequence, presents a slow, uniform and predictable variation with altitude. Its dependence on the radiation frequency follows a ν^4 law. A simplified model, using an exponential function decreasing with altitude (h) and taking into account the dispersion of the refractive index of the air, is given by Eq. (5) [44].

$$\beta_R(\lambda, h) = \left(\frac{\lambda_0}{\lambda}\right)^{4.09} \exp\left(-\frac{h}{h_0}\right) \times 10^{-7} \text{ m}^{-1}\text{ sr}^{-1} \tag{5}$$

Where $\lambda_0 = 1064$ nm and $h_0 = 8$ km are respectively a reference wavelength and altitude.

3.1.2 Mie scattering

The term Mie scattering is used in atmospheric propagation to describe the scattering by aerosol particles with size comparable or larger than the wavelength of the incident radiation. Aerosol atmospheric particles refer to solid or liquid material suspended in the air. They are produced by a big number of different processes that occur on land and water surfaces and in the atmosphere itself. They can have a natural origin, like dust, sea salt or water vapour droplets or can be produced by human activities, like biomass and fossil fuel burning, agricultural activities or industrial pollution, injecting directly particles to the atmosphere or producing precursor gases that condense in the atmosphere to form aerosols. Most of the aerosol particles are however released by interaction between the lowest atmospheric layer and the surface of the earth. Hence, the greatest variety and concentration of aerosols is found in the lower troposphere, within the planetary boundary layer, whose average thickness is approximately 2 km. The aerosol concentration in this layer displays high variability with time, meteorological conditions, climate, etc. and it is thus not uniformly distributed, being urban and desert areas where largest concentrations can be observed. On the other hand, there are large regions of the southern hemisphere and mid-oceanic regions with very low aerosol concentrations even at low altitudes. In a second region that extends from 2 to 6 km, typically a fast exponential decay of the concentration of aerosols with altitude can be observed, while within the stratospheric layers, up to 30 km, aerosol concentration depends strongly on volcanic activity [45]. A thin layer of sulphurous particles, known as the Junge layer, can be also usually found between the tropopause and 30 km altitude [39].

Concerning the spectral features of the return signal associated to Mie return, it can be assumed that thermal-motion-induced broadening is negligible for the scattering produced by aerosols or droplets (as example, it can be estimated that, in a standard atmosphere, the dispersion of the speed due to this effect on a 1μm-size water droplet, with typical mass 4.2×10^{-15} kg, is less than 1 mm/s (Eqs. (4) and (1)). Hence in practice, it can be considered that the spectrum of the detected signal is approximately the same than the one of the emitted pulse [38].

The size of aerosol particles is very diverse, ranging from 1 nm to about 20 μm with a very complex and variable distribution [39]. The dependence on the wavelength of the associated backscatter coefficient is thus not simple and goes from being proportional to λ^{-3} to $\lambda^{-0.3}$, depending mainly on the aerosol content and the size distribution. The strongest dependence is given in the cleanest conditions, with extremely low aerosol content comprised of newly formed, small particles, and the weakest one takes place in high aerosol-loading conditions. Fig. 5 shows this dependence, modelled in low, moderate and high aerosol-loading conditions [46].

Unlike the Rayleigh case, it is not possible to predict the value of the aerosol volume backscattering coefficient in the atmosphere using simple models. Apart of its non-simple dependence on the propagation wavelength, it depends mainly on the aerosol concentration, which is very variable, and also on other characteristics such as particles size distribution, constituents, humidity effects, time effects, etc.

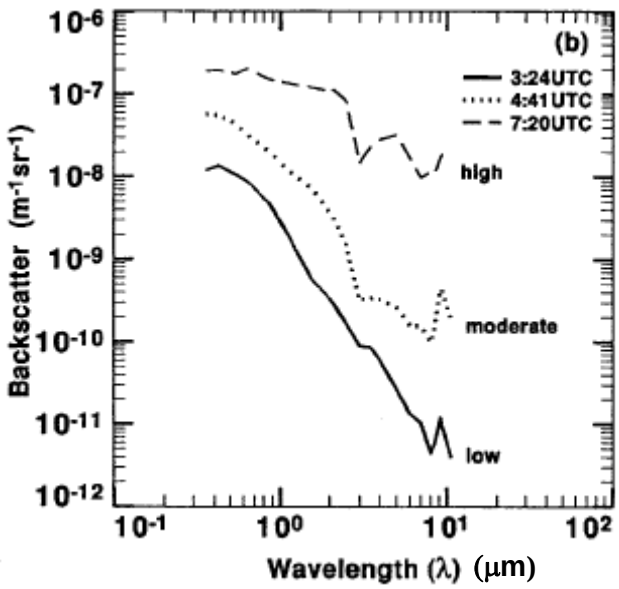

Fig. 5. *Aerosol backscatter coefficient. Dependence with wavelength* [46].

3.1.3 Spectral characteristics of the elastic return

The detected signal corresponding to the elastic return will be actually a compound signal with both Rayleigh and Mie contributions. As seen in sections 3.1.1 and 3.1.2, Rayleigh component of the return signal can be accurately predicted using the pressure and temperature data from radiosoundings or even simple atmospheric models but this is not the case for the Mie component. Several parameters have been defined and can be used to characterize the proportion of both components in the return signal. The aerosol scattering ratio (*ASR*) is one of them and is defined as the ratio of the total (aerosol + molecular) volume backscattering coefficient to the molecular volume backscattering coefficient

$$ASR(\lambda,h)=\frac{\beta_R(\lambda,h)+\beta_M(\lambda,h)}{\beta_R(\lambda,h)}, \tag{6}$$

where $\beta_M(\lambda,h)$ is the Mie volume backscattering coefficient. The aerosol scattering ratio depends on the aerosol content of the atmosphere in the observed region, on the altitude and on the operating wavelength. Obviously, the higher is the concentration of aerosols, the bigger will be the *ASR*. Also, at higher altitudes, the Rayleigh return is weaker and as a consequence, in atmospheric regions with the same aerosol content, the higher is the altitude the bigger will be the *ASR*. Finally, regarding the wavelength dependence of Rayleigh and Mie scattering (λ^{-4} and λ^{-3} at maximum, respectively (see sections 3.1.1 and 3.1.2) the *ASR* will be in general bigger at longer wavelengths. Regarding the respective spectrums, as stated in section 3.1.2, the Mie component has approximately the same spectral width than the emitted pulse, while the Rayleigh spectral width depends basically on the temperature of the observed atmospheric region and is in any case much bigger than the one of the Mie component. Both components will however undergo the same frequency shift (f_D), proportional to the component of the bulk wind velocity along the line-of-sight of the instrument.

As example, Fig. 6 shows a representation of the normalized spectrum of the elastic return when a laser emitting 10 ns duration Gaussian pulses at 1064 nm illuminates a region of the atmosphere where the temperature is 300 K, the aerosol scattering ratio is 1.2 and the radial

velocity of the wind is 25 m/s. A representation of the normalized spectrum of the emitted pulse is also included in the figure.

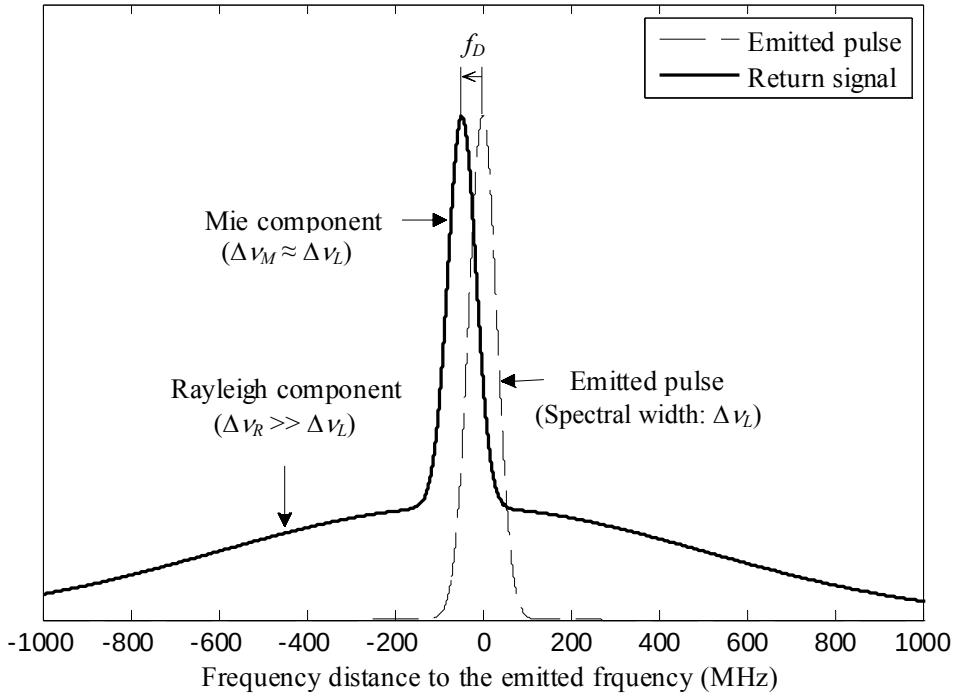

Fig. 6. *Spectral features of the emitted pulse and the elastic return. $\Delta\nu_L$, $\Delta\nu_M$ and $\Delta\nu_R$ are respectively the spectral width of the emitted pulse, the Mie component and the Rayleigh component of the elastic return and f_D is the Doppler frequency shift between the received components and the emitted pulse.*

3.2 The lidar signal. Temporal analysis of the elastic return

In section 3.1, the spectral characteristics of the return signal have been stated. They are important mainly as they determine the configuration of the frequency discriminator. The wavelength dependence of both Rayleigh and Mie return has been also described; it conditions the choice of the operating wavelength as a function of the measuring scenario. In this section, the temporal characteristics of the detected signal and the received power will be derived and discussed in detail. The temporal analysis of the electric field on any point on the receiving area will permit to demonstrate the frequency shifting undergone by the scattered radiation and its relation with the radial velocity of the scatterers (Doppler effect), which is the basic physical principle used by Doppler lidars to measure velocities. The integration of the optical intensity over the receiving area will provide as a result the overall optical power collected by the telescope at any time (or, what is the same, from any distance) as a function of several atmospheric and system parameters, which is commonly referred to as the lidar equation. This result is indispensable to calculate power budgets, carry out performance analysis in different measuring scenarios and design the optimal configuration of the detection unit.

3.2.1 Incident electric field and optical intensity on the receiving area

Fig. 7 shows the schematic of a lidar system in coaxial-monostatic configuration illuminating a region of the atmosphere where an individual static scatterer (aerosol particle or air

molecule) is placed. The optical source is considered as a point and radiating uniformly in a small solid angle.

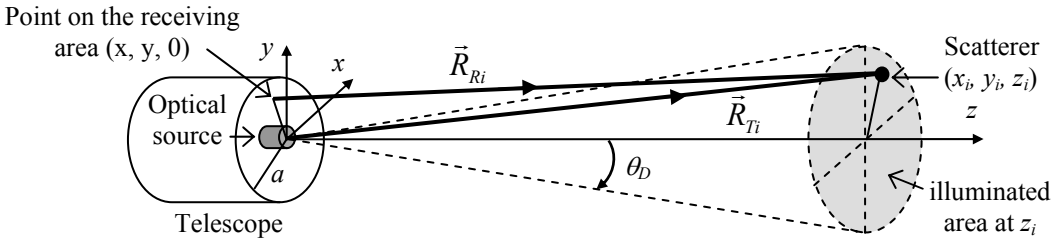

Fig. 7. *Lidar in monostatic configuration and the geometrical arrangement.*

In Fig. 7, a is the radius of the receiving telescope and $2\theta_D$ the divergence angle of the emitted beam, for which the approximation of a uniform intensity is made. The origin of the coordinate system is located at the lidar, with the z axis coincident with the system axis. The coordinates of the scatterer are (x_i, y_i, z_i), so its position vector is $\vec{R}_{Ti} = x_i\hat{x} + y_i\hat{y} + z_i\hat{z}$, $\hat{x}$, $\hat{y}$ and $\hat{z}$ denoting the unit vectors in the direction of the corresponding axes. $\vec{R}_i$ is the vector going from a point $\vec{\rho} = x\,\hat{x} + y\,\hat{y}$ on the entrance pupil of the receiving telescope to the scatterer position. Their respective magnitudes are given by Eqs. (7) and (8).

$$R_{Ti} = \left|\vec{R}_{Ti}\right| = \sqrt{x_i^2 + y_i^2 + z_i^2} \tag{7}$$

$$R_{Ri}(x,y) = \left|\vec{R}_{Ri}(x,y)\right| = \sqrt{(x-x_i)^2 + (y-y_i)^2 + z_i^2} \tag{8}$$

In the following development and only for intensity calculations, the distances between each point of the illuminated plane area at a distance z_i from the source (x, y, z_i) and each point of the receiving area $(x, y, 0)$ will be considered equal to z_i $\left(R_{Ri}(x,y) = z_i\ ;\ \forall(x_i, y_i)\right)$. This is a good approximation if the divergence angle of the beam is small and $z_i \gg a$. The normalized transmitted electric field (in $\mathrm{W}^{1/2}\mathrm{m}^{-1}$ units) illuminating the scatterer, located at the point (x_i, y_i, z_i), can then be expressed as follows.

$$U_T(x_i, y_i, z_i, t) = \left(\frac{P_T}{\pi z_i^2 \theta_D^2}\right)^{1/2} s(t - z_i/c) \exp\left[-\frac{1}{2}\int_0^{z_i} \alpha(z)\,dz\right] \exp(-jkR_{Ti}), \tag{9}$$

where P_T is the is the average power of the transmitted pulse, $\alpha(z)$ is the extinction coefficient along the path, and k is the wave number; $s(t)$ is a function describing the field temporal envelope, such that

$$\frac{1}{\tau_p}\int_{-\infty}^{\infty} s^2(t)\,dt = 1, \tag{10}$$

where τ_p is the nominal pulse duration (see Fig. 8).

When this field illuminates an individual scatterer, part of the incident power is backscattered and collected by the telescope. It can be assumed that all the scatterers in the illuminated area 'see' the receiving area (A_r) through the same solid angle ($\Delta\Omega = A_r / z_i^2$).

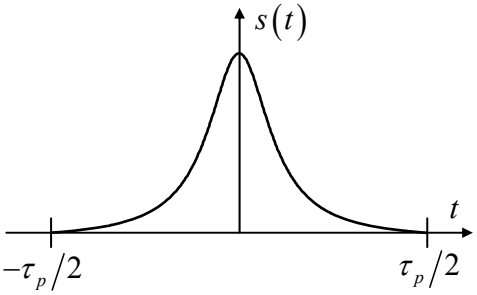

Fig. 8. *Field temporal envelope*

The incident field on each point over the telescope receiving area $(x, y, 0)$ can then be calculated using the following expression.

$$U_i(x, y, 0, t) =$$

$$= U_T(x_i, y_i, z_i, t - z_i/c)\left(\frac{\sigma_{bi}\,\Delta\Omega}{A_r}\right)^{1/2} \exp(\phi_i) \exp\left[-\frac{1}{2}\int_0^{z_i}\alpha(z)\,dz\right] \exp\left[-jkR_{Ri}(x, y)\right] \quad (11)$$

Where σ_{bi} is the cross-section per solid angle (m^2/sr) of the scatterer '*i*' in the direction of the telescope (backscatter direction) and ϕ_i is the phase of the corresponding field reflection coefficient. Substituting now the transmitted field given by Eq. (9)) in the expression of the incident field (Eq. (11)):

$$U_i(x, y, 0, t) = \left(\frac{P_T\,\sigma_{bi}}{\pi\, z_i^4\,\theta_D^2}\right)^{1/2} s(t - 2z_i/c) \exp\left[-\int_0^{z_i}\alpha(z)\,dz\right] \exp\left\{\phi_i - jk\left[R_{Ti} + R_{Ri}(x, y)\right]\right\}, \quad (12)$$

If we consider that the scatterer is moving with respect to the position of the lidar with a rectilinear, constant velocity ($\vec{v}_i$), the propagation distances affecting the phase, R_{Ti} and R_{Ri}, will be respectively

$$R_{Ti} = R_{Ti0} + \left(\vec{v}_i \cdot \hat{R}_{Ti}\right) t = R_{Ti0} + v_{Ti}\, t \quad (13)$$

$$R_{Ri}(x, y) = R_{Ri0}(x, y) + \left[\vec{v}_i \cdot \hat{R}_{Ri}(x, y)\right] t = R_{Ri0}(x, y) + v_{Ri}\, t\,, \quad (14)$$

where v_{Ti} and v_{Ri} are respectively the velocity components in the directions given by the unit vectors $\hat{R}_{Ti} = \vec{R}_{Ti}/R_{T_i}$ and $\hat{R}_{Ri} = \vec{R}_{Ri}/R_{Ri}$. If the beam divergence angle is small and $z_i \gg a$, it can also be assumed that $v_{Ti} = v_{Ri} = v_{ri}$, which is commonly referred to as the radial component of the velocity, in this case corresponding to the scatterer '*i*'. The incident field can be therefore written as

$$U_i(x, y, 0, t) =$$

$$\left(\frac{P_T\,\sigma_{bi}}{\pi\, z_i^4\,\theta_D^2}\right)^{1/2} s(t, z_i) \exp\left[-\int_0^{z_i}\alpha(z)\,dz\right] \exp(-j2kv_{ri}t) \exp\left\{\phi_i - jk\left[R_{Ti} + R_{Ri}(x, y)\right]\right\}. \quad (15)$$

The term $\exp(-j2kv_{ri}t)$ is the expression of a change in the frequency of the received field with respect to the transmitted one that is proportional to the radial velocity of the scatterer;

this phenomenon is known as Doppler effect. This Doppler frequency shift is, in general, for a target moving away from the observer at a radial velocity v_r,

$$f_D = -\frac{2kv_r}{2\pi} = -\frac{2}{\lambda_0}v_r \,. \tag{16}$$

In practice one never meets the situation described above. Rather the emitted radiation will encounter an atmosphere composed of more or less (depending on the atmospheric pressure) tightly packed gas molecules and suspended particles. The backscattered field on the telescope area at any time includes the contribution of all the scatterers within a layer of the atmosphere located at a distance $R = c\,t/2$, where t is the time elapsed since the pulse emission, whose thickness $\Delta z = c\,\tau_p/2$ corresponds to the range resolution defined by the effective pulse length (Fig. 9) [37].

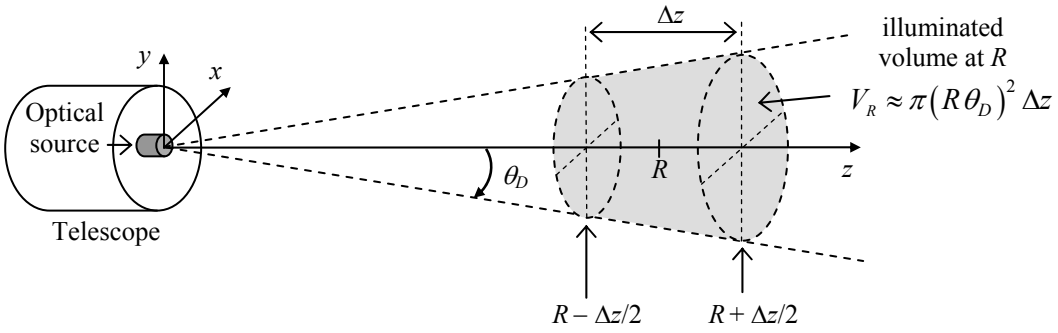

Fig. 9. *Atmospheric layer of thickness Δz at distance R.*

The field on the receiving area can therefore be calculated as

$$U(x,y,0,t) = \sum_{i=1}^{N_{vR}} U_i(x,y,0,t) =$$

$$= \sum_{i=1}^{N_{V_R}} \left\{ \left(\frac{P_T\,\sigma_{bi}}{\pi\, z_i^4\, \theta_D^2} \right)^{1/2} s(t - 2z_i/c) \exp\left[-\int_0^{z_i} \alpha(z)\,dz \right] \exp(-j2kv_{ri}t) \exp\left\{ \phi_i - jk\left[R_{Ti} + R_{Ri}(x,y) \right] \right\} \right\} \tag{17}$$

with $N_{V_R} \approx n(R)\pi(R\theta_D)^2 \Delta z$ the number of scatterers in the volume $V_R = \pi(R\theta_D)^2 \Delta z$, located at a distance R from the receiver (Fig. 9), and $n(R)$ the scatterer number concentration (m^{-3}) at that distance. It will be considered that the layer thickness is small enough to assume that the velocity of all the scatterers within the volume is the same ($v_{ri} = v_r \;;\; \forall i$). This is a good approximation when the scatterers are aerosol particles of size comparable or larger than the wavelength of the incident radiation. In the case of much smaller particles or molecular scattering, this assumption cannot be made and consequences will be discussed later. Under the very good approximation that the different z_i in the denominator of the first factor in the sum terms of Eq. (17) within the volume V_R can be replaced by R and considering moreover the same extinction, the electric field on the telescope area at any time can be written as

$$U(x,y,0,t) =$$

$$\left(\frac{P_T}{\pi R^4 \theta_D^2}\right)^{1/2} \exp\left[-\int_0^R \alpha(z)dz\right] \exp(-j2kv_r t) \sum_{i=1}^{N_{V_R}} \left[\sigma_{bi}^{1/2}\, s(t-2z_i/c) \exp\left\{\phi_i - jk\left[R_{Ti} + R_{Ri}(x,y)\right]\right\}\right]. \tag{18}$$

The instant incident field on an individual point of the telescope area (x, y, 0), received from an atmospheric layer at a distance R, can be obtained as the sum of a big number of complex-valued contributions (phasors) with random amplitude and phase, which results in a so-called circular complex Gaussian random variable [47]. As time passes and the transmitted pulse propagates the collection of illuminated scatterers changes and the incident field becomes a circular complex random process:

$$\tilde{U}(x,y,0,t) = \left(\frac{P_T}{\pi R^4 \theta_D^2}\right)^{1/2} \exp\left[-\int_0^R \alpha(z)dz\right] \exp(-j2kv_r t)\, \tilde{c}(x,y,t), \tag{19}$$

proportional to the circular complex random process $\tilde{c}(x,y,t)$

$$\tilde{c}(x,y,t) =$$

$$= \sum_{i=1}^{N_{V_R}} s(t-2z_i/c)\, \sigma_{bi}^{1/2} \exp\left\{j\phi_i - jk\left[R_{Ti} + R_{Ri}(x,y)\right]\right\} = \tilde{\mu}(x,y,t) \exp\left[j\tilde{\theta}(x,y,t)\right] \tag{20}$$

At any time, the phase of $\tilde{c}$ is uniformly distributed and its magnitude is a Rayleigh-distributed random variable, with probability density function [47]

$$f(\mu) = \frac{\mu}{\rho^2} \exp\left(-\frac{\mu^2}{2\rho^2}\right);\ \mu \geq 0, \tag{21}$$

with a Rayleigh parameter ρ

$$\rho^2 = \frac{1}{2} N_{V_R} \left\langle \sigma_{bi}\, s^2(t-2z_i/c) \right\rangle_{V_R}, \tag{22}$$

where $\langle\cdot\rangle_{V_R}$ denotes the mean over the volume V_R. The backscatter cross-section per unit solid angle σ_{bi}, which depends on the microphysical properties of each particle in V_R and $s(t-2z_i/c)$, with $t = 2R/c$, which depends on its position in that volume (z_i), are independent. The parameter of the Rayleigh distribution can be therefore calculated as follows:

$$\rho^2 = \frac{1}{2} N_{V_R} \langle \sigma_{bi} \rangle_{V_R} \left\langle s^2(t-2z_i/c) \right\rangle_{V_R} = \frac{1}{2} N_{V_R} \langle \sigma_{bi} \rangle_{V_R}, \tag{23}$$

where $\langle \sigma_{bi} \rangle_{V_R}$ is the mean cross-section per solid angle in the backscatter direction of the scatterers in the volume V_R, and the fact that $\left\langle s^2(t-2z_i/c) \right\rangle_{V_R} = 1$ has been taken into account . The mean and the variance of the Rayleigh distribution are respectively:

$$\langle \mu \rangle = \sqrt{\pi/2}\ \rho \tag{24}$$

$$\sigma_\mu^2 = (2 - \pi/2)\,\rho^2 . \tag{25}$$

The optical intensity at each point of the receiving area can be obtained thus as

$$\tilde{I}(x,y,0,t) = \left|\tilde{U}(x,y,0,t)\right|^2 = \frac{P_T}{\pi R^4 \theta_D^2} \exp\left[-2\int_0^R \alpha(z)\,dz\right] \tilde{\eta}(x,y,t), \tag{26}$$

where $\tilde{\eta} = \tilde{\mu}^2$ is an exponential random process as the square of a Rayleigh variable is an exponential one. At any time, the probability density function, mean and variance of the corresponding exponential random variable are respectively

$$f(\eta) = \varepsilon \exp(-\varepsilon \eta);\quad \eta \geq 0;\quad \varepsilon = 1/\left(2\rho^2\right) = 1/\left(N_{V_R} \langle \sigma_{bi} \rangle_{V_R}\right) \tag{27}$$

$$\langle \eta \rangle = 1/\varepsilon = N_{V_R} \langle \sigma_{bi} \rangle_{V_R} = n(R)\,\pi (R\theta_D)^2\,\Delta z \langle \sigma_{bi} \rangle_{V_R} = \beta(R)\,\pi (R\theta_D)^2\,\Delta z \tag{28}$$

$$\sigma_\eta^2 = 1/\varepsilon^2 , \tag{29}$$

where $\beta(R) = n(R) \langle \sigma_{bi} \rangle_{V_R}\ \left[\mathrm{m^{-1}sr^{-1}}\right]$ is the atmospheric volume backscatter coefficient at a distance R. The characteristics of the instant optical intensity at each point of the telescope receiving area are therefore described by a random variable with a standard deviation that is equal to its mean, which indicates great variability. Considering that the illuminated region is actually a collection of independent radiators, which can be seen as a spatially incoherent source of light (see Fig. 10), the theorem of Van Citter-Zernike can be applied to determine the corresponding spatial coherence area on the telescope receiving area (A_c) [47]:

$$A_c = (\lambda_0 R)^2 / A_s = \lambda_0^2 / (\pi \theta_D^2) \tag{30}$$

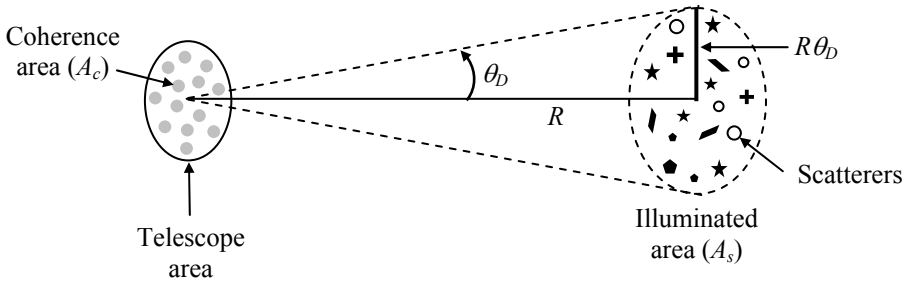

Fig. 10. *Calculation of the coherence area over the telescope plane.*

For typical values of the wavelength (1064 nm) and the divergence angle (1 mrad), the spatial coherence area is 3.38×10^{-8} m^2, which is in any case much smaller than the telescope area (about 7×10^{-2} m^2 for a 30 cm diameter telescope). Over the receiving area, therefore, there are a big amount of spots with independent and very variable luminosity similar to the classical speckle produced by a rough surface when is illuminated by a coherent source of light. Moreover, as the laser pulse propagates, the illuminated scatterers are different, which will result in a total scattered field undergoing amplitude and phase random fluctuations, limiting the coherence time of the return signal to the pulse duration τ_p, hence the minimum spectral width approximately to $B_\tau = 1/\tau_p$ [1], [48].

3.2.2 The lidar equation

The instant incident optical power onto the telescope, received from a scattering volume at a distance $R = c\,t/2$, is obtained by integrating the optical intensity over the receiving area.

$$\tilde{P}(R) = \iint_{A_r} \tilde{I}(x, y, 0, t)\, ds \tag{31}$$

As seen at the end of section 3.2.1, the coherence area at the receiver location is, in a typical scenario, much smaller than the collecting area and as a consequence, the number of integrated independent spots is usually very big (for the typical values used at the end of section 3.2.1, more than 2×10^6). The variance of the resulting detected power, which can be estimated dividing the variance of the intensity in each point by the number of independent coherence areas, is therefore very small. In practice, thus, the detected power can be treated as a deterministic value that can be calculated as

$$P(R) = \left\langle \tilde{I}(x, y, 0, t) \right\rangle A_r = \frac{P_T\, A_r}{\pi\, R^4\, \theta_D^2} \exp\left[-2\int_0^R \alpha(z)\, dz \right] \langle \chi \rangle =$$

$$= \frac{P_T\, A_r}{R^2} \Delta z\, \beta(R) \exp\left[-2\int_0^R \alpha(z)\, dz \right]. \tag{32}$$

If the emitted pulse energy ($E_T = P_T/\tau_p$) is introduced as parameter and the spatial resolution is expressed in terms of the pulse duration ($\Delta z = c\,\tau_p/2$).

$$P(R) = \frac{E_T\, A_r\, c}{2\, R^2} \beta(R) \exp\left[-2\int_0^R \alpha(z)\, dz \right] \tag{33}$$

Eq. (32) and Eq. (33) are two forms of the so-called lidar equation, which provides the received power from a distance *R* in a coaxial, monostatic lidar system as a function of transmistter, receiver and atmospheric parameters. Note that no efficiency and overlap coefficients depending on the range have been however included in these expressions.

4 The edge technique

As mentioned in section 2.3.2, a group of direct-detection techniques use optical filters to convert frequency shifts into intensity changes. There are two variations of this principle: the so-called 'Edge Technique', if a single filter is used to perform the frequency to intensity conversion [2], [34], [49], and the 'Double Edge Technique', if the conversion is carried out using a set of two filters [3], [5], [50], [51].

As it is the technique that will be implemented both in the planned *UPC* Doppler wind lidar and in the laboratory prototype, the single-edge technique is described in this section and the expressions required for analyzing and designing a Doppler lidar based on this technique are derived.

4.1 The edge technique principle

The method [2] consists in comparing, for each range resolution cell, the transmittance of an optical filter at two different frequencies: that of the emitted light and that of the received one. From these measurements and using a previous calibration of the frequency response of the filter and of optical and optoelectronic constants, the Doppler shift (f_D), hence the speed of the target that produced it, can be derived. For efficient operation, the frequency of the transmitting laser (ν_0) has to lie on the zone of maximum filter slope, where a given frequency change produces the biggest changes in transmission (Fig. 11, left). The emitted frequency is obtained from a sample of the outgoing laser pulse that is usually introduced in the receiving telescope. Two detectors are used to measure the transmittance of the optical filter: one to monitor the total received power (det 2) and another (det 1) to measure the filter output signal (Fig. 11, right). A proper time resolved analysis of the detected signal will provide both separation between the emitted and the received frequencies and range resolution in the measurement of the Doppler shift.

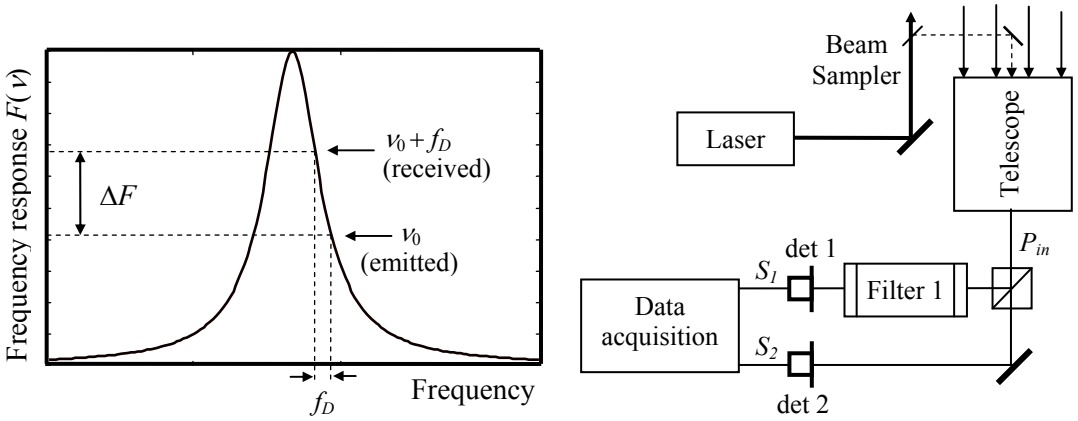

Fig. 11. *Principle (left) and a basic layout (right) of an Edge Technique system.*

The frequency response of the filter, $F(\nu)$, is recorded during the calibration stage and is used to measure the Doppler shift between the emitted and the received frequencies. For an incoming frequency, ν_{in}, its value can be calculated from the detected signals, S_1 and S_2.

$$\left.\begin{aligned} S_1 &= \alpha_1 P_{in} F(\nu_{in}) \\ S_2 &= \alpha_2 P_{in} \end{aligned}\right\} \rightarrow F(\nu_{in}) = \frac{\alpha_2}{\alpha_1}\frac{S_1}{S_2}, \tag{34}$$

where P_{in} is the incident optical power (i.e. the integrated area of its power spectrum) and α_1 and α_2 are system constants, including the gain and responsivity of the detectors, the transimpedance gain of the receivers and losses in the optic elements in each one of the measuring channels, that have also to be calibrated.

4.2 High resolution optical filter: The Fabry Perot interferometer

Different types of optical filters can be used as frequency discriminator in an edge-technique-based Doppler lidar. Fabry-Perot interferometers [52], [49], iodine vapour filters [53] or Max-Zehnder interferometers [54] have been considered and used in different systems. In this work, a Fabry-Perot interferometer, which offers great flexibility in fixing the desired filtering features, is the choice that will be used as frequency discriminator in the systems to be analyzed, designed and built.

A Fabry-Perot Interferometer is a resonant cavity working at optical frequencies, consisting in 2 parallel mirrors with high reflectivity where light is repeatedly reflected with very low losses. Such a structure resonates at certain frequencies and light is transmitted with low loss through the cavity. In ideal conditions (flat mirrors and collimated incident beam) the frequency transmission function of a Fabry-Perot interferometer using 2 mirrors with the same reflectivity is [35]

$$f(\varphi) = \frac{(1-\rho)^2}{1+\rho^2-2\rho\cos\varphi};\ \varphi = \frac{2\pi}{\lambda}2d = \frac{2\pi\nu}{c}2d, \tag{35}$$

where ρ is the reflectivity of the mirrors, φ is the round trip phase shift, d is the cavity length, ν is the frequency, λ is the wavelength and c is the speed of light in vacuum. Fig. 4 shows the transmission function of the interferometer; plotting 3 peaks of the periodic function (left) and a more detailed representation of one of the resonance peaks (right).

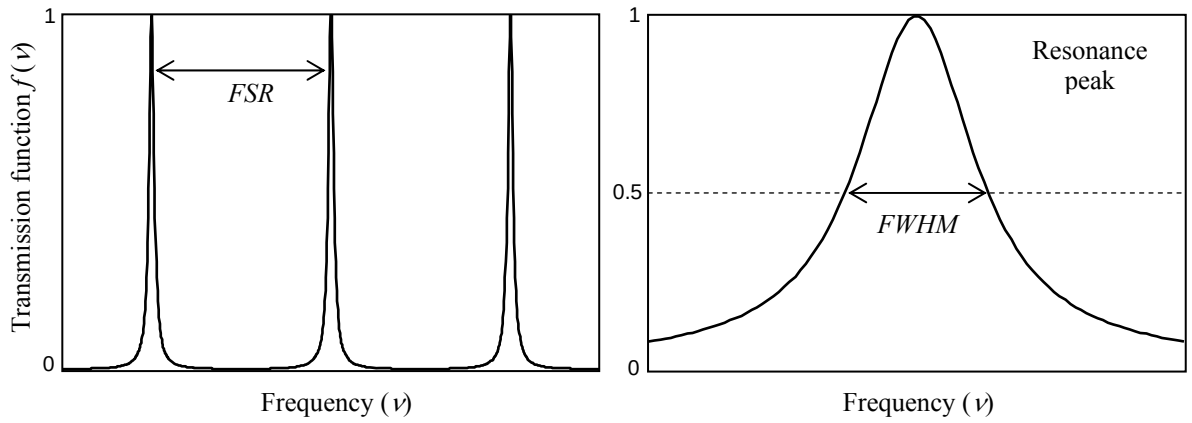

Fig. 12. *Graphic representations of the transmission function of a Fabry-Perot interferometer.*

The parameters commonly used for describing the transmission function of a Fabry-Perot interferometer are the free spectral range (*FSR*), which is the difference in terms of frequency between two consecutive peaks of resonance and the finesse (*F*), which is defined as the ratio between *FSR* and the full-width half-maximum of each resonance peak (*FWHM*).

$$FSR = \frac{c}{2\,d} \tag{36}$$

$$F = \frac{FSR}{FWHM} \tag{37}$$

In ideal conditions (ideally flat plates and perfectly collimated incident beam) the finesse depends only on the reflectivity of the mirrors [35]. This term is commonly called 'reflectivity finesse'.

$$F_\rho = \frac{\pi\sqrt{\rho}}{1-\rho} \tag{38}$$

However, different non-ideal conditions limit the finesse of the cavity to values smaller than the reflectivity finesse. This effect can come from defects in the mirrors, such as absorption, surface defects or lack of parallelism and from non-ideal characteristics of the beam, such as diffraction or aperture effects. The effective finesse, F_{eff}, can be calculated as follows.

$$1/F_{eff}^2 = 1/F_\rho^2 + \sum_i 1/F_i^2 \tag{39}$$

where F_i is associated with each one of the limiting effects mentioned above.

4.3 Frequency response for lidar signals

Doppler wind lidar systems use pulsed radiation to illuminate the region of the atmosphere to be sensed. This is necessary both for obtaining range resolution and for having enough peak power to perform atmospheric measurements. As a consequence, the return signal is, in any case, not a pure sinusoid but a finite energy signal, with a spectrum that is broadened around a carrier frequency (section 3.1). When this is the case, the transmittance of the filter as a function of the frequency of the incident signal (the frequency response of the filter from here on) does not coincide with its continuous-wave (CW) transmission function ($f(\nu)$, Eq.(35)).

Instead, it must be calculated as the frequency-domain convolution of the continuous-wave (CW) transmission function ($f(\nu)$, Eq. (35)) and the energy-normalized energy spectrum of the incident signal ($h(\nu)$) [2].

$$F(\nu) = h(\nu) * f(\nu) = \int_{-\infty}^{\infty} h(\nu' - \nu) f(\nu') d\nu' . \tag{40}$$

The response and, as a result, some of the parameters of the measuring system depend on the spectrum of the collected light, which in turn depends on the shape and duration of the emitted pulse and on the type of atmospheric scattering used to measure the Doppler shift. Because of this there exist big differences between aerosol (Mie) and molecular (Rayleigh) systems.

As explained in section 3.1.2, in practice, the spectral broadening of the Mie return due to Brownian motion can be neglected and it can be assumed that the energy spectrum bandwidth of the detected signal is approximately the same as that of the emitted pulse. For aerosol systems, therefore, the frequency response can be calculated as

$$F_M(\nu) \approx h_L(\nu) * f(\nu), \tag{41}$$

where $F_M(\nu)$ is the frequency response of the filter for Mie signals and $h_L(\nu)$ is the energy-normalized energy spectrum of the laser emitted pulse. The calibration process of $F_M(\nu)$ starts by sampling a portion of the emitted pulses to illuminate the interferometer. Then, some kind of scanning procedure between the laser spectrum and the CW transmission curve of the filter has to be done in order to sample the frequency response. If the filter is a Fabry-Perot interferometer, the scanning is generally performed by controlling either the cavity length [52], the pressure [26] or the temperature [8] to change the resonance frequency. Finally, fitting techniques are used to obtain the calibration curve.

Concerning molecular systems, although the average velocity of the air molecules is the wind speed, random motion of the molecules by thermal agitation and collisions results in a non-negligible broadening of the return-signal spectrum –about two orders of magnitude larger than the spectral width of the emitted pulse (see section 3.1.1)–. The normalized energy spectrum of the Rayleigh return ($h_R(\nu)$) can be calculated as the convolution between the spectrum of the emitted laser pulse ($h_L(\nu)$) and the Rayleigh spectrum for CW illumination ($h_{R-CW}(\nu)$, which is the spectrum described by Eqs. (3) and (4) in section 3.1.1) [1], [50].

$$h_R(\nu) = k\left[h_{R-CW}(\nu) * h_L(\nu)\right] \tag{42}$$

Where *k* is a constant used to normalize the Rayleigh energy spectrum. Therefore, the frequency response of the filter for Rayleigh signals is

$$F_R(\nu) = k\left[h_{R-CW}(\nu) * h_L(\nu)\right] * f(\nu). \tag{43}$$

If the frequency response of the filter when it is illuminated by the laser pulses is defined ($F_L(\nu) = h_L(\nu) * f(\nu)$), the frequency response for Rayleigh return signals can be rewritten as

$$F_R(\nu) = k\left[h_{R-CW}(\nu) * F_L(\nu)\right]. \quad (44)$$

To avoid a dramatic loss of transmission when the return is processed by the filter, in these systems the CW transmission function of the filter ($f(\nu)$) is set to be also much wider than in the Mie case. Due to both wider return and wider CW transmission function, the frequency response of the filters in molecular systems is much wider than in aerosol ones. Because of this wider response and its consequent lower slope, and although Doppler wind lidars based on Rayleigh scattering tend to use shorter wavelengths providing larger Doppler frequency shift for the same speed, the sensitivity to velocity variations of these systems is significantly lower than in Mie-scattering based systems.

Calibration in molecular systems is more complicated than in aerosol ones because, besides measuring $F_L(\nu)$, an accurate estimation of the CW Rayleigh spectrum ($h_{R-CW}(\nu)$) is required to calculate the frequency response of the filter to Rayleigh signals. The shape of this spectrum depends on the temperature and the pressure within the sensing volume and therefore, estimations of these atmospheric parameters must be made. The accuracy requirements in the estimation of the pressure are not very strict and standard profiles can satisfactorily be used but this is not the case of the temperature, which may be needed with an accuracy of 1 or 2 K for typical measurement specifications. This makes indispensable the use of numerical weather prediction systems in the calibration procedures [38].

4.4 Quality parameters of the velocity measurements: Precision and accuracy

In an ideal measuring system not affected by noise and systematic errors, the measured velocity would coincide always with the true value. Noise, however, always exists in the measuring process, resulting in random variations of the detected value when the same true velocity is repeatedly measured. The precision of the measuring system, that is, the degree of repeatability of the measurements, is usually expressed in terms of their standard deviation or uncertainty. At the same time, systematic errors, leading to bias in the velocity determination and producing therefore a loss of accuracy of the measurements, will always occur too. Accuracy refers to the degree of closeness of the measurements (their mean value) to the true value. They can be inherent to the technique or due to tolerances introduced in the implementation of the measuring system or during the measurement procedures.

4.4.1 Precision. Uncertainty of the measurements

The uncertainty is the parameter that will be used from here on to characterize the effect of statistical noise on the velocity determination and to quantify the precision of the measuring system. It is defined as the expected error in the determination of the velocity when no systematic errors are taken in account, i. e., the standard deviation of the detected value when the same true velocity is repeatedly measured.

This expected error ($\varepsilon(v_r)$) depends on the expected error in the measurement of the filter response, $\varepsilon\left[F_v(v_r)\right]$, where F_v is the velocity response, that is, the response of the filter as a function of the measured radial velocity. In a first order linear approximation, valid for small velocity fluctuations, the ratio between a given velocity change and the corresponding variation of the filter response is its slope [55].

$$\varepsilon\left[F_{\mathrm{v}}\left(v_r\right)\right]=\frac{\partial F_{\mathrm{v}}\left(v_r\right)}{\partial v_r}\,\varepsilon\left(v_r\right) \tag{45}$$

The uncertainty in the velocity determination can be thus written as follows:

$$\varepsilon\left(v_r\right)=\frac{\varepsilon\left[F_{\mathrm{v}}\left(v_r\right)\right]}{\dfrac{\partial F_{\mathrm{v}}\left(v_r\right)}{\partial v_r}}=\frac{1}{SNR(v_r)\;\theta_{\mathrm{v}}\left(v_r\right)}, \tag{46}$$

where $SNR\,(v_r)$ is the signal-to-noise ratio in the measurement of the response, i. e., the ratio between the measured value of the response and the expected error in its determination

$$SNR\left(v_r\right)=\frac{F_{\mathrm{v}}\left(v_r\right)}{\varepsilon\left[F_{\mathrm{v}}\left(v_r\right)\right]} \tag{47}$$

and $\theta(v_r)$ can be then identified as the so-called sensitivity to velocity changes, i. e. the relative value of the slope in each point of the response:

$$\theta_{\mathrm{v}}\left(v_r\right)=\frac{1}{F_{\mathrm{v}}\left(v_r\right)}\frac{\partial F_{\mathrm{v}}\left(v_r\right)}{\partial v_r}. \tag{48}$$

To calculate the signal-to-noise ratio, both detectors have to be taken into account (see Fig. 11 right). If the noise in the detectors is considered uncorrelated and assuming high enough signal-to-noise ratio in both detectors, the composite signal-to-noise ratio is given by

$$\frac{1}{SNR}=\sqrt{\frac{1}{SNR_1^2}+\frac{1}{SNR_2^2}}, \tag{49}$$

where SNR_1 and SNR_2 are, respectively, the signal-to-noise ratio in each one of the detectors [2].

4.4.2 Signal-to-noise ratio in optical receivers

As seen in section 4.4.1, for analyzing the precision of the measuring system it is indispensable to estimate of the signal-to-noise ratio at the output of the receivers. General expressions for this parameter will be presented in this section.

The signal-to-noise ratio at the output of a photo-receiver (SNR_{PR}) can be referred at the output of the photo-detector as the ratio of the mean value of the signal photocurrent $\langle i_{PD}\rangle$ to the uncertainty or expected error (standard deviation) in its determination σ_{PD}.

$$SNR_{PR}=\frac{\langle i_{PD}\rangle}{\sigma_{PD}} \tag{50}$$

As schematically indicated in Fig. 13, the noise arises from four independent sources: the shot-noise associated to the signal, i. e. the one related to the randomness of the arrival and multiplication of the signal photons, the multiplied dark current noise, which can be important for low-signal level operation of avalanche photodiodes at 1064 nm, the shot-noise in the detected and multiplied background photons and the noise in the receiver circuitry.

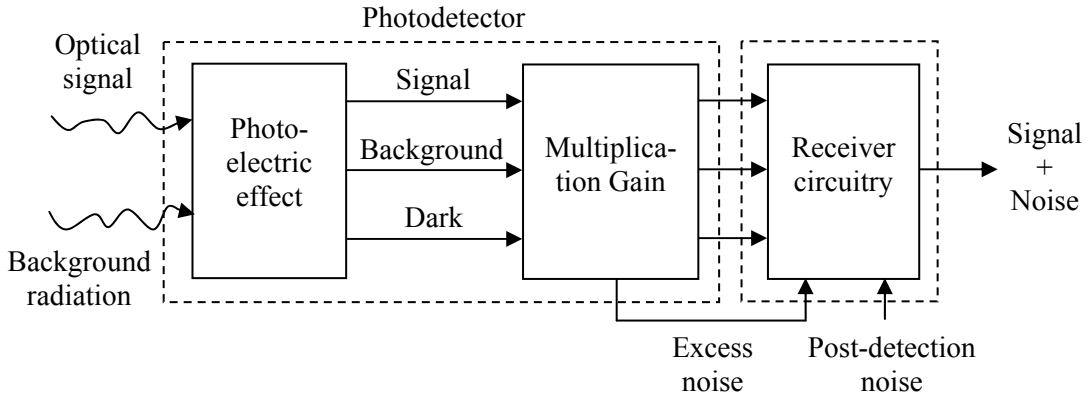

Fig. 13. *Photodetection process in an optical receiver (after ref.* [56])

These noise sources can be considered independent. The total noise power can be therefore obtained as the sum of their respective variances and the signal-to-noise ratio can be calculated using Eq.(51) [56].

$$SNR_{PR} = \frac{R_0 P_S \langle M \rangle}{\sqrt{2q \langle M \rangle^2 F_{en} B R_0 \left(P_S + P_{BG} + i_{DK}/R_0\right) + \left\langle i_{IEN}^2 \right\rangle B}} \tag{51}$$

Where P_S is the incident optical power, R_0 is the detector current responsivity without multiplication, $\langle M \rangle$ is the mean multiplication factor of the detector, q is the electron charge, and B is the equivalent noise bandwidth of the receiver. Because of the statistic nature of the multiplication process in APD or PMT detectors, the gain fluctuates and the mean square value of the gain is greater than the square of the mean. The excess noise factor $F_{en} = \langle M^2 \rangle / \langle M \rangle^2$ is a measure of the inherent APD or PMT excess noise, in terms of electrical power, resulting from the statistical fluctuation in the multiplication process [56]. P_{BG} is the background optical power and i_{DK} the bulk dark current before multiplication. T is the system temperature, k is the Boltzmann's constant and i_{IEN} is the input-referred equivalent noise current (spectral density in $\mathrm{A}/\sqrt{\mathrm{Hz}}$) generated in the receiver circuitry.

The electrical bandwidth is usually designed depending on the sampling rate f_S ($B \le f_S/2$), which is conditioned by the required range resolution ($\Delta R = c/2f_S$). For instance, a range resolution of ΔR = 7.5 m implies a sampling rate of $f_S = 20$ MHz and an electrical bandwidth of $B = 10$ MHz.

Time and range averaging are commonly used in lidar systems for increasing the number of detected photons and improving the signal-to-noise ratio. Time averaging consists in accumulating samples of the same measurement at different time instants (usually, in pulsed systems, from different shots) while –in systems with range resolution–, range averaging is performed by the accumulation, or some sort of weighted average, of consecutive range samples. In both cases, averaging is equivalent to multiply both the number of detected photons (or generated electrons) and the noise variances (σ_i^2) by an averaging factor (AF), which is equal to the number of accumulated samples. As the sources of noise are independent and the variance of the total noise is therefore equal to the sum of the individual

variances, the resulting signal-to-noise ratio is multiplied by the square root of the corresponding averaging factor:

$$SNR_{avg} = \frac{AF \left\langle i_{PD} \right\rangle}{\sqrt{\sum_i AF\, \sigma_i^2}} = \sqrt{AF}\; SNR_{PD} \tag{52}$$

4.4.3 Accuracy. Effect of the Rayleigh background on measurement bias

Bias error in the velocity measurements, that is, the distance between the measured velocity (or the mean of the individual measurements if noise is considered) and the true value, is due to systematic errors in the measuring process. If these errors are due to tolerances introduced in the process in the implementation of the system or during the measurement procedures they cannot be characterized exclusively as a function of system parameters or the measuring conditions. It is possible to identify, however, a source of systematic error that is inherent to the aerosol-based edge-technique, arising from the presence of a Rayleigh component in the signal return. This error can be estimated from the system parameters and the measuring conditions.

Although under some operating conditions the consideration of pure Mie return can be a good approximation, in general, both Mie and Rayleigh components are present in the collected light and contribute to the detected signals. The incident optical power on the Doppler receiver (P_{in} , see Fig. 11 (right)) can be expressed therefore as the sum of both contributions:

$$P_{in} = P_M + P_R \tag{53}$$

where P_M and P_R are respectively the Mie and Rayleigh components of the collected optical power. Besides the shot-noise associated with the detection of the molecular component, counted as background radiation –already taken into account in the analysis of the signal-to-noise ratio and the uncertainty–, the presence of a Rayleigh component in the return affects the performance of the aerosol-based measuring system introducing also a bias error in the velocity determination.

Indeed, the frequency response of the filter, which depends on the spectral features of the signal, is different for each component and the detected signals for an incoming frequency ν can therefore be expressed as

$$S_1 = \alpha_1 \left[P_M\, F_M(\nu) + P_R\, F_R(\nu) \right] \tag{54}$$

$$S_2 = \alpha_2 \left(P_M + P_R \right), \tag{55}$$

where $F_M(\nu)$ and $F_R(\nu)$ are the frequency responses of the filter when Mie and Rayleigh components are considered separately, while α_1 and α_2 are opto-electronic constants including the overall gain of the photo-receivers (counting the responsivity of the photo-detectors and the transimpedance gain of the receivers) and respectively the transmittance and the reflectance of the beamsplitter used in Fig. 11 (right) to divert the collected light to either receiver.

Aerosol systems are designed however to rely on Mie return, using $F_M(\nu)$ for retrieving the Doppler shift. The Rayleigh component of the detected signal in such systems is essentially insensitive to Doppler shift because its spectral width is much larger than the bandwidth of

the filters (typically more than 10 times), acting therefore as a quasi-constant, a priori unknown, background term that results in a bias error when deriving the Doppler shift from the detected voltages.

When using Eq. (34) to calculate the frequency response to the detected signals, the value that is measured $F_{Mm}(\nu)$ does not coincide with the calibrated response $F_M(\nu)$.

$$F_{Mm}(\nu) = \frac{\alpha_2}{\alpha_1}\frac{S_1}{S_2} = F_M(\nu) + \frac{P_R}{P_R + P_M}F_R(\nu) \tag{56}$$

The power of the Mie and the Rayleigh components collected from a distance (R) can be calculated from the lidar equation (Eq.(33)) using different volume backscattering coefficients, β_M and β_R respectively, being the rest of parameters common for both components. Taking this in account and using the definition of aerosol scattering ratio (ASR, Eq. (6)), Eq. (56) can be re-written as:

$$F_{Mm}(\nu) = F_M(\nu) + \frac{F_R(\nu)}{ASR} = F_M(\nu) + \delta F_M(\nu). \tag{57}$$

The error in the measurement of the frequency response $\delta F_M(\nu)$ provokes in turn an error in the determination of the received frequency $\delta\nu$. In each point of the Mie response and assuming a linear approximation, the relation between $\delta F_M(\nu)$ and $\delta\nu$ is given by the derivative of the response. This approximation is only valid for small errors but can be useful for evaluating the effect of the Rayleigh component contamination.

$$\delta\nu = \frac{\delta F_M}{\partial F_M(\nu)/\partial\nu} \tag{58}$$

$\delta F_M(\nu)$ can be obtained from Eq. (57) and the derivative of the Mie response can be expressed in terms of the sensitivity to frequency changes (Eq. (48)).

$$\left.\begin{aligned} \delta F_M &= F_R(\nu)/ASR \\ \partial F_M(\nu)/\partial\nu &= F_M(\nu)\theta(\nu) \end{aligned}\right\} \rightarrow \delta\nu = \frac{F_R(\nu)}{ASR\ F_M(\nu)\theta(\nu)} \tag{59}$$

Because it is usually obtained from a sample of the emitted pulse, the measurement of the emitted frequency is not affected by Rayleigh contamination, therefore the error given by Eq. (59) is directly the error in the Doppler shift determination. The error in the measurement of the radial velocity δv_r can be obtained therefore as

$$\delta v_r = \frac{1}{2}\lambda\,\delta\nu = \frac{\lambda\,F_R(\nu)}{2\,ASR\,F_M(\nu)\theta(\nu)} \tag{60}$$

The bias error in the velocity determination due to Rayleigh contamination depends therefore, not only on the Rayleigh-to-Mie ratio but also on the detected frequency (ν), that is, on the measured velocity.

As it will be later calculated in section 0, in a Doppler wind lidar using the edge technique the bias error originated by the Rayleigh contamination cannot be neglected and must be avoided or removed. Contrarily to what happens with the noise-induced error, this error does not arise

from random processes and cannot be reduced by means of sample averaging. A suitable solution in this case consists in adding to the system the capability of separating both components and subtracting the Rayleigh background from the detected signals [2], [57], [49]. A way to do it is using a second optical filter (Filter 2 in Fig. 14) whose response transmits the aerosol component (and also a small part of the molecular return) and rejects most of the Rayleigh component. With the knowledge of the filter response and an estimate of the Rayleigh spectral width, the magnitude of the Rayleigh background component in the detected signals can be determined and its effect removed.

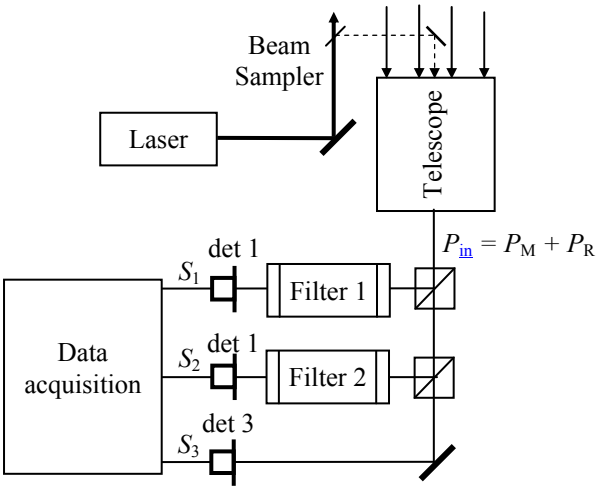

Fig. 14. *Edge-technique-based Doppler wind lidar with detection of the Rayleigh component. Filter 1 is used for the edge-technique implementation while Filter 2 helps to determine the Rayleigh component in the detected signals.*

The detected signals S_1, S_2, and S_3 at the outputs of the three photoreceivers can be expressed as a function of Mie and Rayleigh components of the incident signal as

$$S_1 = \alpha_1 \left[P_M \, F_{1M}(\nu) + P_R \, F_{1R}(\nu) \right] \tag{61}$$

$$S_2 = \alpha_2 \left[P_M \, F_{2M}(\nu) + P_R \, F_{2R}(\nu) \right] \tag{62}$$

$$S_3 = \alpha_3 \left(P_M + P_R \right), \tag{63}$$

where $F_{1M}(\nu)$, $F_{1R}(\nu)$, $F_{2M}(\nu)$ and $F_{2R}(\nu)$ are the frequency responses of filters 1 and 2 when Mie and Rayleigh components are considered separately and α_1, α_2 and α_3 are constants including the gain of the photo-receivers and constants in the respective optical paths to the detectors. From the signals in the photo-receivers 2 and 3 (Eqs. (62) and (63)) the Rayleigh component of the incident signal can be derived.

$$P_R = \frac{S_3 \, F_{M2}(\nu)/\alpha_3 - S_2/\alpha_2}{F_{M2}(\nu) - F_{R2}(\nu)} \tag{64}$$

For Eq. (64) to be a useful expression, it is necessary that both frequency responses ($F_{2M}(\nu)$ and $F_{2R}(\nu)$) do not change significantly within the range of signal frequencies so that they can be considered as constants that can be calibrated. Filter 2 should present therefore a bandwidth significantly bigger than this frequency range and should be tuned to the emitted frequency. Fig. 15 shows a representative example of such configuration: its bandwidth is

500 MHz (e. g., F = 12.5 and d = 2.4 cm), the maximum range of measurable velocities is ± 25 m/s, the temperature is 300ºK and the laser emits 10 ns pulses at 1064 nm.

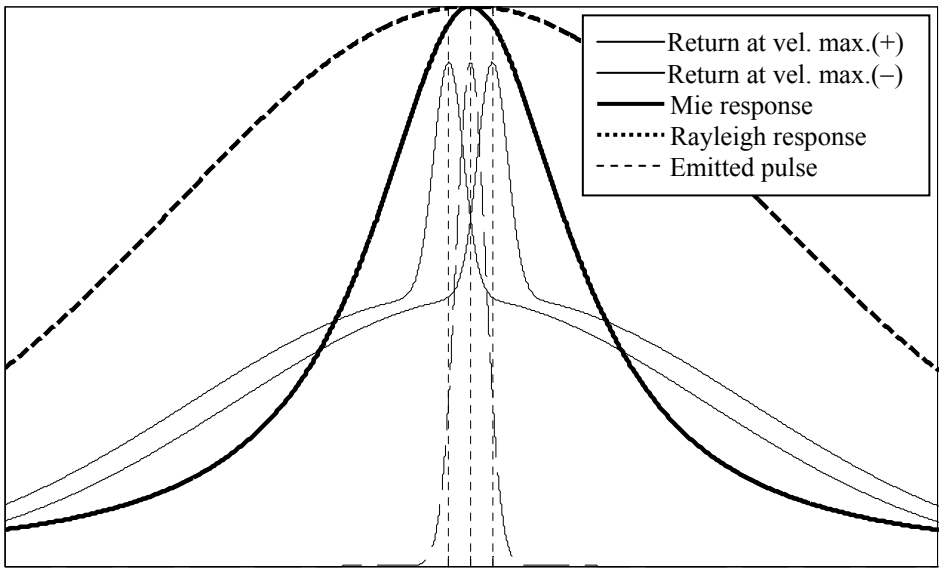

Fig. 15. *Mie and Rayleigh responses of filter 2, along with the spectrums of the emitted pulse and the return at the extremes of the measurable velocity range (HMFW = 500 MHz, velocity range is ±25 m/s, T = 300ºK, τ_p = 10 ns and λ_0 = 1064 nm).*

Once the Rayleigh component of the incident light is known, the Mie components of the signals in detectors 1 and 3 can be determined as

$$S_{1M} = S_1 - \alpha_1 P_R F_{1R}(\nu) = S_1 - \frac{\alpha_1 F_{1R}(\nu)\left[S_3 F_{M2}(\nu)/\alpha_3 - S_2/\alpha_2\right]}{F_{M2}(\nu) - F_{R2}(\nu)}, \tag{65}$$

$$S_{3M} = S_3 - \alpha_3 P_R = S_3 - \frac{S_3 F_{M2}(\nu) - S_2 \alpha_3/\alpha_2}{F_{M2}(\nu) - F_{R2}(\nu)}, \tag{66}$$

where the Rayleigh response in filter 1 and, as stated above, both Mie and Rayleigh responses in filter 2 do not change significantly in the dynamic range of signal frequencies and can be determined from the knowledge of the frequency response of the filters and the estimation of the spectral width of the Rayleigh return. Once the detected signals are clean of Rayleigh contamination, the measurement of the velocity is, if the residual error arising from the fact that $F_{1R}(\nu)$, $F_{2M}(\nu)$ and $F_{2R}(\nu)$ are not strictly constant in the velocity range is neglected, free of the Rayleigh-induced bias error.

5 Design and performance analysis of the Doppler receiver in edge-technique-based lidars

General expressions for characterizing the quality of the velocity measurements –uncertainty and bias– by an edge-technique-based Doppler lidar using a Fabry-Perot interferometer as frequency discriminator have been derived in chapter 4.

In this chapter, the expressions obtained to calculate de uncertainty of the measurements will be first used both to calculate the optimal configuration of the frequency discriminator and to estimate the precision of the measurements. This design and analysis will be carried out for two different edge-technique-based Doppler lidar systems: a Doppler velocimeter using continuous-wave radiation (section 5.2) and a range resolving edge-technique-based Doppler wind lidar relying on aerosol return (section 5.3).

In both cases, the calculations will be made, first, as a function of the received power and, in the case of the atmospheric system, also the aerosol scattering ratio (*ASR*). The corresponding conclusions will be therefore in this stage independent of the power budget of the instrument.

In the case of the wind lidar, after this power-budget-independent, general analysis, power budgets in different measuring scenarios will be also calculated for the planned *UPC* system (section 5.3.4). Then, precision parameters (uncertainty, range resolution and temporal resolution) will be estimated and compared with several reference examples (section 5.3.4.3).

Finally, the effect of the Rayleigh contamination on the accuracy of aerosol-based velocity measurements that has been described in section 4.4.3 will be also calculated for the *UPC* system in different measuring scenarios (section 0).

5.1 Design parameters

In sections 5.2.2 (continuous wave velocimeter) and 5.3.2 (wind lidar) the optimal configuration of the frequency discriminator of the edge-technique receiver –in this case a Fabry-Perot interferometer– will be calculated by means of minimizing the uncertainty and respecting some design constraints. As seen in section 4.4.1, the uncertainty depends on the sensitivity to velocity changes and on the signal-to-noise ratio (Eq. (46)). The signal-to-noise ratio depends on the distance and the scattering properties of the target and on a variety of transmitter and receiver parameters. Distance and scattering properties of the target define different measuring scenarios to have into account in the calculation of the system power budget but they are not parameters of the lidar instrument. The transmitter and the receiver parameters that have influence only on the signal-to-noise ratio (transmitted power, receiving area of the telescope, responsivity of the detectors, etc.) will not be considered a design parameter in this section. Of course, they must provide the best signal-to-noise-ratio possible and their characteristics have been chosen, according to this criterion, depending on the type of system to be designed and on availability and budget considerations. The second term appearing in the uncertainty expression, the sensitivity to velocity changes, depends basically on the slope of the frequency response of the optical filter used as discriminator. Without considering other effects, the response should be, in the frequency zone where measurements have to be made, as steep as possible, which implies that the filter should be as selective as possible. This condition however is limited by two constraints. First, a very selective filter can result in a working frequency range, defined by the zone of the response where the slope is steep enough, smaller than the required. Second, in pulsed regime, a smaller bandwidth results in a loss of transmission that, as a side effect, impairs the signal-to-noise ratio and as a consequence, the uncertainty. The frequency response bandwidth will be thus the design parameter of the Doppler receiver that will be calculated to optimize the system precision respecting the minimum measurable velocity range of the system.

5.2 Continuous-wave hard-target velocimeter

As mentioned in the introduction of this chapter, in the frame of the development process of an aerosol Doppler wind lidar based on the edge-technique, a low-power, continuous-wave velocimeter, designed for measuring the speed of hard-targets, has been built and assessed. The use of this prototype permits to avoid difficulties related to the use of atmospheric lidar signals when assessing the edge-technique implementation. Contrary to what happens in atmospheric lidar systems, the processed signals have, in this case, continuous, constant and predictable power. It is also easier to obtain independent reference measurements of the detected velocity. In this section, the design and the performance analysis of the Doppler receiver in such a prototype is presented.

5.2.1 Main system parameters

The parameters of the transmitter, the Fabry-Perot interfometer and the optical receiver that have been used in the prototype and that are required for carrying out the calculations presented in this section are summarized in Table 1.

Transmitter	Nd:YAG laser Spectra Physics 6350-ETN
Wavelength	1064 nm
Linewidth	< 10 kHz
Detector	Hamamatsu S8890-15 APD
Avalanche gain	100
Intrinsic responsivity	0.25 (A/W) (@ 1064 nm)
Dark current (before multiplication)	10 nA (Typ)
Receiver	Transimpedance amplifier
Bandwidth	100 kHz
Input equivalent noise current	$6.12\ \text{pA}/\sqrt{\text{Hz}}$
Optical filter	Fabry-Perot interferometer Melles Griot 13 FPI-025
Finesse	45
Cavity length	0.8 – 10 cm (adjustable)

Table 1. *Parameters of the laser, the optical receiver and the optical filter in the continuous-wave prototype.*

5.2.2 Optimization of the frequency discriminator

The bandwidth of the frequency response of a Fabry-Perot interferometer –the parameter to be optimized– depends on the finesse and on the cavity length. The finesse of the interferometer is not an easily adjustable parameter; it has been measured in the laboratory under the operating conditions resulting in $F = 45$. On the other hand, the cavity length is, in the case of the instrument used at the *UPC* laboratory, adjustable (from 0.8 to 10 cm) and it will be therefore the parameter that will be used to tune the response bandwidth.

5.2.2.1 Frequency response

The frequency response of a Fabry-Perot interferometer to continuous-wave radiation is given by Eq. (35). Fig. 16 shows this response for different configurable cavity lengths when the finesse is fixed to the measured value ($F = 45$).

Fig. 17 shows, also for the measured finesse ($F = 45$, highlighted curve), the filter bandwidth as a function of the cavity length. The filter bandwidth ranges from 33 MHz ($d = 10$ cm) to 417 MHz ($d = 0.8$ cm). It is worth to be noted that, comparing these values with the linewidth of the laser that will be used, the assumption of pure sinusoidal operation is valid. The figure also shows the same curve for other values of the finesse (from 30 to 55). As stated by Eqs. (37) and (36), the filter bandwidth decreases for longer cavities and higher finesse.

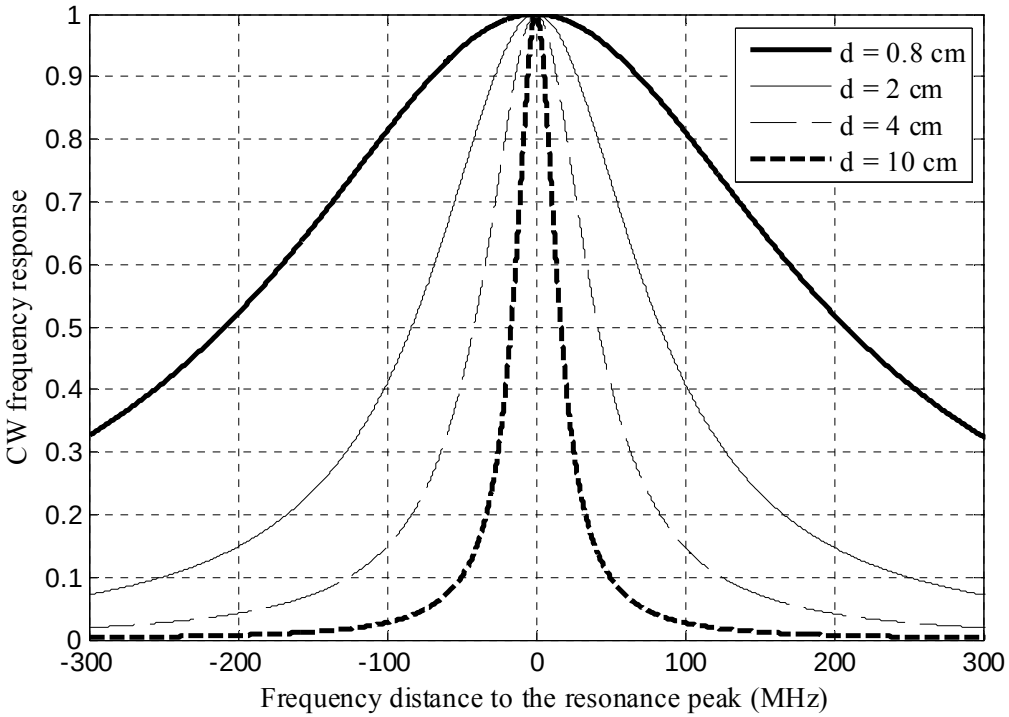

Fig. 16. *CW frequency response for configurable values of the cavity length when F = 45.*

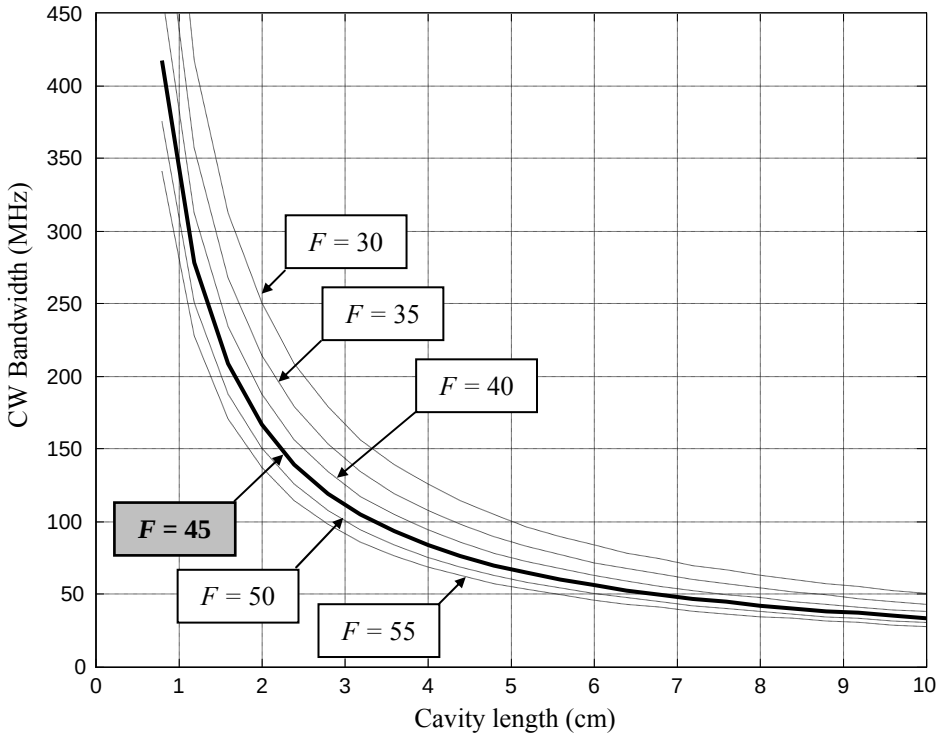

Fig. 17. *Bandwidth of the CW frequency response as a function of the cavity length for different values of the finesse.*

5.2.2.2 Sensitivity to velocity changes

Since the measured velocities are related to Doppler frequency shifts (Eq. (1)), the sensitivity to velocity changes along the slope of the filter response, defined in section 4.4.1 as a

function of the measured radial velocity (v_r), (Eq. (48)), can be expressed also as a function of the detected frequency (ν):

$$\theta(\nu) = \theta_{\mathrm{v}}\left[v_r(\nu)\right] = \frac{1}{F_{\mathrm{v}}\left[v_r(\nu)\right]}\frac{\partial F_{\mathrm{v}}\left[v_r(\nu)\right]}{\partial v_r}. \tag{67}$$

Calling $F_{\mathrm{v}}\left[v_r(\nu)\right] = F(\nu)$:

$$\theta(\nu) = \frac{1}{F(\nu)}\frac{\partial F(\nu)}{\partial \nu}\frac{\partial \nu}{\partial v_r} = \frac{2}{\lambda_0}\frac{1}{F(\nu)}\frac{\partial F(\nu)}{\partial \nu} \tag{68}$$

where $F(\nu)$ is the frequency response of the filter. In the case of continuous-wave illumination, the frequency response is the continuous-wave transmission function ($f(\nu)$, Eq. (35)) and the sensitivity to frequency changes can be written as

$$\theta_{CW}(\nu) = \frac{2}{\lambda_0}\frac{1}{f(\nu)}\frac{\partial f(\nu)}{\partial \nu}. \tag{69}$$

Fig. 18 shows the sensitivity to frequency changes along the filter slope for different configurable values of the mirror spacing when the finesse is equal to the measured value F = 45.

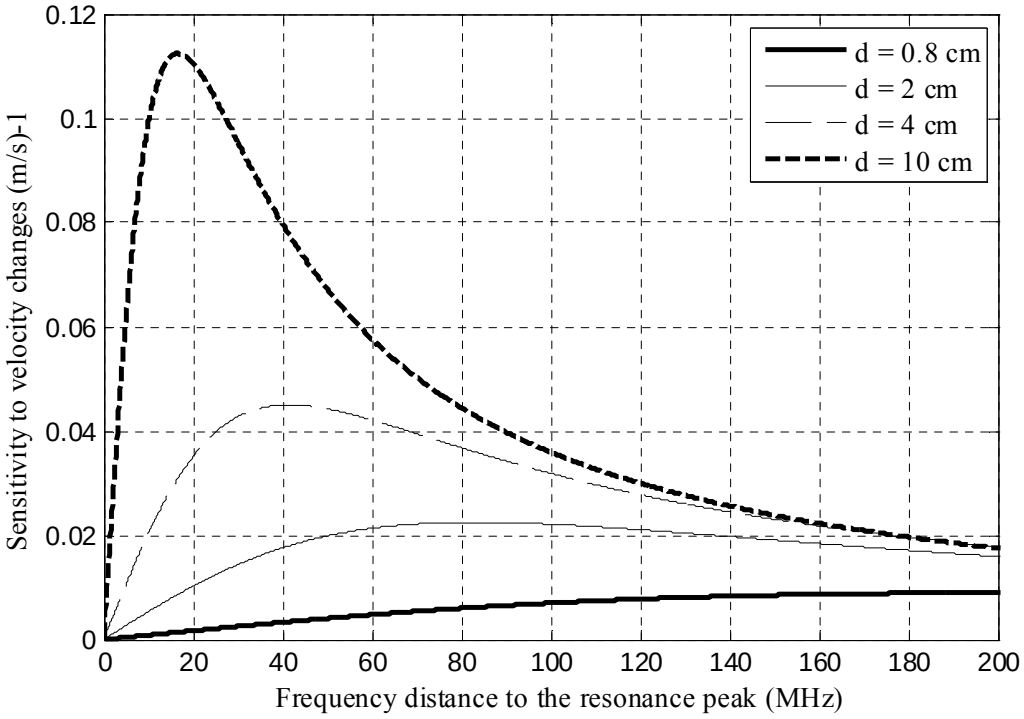

Fig. 18. *Sensitivity to velocity changes along the slope for different values of the cavity length when F = 45.*

As the cavity length grows, the filter becomes more selective and as a consequence, the sensitivity increases. However, as mentioned in section 5.1, there exists another effect that has to be considered. Besides higher sensitivity, the response of a selective filter also has a

narrower sensitive zone, i. e. the frequency zone where the slope is steep enough, limiting the range of measurable Doppler frequency shifts. Sensitivity-based bandwidth is a new parameter defined here for quantifying, using the sensitivity as criterion, the usable range of the slope. Locating the emitted frequency in the point of maximum sensitivity and considering a symmetric measurable range of frequencies with respect to zero, it is defined as the frequency range where the sensitivity of the response is at least the 50% of its maximum. If received frequencies are translated to measured radial velocities using Eq. (1), it can be defined the sensitivity-based velocity range of the measuring system. Fig. 19 shows, for different values of the finesse, the maximum sensitivity to velocity changes (left) –which grows with the cavity length– and the sensitivity-based velocity range –smaller for longer cavities– as a function of the cavity length for different values of the finesse.

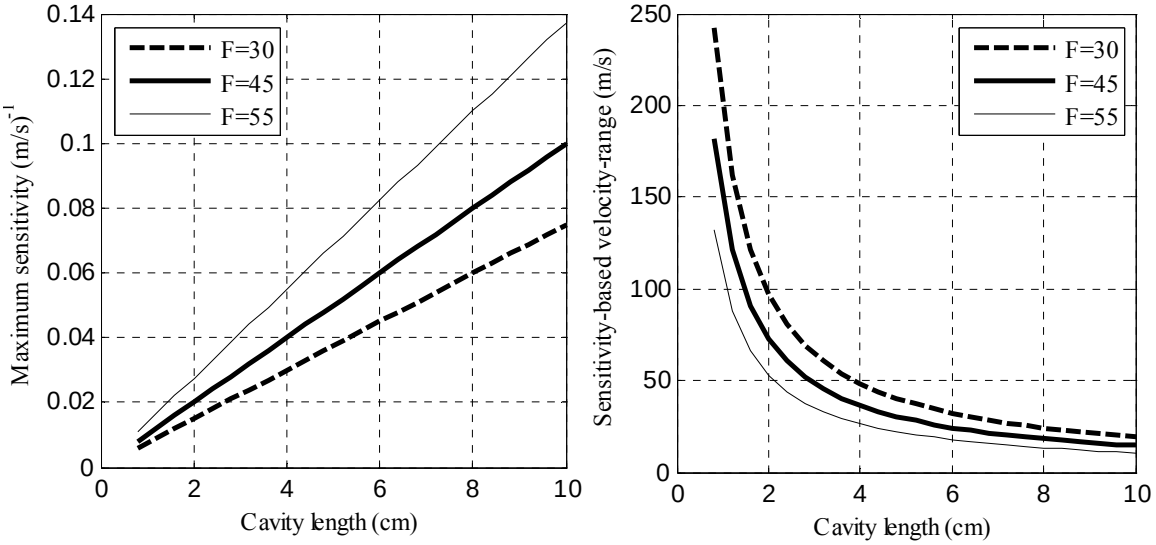

Fig. 19. *Maximum sensitivity to velocity changes (left) and sensitivity-based velocity range as a function of the cavity length (right) for F = 30, 45 and 55.*

5.2.2.3 Signal-to-noise ratio

After the sensitivity to velocity changes, the signal-to-noise ratio in the determination of the frequency response is the second term required for calculating the uncertainty of the measurements (Eq. (46)). In this section, this parameter will be calculated, using Eqs. (49) and (51), for different values of the cavity length along the slope of the filter response. The continuous-wave analysis of the Doppler detector is carried out for designing a prototype that will be operated under controlled conditions in a laboratory, where no background radiation will be collected by the receivers. Considering this and also identical photo-receivers, the signal-to-noise ratio at the output of both devices (det 1 and det 2 in Fig. 11 (right)) is calculated as

$$SNR_i = \frac{R_0 P_{Si} \langle M \rangle}{\sqrt{2q \langle M \rangle^2 F_{en} B R_0 \left(P_{Si} + i_{DK}/R_0 \right) + \left\langle i_{IEN}^2 \right\rangle B}} \quad ; \quad i = 1,2 \,, \tag{70}$$

where P_{S1} and P_{S2} are the optical powers on detectors 1 and 2:

$$P_{S1} = T_{BS} P_{in} f\left(v_{in}\right), \tag{71}$$

$$P_{S2} = R_{BS} P_{in} \,. \tag{72}$$

In the equations above, T_{BS} and R_{BS} are respectively the transmittance and reflectance of the beamsplitter used to separate the collected light in two channels (Fig. 11 (right)), P_{in} is the incident optical power before the beam-splitter and $f(\nu_{in})$ is the frequency response of the filter for continuous-wave illumination at the incident frequency ν_{in}. As an example, a representation of the signal-to-noise ratio along the slope of the response for the available range of the cavity length is displayed in Fig. 20 when the incident power is 100 nW and no averaging is performed (AF = 1). The rest of parameters of the Doppler receiver are the ones listed in Table 1.

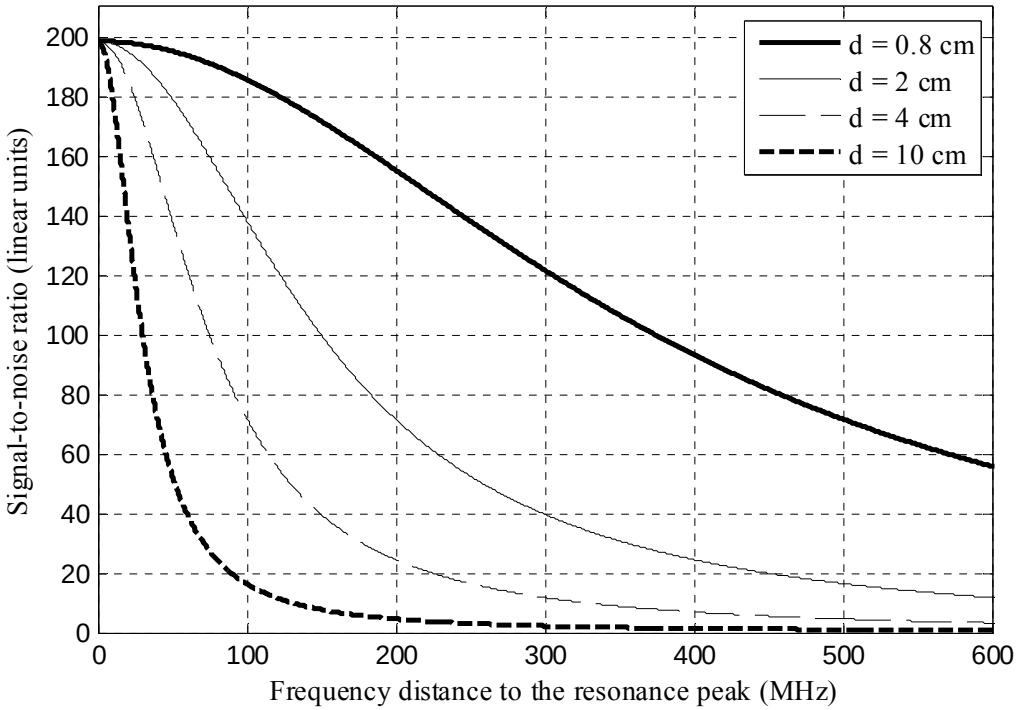

Fig. 20. *Signal-to-noise ratio of the frequency response measurement along the slope, when P_{in} = 100 nW and no averaging is performed*

As it can be observed, along with the sensitivity to velocity changes, the signal-to-noise ratio also imposes restrictions on the measurable velocity range. The combination of both contributions will become apparent in the analysis of the uncertainty.

5.2.2.4 Uncertainty-based velocity-range. Optimal cavity length

The uncertainty of the measurements can be calculated from the signal-to-noise ratio and the sensitivity to velocity changes (Eq. (46)). As an example, Fig. 21 shows the uncertainty along the slope of the filter response for a set of configurable cavity lengths under the same conditions than in Fig. 20.

The effect of both the sensitivity to velocity changes and the signal-to-noise ratio limit the measurable velocity range, and, due to the narrower response, this constraint is more restrictive for long cavity lengths. As the uncertainty includes both contributions, a new parameter, the uncertainty-based velocity-range, has been introduced in order to valuate the measurable velocity range of the system in each measuring condition. This parameter is defined, similarly to the sensitivity-based velocity-range parameter (section 5.2.2.2), as the range of velocities for which the expected error remains below the double of its minimum. It

has been calculated assuming that zero velocity is located at the point of maximum precision (minimum uncertainty) and considering that the velocity range to be measured is symmetric with respect to zero. Fig. 22 illustrates this definition for a fixed value of the cavity length.

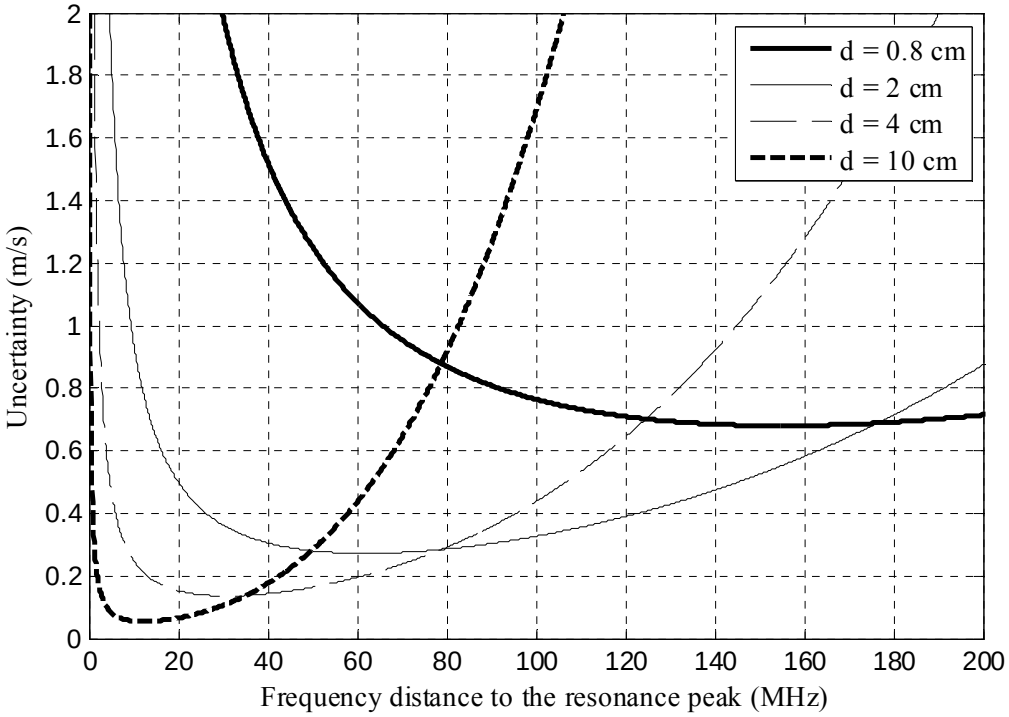

Fig. 21. *Calculated uncertainty of the measurements along the slope of the filter for different configurable values of the cavity spacing (d), when P_{in} = 100 nW and no averaging is performed.*

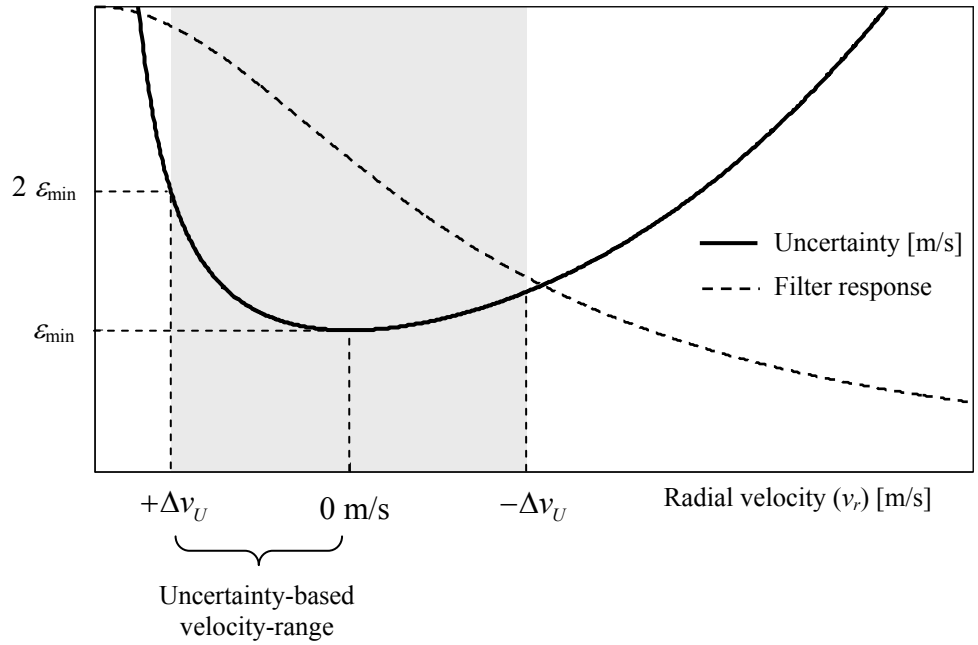

Fig. 22. *Definition of the uncertainty-based velocity-range using the calculation of the measurement uncertainty as a function of the measured radial velocity.*

An analysis of the uncertainty-based velocity range is carried out here for establishing the range of useful cavity lengths. By useful cavity length it is meant the one with a resulting

uncertainty-based velocity-range greater than the required velocity dynamic range, which has to be a specification of the measuring system. This analysis, and also further uncertainty calculations, is made for different values of the incident power P_{in}. Table 2 shows the uncertainty-based velocity-range for different values of the incident power and the cavity length. The rest of system parameters are the same than those in section 5.3.2.3.

d	**Uncertainty-based velocity-range (±m/s)**				
	P_{in} **= 1 nW**	P_{in} **= 10 nW**	P_{in} **= 0.1 μW**	P_{in} **= 1 μW**	P_{in} **= 10 μW**
0.8	50.85	52.62	58.22	61.48	61.96
1.2	33.85	35.10	38.83	40.99	41.32
1.6	25.38	26.29	29.11	30.74	30.98
2.0	20.30	21.02	23.27	24.56	24.75
2.4	16.95	17.52	19.39	20.49	20.64
2.8	14.51	15.03	16.61	17.52	17.72
3.2	12.69	13.12	14.56	15.37	15.47
3.6	11.25	11.68	12.93	13.65	13.74
4.0	10.15	10.49	11.63	12.26	12.40
4.4	9.24	9.58	10.58	11.16	11.25
4.8	8.47	8.76	9.67	10.20	10.29
5.2	7.80	8.09	8.91	9.43	9.53
----	**----**	**----**	**----**	**----**	**----**
9.6	4.21	4.36	4.84	5.12	5.12
10.0	4.02	4.17	4.64	4.88	4.93

Table 2. *Uncertainty-based velocity-range for configurable cavity lengths.*

Shaded cells correspond to non-usable cavity lengths in each measuring condition when the velocity dynamic range is fixed to ± 10 m/s. In the case of the system parameters used in these calculations (Table 1), it is shown that for measuring velocities up to 10 m/s within the uncertainty-based velocity-range of the response, it is necessary that the cavity is shorter than 4 cm.

It can also be observed that the uncertainty-based velocity-range presents certain dependence on the incident power. This is due to the effect of the signal-to-noise ratio, whose dependence on the detected frequency is stronger at low incident power, when the dark current and the thermal noise dominate over the signal shot-noise. In such case, the signal-to-noise ratio in the detector at the output of the filter is proportional to the incident power and, as a consequence, to the frequency response. On the other hand, if the signal shot-noise is the dominant term, the signal-to-noise ratio results to be proportional only to the square root of the signal, being therefore less frequency selective (see Eqs. (70) and (71) in section 5.2.2.3).

Table 3 shows, for the useful values of the plate spacing, the measurement uncertainty averaged along the whole measurable velocity range (Eq. (73)).

$$\left\langle \varepsilon \right\rangle_{2\Delta v_U} = \frac{1}{2\,\Delta v_U} \int_{-\Delta v_U}^{+\Delta v_U} \varepsilon\left(v_r\right) dv_r \,, \tag{73}$$

where Δv_U is the uncertainty-based velocity-range and $\varepsilon\left(v_r\right)$ is the uncertainty as a function of the measured radial velocity. As expected, the longer is the cavity lower is the uncertainty, being therefore d = 4 cm the best value of the cavity spacing respecting the system uncertainty-based velocity-range constraint.

***d*(cm)**	**Mean uncertainty $\langle\varepsilon\rangle_{2\Delta v_U}$ (m/s)**				
	P_{in} **= 1 nW**	P_{in} **= 10 nW**	P_{in} **= 0.1 μW**	P_{in} **= 1 μW**	P_{in} **= 10 μW**
0.8	33.921	3.843	0.683	0.190	0.059
1.2	22.757	2.577	0.457	0.127	0.040
1.6	17.223	1.949	0.345	0.096	0.030
2.0	13.943	1.576	0.278	0.077	0.024
2.4	11.795	1.332	0.234	0.065	0.020
2.8	10.298	1.161	0.204	0.056	0.018
3.2	9.222	1.037	0.181	0.050	0.016
3.6	8.429	0.946	0.164	0.045	0.014
4.0	7.858	0.878	0.151	0.041	0.013

Table 3. *Average uncertainty within the measurable velocity range for useful values of the cavity length.*

5.2.3 Precision of the velocity measurements

5.2.3.1 Uncertainty of the individual measurements

Table 4 shows, for the best value of the cavity length (d = 4 cm), a more detailed description of the uncertainty, including the location of the minimum uncertainty. For these calculations it has been assumed that the zero velocity, i. e. the emitted frequency, has been locked in each case at that point of the response.

Uncertainty parameters	P_{in} **= 1 nW**	P_{in} **= 10 nW**	P_{in} **= 0.1 μW**	P_{in} **= 1 μW**	P_{in} **= 10 μW**
Location of zero velocity (MHz)	27.36	28.26	31.05	32.49	32.76
Uncertainty at +10 m/s (m/s)	13.118	1.396	0.212	0.056	0.017
Uncertainty at 0 m/s (m/s)	6.752	0.765	0.136	0.038	0.012
Uncertainty at -10 m/s (m/s)	8.660	0.965	0.163	0.044	0.014
Mean Uncertainty (m/s)	7.858	0.878	0.151	0.041	0.013

Table 4. *Uncertainty parameters (d = 4 cm, F = 45).*

5.2.3.2 Measurements averaging. Time resolution

For improving these uncertainty figures, sample averaging should be performed. It can be derived from Eqs. (46), (49) and (52) that applying an averaging factor AF would reduce the uncertainty in each case by a factor equal to $\sqrt{AF}$. As a result, if the incident optical power is for instance 10 nW (for which the mean uncertainty without averaging is 0.878 m/s) and an average uncertainty of 0.2 m/s is required, the averaging factor should be $AF \geq \left(0.878/0.2\right)^2 = 19.27$. Table 5 shows the mean uncertainty in the whole velocity dynamic range for different values of the averaging factor AF (number of accumulated samples), whereas Table 6 shows the averaging factor needed to achieve, for each incident optical power, a given expected error.

For an optimal noise performance, the electrical bandwidth of an optical receiver should be limited by the sampling rate of the acquisition system. In the case of the receiver considered in these calculations, an electrical bandwidth of 100 kHz, permits a sampling rate ΔT = 200 ks/s and a time resolution of the measurements equal to 1/200000 = 5 μs. Performing sample averaging makes the time resolution decrease proportionally to the applied averaging factor.

AF	P_{in} = 1 nW	P_{in} = 10 nW	P_{in} = 0.1 μW	P_{in} = 1 μW	P_{in} = 10 μW
1	7.858	0.878	0.151	0.041	0.013
10	2.485	0.278	0.048	0.013	0.004
100	0.786	0.088	0.015	0.004	0.001
1000	0.248	0.028	0.005	0.001	0.000
10000	0.079	0.009	0.002	0.000	0.000
100000	0.025	0.003	0.000	0.000	0.000

Table 5. *Mean uncertainty when sample averaging is applied (d = 4 cm, F = 45)*

Required uncertainty (m/s)	Required averaging factor				
	P_{in} = 1 nW	P_{in} = 10 nW	P_{in} = 0.1 μW	P_{in} = 1 μW	P_{in} = 10 μW
0.10	6175	78	3	1	1
0.20	1544	20	1	1	1
0.30	687	9	1	1	1
0.40	386	5	1	1	1
0.50	247	4	1	1	1
0.60	172	3	1	1	1
0.70	127	2	1	1	1
0.80	97	2	1	1	1
0.90	77	1	1	1	1
1.00	62	1	1	1	1

Table 6. *Required averaging factor for different values of uncertainty and incident power (d = 4 cm, F = 45)*

From the previous results it can be said that, as long as there are not strict time restrictions and a time integration of 50 ms is allowed (*AF* = 10000), such a system is able to obtain measurements with low uncertainty (better than 0.08 m/s) even when the received optical power is as low as 1 nW. If more dynamic measurements have to be made and the integration time is limited, the expected error grows. As example, for an integration time fixed to 5 ms (*AF* = 1000), the error rises up to 0.25 m/s if the incident power P_{in} is 1 nW and 0.03 m/s when P_{in} = 10 nW. Finally, if the incident optical power is greater than 100 nW, velocity measurements with an error equal to 0.15 m/s can be obtained with a time resolution of 5 μs (no averaging). If the acquisition rate was different than 200 ks/s, the time resolution figures presented here would of course also change in the same proportion (as far the electrical bandwidth was the same).

5.3 Aerosol Doppler wind lidar

The design and the performance analysis of the Doppler receiver of an edge-technique-based aerosol Doppler wind lidar will be made in this section.

5.3.1 Main system parameters

The parameters of the transmitter, the receiving optics, the frequency discriminator and the optical receiver that will be used in this section to carry out the calculations are the ones of the available instruments that will eventually be part of the *UPC* aerosol Doppler wind lidar. They are summarized in Table 7. The main differences with respect to the continuous-wave prototype are of course in the transmitter, in this case a 1 J pulse energy, injection-seeded pulsed laser. However, some differences can be also found in the receiver. First, its bandwidth is significantly bigger in order to permit a sampling rate adapted to the high range resolution required in wind measurements. This affects strongly to the resulting signal-to-

noise ratio and to the measurement uncertainty. On the other hand, and as a consequence of this bigger required bandwidth, the transimpedance amplifiers have to be implemented using wideband operational amplifiers, whose noise parameters are also different than those ones used in the continuous-wave velocimeter. Finally, a conservative value of the Finesse, lower than the one used in the continuous-wave case, has been used in the calculations.

Transmitter	Injection-seeded Nd:YAG laser Spectra Physics GCR-190
Wavelength	1064 nm
Pulse energy	1 J
Pulse duration	10 ns
Telescope	
Diameter	20 cm
Detector	Hamamatsu S8890-15 APD
Avalanche gain	100
Intrinsic responsivity	0.25 (A/W) (@ 1064 nm)
Dark current (before multiplication)	10 nA (Typ)
Receiver	Transimpedance amplifier
Bandwidth	10 MHz
Input equivalent noise current	$2.97\ \text{pA}/\sqrt{\text{Hz}}$
Optical filter	Fabry-Perot interferometer Melles Griot 13 FPI-025
Finesse	35
Cavity length	0.8 – 10 cm (adjustable)

Table 7. *Parameters of the laser, the telescope, the optical receivers and the optical filter in the aerosol system.*

5.3.2 Optimization of the frequency discriminator

Regarding the pulsed operation of the transmitter in this type of system, the spectral width of the filter response depends not only on the finesse and the cavity length, but also on the pulse duration (see section 4.3). Nevertheless, this parameter –which depends on the laser– is not adjustable in the transmitter and has to be again the interferometer the element to be optimized. Like in section 5.1, the cavity length will be the parameter that will be tuned for optimal performance.

5.3.2.1 Frequency response

The resulting frequency response of any filter to a band-pass signal is broader than in the case of continuous-wave operation (see section 4.3). One of the direct consequences of this broadening is a smaller slope, which implies lower sensitivity to velocity changes and, under the same conditions, bigger expected error (uncertainty) in the velocity determination. Secondly, the maximum transmission of the filter suffers a loss with respect to the continuous-wave case. As example of these effects in an aerosol based system, Fig. 23 shows, comparing with the CW case, the resulting normalized frequency response of a Fabry-Perot interferometer (finesse F = 35 and cavity spacing d = 3.6 cm) to a Fourier-limited Gaussian pulse of light (duration τ_p = 10 ns).

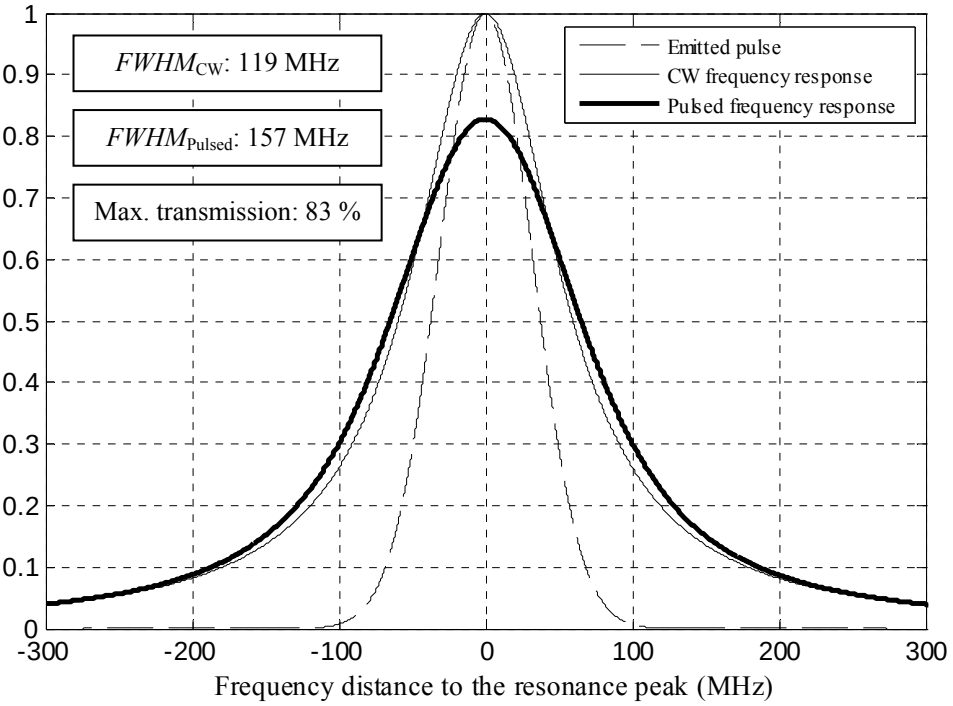

Fig. 23. *Frequency response of a Fabry- Perot interferometer to pulsed light (F = 35, d = 3.6 cm and τ_p = 10 ns).*

Fig. 24 shows the normalized frequency response of the Fabry-Perot for different configurable values of the cavity length, also when F = 35 and τ_p = 10 ns. Fig. 25 shows the cavity length dependence of the resulting bandwidth and the maximum transmission of the frequency response.

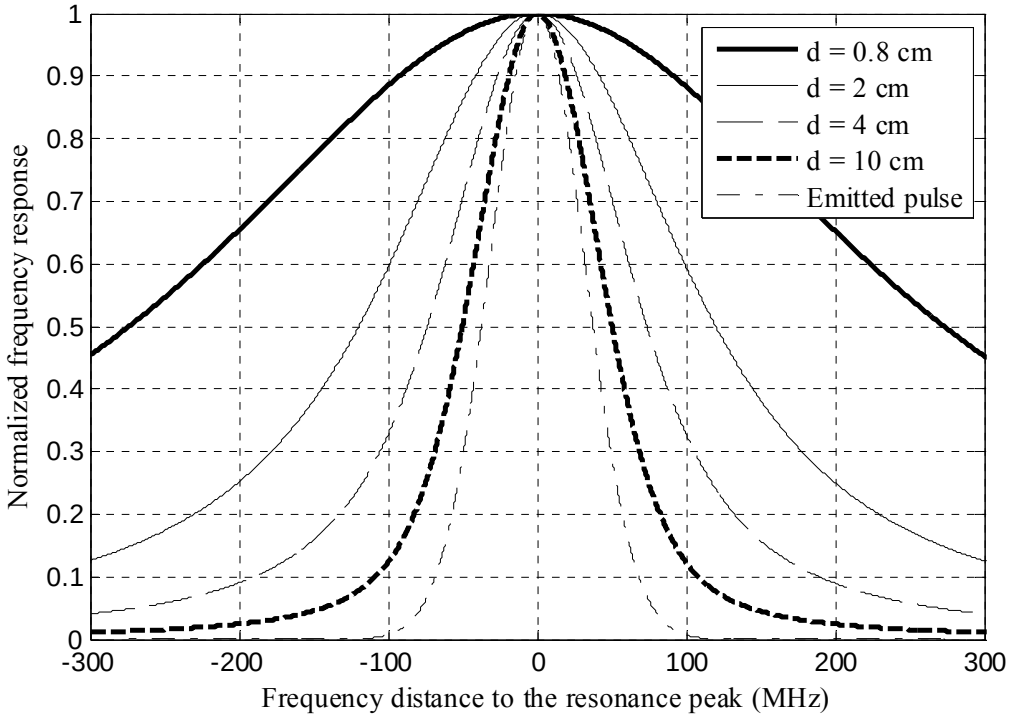

Fig. 24. *Frequency response for configurable values of the cavity length for F = 35 and τ_p = 10 ns.*

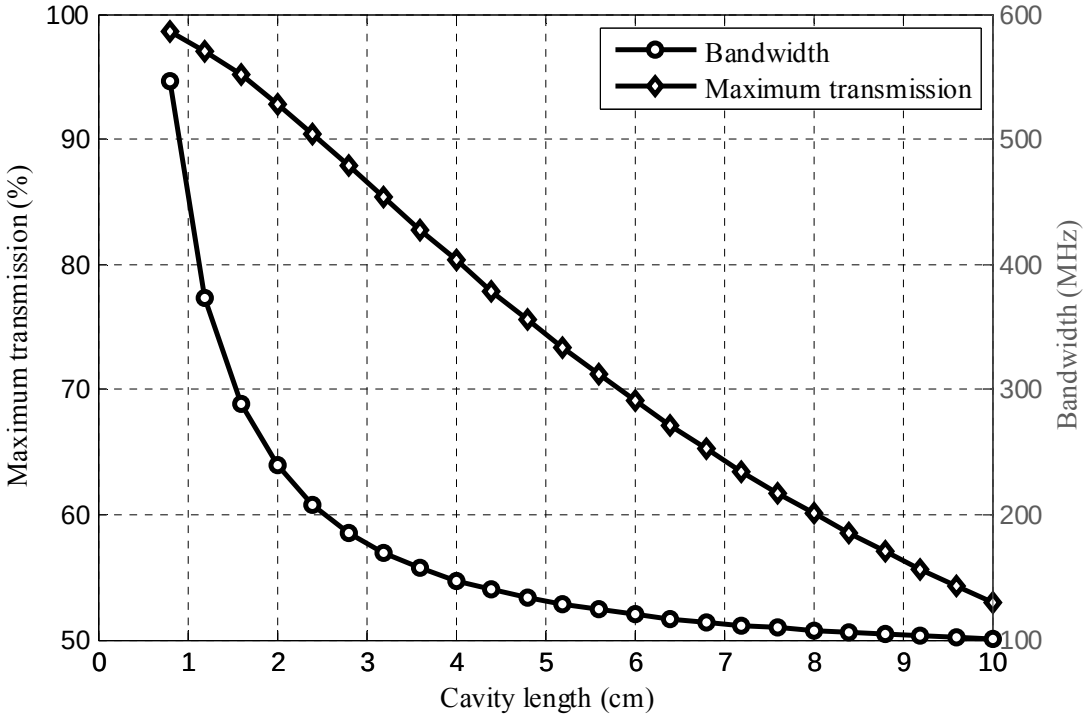

Fig. 25. *Maximum transmission and bandwidth of the frequency response as a function of the cavity length for F = 35 and τ_p = 10 ns.*

As expected, a longer cavity results in a more selective response (Eqs. (36) and (37)). Nevertheless, since the pulse duration is a fixed parameter, there is a saturation value for the bandwidth of the pulsed frequency response given by the spectral width of the emitted pulse (in this case 88 MHz). However, as mentioned above, it can be seen that, apart from providing narrower filters, steeper slope and higher sensitivity to velocity changes, the longer is the cavity the smaller is the transmission of the filter, which will affect, in this case negatively, the signal-to-noise ratio and the uncertainty of the measurements.

5.3.2.2 Sensitivity to velocity changes

As example of the effect of the pulsed illumination on the system sensitivity to velocity changes, Fig. 26 displays, comparing with the CW case, the overall sensitivity of the interferometer (finese F = 35, cavity spacing d = 3.6 cm and λ = 1064 nm) to 10 ns duration Gaussian pulses of light.

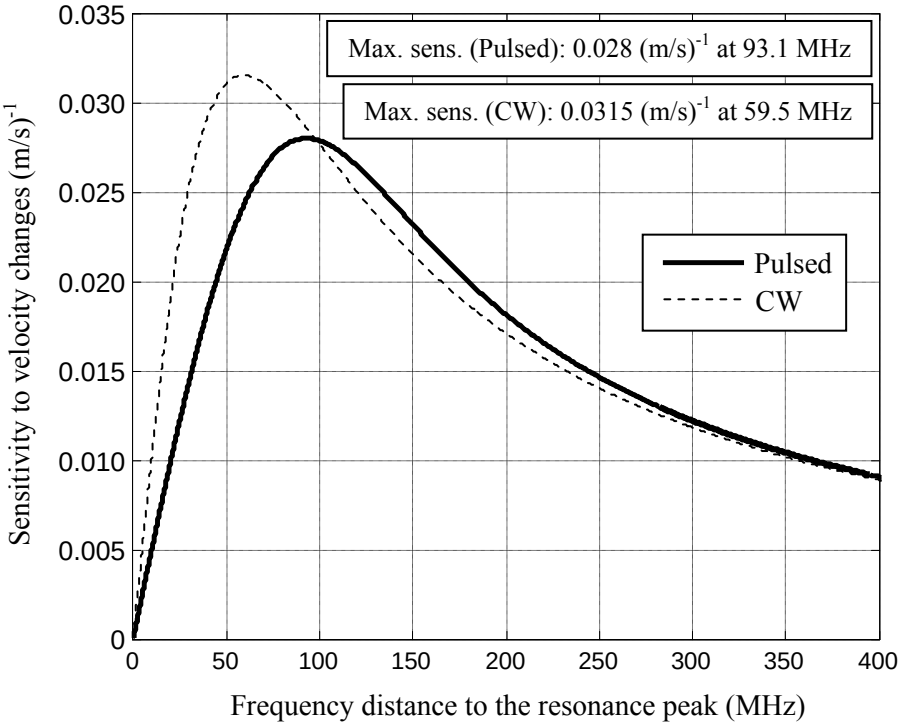

Fig. 26. *Sensitivity to velocity changes (F = 35, d = 3.6 cm, τ_p = 10 ns and λ = 1064 nm)*

Fig. 27 shows the sensitivity to velocity changes along the slope of the frequency response for different values of the cavity length.

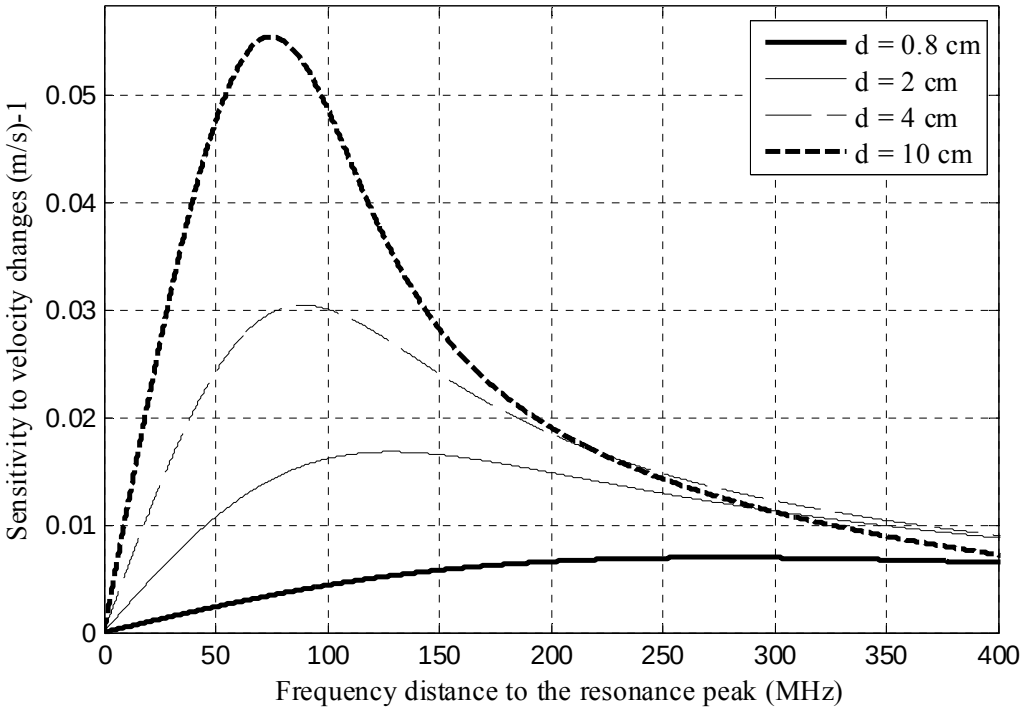

Fig. 27. *System Sensitivity to velocity changes along the filter slope for different configurable cavity lengths for F = 35, τ_p = 10 ns and λ = 1064 nm.*

As in the continuous-wave case, longer cavities provide higher maximum sensitivity and, at the same time, a narrower sensitive zone in the response that limits the measurable velocity

range. In Fig. 28, two plots can be found: one shows the maximum sensitivity and the other one the sensitivity-based velocity-range (defined as in section 5.2.2.2), both of them as a function of the cavity length.

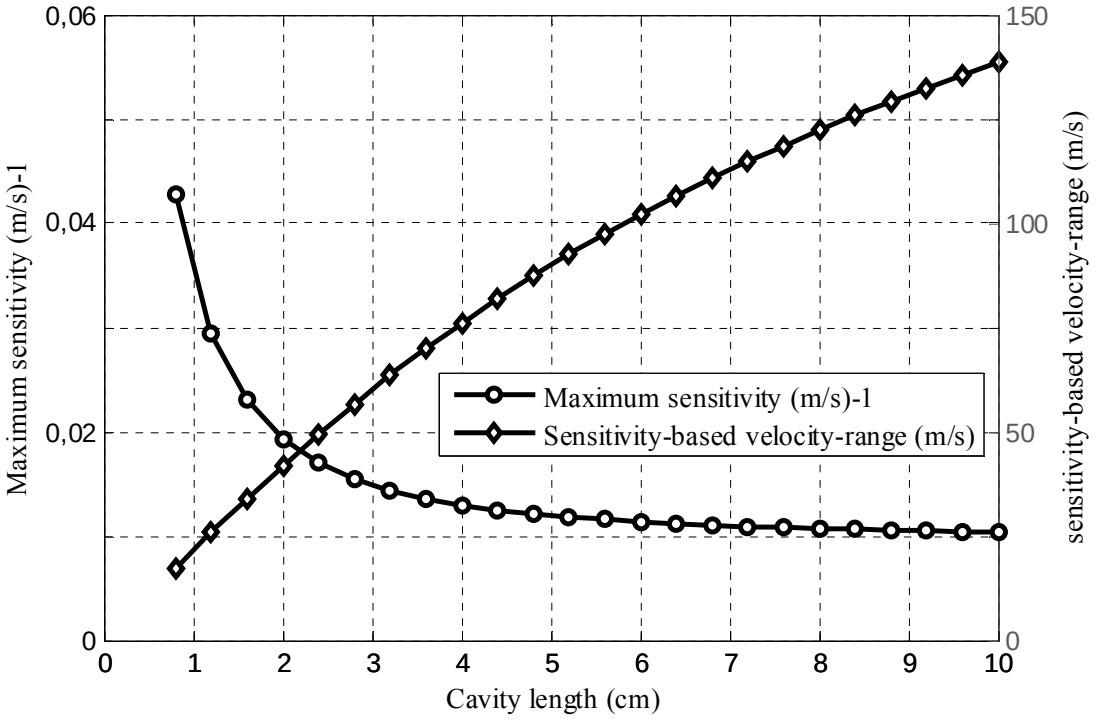

Fig. 28. *Maximum system sensitivity and sensitivity-based velocity-range as a function of the cavity length for F = 35, τ_p = 10 ns and λ = 1064 nm.*

5.3.2.3 Signal-to-noise ratio

Eqs. (51) and (52) will be used in this section for calculating the signal-to-noise ratio at the output of each receiver and Eq. (49) will provide the signal-to-noise ratio in the measurement of the frequency response. In a Doppler wind lidar relying in aerosol return, the Rayleigh component of the detected signal is essentially insensitive to Doppler shifts because of its wide spectrum with respect to the filter response and consequently can be considered as a background component that contributes to the overall shot-noise. Considering identical detectors, the signal-to-noise ratio at the output of each receiver when no averaging is applied will be therefore calculated as follows:

$$SNR_i = \frac{R_0\, P_{iM}\, \langle M \rangle}{\sqrt{2\, q \langle M \rangle^2\, F\, B\, R_0 \left[P_{iM} + P_{iR} + i_{DK}/R_0 \right] + \left\langle i_{IEN)}^2 \right\rangle B}} \quad ; \quad i = 1,2\,. \tag{74}$$

P_{1M} and P_{2M} are the Mie components of the optical power on the receivers:

$$P_{1M} = T_{BS}\, P_M\, F_M \left(\nu_p + f_D \right), \tag{75}$$

$$P_{2M} = R_{BS}\, P_M\,, \tag{76}$$

with P_M the Mie (aerosol) component of the collected optical power, $F_M(\nu)$ the frequency response of the filter for the Mie component, and T_{BS} and R_{BS} respectively the transmittance

and reflectance of the beamsplitter used in Fig. 11 (right) to divert the collected light to either receiver. P_{1R} and P_{2R} are the Rayleigh background components:

$$P_{1R} = T_{BS}\, P_R\, F_R\left(\nu_p + f_D\right), \tag{77}$$

$$P_{2R} = R_{BS}\, P_R\,, \tag{78}$$

with P_R the Rayleigh (molecular) component of the collected optical power and $F_R(\nu)$ the frequency response of the filter for the Rayleigh component.

The lidar equation (Eq. (33)) permits to calculate the power received from a distance *R*. The difference between the Mie and the Rayleigh components will be given by the use of different volume backscattering coefficients.

$$P_M(R) = \frac{E_T\, A_r\, c}{2R^2}\, \beta_M(R) \exp\left[-2\int_0^R \alpha(z)\, dz\right], \tag{79}$$

$$P_R(R) = \frac{E_T\, A_r\, c}{2R^2}\, \beta_R(R) \exp\left[-2\int_0^R \alpha(z)\, dz\right], \tag{80}$$

where E_T is the transmitted pulse energy and A_r the telescope receiving area; $\beta_M(R)$ and $\beta_R(R)$ are respectively the Mie and Rayleigh volume backscattering coefficients at range *R* and $\alpha(z)$ is the extinction coefficient along the path. The extinction coefficient depends on both aerosol and molecular absorption and scattering and is common to both components.

In this section, the power of the Mie return ($P_M(R)$), which is the signal term in the expressions of the signal-to-noise ratio, will be used as the primary input parameter. In such way, the conclusions will have a more general nature: they will refer to the Doppler receiver independently of the power budget of the system. The Rayleigh component on the return signal, which determines the background shot-noise and, as a result, has an influence on the expected error, will be calculated from the Mie component and the aerosol scattering ratio ($ASR(R)$) (see Eq. (6) in section 3.1.3), which describes the proportion of the Rayleigh component in the overall return. Taking thus in account the expressions of the Mie and the Rayleigh components (Eq. (79) and Eq. (80)) and the definition of the aerosol scattering ratio given by Eq. (6), the power of the Rayleigh component can be calculated as

$$P_R(R) = \frac{P_M(R)}{ASR(R) - 1}. \tag{81}$$

As example, the signal-to-noise ratio of the measurement has been calculated for an aerosol return of 10 nW and an aerosol content described by *ASR* = 2 when an averaging factor *AF* = 1000 is applied. The results are shown in Fig. 29 for different values of the cavity length.

As expected, the combined effect of both a narrower bandwidth and –contrary to the continuous-wave case– lower filter transmission can be noticed as the cavity length grows.

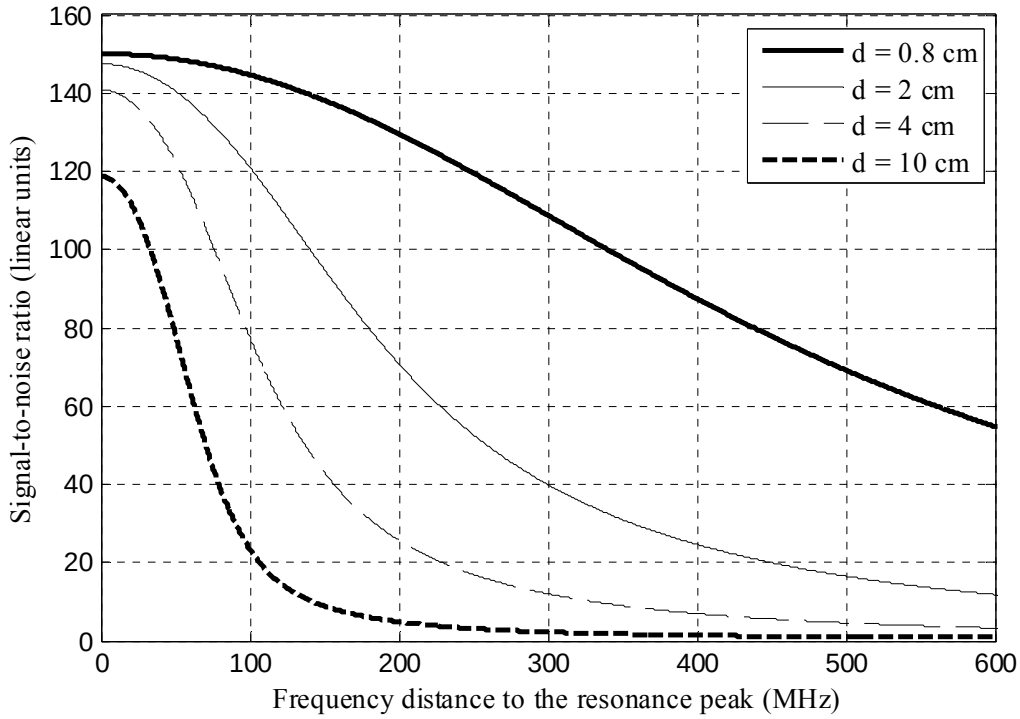

Fig. 29. *Signal-to-noise ratio for P_M = 10 nW, ASR = 2 and AF = 1000, for different values of the cavity length.*

5.3.2.4 Uncertainty-based velocity-range. Optimal cavity length

Fig. 30 shows, as example, the uncertainty of the measurements (Eq. (46)) along the slope of the filter response for a number of cavity lengths, under the same conditions than in Fig. 29.

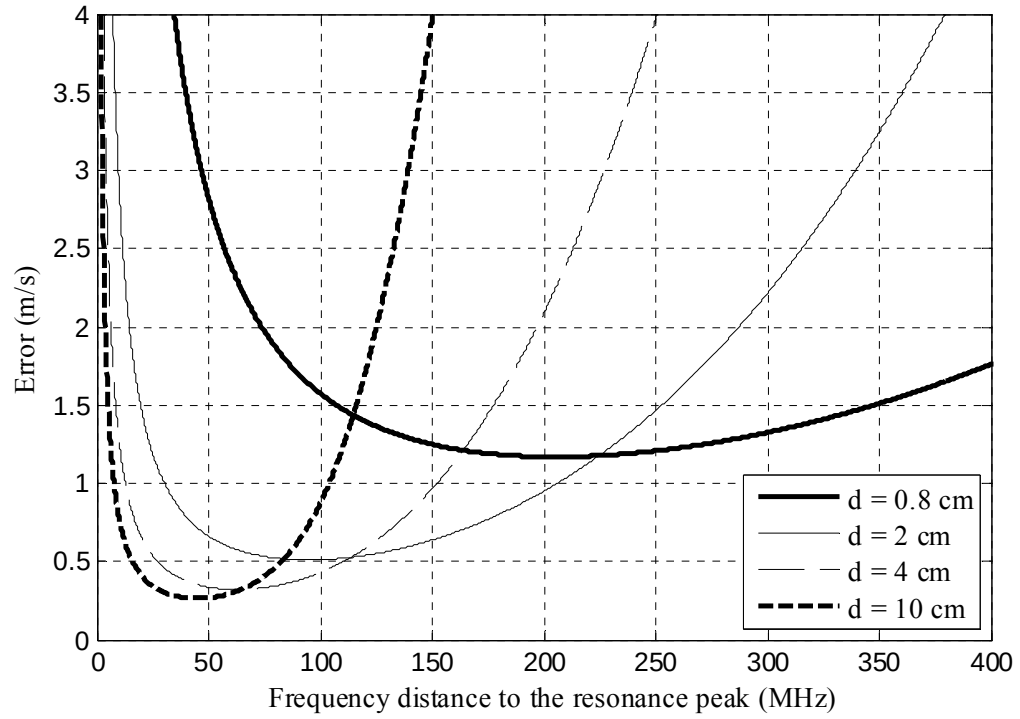

Fig. 30. *Calculated uncertainty P_M = 10 nW, ASR = 2 and AF = 1000 for different values of the cavity length.*

Similarly to the continuous-wave case, the effect of both the sensitivity to velocity changes and the signal-to-noise ratio limits the measurable velocity range and, due to the narrower response, this constraint is more restrictive for longer cavity lengths. The uncertainty-based velocity-range, defined in the same way than in section 5.2.2.4, will be calculated too in this case and will be used as a design constraint when minimizing the uncertainty.

The uncertainty analysis will be carried out for different values of the Mie return power. For each instance, different aerosol loading conditions will result in different uncertainty figures as the Rayleigh background has different influence on the signal-to-noise ratio. In this sense, three values of *ASR* are tested for each received power. *ASR* = 11 corresponds to an atmosphere with high aerosol content, a typical situation within the boundary layer and on clouds, *ASR* = 2 describes a clean atmosphere that can be found at low altitudes above the boundary layer and *ASR* = 1.1 defines a practically aerosol-free atmosphere, which can be usually found above 6 km altitude. The optimal cavity length in each case will be found applying the same design conditions and constraints than in section 5.2.2.4.

First, an analysis of the uncertainty-based velocity-range is carried out for establishing the range of usable cavity lengths. Table 8 shows this parameter for each considered Mie received power in each aerosol loading condition for different values of the cavity length. The rest of system parameters used in these calculations are the same than those in section 5.3.2.3.

d **(cm)**	**Uncertainty-based velocity-range (± m/s)**											
	P_M **=1 nW**			P_M **=10 nW**			P_M **=100 nW**			P_M **=1 μW**		
	***ASR* 1.1**	***ASR* 2**	***ASR* 11**	***ASR* 1.1**	***ASR* 2**	***ASR* 11**	***ASR* 1.1**	***ASR* 2**	***ASR* 11**	***ASR* 1.1**	***ASR* 2**	***ASR* 11**
0.8	73.58	69.00	68.36	85.44	76.45	74.11	90.28	83.58	80.81	90.92	85.07	82.46
1.2	50.70	47.61	47.19	58.57	52.67	51.18	61.82	57.56	55.86	62.24	58.63	56.98
1.6	39.63	37.35	37.03	45.70	41.23	40.11	48.20	45.06	43.84	48.52	45.91	44.74
2.0	33.30	31.44	31.18	38.25	34.69	33.78	40.38	37.93	36.97	40.64	38.62	37.77
2.4	29.21	27.66	27.45	33.52	30.48	29.69	35.38	33.41	32.61	35.64	34.05	33.30
2.8	26.39	25.00	24.84	30.22	27.56	26.87	31.92	30.27	29.53	32.13	30.91	30.27
3.2	24.31	23.09	22.93	27.88	25.48	24.84	29.42	28.04	27.40	29.63	28.62	28.09
3.6	22.77	21.65	21.55	26.01	23.83	23.30	27.56	26.28	25.75	27.72	26.87	26.44
4.0	21.49	20.54	20.38	24.58	22.61	22.08	26.01	24.95	24.47	26.23	25.54	25.22
4.4	20.59	19.63	19.47	23.41	21.60	21.12	24.79	23.89	23.51	25.06	24.47	24.15
4.8	19.74	18.89	18.78	22.45	20.69	20.27	23.83	22.98	22.66	23.99	23.57	23.35
----	----	----	----	----	----	----	----	----	----	----	----	----
9.6	15.37	14.95	14.90	17.24	16.17	15.96	18.30	18.25	18.25	18.46	18.99	19.21
10.0	15.22	14.79	14.74	17.02	16.01	15.80	18.03	18.09	18.09	18.19	18.78	19.05

Table 8. *Uncertainty-based velocity-range for configurable cavity lengths.*

Not-shaded cells correspond to usable cavity lengths in each measuring condition when the velocity dynamic range is fixed to ± 25 m/s. In this case, measuring velocities up to 25 m/s within the uncertainty-based velocity-range of the response in all the situations require a cavity not longer than 2.4 cm.

Table 9 shows, for usable values of the plate spacing, the mean uncertainty (calculated from the values along the whole measurable frequency range (Eq. (73))).

d (cm)	Mean uncertainty: expected error (m/s)											
	P_M =1 nW			P_M =10 nW			P_M =100 nW			P_M =1 μW		
	ASR 1.1	*ASR* 2	*ASR* 11	*ASR* 1.1	*ASR* 2	*ASR* 11	*ASR* 1.1	*ASR* 2	*ASR* 11	*ASR* 1.1	*ASR* 2	*ASR* 11
0.8	292.42	246.80	241.63	61.00	37.49	34.15	17.88	9.58	8.29	5.61	2.95	2.53
1.2	203.43	172.66	169.20	41.95	25.98	23.72	12.26	6.59	5.71	3.84	2.02	1.74
1.6	161.43	138.02	135.39	32.78	20.51	18.79	9.53	5.15	4.48	2.98	1.58	1.36
2.0	138.18	119.13	116.99	27.57	17.45	16.04	7.96	4.33	3.77	2.49	1.32	1.14
2.4	124.25	108.07	106.27	24.31	15.59	14.38	6.97	3.82	3.34	2.18	1.16	1.01

Table 9. *Mean uncertainty along the measurable frequency range for usable values of the cavity length.*

As expected, the longer is the cavity the lower is the uncertainty, being therefore d = 2.4 cm the best value of the cavity spacing respecting the system uncertainty-based velocity-range constraint.

5.3.3 Precision of the velocity measurements

In this section, the uncertainty of the velocity measurements will be analyzed in detail when the configuration of the frequency discriminator is the one calculated in section 5.3.2.4 (cavity length $d = 2.4$ cm).

5.3.3.1 Zero velocity location

The uncertainty calculations presented in section 5.3.2.4, used to optimize the interferometer configuration, have been made assuming that the zero velocity is located on the point of the filter response with maximum precision (minimum uncertainty). This point depends, for each value of the cavity length, on the received power and on the characteristics of the atmosphere (*ASR*). Table 10 shows, when the interferometer is set to its optimal configuration (d = 2.4 cm), this position in terms of distance to the resonance peak of the response in all the measurement conditions considered in the previous sections.

Zero velocity location, which is the point where the emitted frequency has to be locked, has nevertheless to be a fixed input parameter of the measuring system. It is not possible to optimize this parameter in all conditions; hence the mean of all the values (87.3 MHz) has been chosen as system parameter and will be used from now on.

P_M	*ASR*	Minimum Uncertainty location (MHz)
1 nW	**1.1**	80.60
	2	76.00
	11	75.40
10 nW	**1.1**	92.20
	2	83.70
	11	81.40
100 nW	**1.1**	96.90
	2	91.20
	11	88.80
1 μW	**1.1**	97.50
	2	92.80
	11	90.50

Table 10. *Position of the point with minimum uncertainty for d = 2.4 cm, F = 35, τ_p = 10 ns and λ = 1064 nm.*

5.3.3.2 Uncertainty along the velocity range

Table 11 shows more detailed uncertainty parameters of the system when 87.3 MHz is the emitted frequency location and the cavity length is fixed to 2.4 cm.

P_M	*ASR*	Uncertainty at +25 m/s (m/s)	Uncertainty at 0 m/s (m/s)	Uncertainty at -25 m/s (m/s)	Mean uncertainty (m/s)
1 nW	**1.1**	151.11	110.93	150.28	123.08
	2	123.62	96.33	137.99	106.94
	11	120.53	94.75	136.70	105.18
10 nW	**1.1**	33.78	22.35	26.05	24.62
	2	19.65	14.03	18.00	15.49
	11	17.63	12.91	16.99	14.25
100 nW	**1.1**	10.13	6.53	7.21	7.17
	2	5.22	3.52	4.07	3.86
	11	4.43	3.06	3.61	3.35
1 μW	**1.1**	3.19	2.05	2.25	2.25
	2	1.61	1.08	1.23	1.18
	11	1.36	0.93	1.07	1.01

Table 11. *Uncertainty parameters for d = 2.4 cm, F = 35, τ_p = 10 ns, λ = 1064 nm and f_0 = 87.3 MHz.*

5.3.3.3 Measurements averaging. Range and time resolution

It is clear that the uncertainty figures shown in Table 11 are not good enough for practical wind measurements: only collecting a minimum return power of 1 μW –which could correspond, in a standard system configuration, to measurements at short ranges in atmospheric layers with high aerosol content (see section 5.3.4)– is possible to achieve moderately good accuracy (uncertainty above 1 m/s). Thus it is indispensable to average velocity measurements for reducing the uncertainty in other measurement scenarios. Table 12 shows the averaging factor *AF* (number of accumulated samples) needed to achieve, in each measurement condition, different uncertainty figures (mean value (Eq. (73)) from 0.2 to 2 m/s). In all the cases *d* = 2.4 cm.

Error (m/s)	Required averaging factor (number of accumulated bins)											
	P_M =1 nW			P_M =10 nW			P_M =100 nW			P_M =1 μW		
	ASR 1.1	ASR 2	ASR 11	ASR 1.1	ASR 2	ASR 11	ASR 1.1	ASR 2	ASR 11	ASR 1.1	ASR 2	ASR 11
0.2	385981	291998	282309	14779	6075	5172	1217	365	279	119	34	26
0.4	96496	73000	70578	3695	1519	1293	305	92	70	30	9	7
0.6	42887	32445	31368	1643	675	575	136	41	31	14	4	3
0.8	24124	18250	17645	924	380	324	77	23	18	8	3	2
1.0	15440	11680	11293	592	243	207	49	15	12	5	2	2
1.5	6862	5192	5019	263	108	92	22	7	5	3	1	1
2.0	3860	2920	2824	148	61	52	13	4	3	2	1	1

Table 12. *Required averaging factor for achieving a given mean uncertainty within the measurable frequency range (d = 2.4 cm).*

The price paid when averaging is a loss in range and/or time resolution. The range resolution along the line-of-sight (LOS) of the instrument provided by the receiver considered in these calculations (sampling rate f_s = 20 MHz) when no range averaging is performed is ΔR = 7.5 m. The resulting range resolution when range averaging is applied can be obtained by multiplying ΔR by the number of accumulated range bins. Time averaging consists in accumulating measurements from consecutive pulses. The corresponding single-shot time resolution when the pulse repetition frequency is PRF = 20 Hz is ΔT = 50 ms. The resulting time resolution when pulse averaging is performed is obtained by multiplying this value by the number of accumulated shots. Range bin averaging and shot accumulation can of course be conveniently combined to obtain the required averaging factor (overall number of accumulated samples).

Using approximate indicative values of the time and the range resolution, Table 13 shows instances of combinations of these parameters for achieving respectively 0.2 m/s, 1 m/s and 2 m/s uncertainty as a function of the received Mie power. The aerosol scattering ratio is not used here as input parameter since the measurement uncertainty depends only weakly on it in most of typical scenarios (see Table 11)).

P_M	Range – Time resolution		
	Uncertainty: 0.2 m/s	Uncertainty: 1 m/s	Uncertainty: 2 m/s
1 nW	ΔR > 2000 m – ΔT > 75 s ΔR > 300 m – ΔT > 500 s	ΔR > 1500 m – ΔT > 4 s ΔR > 150 m – ΔT > 40 s	ΔR > 300 m – ΔT > 5 s ΔR > 50 m – ΔT > 30 s
10 nW	ΔR > 1500 m – ΔT > 5 s ΔR > 150 m – ΔT > 50 s	ΔR > 500 m – ΔT > 500 ms ΔR > 50 m – ΔT > 5 s	ΔR > 125 m – ΔT > 500 ms ΔR > 40 m – ΔT > 1.5 s
100 nW	ΔR > 500 m – ΔT > 1 s ΔR > 100 m – ΔT > 5 s	ΔR > 100 m – ΔT > 250 ms ΔR > 50 m – ΔT = 500 ms	ΔR > 100 m – ΔT > 50 ms ΔR > 50 m – ΔT = 100 ms
1 μW	ΔR > 250 m – ΔT > 200 ms ΔR > 100 m – ΔT > 500 ms	ΔR > 50 m – ΔT > 50 ms ΔR > 7.5 m – ΔT = 250 ms	ΔR = 15 m – ΔT = 50 ms ΔR > 7.5 m – ΔT > 100 ms

Table 13. *Range – time resolution combinations to achieve 0.2, 1 and 2 m/s uncertainty for each value of the Mie return power.*

In situations in which the received power is 1 μW, a value that could be obtained at low ranges and from an atmosphere with high aerosol content, very good precision can be achieved with high both range and time resolution. Obviously, as the received power

decreases, a loss of resolution has to be accepted for achieving the same uncertainty. In the other extreme, if the return power is in the range of 1 nW, the required loss of resolution becomes significant for wind measurements if good precision is needed (ΔR > 2000 m and ΔT > 75 s (more than 1 minute) for uncertainty equal to 0.2 m/s). An important loss of precision should then be allowed for maintaining good resolution figures. For this received power, even if the permitted uncertainty grows up to 2 m/s, the required combination range – time resolution is still poor for typical aerosol-based measurements (ΔR > 300 m – ΔT > 5 s, or ΔR > 50 m – ΔT > 30 s).

5.3.3.4 Uncertainty dependence on the received power and the aerosol scattering ratio

As seen in previous sections, the uncertainty of the wind measurements depends, for a given receiver, both on the received Mie return power (P_M) and on the proportion of the Rayleigh component on the total signal (*ASR*). In this section, these dependences are analyzed in more detail.

First, Fig. 31 displays the uncertainty (mean value in the velocity range) as a function of the received power for different aerosol loads when the cavity length is fixed to 2.4 cm and no averaging is applied (*AF* = 1).

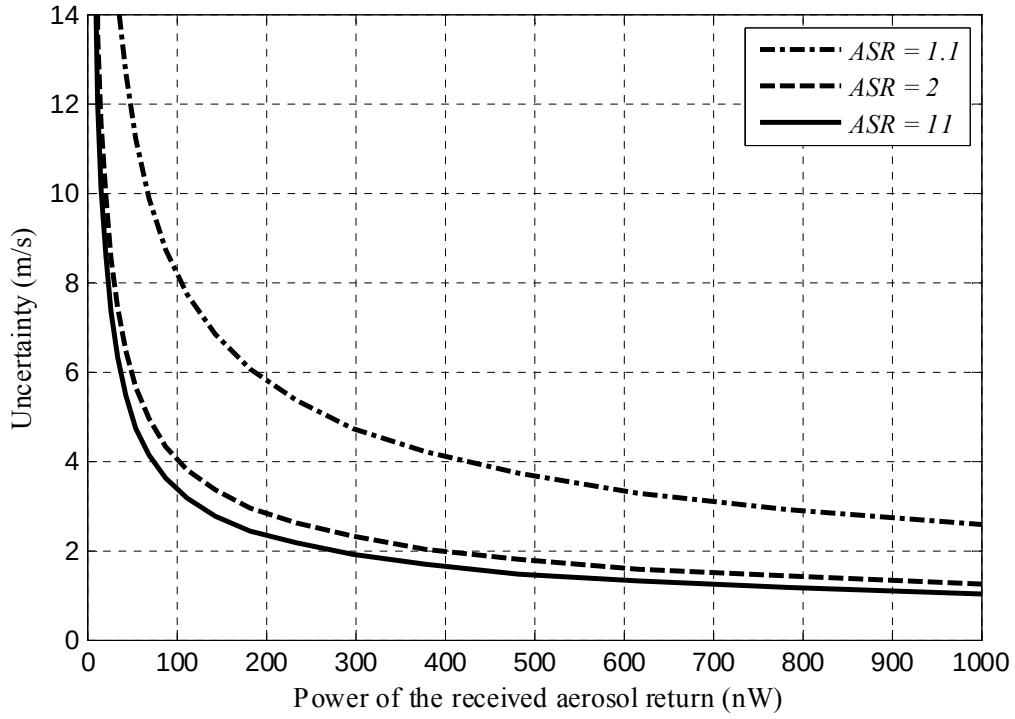

Fig. 31. *Mean uncertainty (along the whole velocity measurable range) as a function of the Mie return power for different values of the ASR (d = 2.4 cm, F = 35, τ_p = 10 ns and λ = 1064 nm).*

As expected, due to the higher signal-to-noise ratio, the greater is the received aerosol power the better is the performance, with lower expected error in the velocity determination. The uncertainty depends inversely both on the signal-to-noise ratio and on the sensitivity to velocity changes. The uncertainty dependence on the received power, however, comes exclusively through the signal-to-noise ratio term and, although this cannot be clearly seen in Fig. 31 due to their inverse relation, this dependence should be stronger for low levels of the received power. In this case, the dark current and the electronic noise of the receiver

dominate over the Mie signal shot-noise and, as a consequence, the signal-to-noise ratio is proportional to the received signal. On the other hand, if the Mie return is intense, the signal shot-noise is the dominant term and the signal-to-noise ratio grows only proportionally to the square root of the Mie power (see Eq. (74)). In order to visualize this feature, Fig. 32 plots, using the same parameters than in Fig. 31, the signal-to-noise (also averaged in the measurable velocity range) versus the Mie received power.

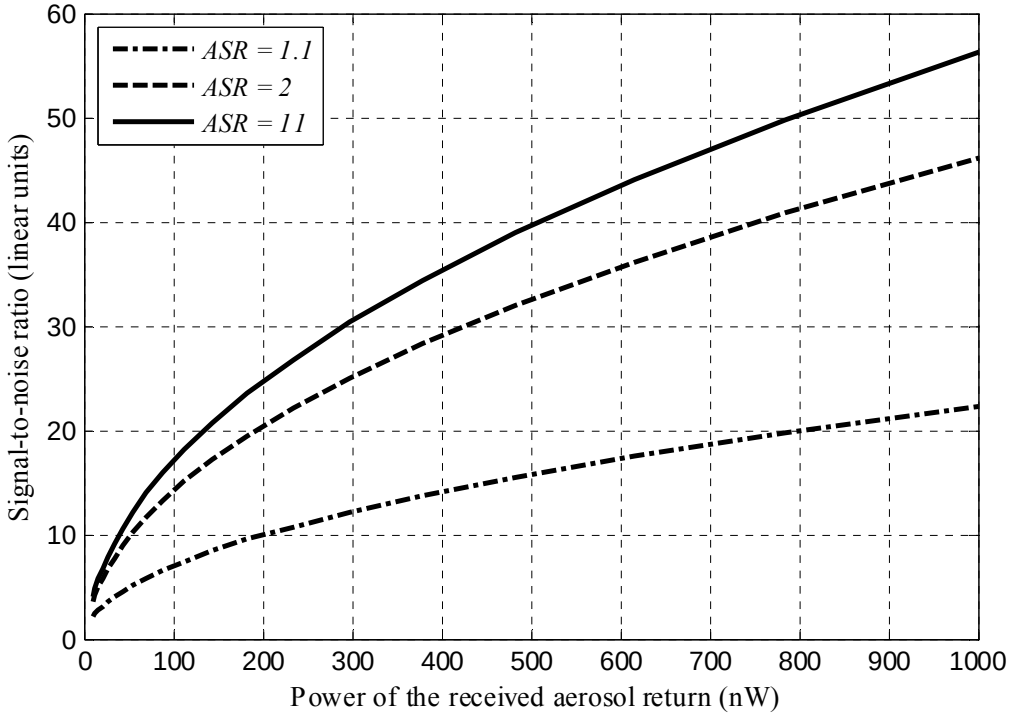

Fig. 32. *Signal-to-noise ratio dependence on the aerosol received power for different values of the aerosol scattering ratio.*

Carrying out a similar analysis for the *ASR* dependence, Fig. 33 shows respectively the uncertainty and the signal-to-noise ratio as a function of the *ASR* for different values of the incident Mie Power.

As expected, for the same received aerosol power, if the atmosphere is cleaner, the uncertainty is higher because the Rayleigh background shot-noise increases with respect to the Mie return and, as a consequence, the signal-to-noise ratio decreases.

The influence of the *ASR* on the signal-to-noise ratio and the uncertainty, however, is only significant, for each value of the incident power, when the shot-noise associated to the detection of the background Rayleigh component of the return is the main source of noise. This only happens in very clean atmospheres, where *ASR* is very small and consequently the Rayleigh shot-noise dominates over the Mie one and at low altitudes, where the Rayleigh return is intense enough to make the corresponding detection shot-noise being much greater than both the dark current noise and the one added by the receiver circuitry. Both conditions –low altitude and very clean atmosphere– will rarely coincide and in fact it can be stated that in most of typical measuring scenarios the effect of Rayleigh contamination on the system precision is not significant.

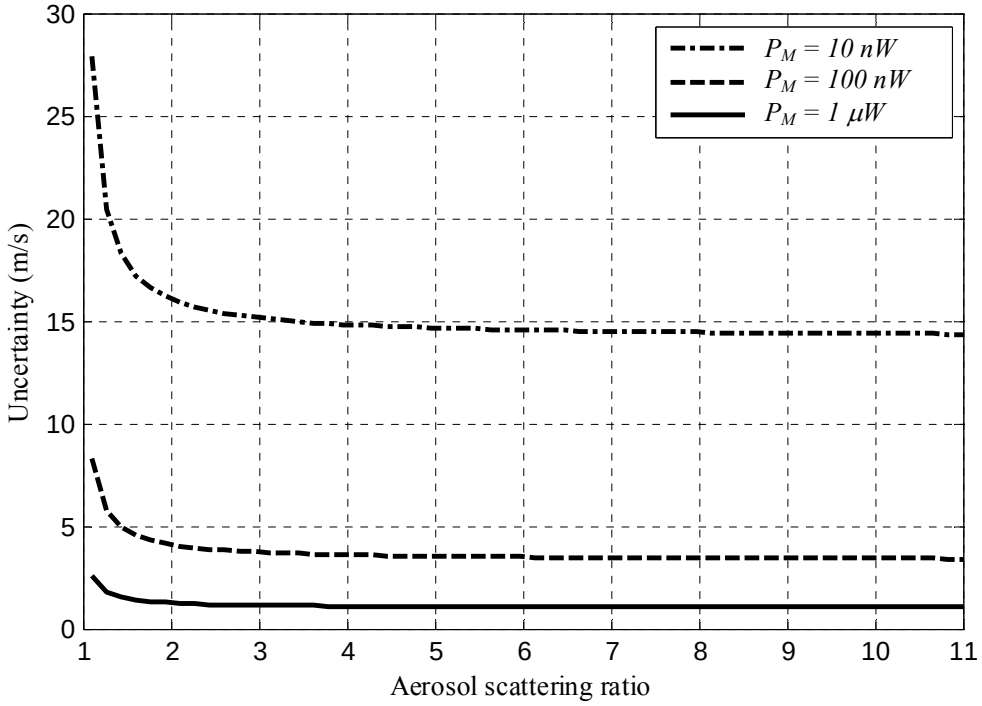

Fig. 33. *Uncertainty dependence on the aerosol scattering ratio for different values of the incident Mie return power.*

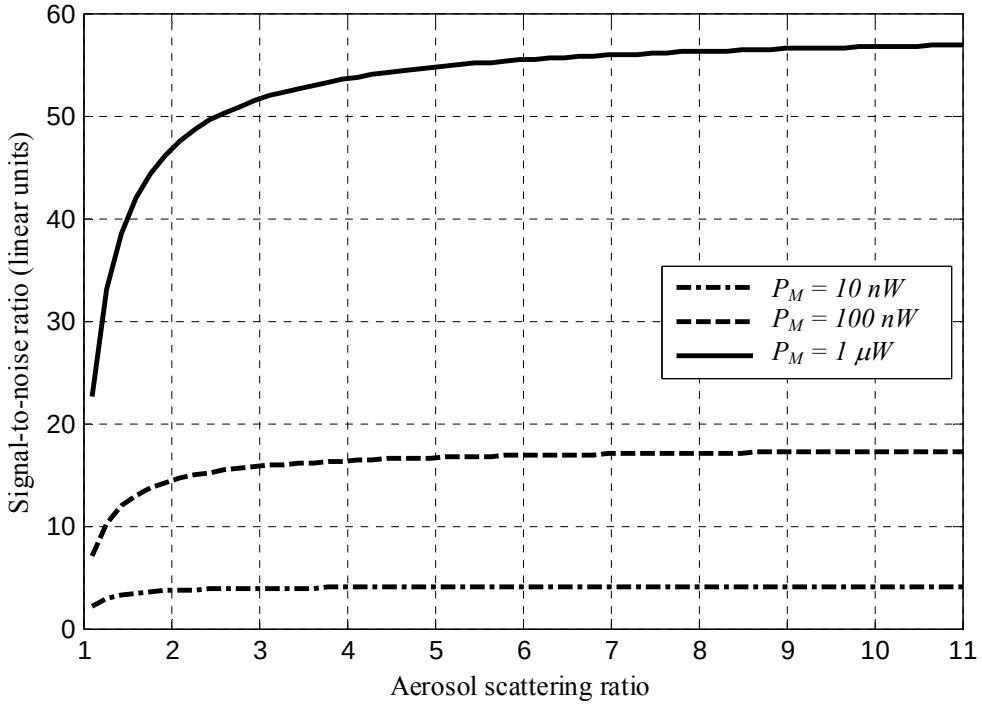

Fig. 34. *Signal-to-noise ratio (mean value in the measurable velocity range) dependence on the aerosol scattering ratio for different values of the incident Mie return power.*

5.3.4 System performance in typical measuring scenarios

5.3.4.1 Power budgets

In the previous sections, the uncertainty calculations have been made using the received aerosol return power as the input parameter with the objective of deriving conclusions that are not dependent on the power budget of the particular system.

Of course, the Mie return depends on the emitted power, on the receiving optics and on the range and physical properties of the atmospheric region where the wind measurements are being made. If a performance analysis of the considered instrument wants to be made under different typical measuring scenarios, this dependence has to be explicitly taken in account and the power link budget of the system has to be calculated.

Eq. (79) provides the expression to calculate the power of the Mie return collected by the telescope from an atmospheric region at a range R.

$$P_M(R) = \frac{E_T\, A_r\, c}{2R^2}\, \beta_M(R) \exp\left[-2\int_0^R \alpha(z)\,dz\right] \tag{82}$$

There are three parameters in this expression depending on the atmospheric cell where the measurement is made: the range of the measurement (R), the volume backscattering coefficient for the Mie return at that range ($\beta_M(R)$) and the total extinction in the propagation path ($\exp\left[-2\int_0^R \alpha(z)\,dz\right]$). The Mie volume backscatter coefficient $\beta_M(R)$ is obtained from $\beta_R(R)$, which can be accurately modelled using simple expressions (see Eq. (5) in section 3.1.1), and from the aerosol scattering ratio ($ASR(R)$).

$$\beta_M(R) = \left[ASR(R) - 1\right]\beta_R(R) \tag{83}$$

As already pointed out in section 5.3.2.3, the extinction coefficient term in the Mie lidar equation has to be computed as the sum of the Mie and the Rayleigh extinction coefficients.

$$\alpha(z) = \alpha_M(z) + \alpha_R(z) \tag{84}$$

Like the volume backscattering coefficient, the Rayleigh component of the extinction coefficient is easy to model. The molecular lidar ratio $L_R(R)$, i. e., the Rayleigh extinction-to-backscatter ratio has a well known non-range-dependent value in any atmospheric condition [58]:

$$L_R(z) = \frac{\alpha_R(z)}{\beta_R(z)} = \frac{8\pi}{3}\ \text{sr}. \tag{85}$$

This is not the case for the aerosol lidar ratio ($L_M(z)$), which depends on size distribution, shape and chemical composition of the aerosol particles and is not easy to model. The objective of the calculations presented here is obtaining uncertainty figures that can be representative of the performance of the measuring system. For that purpose, a fixed value of the aerosol lidar ratio, yet typical in urban regions, of $L_M(z) = 50$, will be used in the calculations (see Table 14).

Type of aerosol	Lidar ratio @ 532 nm
Marine particles	20 – 35 sr
Saharan dust	50 – 80 sr
Urban particles	35 – 70 sr
Biomass burning smoke	70 – 100 sr

Table 14. *Typical lidar ratios for different aerosol types at 532 nm wavelength determined with a Raman lidar* [58]

The total extinction coefficient along the propagation path (z) can be therefore approximately estimated using the following equation.

$$\alpha(z) = 50\,\beta_M(z) + \frac{8\pi}{3}\,\beta_R(z) = \left\{50\left[ASR(z) - 1\right] + \frac{8\pi}{3}\right\}\beta_R(z) \tag{86}$$

To calculate the Mie return power using Eqs. (82), (83) and (86), besides the transmitter and the receiver parameters, it is necessary to compute the Rayleigh volume backscattering coefficient ($\beta_R(z)$), which is given by Eq. (5), and to estimate the profile of the aerosol scattering ratio in the atmosphere ($ASR(z)$).

Since it is not possible to take into account every atmospheric situation, a schematic structure in terms of aerosol load will be used in this section to compute the power budgets. In this model [45], three atmospheric regions will be considered, the first one, from 0 to 2 km corresponds approximately to the aerosol-mixing boundary layer, where the aerosol scattering ratio is fixed to be *ASR* = 11. In the second layer, from 2 to 6 km a fast exponential decay from 11 to 1.1 is modeled. For ranges higher that 6 km the aerosol content remains constant with *ASR* = 1.1. A first set of calculations are made in this atmospheric structure at three different altitudes. Afterwards, as variations of this basic scheme, measurements at superposed layers with high aerosol content located respectively at 4 and 6 km, modeling dust, ashes, or any other thin aerosol layer, will be also considered. Fig. 35 shows these three *ASR* profiles.

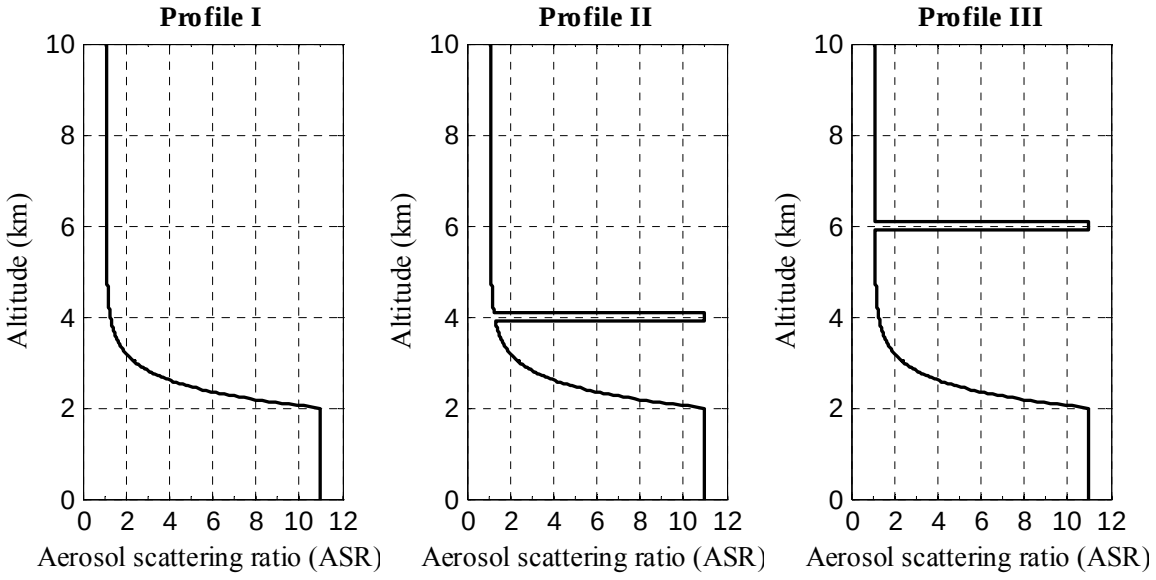

Fig. 35. *Aerosol scattering ratio profiles used for power calculations*

If vector wind estimations are required, radial velocity measurements from at least three independent directions are necessary, usually azimuth variations at the same elevation angle [59]. Moreover, since the main component of the atmospheric wind is the horizontal one, sensitive wind measurements require the use of non-zenithal directions. Power budgets made from now on using the aerosol vertical distributions modelled in Fig. 35 will consider therefore observations with an elevation angle of 45º. Fig. 36 illustrates the measurement geometrical scheme.

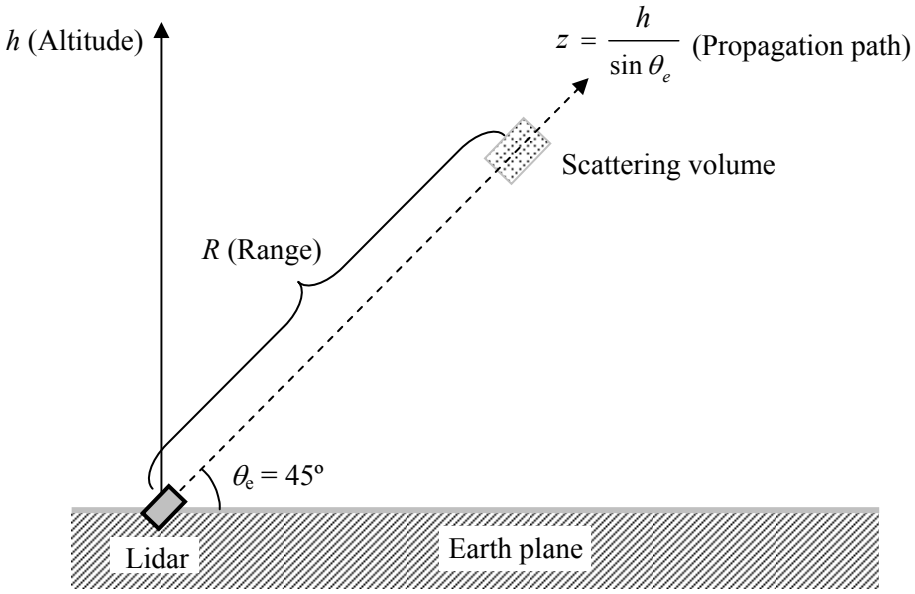

Fig. 36. *Orientation of the observation for horizontal wind measurements.*

As numerical examples, the Mie power at three ranges in profile I and the one received from the aerosol layers defined in profiles II and III (Fig. 35) are presented in Table 15. 45º degrees observation has been considered in these calculations.

Profile	**I**			**II**	**III**
Altitude	***h* = 1 km**	***h* = 3 km**	***h* = 6 km**	***h* = 4 km**	***h* = 6 km**
ASR	11	2.44	1.10	11	11
β_M **(**m^{-1} sr^{-1}**)**	$8.82 \cdot 10^{-7}$	$9.90 \cdot 10^{-8}$	$4.88 \cdot 10^{-9}$	$6.07 \cdot 10^{-7}$	$4.72 \cdot 10^{-7}$
Extinction: $\exp\left[-2\int_0^R \alpha(z)\,dz\right]$	0.88	0.75	0.74	0.74	0.73
P_M (nW)	1838	19	0.24	66	23

Table 15. *Power calculations at different measuring scenarios*

As graphical example of the power calculations, Fig. 37 shows the Mie power (in a logarithmic scale) collected by the telescope as a function of the altitude, for an aerosol scattering ratio vertical distribution like the one described by profile I (Fig. 35) when an elevation angle of 45º is used for the observation.

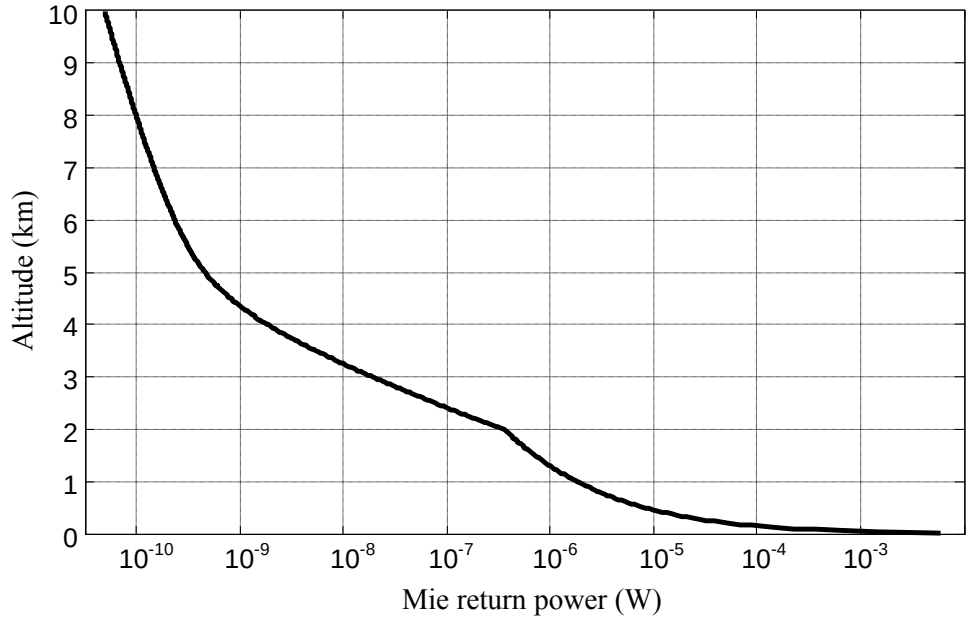

Fig. 37. *Mie return power in an atmosphere with the aerosol load described by profile I.*

5.3.4.2 Uncertainty, range and time resolutions in typical measuring scenarios

If uncertainty calculations are made using these power and *ASR* values, it is possible to estimate the expected error in each measuring condition when different averaging factors are applied. Table 16 shows these results and combination examples of altitude–time resolution ($\Delta h - \Delta T$) corresponding to each averaging factor. In these calculations, the altitude resolution has been obtained from the range resolution (ΔR), which depends on the sampling frequency of the acquisition system (7.5 m if no averaging is applied), and the elevation angle of the observations (θ_e) as

$$\Delta h = \Delta R \sin \theta_e \,. \tag{87}$$

AF	**$\Delta h - \Delta T$**	**Mean uncertainty (m/s)**				
		Profile I			**P. II**	**P. III**
		1 km	**3 km**	**6 km**	**4 km**	**6 km**
1	5 m – 50 ms	0.75	10.01	449.56	4.24	8.01
10	50 m – 50 ms 5 m – 0.5 s	0.24	3.17	142.30	1.34	2.53
100	50 m – 0.5 s 5 m – 5 s	0.08	1.00	45.00	0.42	0.80
1000	50 m – 5 s 500 m – 0.5 s	0.02	0.32	14.23	0.13	0.25
10000	50 m – 50 s 500 m – 5 s	0.01	0.10	4.50	0.04	0.08
100000	500 m – 50 s 1 km – 25 s	0.00	0.03	1.42	0.01	0.03

Table 16. *Mean uncertainty for different measuring situation with different range – time averaging combinations*

Also, the required averaging factor (not shaded cells) and an instance of corresponding resolution combination (shaded cells) for obtaining given uncertainty figures can be calculated and are presented in Table 17.

Uncertainty (m/s)	Profile I			Profile II	Profile III
	1 km	**3 km**	**6 km**	**4 km**	**6 km**
0.1	*AF* = 57	*AF* = 10021	*AF* = 20110456	*AF* = 1798	*AF* = 6417
	40 m – 400 ms	500 m – 5 s	2 km – 40 min	200 m – 2.5 s	400 m – 4 s
0.5	*AF* = 3	*AF* = 401	*AF* = 808419	*AF* = 72	*AF* = 257
	10 m – 100 ms	100 m – 1 s	1 km – 3 min	50 m – 500 ms	150 m – 500 ms
1.0	*AF* = 1	*AF* = 101	*AF* = 202105	*AF* = 18	*AF* = 65
	5 m – 50 ms	50 m – 500 ms	500 m – 100 s	20 m – 250 ms	40 m – 400 ms
2.0	*AF* = 1	*AF* = 26	*AF* = 50527	*AF* = 5	*AF* = 17
	5 m – 50 ms	25 m – 250 ms	500 m – 25 s	10 m – 150 ms	20 m – 200 ms
3.0	*AF* = 1	*AF* = 12	*AF* = 22457	*AF* = 2	*AF* = 8
	5 m – 50 ms	15 m – 200 ms	300 m – 20 s	5 m – 100 ms	15 m – 150 ms

Table 17. *Averaging factor and example of resolution combination to obtain fixed values of uncertainty in different measuring situations.*

5.3.4.3 Comparison with reference examples

For evaluating the performance of the system from the results shown in Table 17, it is necessary to have references about precision, range resolution and temporal resolution that can be considered good in wind measurements.

These requirements can be, however, very different depending on the type of measurement and its application. Three reference examples will be taken in account for comparisons. The first one corresponds to data requirements for space-borne measurements of global winds that were formulated in 2001 by the Global Tropospheric Wind Sounder (GTWS) Science Definition Team (SDT), a joint NASA-NOAA effort formed for this purpose [7]. The second and the third references are defined by the performance parameters of two different ground-based Doppler wind lidar systems, relying both on aerosol return, successfully used in two different applications employing two different detection techniques. In the first place, an edge-technique-based system, in this case using an iodine filter as discriminator and a high pulse-repetition-rate laser as transmitter, that was operated during 2007 Qingdao International Regatta and 2008 Beijing Olympic Games to measure the distribution of sea surface wind in the racing area [60], [61]. Secondly, the performance of a system using coherent detection (inherently more sensitive if aerosols are present), the Lidar Windshear Alerting System (LIWAS), used in the Hong Kong International Airport since 2005 for windshear detection [62], will be taken in account as the most demanding reference example.

Parameter	GTWS-SDT [7]		Quingdao [61]	LIWAS [62]
	Boundary layer	Free troposphere		
Uncertainty	1 – 2 m/s *	2 – 3 m/s *	1 – 4 – 8 m/s **	1 m/s
Range resolution	500 m	1000 m	30 m	100 m
Integration time	15 s	15 s	100 s	0.1 s
Maximum range	–	–	3 – 8 km	7.5 km

* Objective – threshold
** At 1, 6 and 8 km respectively

Table 18. *Standard requirements of wind measurements for space-borne global wind measurements and performance parameters of a coherent lidar used for windshear detection.*

Some conclusions can be derived if the results obtained in section 5.3.4.2 are compared with the performance parameters shown in Table 18.

In a standard atmosphere like the one described by the profile I, very precise wind measurements with high both range and time resolution can be made within the boundary layer. For example, measurements at 1 km range can be made with uncertainty lower than 0.1 m/s and a combination of range – time resolution as good as 40 m – 400 ms. If the uncertainty requirements are relaxed up to 1 m/s, both range and time resolution can decrease down to their minimum possible values in this system: 5 m – 50 ms. The three values – uncertainty, range and temporal resolution– are far better than the data requirements defined by GTWS-SDT for measurements within the boundary later (1–2 m/s, 500 m and 15 s). It has to be taken in account, however, that these requirements are formulated for space-borne measurements, which precision is limited by their long range. They are also better –especially in time resolution– to the performance parameters of the Qingdao system (1 m/s, 30 m and 100 s at 1 km). Finally, there are not available data at 1 km for the coherent-detection-based LIWAS; the listed performance parameters (1 m/s, 100 m and 100 ms) refer to a limit valid up to 7.5 km altitude. However, the comparison between these figures and the ones calculated at 6 km (1 m/s, 500 m, 100 s) permits to guess that the performance is clearly poorer.

Above the boundary layer, the system performance decays rapidly as the aerosol content decreases. At 3 km, where according to the atmospheric model used in these calculations certain aerosol content can be found ($ASR = 2.44$), uncertainty and resolution values (1 m/s, 50 m, 500 ms) are still significantly better than the GTWS-SDT requirements for space-borne measurements, even if the boundary layer case is considered (1–2 m/s, 500 m and 15 s). At 6 km, the measurements show quality parameters (2 m/s, 500 m and 25 s) that are still acceptable for atmospheric research above the boundary layer (2–3 m/s, 1 km and 15 s), but clearly worse than the ones provided by the LIWAS coherent system at 7.5 km (1 m/s, 100 m and 100 ms). The Quingdao Doppler wind lidar, direct-detection instrument also designed for operating using Mie return, shows comparable figures at the same altitude (4 m/s, 30 m, 100 s).

This significant loss of precision above the boundary layer is due to the lack of aerosol in the atmosphere at that altitude –space-borne measurements above the boundary layer are in all the cases made relying on molecular return– and not so much on the altitude: if measurements are made at aerosol layers located above the boundary layer (profiles II and III), good precision and resolution can be achieved too. If the layer is at 4 km and the uncertainty is fixed to 1 m/s, a resolution combination of 50 m – 100 ms, which is close to the coherent LIWAS parameters at 7.5 km, is possible; whereas, at 6 km altitude, 1 m/s would

require a resolution combination of 40 m – 400 ms, which would be acceptable for many aerosol-based applications.

As a general conclusion it can be said that this is a system designed to operate relying on aerosol return and, as a consequence, its performance is good only in regions with high aerosol loads, which are only common within the boundary layer. In the free troposphere, only if aerosol or clouds layers are present, good measurements can be obtained. Although the Qingdao system uses different technology in the transmitter and in the frequency discriminator, is applying the same detection principle, and, as a consequence, is the reference example whose performance is closer to the expected one for the designed instrument. LIWAS Doppler wind lidar shows better performance because uses coherent detection, whose sensitivity in the presence of aerosols is inherently higher. On the other side, space-borne measurements are valuable since they permit scanning large regions, but their performance figures are necessarly poor because they are made made at ranges of hundreds of kilometres. This strongly limits their precision, even in the boundary layer using the aerosol return, and makes that the data requirements calculated for such systems are clearly below the ones of the system analyzed here.

5.3.5 Accuracy of the measurements: Effect of Rayleigh contamination on measurement bias

In this section, the Rayleigh-induced bias error is calculated for an edge-technique-based Doppler wind lidar relying on aerosol return in different aerosol loading conditions. The parameters of the system are the ones considered and calculated in the previous sections and the expressions used to estimate the error are the ones derived in section 4.4.3.

Fig. 38 shows, for different values of the aerosol scattering ratio (*ASR*), the absolute error in the determination of the frequency response due to this effect $\delta F_M(\nu)$ as a function on the position of the detected frequency on the filter the slope (Eq. (57)). This position is expressed in terms of detected velocity and the results are displayed within the velocity dynamic range of the system (± 25 m/s). The calculations are carried out for an atmospheric system like the one considered in the uncertainty analysis from section 5.3.3 (F = 35, d = 2.4 cm, τ_p = 10 ns, λ = 1064 nm and f_0 = 87.3 MHz).

As it can be observed, in each condition, this error is practically constant along the velocity dynamic range. This is due, as previously mentioned, to the broad spectrum of the Rayleigh component with respect to the Mie frequency response.

Fig. 39 displays the error in the velocity determination due to the Rayleigh contamination δv_r for different values of the aerosol scattering ratio (Eq. (60)). Results are calculated as a function of the measured velocity and are displayed within the velocity dynamic range of the system (± 25 m/s).

Table 19 shows the mean value of the velocity error within the velocity dynamic range of the system.

ASR	11	6	3	2	1.5	1.2
Bias error (m/s)	0.92	1.69	3.38	5.06	6.75	8.44

Table 19. *Mean Rayleigh-induced bias error within the velocity dynamic range*

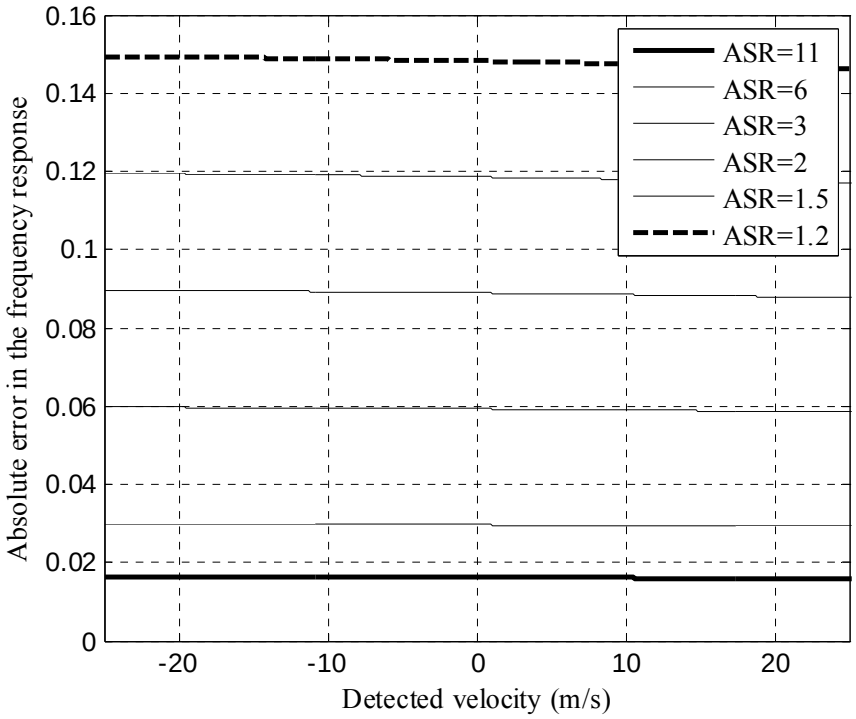

Fig. 38. *Absolute error in the determination of the frequency response along the filter slope as a function of the detected velocity for different atmospheric conditions*

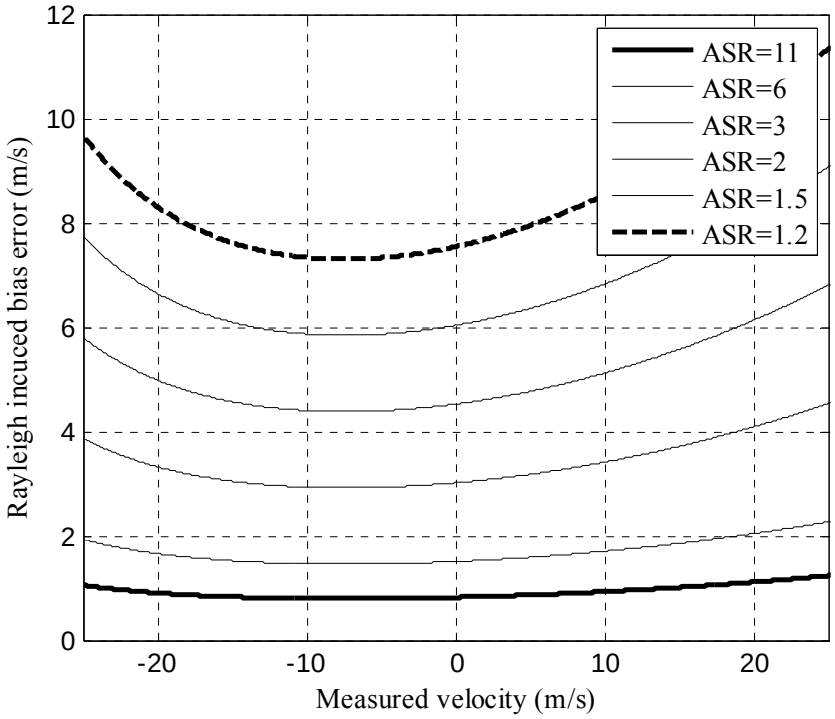

Fig. 39. *Rayleigh-induced bias error in frequency determination within the velocity dynamic range (F = 35, d = 2.4 cm, τ_p = 10 ns, λ = 1064 nm and f_0 = 83.1 MHz).*

Even in an atmosphere with high aerosol content (*ASR* = 11) the mean Rayleigh-induced bias error has a significant value (0.92 m/s). It is obvious hence that in a Doppler wind lidar using the edge technique, the bias error originated by the Rayleigh contamination is not acceptable and must be avoided or removed.

If a solution like the one described in 4.4.3 is implemented to calculate the Rayleigh component in the detected signals, this effect can be removed. As already stated, for eliminating the bias error, the Mie and Rayleigh responses of the filter used to discriminate the components of the return (filter 2 in Fig. 14) should be approximately constant in the whole frequency range of the measurements and as a consequence, both responses have to be significantly wider than this range. As an example, if the filter used to discriminate components (filter 2 in Fig. 14) has a bandwidth of 500 MHz (e. g., $F = 12.5$ and $d = 2.4$ cm), the maximum range of measurable velocities is ± 25 m/s, the temperature is 300ºK and the laser emits 10 ns pulses at 1064 nm, the mean deviation of the responses with respect to their maximum value within the velocity dynamic range is 0.97 % for the Mie response and 0.08 % for de Rayleigh response. The effect of this error can be therefore neglected.

5.4 Conclusions of this chapter

Two types of edge-technique-based system have been analyzed in this chapter. First, a continuous-wave velocimeter used to measure the speed of hard targets. Secondly, an edge-technique-based Doppler wind lidar relying on aerosol return.

In both cases, a method to set the best configuration of the frequency discriminator –a Fabry-Perot interferometer– has been presented and applied. This method is based on the optimization of the trade-off between the measurement uncertainty and the constraint fixed by the measurable velocity range.

The performance of a continuous-wave velocimeter like the prototype that has been built and assessed has been analyzed in first place. The uncertainty of the measurements has been calculated for different operating conditions (received power from 1 nW to 10 μW). The results of these calculations permit to say, as a first conclusion, that the system is able to measure the velocity of hard targets with good precision figures. Sample averaging, nevertheless, is necessary for low incident power and an analysis of its effect on the time resolution of the measurements has been also carried out. These results will be further used in the performance evaluation of the implemented prototype (chapter 7).

For the atmospheric Doppler wind lidar, an uncertainty-based analysis has been also carried out for different operating conditions (detected power and molecular background contamination). From these results it has been possible to establish that the calculated uncertainty depends mainly on the aerosol return power and, in most of common scenarios, only weakly on the proportion of the Rayleigh component.

Power budgets in different realistic scenarios have been calculated using the system parameters of the planned *UPC* Doppler wind lidar. As expected, the analyzed instrument results to be capable to provide precise wind measurements in atmospheric regions with high or moderate aerosol content. Its precision, resolution and maximum range are comparable to other operative direct-detection-based Doppler wind lidars relying also on aerosol return and worse than the ones provided by typical coherent-systems.

As mentioned above, precision is not significantly impaired by Rayleigh contamination; nevertheless, its presence produces a bias error in the velocity determination that it has been proved that needs to be eliminated. The effectiveness of one of the possible solutions to this problem –using a second filter to measure Rayleigh component and removing it form the detected signal– has been also analyzed and evaluated in this section.

6 Continuous-wave solid-target prototype

An edge-technique based Doppler lidar velocimeter, using continuous-wave radiation for measuring the speed of solid targets has been designed and built in order to verify the characteristics of the edge technique as a method to measure velocities and to test, in controlled conditions, the performance of some of the critical subsystems that will be part of the wind lidar. Pulsed atmospheric lidar signals are not convenient for such tasks: their power is neither constant nor predictable, their duration is very short (for a maximum range of 6 km the whole profile has a duration of 40 μs) and the variable to be detected –the speed of the wind– is not easy measurable by independent means for validating the results. The use of the continuous-wave hard-target prototype has permitted to avoid these difficulties during the assessment of the edge technique implementation. In this section, a complete description of the prototype and all its subsystems will be laid out, including acquisition, control and processing routines.

6.1 General description of the prototype

In the prototype described in this chapter, a low-power, continuous-wave optical source is used to illuminate a solid target moving at a speed that can be controlled. The detection unit is designed to alternatively process two different signals, namely the Doppler-shifted backscattered signal and a sample of the transmitted one. The system will use the edge-technique (Chapter 4) for determining the frequency separation between them and the velocity of the moving solid target. Fig. 40 shows the general scheme of the laboratory set-up.

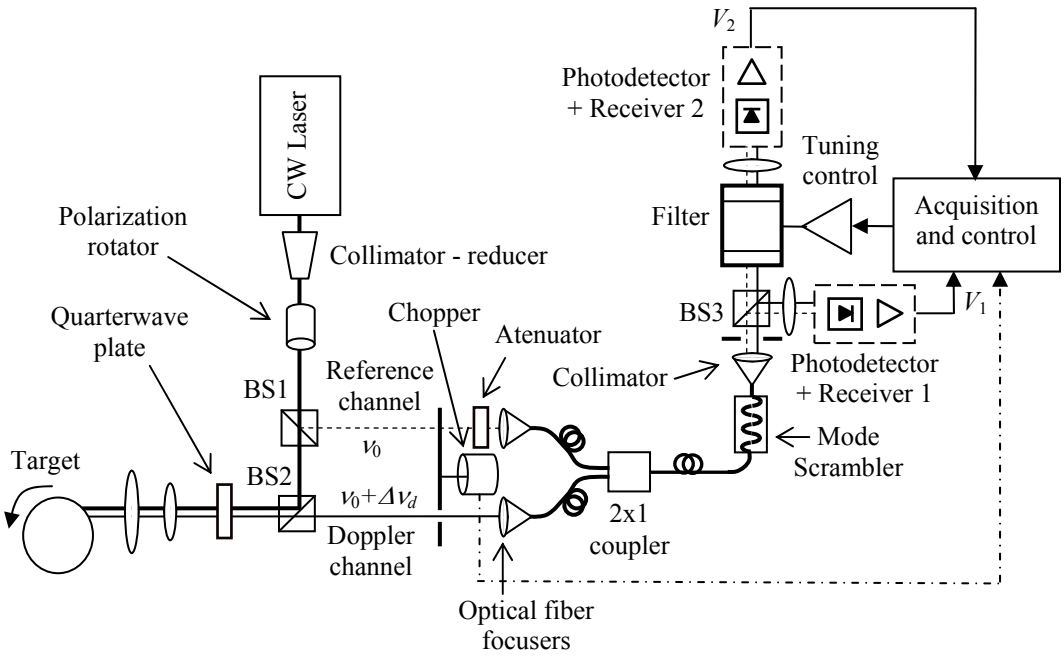

Fig. 40. *General scheme of the continuous-wave solid-target prototype*

The optical source is a continuous-wave laser. First, the size, collimation and polarization of the transmitted beam are conditioned. Then, a beam-sampler (BS1) extracts a sample from the beam that will be used as a reference of the emitted frequency (reference channel). The transmitted beam is sent to the target (a rotating wheel). An assembly including a polarizing beam-splitter (BS2), a quarter-wave plate and a focusing system forms an optical duplexor. It separates the transmitted beam from the received signal, which is led to the detection unit (Doppler channel). An optical chopper commutates alternatively reference and Doppler channels. The reference channel is attenuated in order to balance the power in both optical paths. Focusing lenses are used to couple the respective beams into graded-index multimode optical fibres. A low cost 2×1 optical fiber coupler combines both signals in a single optical fiber. A mode scrambler is used at this point to produce a mode distribution in the fiber independent of the launch conditions of the light. This helps to equal the beam features in the reference and the Doppler channels, which is a critical condition of the measuring system. After collimating and spatially filtering the outgoing light, a third beam-splitter (BS3) divides the beam in two paths: one of them is focused directly onto an APD-based optical receiver, whose function is monitoring the incident intensity, and the second one excites the high resolution optical filter, in this case a tuneable Fabry-Perot interferometer. Its output is also focused onto a second receiver (also APD-based), whose function is detecting the optical intensity transmitted through the filter. A 16-bit, up to 250 ks/s multifunction acquisition board samples the output signals of both receivers (V_1 and V_2), and feeds them to a personal computer that processes the data and calculates the radial velocity of the target.

At the same time, a real-time control loop acts on the interferometer to compensate the frequency drifts between the laser and the filter and maintain the right location of the emitted frequency on the filter slope.

6.2 Detailed description of the prototype

6.2.1 Laser source

A single-mode, diode pumped Nd:YAG laser emitting at 1064 nm (Spectra-Physics 6350) has been used as transmitting continuous-wave optical source. This transmitter is the seeder of the pulsed Spectra Physics GCR-190 that is in the *UPC* laboratory and will be eventually used in the atmospheric Doppler wind lidar. Its main parameters and characteristics are shown in Table 20.

Reference	Spectra – Physics 6350
Wavelength	1064 nm
Linewidth	< 10 KHz
Beam diameter	9 mm
Output power	1 mW
Polarization	Linear

Table 20. *Main parameters of the Continuous-wave laser*

6.2.2 Beam reducer - collimator

The size of the outgoing beam (∅ 9 mm) is too big for some of the optical and opto-mechanical elements of the system. A set of two lenses (the first bi-convex and the second one bi-concave) with adjustable distance between them has thus been introduced in the output path of the laser to reduce the size of the beam down to 4.5 mm and to adjust the collimation of the transmitted beam. The focal lengths have been chosen to enable the desired beam reduction. Fig. 41 and Table 21 show respectively the arrangement and the lens parameters.

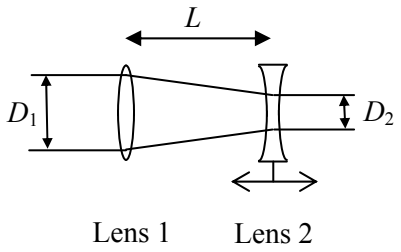

Fig. 41. *Beam reducer - collimator*

	Lens 1	**Lens 2**
Reference	Newport KBX076	Newport KBC037
Type	Bi-convex	Bi-concave
Focal length	200 mm	-100 mm
Diameter	25.4 mm	25.4 mm
Lens material	Graded A BK7	Graded A BK7
Coating	Uncoated	Uncoated

Table 21. *Parameters of the beam reducer – collimator lenses*

The beam reduction ratio and the separation between lenses required to reduce a collimated beam can be calculated as follows

$$\frac{D_2}{D_1} = \frac{f_2}{f_1} = 0.5 \rightarrow L = f_1 - f_2 = 10 \text{ cm}$$

The distance L is adjustable for correcting and accurately adjusting the collimation of the transmitted beam.

6.2.3 Polarization rotator

A lossless polarization rotator (ref. Newport PR-950) has been included in the transmission path for matching the polarization plane to the one required at the input of the transmitting – receiving optical assembly (see section 6.2.6).

Fig. 42 shows the set formed by the beam reducer – collimator and the polarization rotator.

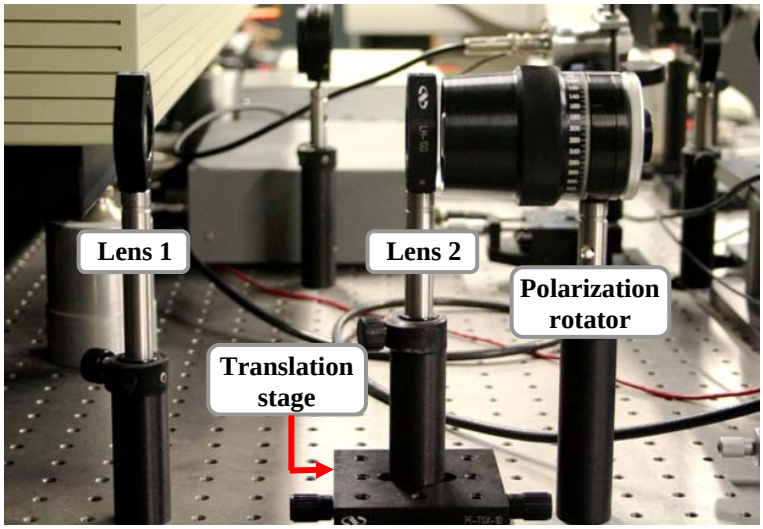

Fig. 42. *Beam reducer - collimator and polarization rotator.*

6.2.4 Beam-sampler

A beam-sampler extracts a portion of the emitted signal in order to provide information of the emitted frequency, necessary to carry out the differential measurement of the filter response. A small reflection-to-transmission ratio is desirable because the loss of power in the Doppler channel is much larger than in the reference channel. In this case, a 25.4 mm diameter BK7 beam-sampler (Newport 10B10NC.3) has been used, whose reflectance-transmittance ratio depends on the incidence angle and on the polarization of the light. Once mounted, the measured reflectance-to-transmittance ratio has resulted to be approximately 10/90. The beam sampler can be seen in the photography in Fig. 47.

6.2.5 Target

A feasible and affordable solution for having available in a research laboratory a solid target able to move at velocities in the range of those of the atmospheric wind is using a rotating disc with controlled angular speed (ω). A non-perpendicular ($\theta_i \neq 0^o$) incidence of the emitted radiation onto the edge of the wheel provides a measurable radial speed on the line-of-sight of the transmitter-receiver arrangement (v_r) (Fig. 43 (right) and Eq. (88)).

The target is a 1-cm thick and 50-cm diameter disc built in PVC and driven by a voltage-controlled DC motor (DOGA 168.4107.20.04) (Fig. 43 (left) and Fig. 44). The rim surface of the wheel has been covered with a highly reflective strip for increasing the scattered power.

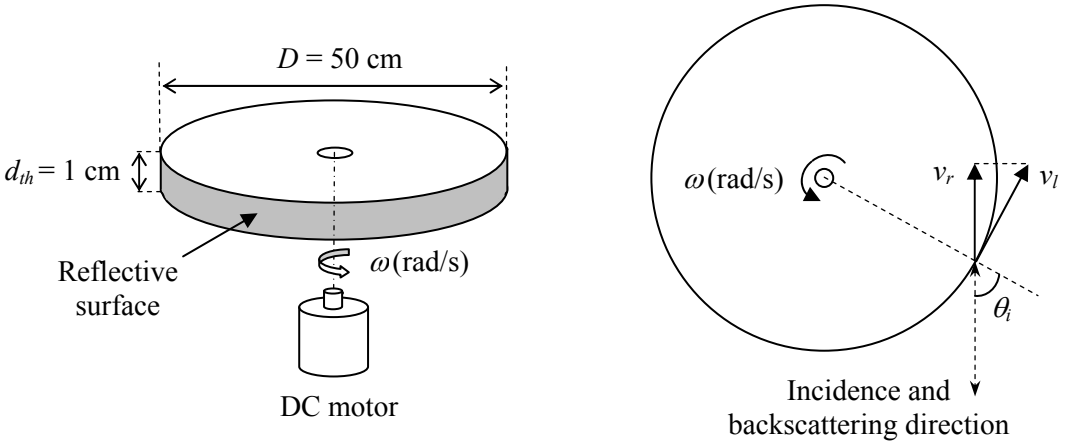

$$v_r = v_l \sin\theta_i = \omega R \sin\theta_i \tag{88}$$

Fig. 43. *Voltage-controlled rotating disc. ω, v_l and v_r are respectively the angular, linear and radial velocities and θ_i is the incidence angle.*

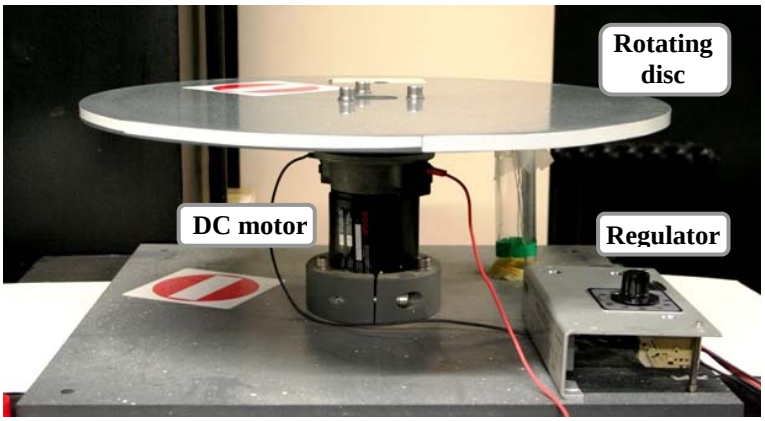

Fig. 44. *Voltage-controlled rotating disc*

6.2.6 Transmitting - receiving optical assembly

The transmitting – receiving subsystem includes a polarizing beam-splitter, a quarter-wave plate with its fast axis under 45 degrees and a set of two lenses. The function of the polarizing beam splitter BS2 (Newport 10BC16PC.9) is to direct the transmitted beam towards the target and the reflected light towards the measuring subsystem. The emitted radiation, vertically polarized, is completely reflected by BS2 and directed to the target. After passing through the 45º orientated quarter-wave plate (Newport 10RP14-34), the incident radiation on the target will be circularly polarized. If it were assumed that the light does not change its polarization when is reflected by the solid target, the reflected light, after having passed for second time through the quarter-wave plate, will be horizontally polarized. The polarizing beam-splitter will therefore transmit it to the detection subsystem without attenuation. Fig. 45 shows the polarization transformations in the optical arrangement when it is assumed that the reflection on the target does not change the polarization of the wave. An image of this arrangement can be seen in Fig. 47.

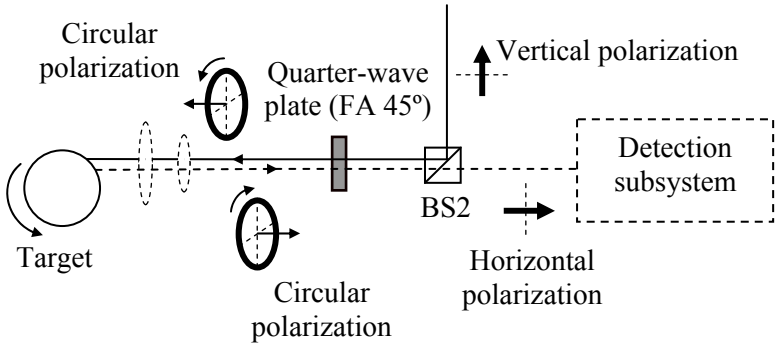

Fig. 45. *Polarization processing in the transmitting – receiving optical assembly*

The Jones vector of the vertically polarized transmitted beam (J_T) and the Jones matrix of an ideal 45º orientated quarter-wave plate ($J_{\lambda/4}$) and of an ideal non-polarizing reflecting surface (J_{RS}) are respectively

$$J_T = U_0 \begin{bmatrix} 1 \\ 0 \end{bmatrix} \quad ; \quad J_{\lambda/4} = \frac{1}{\sqrt{2}} \begin{bmatrix} 1 & -j \\ -j & 1 \end{bmatrix} \quad ; \quad J_{RS} = \alpha \begin{bmatrix} -1 & 0 \\ 0 & -1 \end{bmatrix}, \tag{89}$$

where U_0 is the field magnitude of the emitted light and α is the reflection coefficient in the reflecting surface. The Jones vector of the backscattered light (J_{BL}) can be calculated as

$$J_{BL} = J_{RS}\, J_{\lambda/4}\, J_T = \frac{\alpha\, U_0}{\sqrt{2}} \begin{bmatrix} -1 \\ j \end{bmatrix}. \tag{90}$$

The received radiation, once the backscattered light has passed a second time through the quarter-wave plate, has a Jones vector that indicates horizontal polarization, being as a result completely transmitted by the polarizing beam-splitter.

$$J_R = J_{\lambda/4}\, J_{BL} = \alpha\, U_0 \begin{bmatrix} 0 \\ j \end{bmatrix} \tag{91}$$

Nevertheless, it is reasonable to assume that the light will be partially depolarized when reflecting on the target and, therefore, part of its power will be reflected by the polarizing beam splitter.

The function of the set of two lenses is focusing the transmitted beam onto a point on the target, collecting the backscattered radiation and delivering it to the detection system with approximately the same size than the transmitted beam. Fig. 46 shows a scheme of the focusing subsystem and the design parameters.

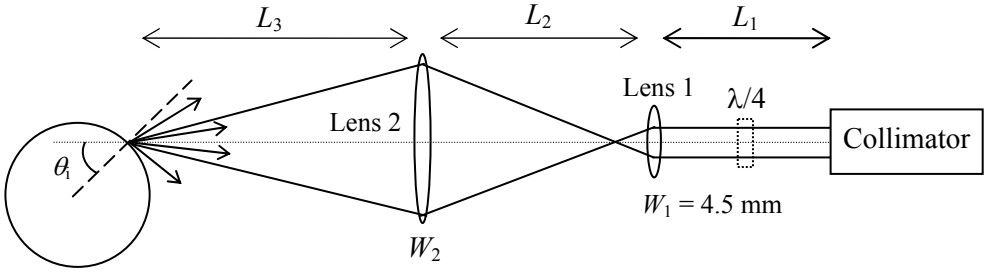

Fig. 46. *Focusing system in the transmitting – receiving assembly.*

Once the focal length of the lenses and the position of the target and lens 2 are fixed, the position of the lens 1 can be calculated for focusing the emitted light onto a point of the target [33]. In the set-up, the focal lengths of the lenses are respectively f_1 = 10 cm and f_2 = 20 cm. If the distances L_1+L_2 and L_3 are respectively 60 cm and 40 cm, L_2 has to be 51.64 cm. Under these conditions the size of the spot on the lens 2 results to be W_2 = 36.2 mm. The diameter of lens 2 should be therefore larger than this for avoiding spillover losses. Table 22 shows the parameters of both lenses and Fig. 48 shows the corresponding laboratory set-up.

	Lens 1	**Lens 2**
Reference	Newport KBX046	Newport KBX166
Type	Bi-convex	Bi-convex
Focal length	100 mm	200 mm
Diameter	25.4 mm	50.8 mm
Lens material	Grade A BK7	Grade A BK7
Coating	Uncoated	Uncoated

Table 22. *Parameters of the transmitter-receiver assembly lenses*

6.2.7 Optical chopper

The optical chopper has the function to allow pass alternatively the reference and the Doppler channels to temporally separate the emitted and the received continuous-wave frequencies. The chopper used in the prototype (Scitec Instruments Ltd (model: 300CD)) permits chopping frequencies from 5 Hz to 20 kHz and provides a 5V HCT TTL pulse reference signal that will be used to synchronize the acquisition and processing of each channel.

Fig. 47 shows an image where it can be seen the beam sampler, the transmitter-receiver arrangement and the optical chopper and in Fig. 48 the set of lenses used to focus the target.

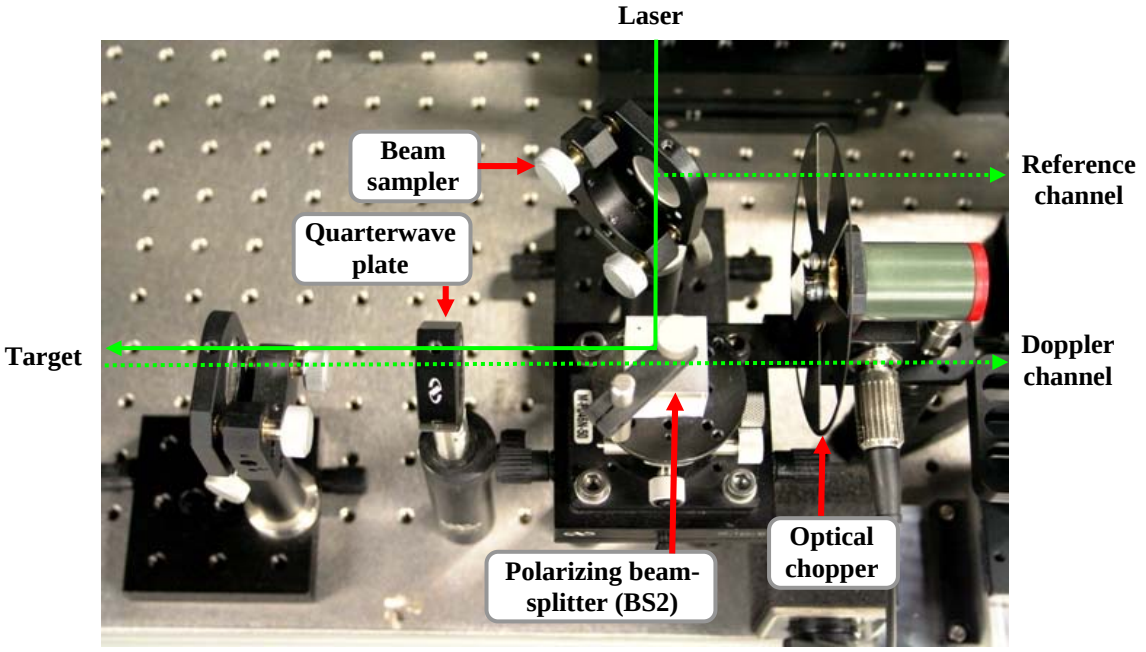

Fig. 47. *Beam sampler, transmitter-receiver assembly and optical chopper.*

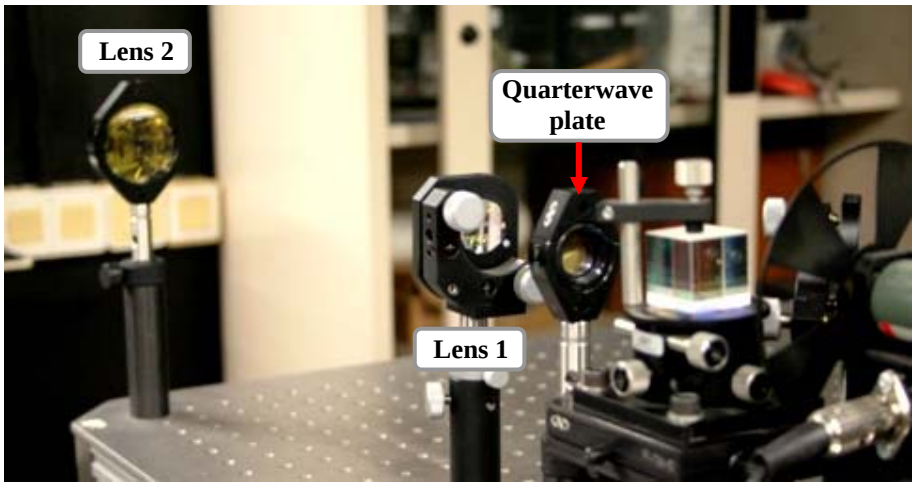

Fig. 48. *Elements in the focusing system*

6.2.8 Optical fiber focusers

The optical fiber focusers, one for the reference channel and the second one for the Doppler channel, have the function of focusing the beams on the core of the corresponding multimode optical fiber. For perfectly collimated incident beams, a lens located at a distance from the output of the optical fiber equal to its focal length would make this function. The main parameters of the couplers used in the prototype are shown in Table 23.

Reference	Edmund Optics NT64-767
Numerical aperture	0.25
Effective focal length	11 mm
Clear aperture	5.5 mm

Table 23. *Parameters of the optical fiber focuser*

6.2.9 Optical fibers

Gradient-index multimode optical fibers are used to lead the light from both the reference and Doppler channels to the frequency discriminator. This solution –instead of the free-space-propagation-based approach– provides robustness to the system, isolating alignment problems between the transmitting-receiving and the frequency discriminator subsystems. Using optical fibers also facilitates conditioning both channels with the same features –indispensable to perform a technique that is based on comparing the frequency response in each case– by means of combining them in the same fiber. The main parameters of the fibers used in the prototype are listed in Table 24.

Reference	Newport MFD-C
Numerical aperture	0.275
Core diameter	62.5 μm
Cladding diameter	125 μm

Table 24. *Parameters of the optical fiber*

Opto-mechanical assemblies used in the prototype to couple the light coming from the reference and Doppler channels into the optical fibers can be seen in Fig. 49.

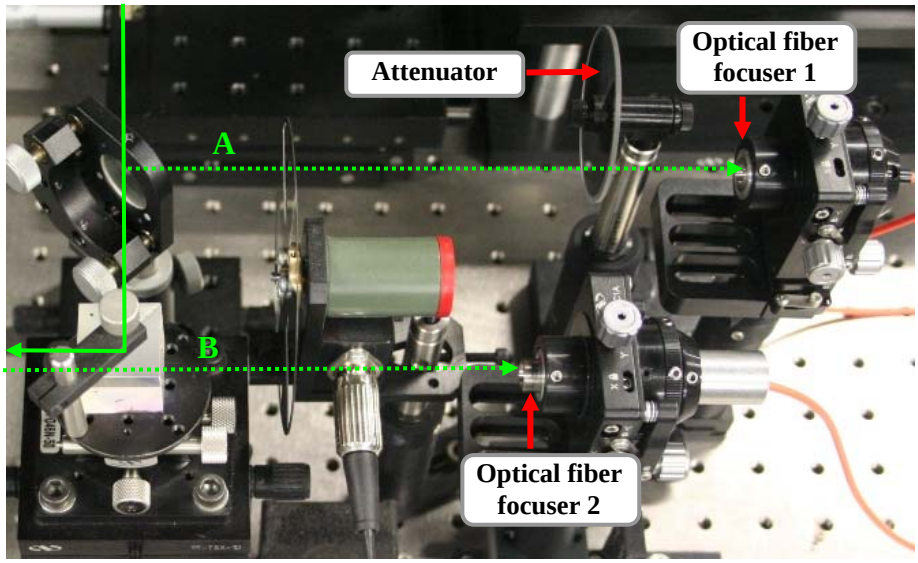

Fig. 49. *Optical fiber focusers. Their function is to couple the light from the reference (A) and Doppler (B) channels to their respective optical fibers.*

6.2.10 Optical fiber 2×1 coupler

The function of the optical fiber 2×1 coupler is combining the measuring channels –reference and Doppler– in a single optical fiber. Since the optical chopper gives alternate pass to each one of them, the signals will never temporally co-exist in the output fiber. In this case, because of availability reasons, a 2×2 optical fiber coupler, with one of the outputs disabled, has been used as 2×1 coupler. Ideal insertion loss for both channels at the design wavelength (900 nm) is therefore 3 dB. The measured insertion loss at 1064 nm is 5.8 dB.

Reference	Fiber instrument sales (FIS) Coupler MM 2x2 50/50 900 µm
Design wavelength	900 nm
Wavelength working range	800 – 1600 nm
Insertion loss (ideal @ 900 nm)	3 dB
Core – cladding diameter	62.5 - 125 µm

Table 25. *Parameters of the optical fiber coupler*

6.2.11 Mode scrambler

The mode distribution in a short multimode optical fiber depends on the light launch conditions, which in general are different in the reference and the Doppler channels. Furthermore, the roughness of the reflecting surface of the rotating wheel produces speckle on the receiving area and makes that the light launch conditions also change when the point of impact of the emitted radiation on the rotating surface changes as the wheel turns. The beam collimation at the output of the fiber differs from ideal and these differences in the mode distribution provoke slight variations in the frequency response that introduce errors in the Doppler frequency determination. A mode scrambler produces an approximately stable mode distribution in a fiber regardless of the light launch conditions and, mounted in the output optical fiber of the coupler, helps reduce this source of error in the measurements.

Fig. 50 shows both 2×1 optical fiber coupler and mode scrambler (Newport FM-1).

Fig. 50. *2x1 coupler and mode scrambler.*

6.2.12 Collimator

The collimator has been implemented using a single lens located at its focal length from the output of the fiber. Lens data are given in Table 26.

Reference	Newport KBX046
Type	Bi-convex
Focal length	100 mm
Diameter	25.4 mm
Lens material	Grade A BK7
Coating	Uncoated

Table 26. *Parameters of the collimating lens*

If the light came from a point source the collimation could be ideal. This is not the case of the multimode optical fiber, with a core diameter of 62.5 μm, resulting in an unavoidable angular divergence (θ_D) at the output of the collimator that can be easily calculated as

$$\theta_D = \arctan\left(\frac{d_c/2}{f}\right) = 312.5\ \mu\text{rad}\,, \tag{92}$$

where f is the focal length of the collimating lens and d_c is the diameter of the core of the optical fiber (Fig. 51).

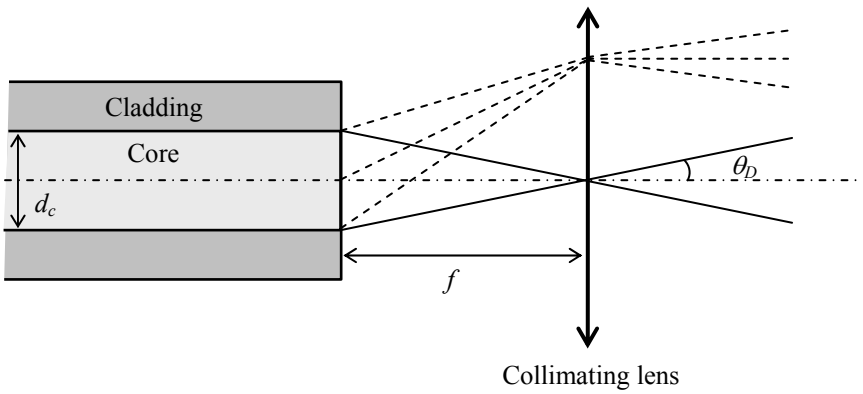

Fig. 51. *Collimating system and maximum divergence*

As mentioned in section 6.2.11, because this divergence, the changing conditions of the light in the optical fiber will produce variations in the frequency response of the interferometer that will in turn induce errors in the velocity determination. The resonance condition in the cavity of an interferometer (Eq. (93)) provides the frequency variation of its response due to an angle divergence:

$$2d\cos\theta = m\lambda \quad \rightarrow \quad \nu = \frac{m\,c}{2\,d\cos\theta} \ , \tag{93}$$

where θ is the incidence angle onto the etalon, d is the cavity length, m is an integer number. If a uniform distribution of angles within the divergence cone is assumed, the expected frequency variation and the associated velocity error can be calculated as:

$$\left\langle \left| \nu_\theta - \nu_0 \right| \right\rangle = \frac{1}{\theta_D} \int_0^{\theta_D} \nu_0 \left(\frac{1}{\cos\theta} - 1 \right) d\theta = 4.71 \text{ MHz} \, , \tag{94}$$

$$\left\langle \varepsilon_v \right\rangle = \frac{\lambda_0}{2} \left\langle \Delta \nu_\theta \right\rangle = 2.5 \text{ m/s} \tag{95}$$

where ν_0 is the resonance frequency for $\theta = 0$.

This value is, however, a limit for the expected error; valid if it is assumed that the light leaves the core of the fiber by changing single angles and individual exit points. The light in the fiber is, nevertheless, distributed in a big number of modes and should only show slight variations as the target turns.

An image of the collimating arrangement can be seen in Fig. 52.

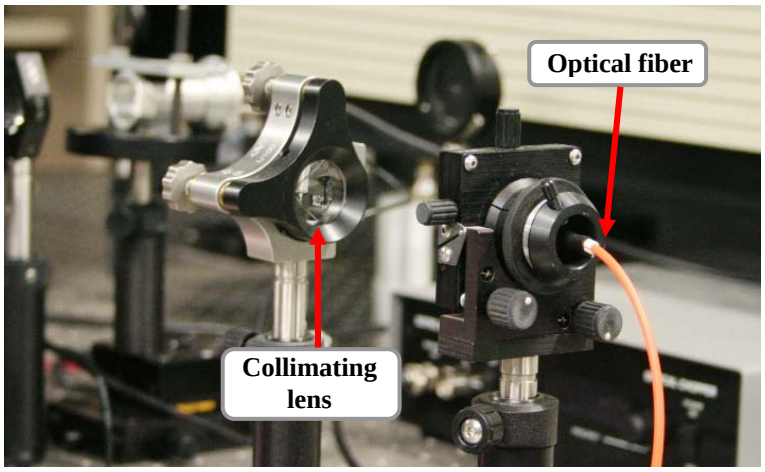

Fig. 52. *Collimator*

6.2.13 Fabry-Perot interferometer

A Fabry-Perot interferometer is used in this prototype as the high-resolution optical filter required for implementing the edge technique. The mirror spacing is manually configurable from 0.5 to 100 mm. Furthermore, the instrument is equipped with three piezoelectric cells for fine adjusting the position and the orientation of one of the mirrors in order to both control the mirror parallelism and fine adjust the cavity length. This permits to control the location of the response peaks and in such way compensate with a control-loop the frequency drifts between the laser emission and the filter resonance. The main parameters of the

interferometer are summarized in Table 27. An image of the instrument can be seen in Fig. 55).

Reference	Melles Griot 13 FPI-025
Plate spacing	0.5 – 100 mm
Free Spectral Range	300 – 1.5 GHz
Mirror reflectance	99 ± 0.5 %
Mirror tuning range	1.2 μm nominal

Table 27. *Main parameters of the Fabry-Perot interferometer*

An interferometer controller (see Fig. 53**)** provides the high-voltages required for adjusting the mirror parallelism and the cavity length. The parallelism is adjusted using four control potentiometers. The cavity length can be either linearly scanned if the interferometer is used as an optical spectrum analyzer or controlled by a low-voltage external input. In the latest option –which is the operation mode used in this prototype– the controller acts as a voltage amplifier.

Fig. 53. *Interferometer controller.*

6.2.14 Optical receivers

Two optical receivers are used in the prototype to monitor both the interferometer input and output optical power, required for measuring its frequency response. Each optical receiver is formed by and avalanche photodiode (APD) as photodetector and a transimpedance amplifier. A simplified scheme of the receiver is shown in Fig. 54.

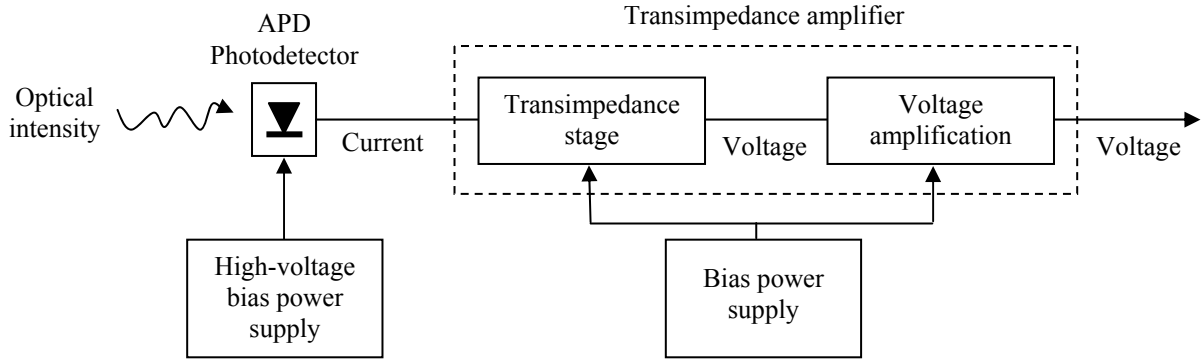

Fig. 54. *Scheme of the photoreceivers.*

The main parameters of the APD used in the prototype are given in Table 28.

Reference	Hamamatsu S8890-15 APD	
Avalanche gain (*M*)	100	
Responsivity (R_0)	0.25 (A/W) (@ 1064 nm)	
Dark current	10 nA (Typ)	100 nA (Max)
Effective area	∅ 1.5 mm	

Table 28. *Parameters of the APD*

Both the transimpedance stage and the voltage amplifier have been designed to provide an adjustable gain. Amplifier parameters are shown in Table 29.

Transimpedance gain	750 – 5750 Ω
Voltage gain	1 – 15
Bandwidth	100 kHz
Input equivalent noise current	6.12 (G_{max}) – 71 (G_{min}) pA / $\sqrt{\text{Hz}}$

Table 29. *Parameters of the amplifier*

An image with the diaphragm used to spatially filter the incident beam, the beam-splitter BS3 (see Fig. 40), the Fabry-Perot interferometer and the photodetectors 1 and 2 can be seen in Fig. 55. Neither the transimpedance amplifiers nor the high-voltage power supplies are visible; coaxial cables are used to connect them with the photodetector heads.

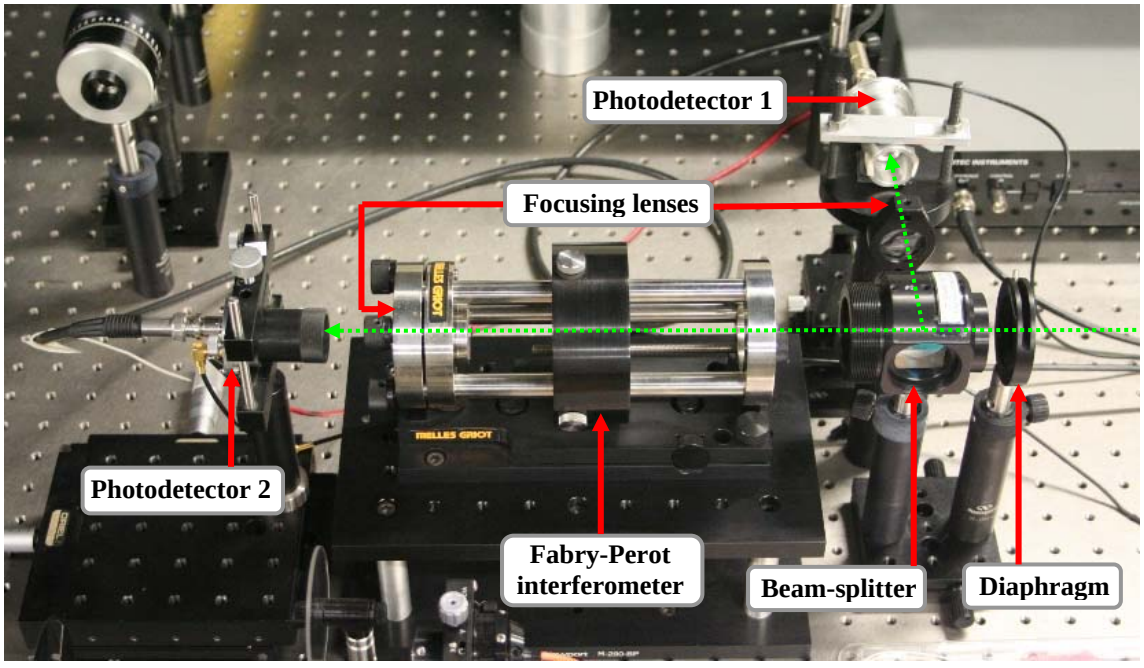

Fig. 55. *The Doppler detection section of the prototype.*

6.2.15 Acquisition board

The output voltage provided by the optical receivers is acquired by a 16 bits, up to 250 ks/s, multifunction acquisition board providing 16 analog inputs and 2 outputs (Ref. National Instruments NI PCI-6221) and the corresponding data are processed by a personal computer

hosting the acquisition board that uses LabVIEW™ routines for obtaining the radial speed. The error voltage used to correct the interferometer cavity length is applied through one of the analogue outputs of the acquisition board.

6.2.16 Other parts of the experimental setup

Several electronic devices not appearing in the previous sections can be seen in Fig. 56.

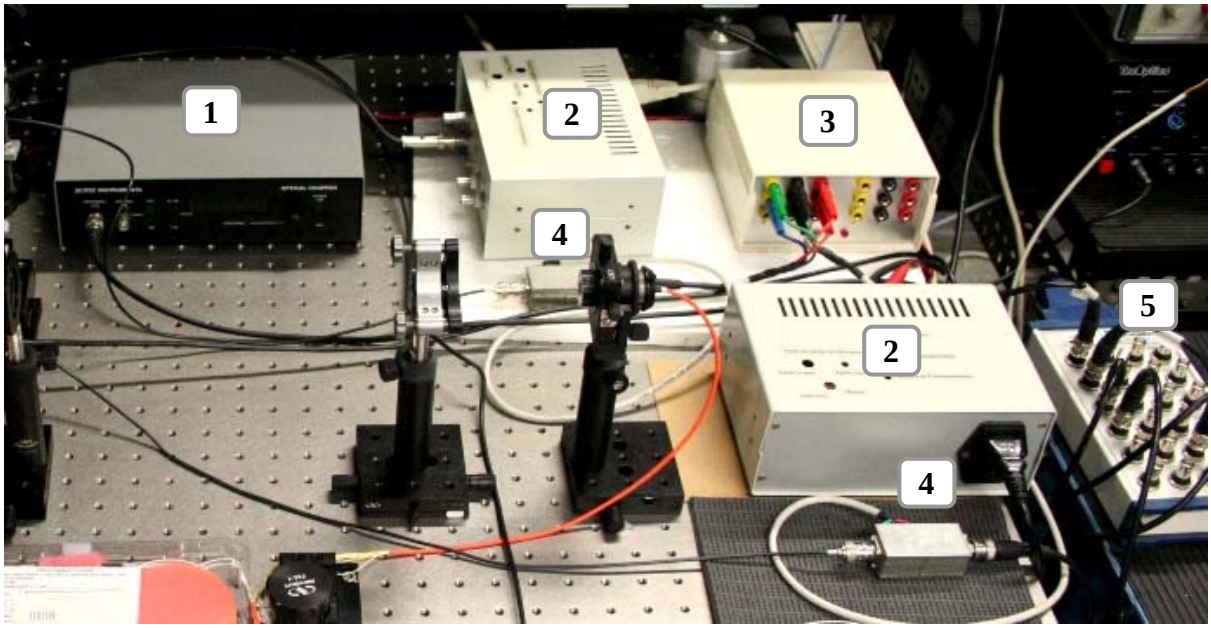

Fig. 56. *Electronic devices not appearing in the previous sections: Chopper controller (1), high-voltage power supplies (2) (one for each photodetector), low-voltage power supply (3), transimpedance amplifiers (4) (one for each photodetector) and BNC connector block for the acquisition card (5).*

General views of the optical section of the laboratory set-up can be seen in Fig. 57 and Fig. 58.

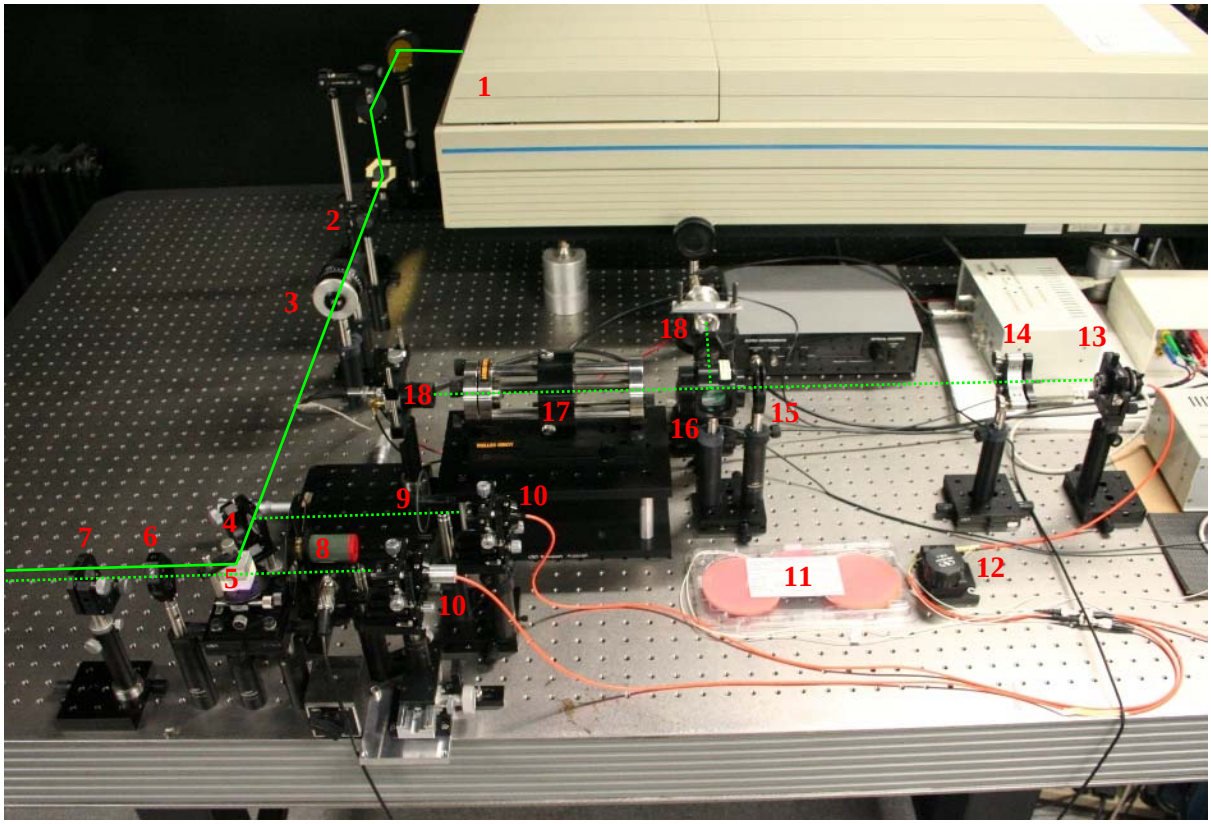

Fig. 57. *Optical section of the laboratory set-up: Laser (1), reducer-collimator (2), polarization rotator (3), beam-sampler (4), polarizing beam-splitter (5), quarterwave plate (6), lens 1 of the focusing system (7), optical chopper (8), attenuator (9), optical fiber focusers (10), 2x1 optical fiber coupler (11), mode scrambler (12), optical fiber end (13), collimating lens (14), diaphragm (15), beam-splitter (16), Fabry-Perot interferometer (17) and photodetectors (18).*

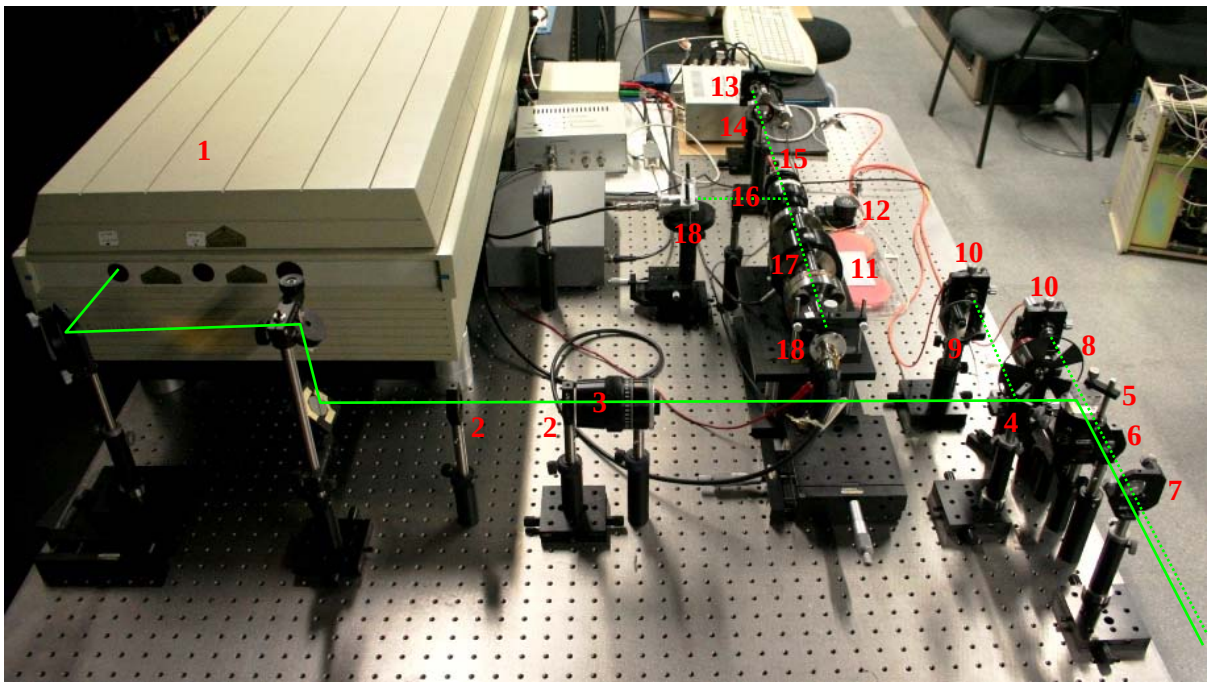

Fig. 58. *Another general view of the laboratory set-up. The numeration is the same than the one defined in the title of Fig. 57.*

6.3 Retrieval of the frequency response from the detected voltages

Doppler-effect-based velocimeters measure the speed of a target by detecting the frequency-Doppler-shift between emitted (ν_0) and received ($\nu_0 + f_D$) signals. Edge-technique-based lidars, like the prototype that is characterized in this section, obtain these frequencies by measuring the normalized response of the optical filter $\overline{F}(\nu)$ to both signals (section 4), which is calculated from the output voltages of the optical receivers V_1 and V_2 (Fig. 40).

In this prototype the optical chopper is the element in charge of temporally separating the reference channel (which supplies a sample of the emitted radiation) and the Doppler channel (with part of the Doppler-shifted scattered power). During each chopper half-period the detection system processes alternatively the emitted and the received radiation.

In the velocity measurements, during the chopper half-periods in which the emitted frequency (reference channel) is being detected, the output voltages, V_{1m} and V_{2m}, are respectively

$$V_{1m} = \alpha_1 P_{ref} \tag{96}$$

$$V_{2m} = \alpha_2 P_{ref} F(\nu_0) = \alpha_2 P_{ref} F_{\max} \overline{F}(\nu_0) \tag{97}$$

where $\overline{F}(\nu)$ is the Fabry-Perot frequency response normalized to its maximum, $F_{\max}$ is the maximum transmission of the filter, P_{ref} is the incident optical power from the reference channel and α_1 and α_2 are system constants, including the gain and responsivity of the detectors, the transimpedance gain of the receivers and losses in optic elements (see section 4.1). The normalized frequency response at the emitted frequency can be therefore calculated, during the reference chopper half-period, as:

$$\overline{F}(\nu_0) = \frac{\alpha_1}{\alpha_2 F_{\max}} \frac{V_{2m}}{V_{1m}} \tag{98}$$

In turn, during the velocity measurements, in the periods when the incident light is the frequency-shifted signal from the Doppler channel, the output voltages are:

$$V'_{1m} = \alpha_1 P_{Dop} \tag{99}$$

$$V'_{2m} = \alpha_2 P_{Dop} F(\nu_0 + f_D) = \alpha_2 P_{Dop} F_{\max} \overline{F}(\nu_0 + f_D) \tag{100}$$

Where P_{Dop} is the optical power of the Doppler-shifted incident signal. The frequency response to the received signal as a function of these voltages is:

$$\overline{F}(\nu_0 + f_D) = \frac{\alpha_1}{\alpha_2 F_{\max}} \frac{V'_{2m}}{V'_{1m}} \tag{101}$$

The factor multiplying the voltage ratio in the processing of both the reference and the Doppler channels (Eqs. (98) and (101)) is obtained in the calibration stage, prior to the measurements. In this stage, the frequency response is stored using the signal of the reference channel as excitation. The output voltage in detector 1 (V_{1c})

$$V_{1c} = \alpha_1 P_{ref} \tag{102}$$

and the output voltage in detector 2 at the peak of the response (V_{2cMax})

$$V_{2cMax} = \alpha_2 \, P_{ref} \, F_{\max} \tag{103}$$

are also recorded and the factor can be calculated from them as

$$\frac{\alpha_1}{\alpha_2 \, F_{\max}} = \frac{V_{1c}}{V_{2cMax}} \tag{104}$$

Substituting this factor in Eqs. (98) and (101), the expressions to be used for calculating the response to both the emitted and the received frequencies can be found:

$$\overline{F}(\nu_0) = \frac{V_{1c}}{V_{2cM\,\mathrm{ax}}} \frac{V_{2m}}{V_{1m}} \tag{105}$$

$$\overline{F}(\nu_0 + f_D) = \frac{V_{1c}}{V_{2cMax}} \frac{V'_{2m}}{V'_{1m}} \tag{106}$$

6.4 Retrieval of the Doppler frequency from the frequency response

If the normalized frequency response of the filter has been acquired and recorded in the calibration phase, the frequency separation between the received and the emitted signals can be derived from comparison of the measured response at both frequencies, which is calculated from the detected voltages (Eqs. (105) and (106)). The calibrated frequency response is nevertheless stored not as a function of the absolute frequency but in terms of frequency distance to the resonance peak, being the differential nature of the measurement what permits the retrieval of the frequency Doppler shift:

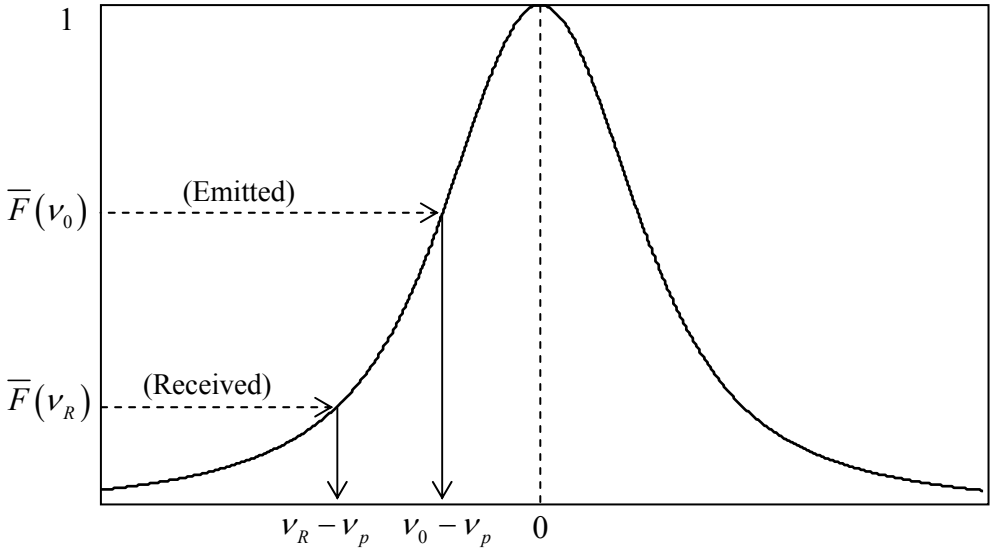

Fig. 59. *Doppler shift measurement from the normalized frequency response*

As illustrated in Fig. 59, the separation between the frequency of the signal (ν_0 for the reference channel and ν_R for the Doppler channel) and the resonance peak of the filter can be estimated in each case from the measured values of the normalized frequency response ($\overline{F}(\nu_0)$ and $\overline{F}(\nu_R)$ respectively):

$$\left.\begin{array}{rcl} \overline{F}(\nu_0) & \rightarrow & \nu_0 - \nu_p \\ \overline{F}(\nu_R) & \rightarrow & \nu_R - \nu_p \end{array}\right\} \tag{107}$$

The Doppler shift between the received and the emitted frequency is then obtained subtracting both frequency separations.

$$f_D = (\nu_R - \nu_p) - (\nu_0 - \nu_p) = \nu_R - \nu_0 \tag{108}$$

6.5 Tuning control subsystem

The method described in sections 6.3 and 6.4 is only feasible if the emitted frequency lies always in the maximum sensitivity zone of the response. Nevertheless, relative frequency drifts between the laser emission and the resonance peaks of the interferometer, mainly due to thermal effects, are unavoidable, and a real-time control loop has to be set to compensate them. This subsystem could actually act either on the laser [53], [57] or on the filter [63]. In our system, it will act on the interferometer, which is equipped with piezoelectric cells to fine tune the cavity length and the corresponding frequency parameters.

During the half-period in which the reference signal is processed, the system checks whether the measured response shows the best available sensitivity for the emitted frequency. If it is not the case, the voltage applied to the piezoelectric cells is modified to achieve the desired response. Fig. 60 shows the scheme of the tuning control loop. The optical chopper provides a synchronization signal that is used to disable this correction during the Doppler channel half-period. The control voltage is applied to the external input of the interferometer controller, which amplifies and applies it to the piezoelectric cells to tune the cavity length.

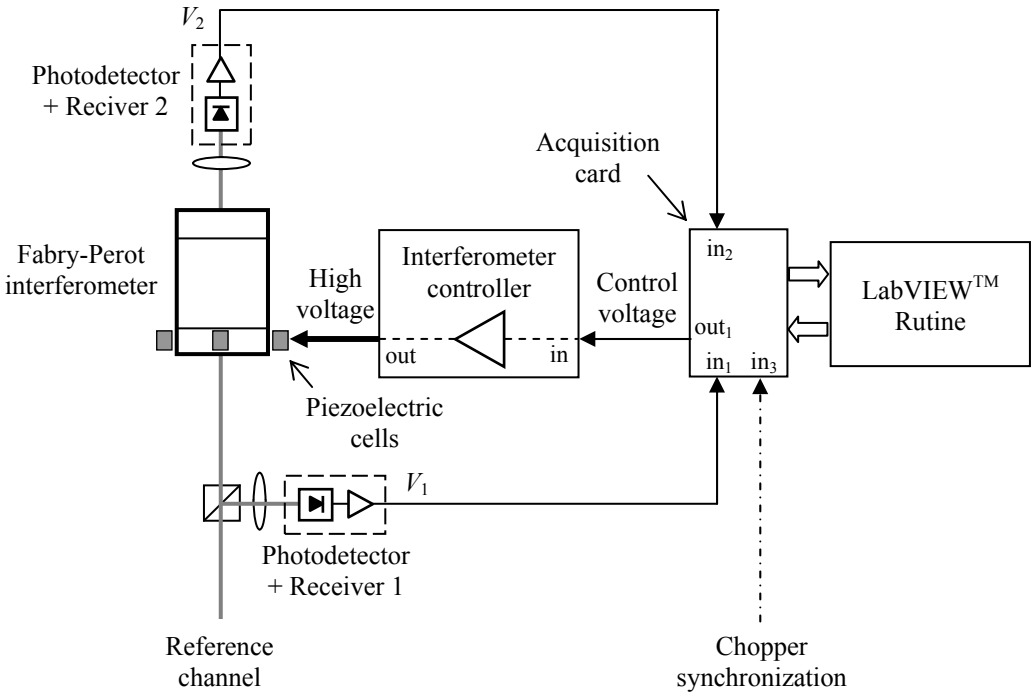

Fig. 60. *Scheme of the tuning control subsystem*

The differential nature of the measurement makes that, as far as the measured frequencies lay in the sensitive zone of the filter response, some variation of the laser location can be permitted without causing a significant error in the Doppler shift determination. It is not

therefore indispensable that the tuning control subsystem compensates every small frequency drift. At the same time, since short-term variations are seldom big enough to induce significant errors, the system is designed to compensate only medium/long-term drifts in the laser-filter mutual tuning. There are two input parameters in the control routine that permit to adjust respectively the minimum error of the laser location to be corrected and the time interval between two consecutive corrections. The effect of these parameters in the prototype performance has been tested and will be analyzed in section 7.3.

6.6 Routines and procedures

When a session of velocity measurements is performed, the sequence of actions presented in Fig. 61 should be carried out. First, in the 'offset calibration' routine, the offset voltages of the receivers are acquired and stored. These values, which will be obtained by blocking the incidence of any optical radiation on the detectors, will be subtracted later from any acquired voltage. Secondly, in the so-called 'frequency response calibration' routine, several data related to the frequency response of the interferometer are stored too: the normalized response, the sweep signal used to scan it, the normalization factor required for obtaining the normalized response from the detected voltages (V_{1c}/V_{2cMax} in Eqs. (105) and (106)) and the frequency sampling interval. These calibration data are measured using the reference channel as incident signal. Finally, the 'measurement and tuning control' routine is run. In this phase, the optical chopper is switched on and the system calculates, from the detected voltages in both chopper half-periods and using the calibration data, the radial velocity of the target. At the same time, the 'tuning control' subroutine, which is enabled only during the reference channel half-period, checks and eventually corrects the location of the emitted frequency on the response.

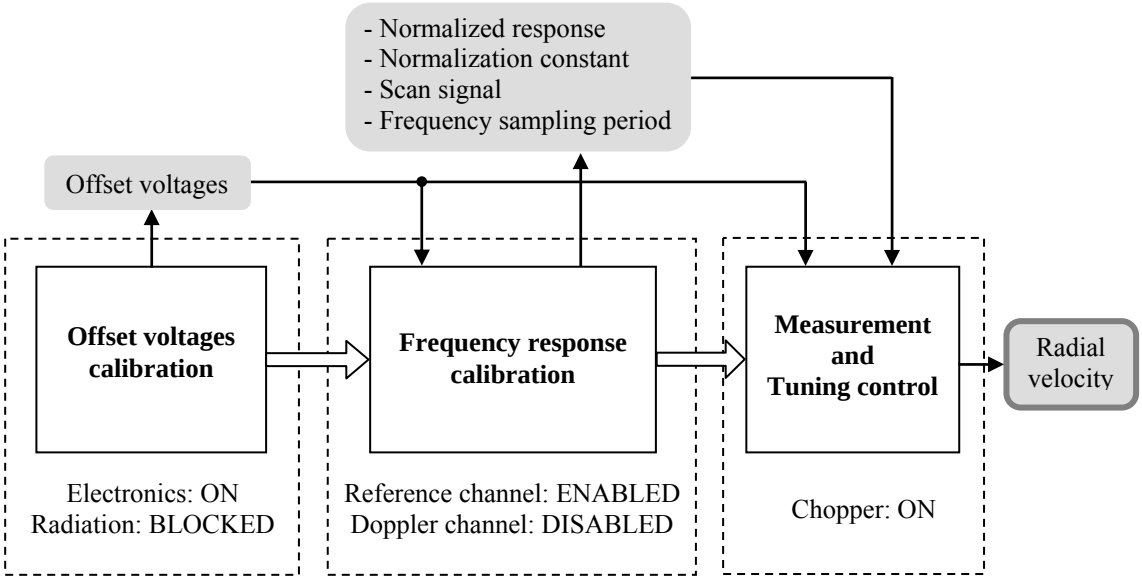

Fig. 61. *Complete sequence of routines in a session of velocity measurements.*

In this section, a description of the functions, the input parameters, the constraints and the internal structure of the routines involved in these actions will be detailed.

6.6.1 Offset-voltages calibration stage

As mentioned above, in this stage the incident optical radiation onto the detectors is completely blocked and all the electric and electronic subsystems that will be used during the

measurements are switched on. Under these conditions, the measured voltages at the output of the receivers can be identified as their offset voltages. After being filtered for minimizing noise errors, these voltages are acquired and stored. They will be used in the following stages of the measuring procedure, including the rest of calibration routines, subtracting them from each detected signal.

6.6.2 Frequency response calibration stage

In this phase of the procedure, the optical chopper is stopped to continuously enable the reference channel. For acquiring the response, some kind of frequency scanning procedure has to be performed between the laser and the filter. In this case, a linear scan of the cavity length, and consequently of the resonance frequency of the filter, is carried out. A triangular sweep signal is generated by software ($V_2(n)$), amplified by the interferometer controller and applied to the piezoelectric cells that control the cavity length. During the scan, the detected voltage at the output of the filter ($V_2(t)$) is acquired, normalized to its maximum and stored as the normalized frequency response ($\overline{F}(n)$). The sweep signal used is stored too to be used during the tuning control phase. The normalization constant required for calculating the response from the detected voltages (Eqs. (105) and (106)) is obtained from the output voltage of the receiver 1, which is constant during the scan ($V_1(n) = V_{1c}$), and from the peak voltage of the response (V_{2cMax}).

For converting the discrete time-signal obtained during the scan into the frequency response, the correspondence between time and frequency sampling intervals has to be determined and it is also stored as a result of the calibration routine. For this purpose, the scan of the cavity length has to be programmed so that it contains two peaks of the periodic frequency response. Since the frequency distance between two consecutive peaks is the free spectral range (*FSR*) of the interferometer (Eq. (36)), if the cavity length of the cavity is known, it is possible to determine the frequency interval (Δf) corresponding to one sampling period:

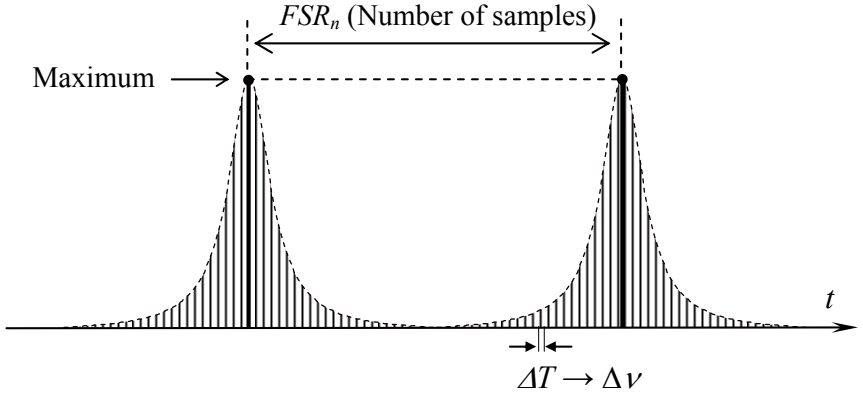

Fig. 62. *Time-to-frequency sampling interval translation.*

$$\Delta f = \frac{FSR(\text{Hz})}{FSR_n(\text{samples})} = \frac{c}{2\,d\,FSR_n}(\text{Hz/sample}) \quad (109)$$

Fig. 63 shows a scheme of the structure of the frequency response calibration routine.

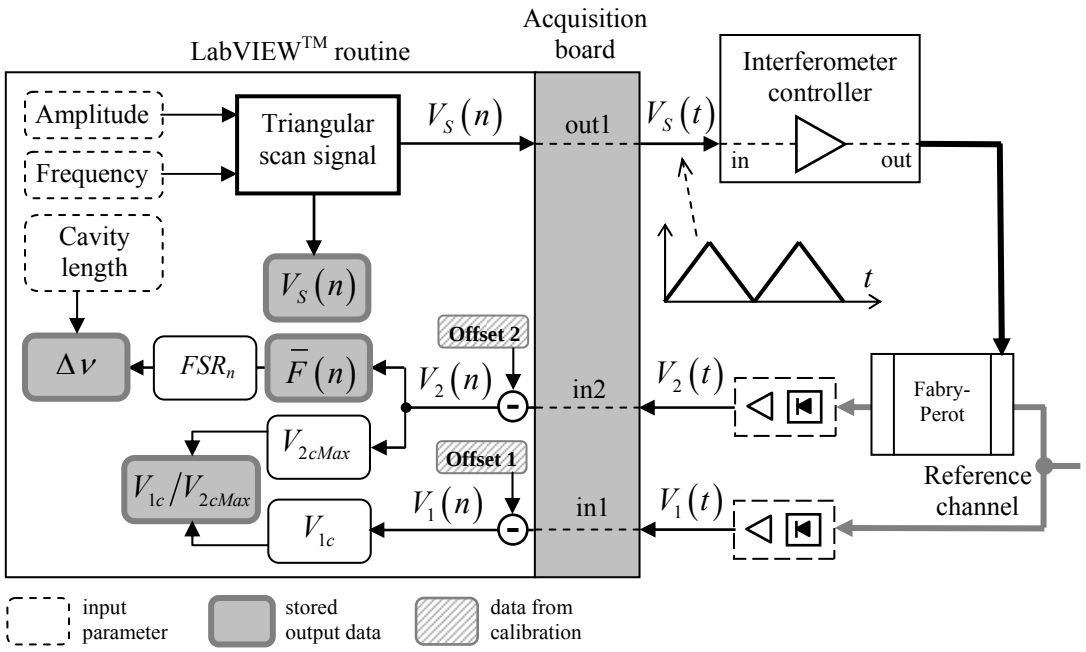

Fig. 63. *Schematic structure of the frequency response calibration routine.*

Fig. 64 shows a view of the control panel of the frequency response calibration routine.

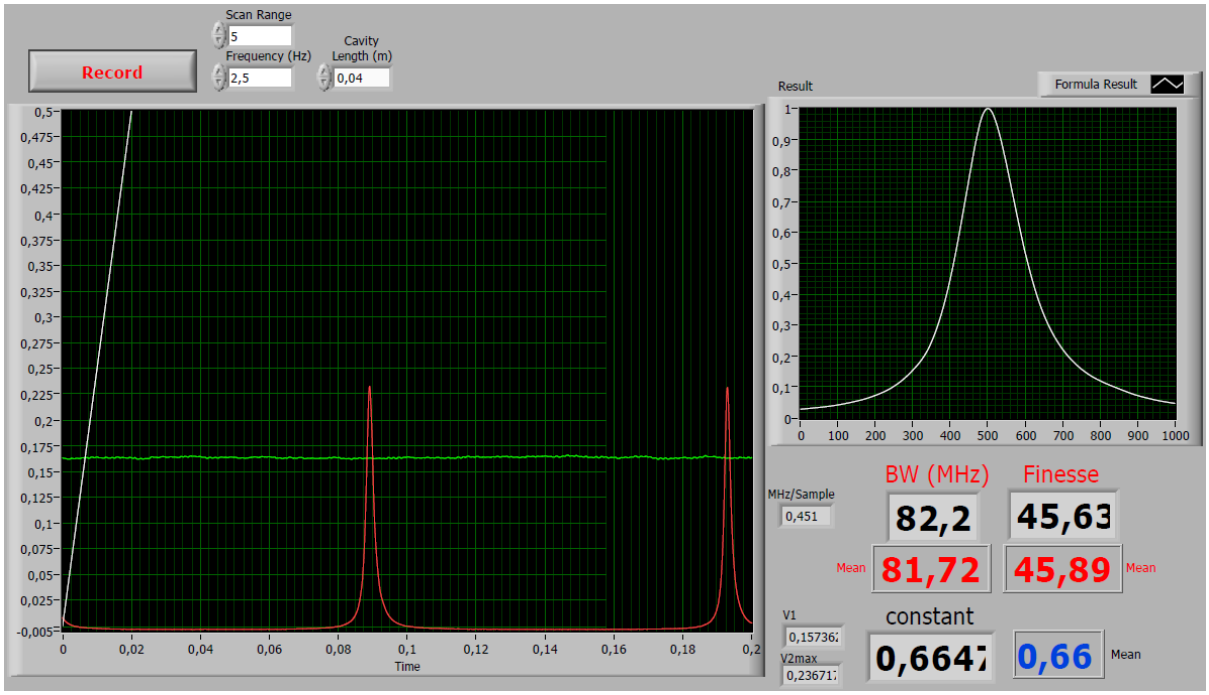

Fig. 64. *Frequency response calibration routine: Control panel.*

6.6.3 Measurement and tuning control stage

Once all the calibration parameters and functions are stored, the optical chopper is switched on and the signals from both optical receivers ($V_1(t)$ and $V_2(t)$) are acquired. The signals corresponding to the reference and the Doppler channels are alternatively present in both detected voltages (Fig. 65); hence a synchronization signal ($V_{ch}(t)$), provided by the chopper controller, is also acquired in order to temporally discriminate each channel.

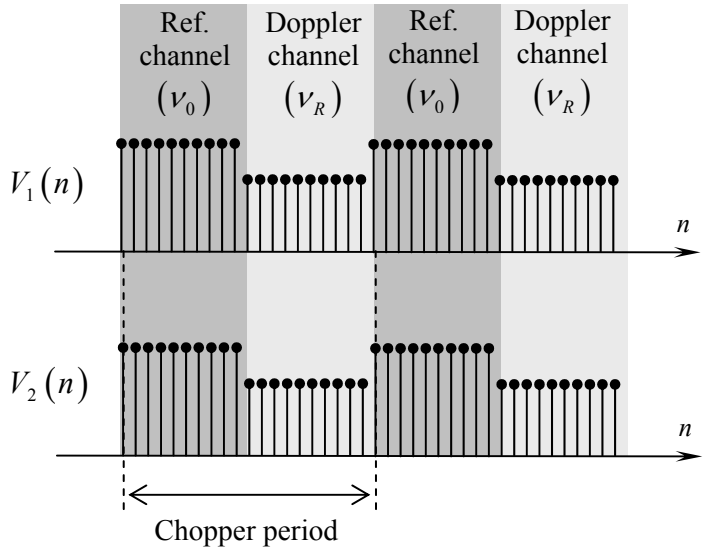

Fig. 65. *Acquired signals during the measuring stage.*

Using the normalization constant stored during the calibration stage (V_{1c}/V_{2cMax}), the normalized response for both emitted and received frequencies ($\bar{F}(\nu_0)$ and $\bar{F}(\nu_R)$) is calculated from the detected voltages (Eqs. (105) and (106)). From these values and using the normalized frequency response recorded during the calibration, the distance between both frequencies in terms of number of samples can be directly derived. Using the frequency interval used to sample the frequency response ($\Delta\nu$) that has been calculated and stored during the calibration phase, the Doppler frequency and the radial velocity can be determined.

During the chopper half-period corresponding to the reference channel, in which the emitted frequency is processed, the system checks and if needed corrects its location on the slope of the response. This test is made comparing the normalized response at the emitted frequency with the value that it should take at the optimal location. When the system detects a difference between these values, it calculates how the control voltage should be changed for compensating it. This calculation is made by using the sweep signal recorded during the calibration phase ($V_S(n)$). Fig. 66 shows the way in which the routine calculates this correction.

Due to the differential nature of the measurements, and as long as measurable frequencies remain in sensitive zones of the response, some error in the laser location on the filter response can be allowed without errors in the measurement and without an important loss of accuracy. This makes unnecessary that the tuning control system acts in a continuous way and for any relative frequency drift. Two parameters permit to control both the minimum time between corrections ('interval' ('int' in Fig. 67)) and the minimum drift that will be corrected ('sensitivity' ('sens' in Fig. 67)), defined as a fractional change of the filter response at the emitted frequency with respect to the optimal one ($\bar{F}(\nu_0)/\bar{F}_{opt}$). Fig. 67 shows the structure of the routine that is run during the simultaneous measurement and tuning control tasks.

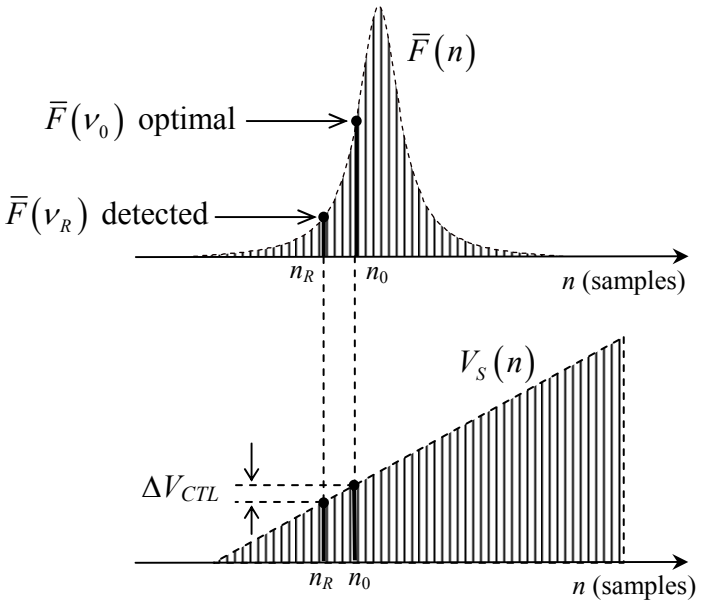

Fig. 66. *Correction of the laser location*

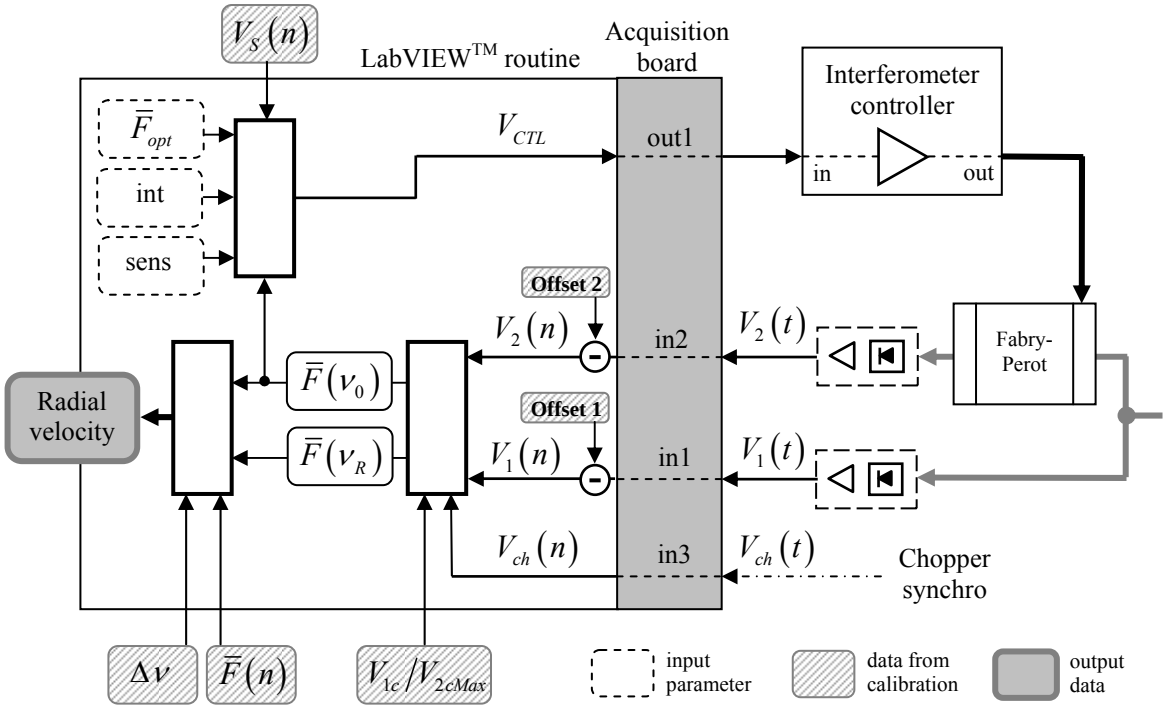

Fig. 67. *Schematic structure of the measurement and tuning control routine.*

7 Measurements

In this chapter different practical results related with the performance of the prototype proposed in chapter 6 will be presented. A set of results concerning the measurement of the radial velocity of a solid target will be presented and analyzed. The objective is the characterization of the proposed continuous-wave prototype as a solid-target velocimeter. Also, the performance of two subsystems that are critical for the operation of the measuring system and will form part of the atmospheric Doppler wind lidar, such as the Fabry-Perot interferometer and the tuning control subsystem, has been independently tested in the laboratory and it is analyzed here.

7.1 Interferometer performance

An accurate retrieval of the frequency Doppler shift requires, in edge-technique-based Doppler lidars, a precise knowledge of the frequency response of the optical filter used to perform the frequency-to-intensity conversion. First, in section 7.1.1, a real acquisition of the frequency response is displayed as an example. In section 7.1.2 the error in the velocity determination due to differences between the true and the stored frequency response is calculated as a function of the measured velocity. Finally, in sections 7.1.3, 7.1.4, 7.1.5 and 7.1.6, the effects on the velocity measurements of different phenomena related to the behaviour of the interferometer response are identified, analyzed and quantified.

7.1.1 Example of acquisition of the frequency response

During the calibration procedure, the frequency response of the interferometer is first optimized by adjusting, both manually and electronically, the parallelism of the mirrors. Afterwards, the response is acquired and recorded for later use in the routines where the intensity-to-frequency conversion is run.

Fig. 68 shows an example of acquisition of the interferometer frequency response. In this case, in which the cavity length was fixed to 4 cm, the measured finesse was 47.62 and the half-width at half-maximum, 39.37 MHz.

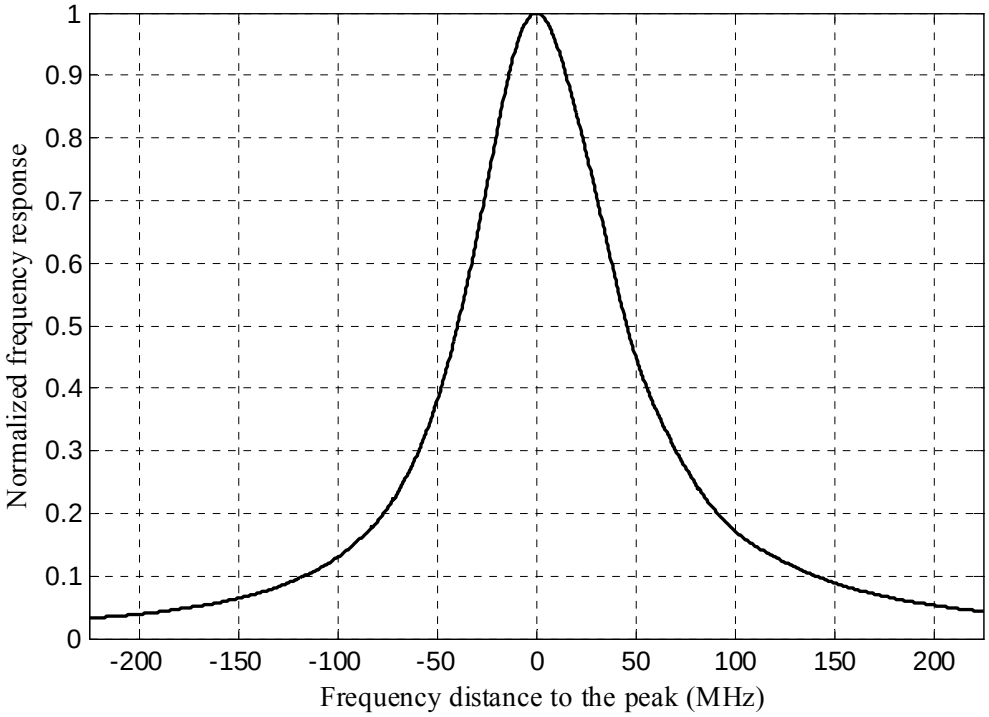

Fig. 68. *Frequency response acquired during calibration. d = 4 cm; F = 47.62; FWHM = 78.74 MHz*

7.1.2 Errors due to variations of the frequency response

Edge-technique measurements are based on the assumption that the frequency response of the filter is equal to the recorded during the calibration phase, which is the one used in the calculations. Any variation during the velocity measurements of the filter frequency response with respect to the recorded curve will result in an error in the determination of the Doppler shift and the radial velocity. These variations can occur in both the reference and the Doppler measuring channels.

In the reference channel, two types of response variation affecting the measurements have been identified. First, random fast fluctuations can be observed when the cavity is repeatedly scanned (section 7.1.3). These fluctuations appear superimposed to a slow degradation of the filter selectivity (section 7.1.4). In both cases the variations arise from the instability of the mirror parallelism, due mainly to mechanical and thermal effects. In the Doppler channel, of course, these effects are present too, but there exist also another source of error. Indeed, the response of the interferometer depends on the point of the target surface where the light impacts. Naturally, this point-of-impact changes continuously when the wheel is rotating, producing certain random noise in the velocity measurement. This phenomenon might be due to the changing speckle patterns on the receiving surface as the disc turns and, as a consequence, to different mode distributions in the optical fiber and variations in the features of the beam illuminating the interferometer. These effects are partially reduced by the use of the mode-scrambler located after the combination of the channels, but, actually, they are not completely eliminated and they will be measured and characterized in sections 7.1.5 and 7.1.6.

In all the cases, it is possible to calculate the velocity error due to variations of the frequency response, both in the reference channel and the Doppler channel. As an example, Fig. 69 shows this error in a system with a recorded finesse F = 47.62 and a cavity length d = 4 cm, operating at 1064 nm. The results are displayed for different target velocities. The error in the frequency response is expressed in terms of the difference of finesses and it is assumed that the speed measurement is made on the positive slope side of the response curve.

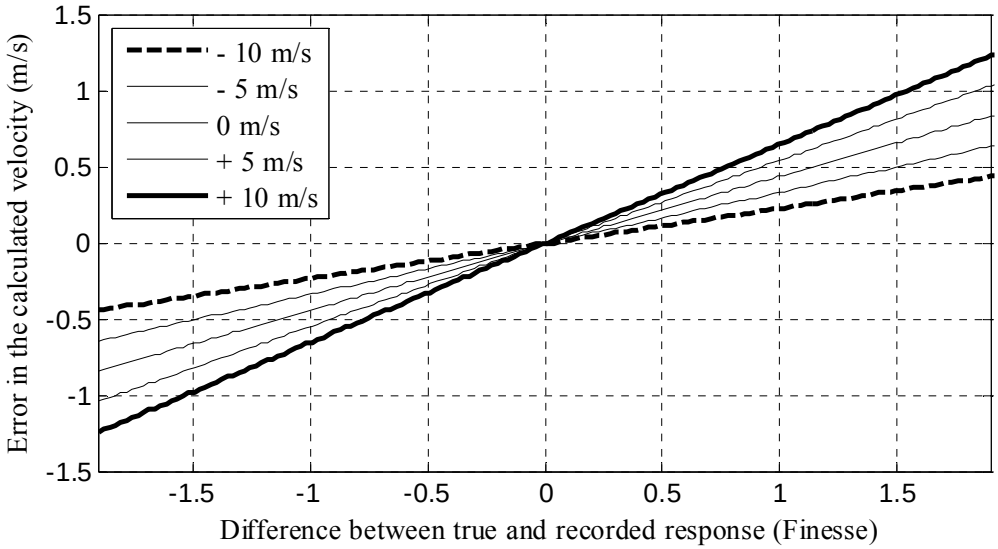

Fig. 69. *Error in velocity determination due to an error in the frequency response for different measured linear speeds.*

Of course, response variations occur both in the reference and in the Doppler channel. The noise in each channel (σ_R and σ_D) affects the measurements during different time intervals (chopper half-periods) and, as a consequence, they can be considered uncorrelated. If furthermore it is assumed that both fluctuations have the same variance ($\sigma_R^2 = \sigma_D^2 = \sigma_{RD}^2$), the expected velocity error due to random variations of the frequency response (σ_{FR}) can be computed as

$$\sigma_{FR}^2 = \sigma_R^2 + \sigma_D^2 = 2\,\sigma_{RD}^2 \tag{110}$$

7.1.3 Stability of the frequency response

In order to estimate the velocity error due to the instability of the frequency response, several 20 minutes duration tests have been carried out. During each of them, the cavity length has been scanned every 400 ms and the resulting response has been acquired. The parameter used to characterize and analyze the stability of the response has been its finesse. Fig. 70 to Fig. 72 show, for four independent 20 minutes duration tests, the measured finesse in successive scans. Results obtained when sliding averaging of 20 and 100 scans is performed are also displayed in each test.

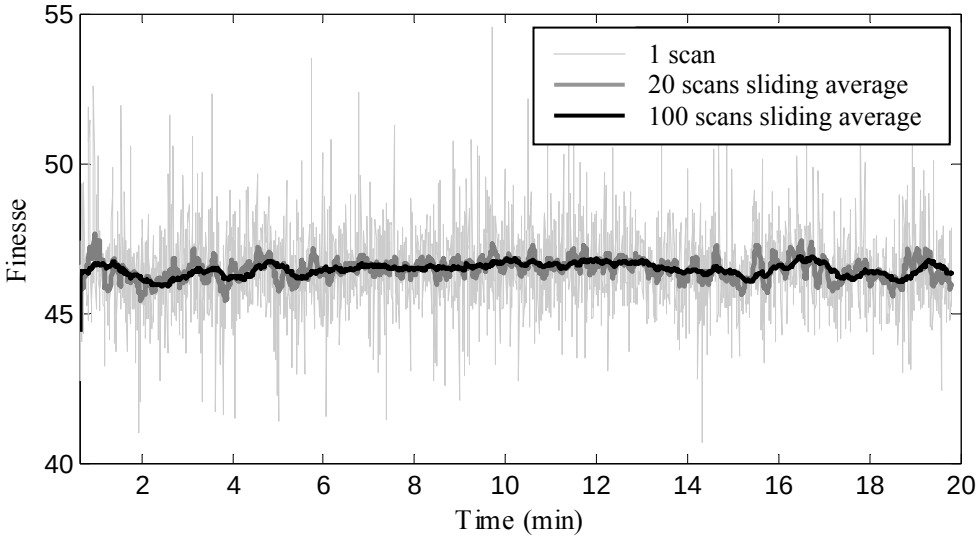

Fig. 70. *Finesse evolution in successive scans during 20 minutes (Test I).*

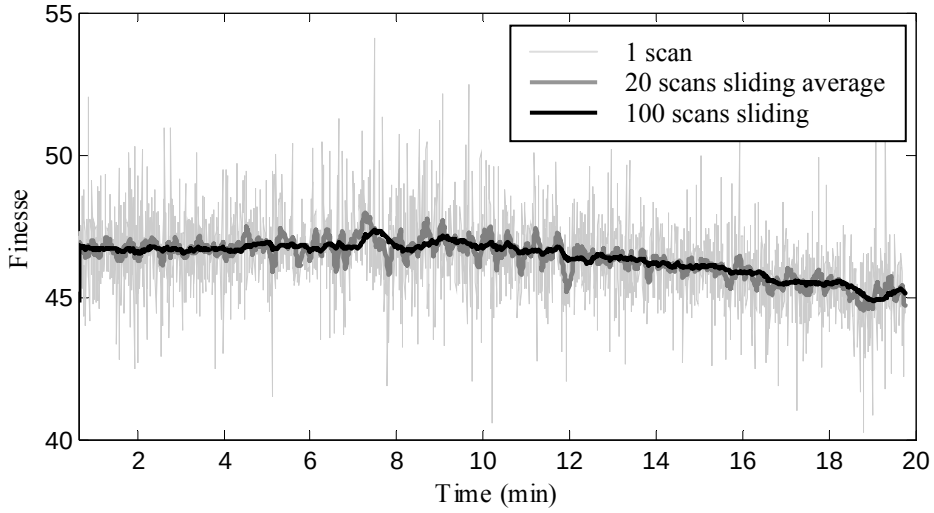

Fig. 71. *Finesse evolution in successive scans during 20 minutes (Test II).*

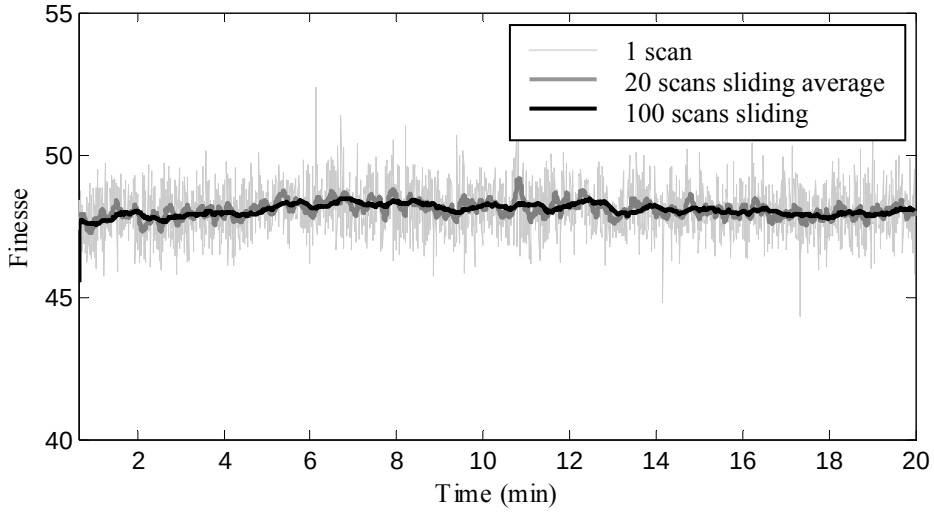

Fig. 72. *Finesse evolution in successive scans during 20 minutes (Test III).*

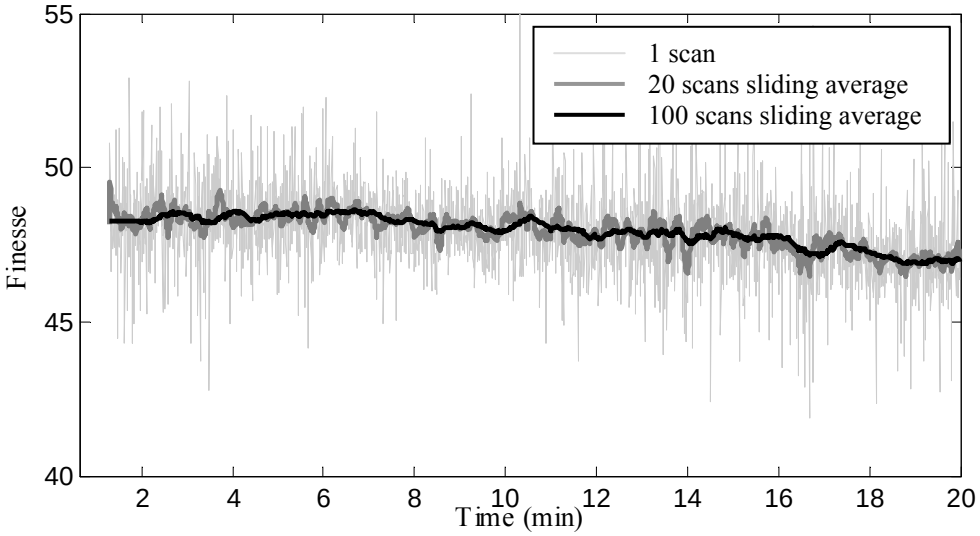

Fig. 73. *Finesse evolution in successive scans during 20 minutes (Test IV).*

As pointed out in section 7.1.2, when comparing the measured finesse from one single scan to another, there exists a noticeable variability, which is partly due to the sensibility of the cavity to mechanical vibrations, coming mainly from the cooling system of the laser.

However, the method used for measuring the finesse is also responsible of part of the observed fluctuations. When the full-width at half-maximum of the response fringes (*FWHM*) is measured after each scan to calculate the finesse of the response (see Eq. (37)), the discrete character of the acquisition becomes a source of uncertainty.

The expected standard deviation of the measured finesse due to this effect can be calculated from the frequency sampling period of the response (Δf) and the interferometer parameters. Indeed, the calibration routine calculates the finesse dividing the theoretical free spectral range by twice the half-width half-maximum (*HWHM*) after each scan. The *HWHM* is obtained by detecting both the maximum and the half-maximum of the scanned curve. The maximum error possible detecting the peak of the curve and its half-maximum are respectively $\pm\Delta f/2$ and $\pm\Delta f$. Both errors can occur simultaneously, resulting in a maximum error of $\pm 1.5\Delta f$ in the determination of the *HWHM* and of $\pm 3\Delta f$ in the case of the full-width half-maximum (*FWHM*). There exist as well an error due to the sampling of the curve when calculating Δf (Eq. (109)), but its value (in the order of 0.1% of Δf) is negligible with respect to the one considered here. The maximum and minimum expected values of the measured finesse are therefore

$$F_{\max} = \frac{FSR}{FWHM_{\min}} = \frac{FSR}{\frac{FSR}{\langle F \rangle} - 3\Delta f} \tag{111}$$

$$F_{\min} = \frac{FSR}{FWHM_{\max}} = \frac{FSR}{\frac{FSR}{\langle F \rangle} + 3\Delta f}, \tag{112}$$

where $\langle F \rangle$ is the mean finesse in the tests, once the random fluctuations are already eliminated. The probability of the measured finesse is uniformly distributed within the limits

set by $F_{\min}$ and $F_{\max}$. The uncertainty of the measured finesse due to the sampling effect ($\sigma_{F(\Delta f)}$) can be thus estimated as follows.

$$\sigma_{F(\Delta f)} = \frac{F_{\max} - F_{\min}}{4} \tag{113}$$

During the tests presented here, the cavity length was set to 4 cm, the mean finesse was in all the cases $\langle F \rangle \approx 45$ and the frequency sampling period $\Delta f = 451\text{kHz}$. Using these values, we obtain $\sigma_{\Delta\nu} = 0.37$.

The velocity measurements are in fact affected by the fluctuations of the frequency response but not by the noise induced by the process of measurement of the finesse. Considering that both sources of fast variation are not correlated, the variance of the fluctuations of the frequency response (characterized by its finesse) ($\sigma^2_{F(FR)}$) can be obtained subtracting the noise due to the sampling process ($\sigma^2_{F(\Delta f)}$) from the overall observed finesse variance (σ^2_F).

$$\sigma^2_{F(FR)} = \sigma^2_F - \sigma^2_{F(\Delta f)} \tag{114}$$

In each one of these tests, the standard deviation of the finesse fluctuations due to instability in the frequency response and the corresponding velocity error (for target speed equal to 0 m/s) have been obtained. The values shown in Table 30 correspond to the non-averaging case. The standard deviation has been calculated here for periods of 2 minutes in order to avoid the effect of trends due to long-term degradation of the response. The fact that these fluctuations affect the frequency retrieval in both the reference and the Doppler channels has been also taken in account when translating the finesse fluctuations to noise in the detected velocity.

Test	σ_F	σ_{FR}	2 min. velocity standard deviation
I	1.15	1.09	0.68 m/s
II	1.10	1.04	0.64 m/s
III	0.75	0.65	0.40 m/s
IV	1.07	1.01	0.63 m/s

Table 30. *Standard deviation of the measured finesse and the zero-velocity corresponding velocity error when no averaging is performed.*

These random fast fluctuations affect the velocity retrieval in two ways. During the speed measurements, there will be a statistical error (noise) in the measured velocity that can be easily reduced by averaging measurements. Nevertheless, if the frequency response recorded during the calibration stage does not correspond to the average response, the measured velocity will be affected not only by noise but also by a bias error. To avoid this second effect, it is necessary to perform scan averaging during the calibration procedure. When 20 scans (8 s) and 100 scans (40 s) are averaged, the standard deviation of the finesse and the corresponding velocity error are the ones presented in Table 31.

Test	20 scans		100 scans	
	2 min. finesse standard deviation	2 min. velocity standard deviation	2 min. finesse standard deviation	2 min. velocity standard deviation
I	0.31	0.20 m/s	0.11	0.07 m/s
II	0.25	0.17 m/s	0.06	0.04 m/s
III	0.22	0.14 m/s	0.09	0.06 m/s
IV	0.25	0.17 m/s	0.13	0.07 m/s

Table 31. *Finesse and velocity standard deviation when 20 and 100 scans are averaged.*

As pointed out above, averaging, both during measurements and during calibration, is a good solution for reducing the error produced by fast random variations in the normalized frequency response. However, and not considering yet the degradation in time of the filter selectivity, when the fast fluctuations are eliminated by averaging, slow and erratic variations of the response figures that will produce errors can be still observed. The expected error in this case is anyway much smaller than the ones related with the non-filtered fast fluctuations analyzed in Table 30 and the only way to reduce them would be by means of improving the mechanical and thermal isolation of the interferometer.

7.1.4 Degradation of the frequency response

Besides the fast and slow fluctuations that have been analyzed in section 7.1.3, the normalized frequency response of the interferometer undergoes an increasing loss of its selectivity that is due to a progressive degradation of the parallelism of the cavity mirrors. The tests presented in section 7.1.3 can be used to estimate how long the filter features remain stable and measurement can be done without requiring re-adjusting the cavity and re-calibrating the response. Table 32 shows the average finesse every 2 minutes in the 20 minutes tests.

Test	I	II	III	IV
0-2 min.	46.36	46.71	47.78	48.36
2-4 min.	46.24	46.68	47.84	48.40
4-6 min.	46.45	46.73	48.12	48.52
6-8 min.	46.48	46.93	48.32	48.17
8-10 min.	46.61	46.86	48.15	48.11
10-12 min.	46.66	46.55	48.20	47.88
12-14 min.	46.54	46.35	48.14	47.82
14-16 min.	46.38	46.02	48.02	47.51
16-18 min.	46.47	45.55	47.90	47.17
18-20 min.	46.33	45.11	47.98	46.99

Table 32. *Two minutes partial mean finesse.*

In two of the tests (I and III), the response remains stable during the whole duration of the test (20 minutes), with differences that do not show a trend but the slow fluctuations described in section 7.1.3. Nevertheless, in tests II and IV, as representative instances of bad observed behaviour, a progressive loss of finesse appears after about ten minutes of continuous scans (shaded cells). In general, it has been observed that for different tests, depending probably on the adjustment of the mirrors and on the conditions of the measurements, the degradation of the response can start before or later. After repeated tests, it has been determined that ten minutes is, in this system, a conservative value of the maximum duration of a velocity measurement without re-adjustment and re-calibration of the cavity.

For longer continuous measurements, a better thermal and mechanical isolation of the interferometer should be implemented. Also it has to be taken into account that, in the interferometer used in this experiment, the flexibility in its configuration, with adjustable free spectral range and changeable set of mirrors, is a key feature that, as a counterpart, suffers from worse stability of its parameters than other less flexible approaches: Fabry-Perot etalons [26], [8] or molecular absorption filters [57].

7.1.5 Dependence of the frequency response with the point-of-impact on the target

Another source of variation of the frequency response with respect to the acquired during the calibration phase, affecting only to the Doppler channel, arises from the frequency response dependence on the point-of-impact on the target. The small size of the illuminated spot, essential for maximizing the collected power, produces rough speckle patterns, with big coherence area, on the receiving area of the optical fiber coupler.

As the target rotates and the point-of-impact moves, these patterns change, producing variations in the fiber mode distribution and, once the light exits the fiber and is collimated, different conditions on the interferometer. The behaviour of a Fabry-Perot interferometer is very sensitive to the characteristics of the incident light and these variations produce slight differences in the frequency response. Since the point-of-impact on the target changes continuously when the wheel is rotating, this phenomenon produces fluctuations in the measured velocity that can be counted as another source of noise. The finesse from the Doppler channel has been measured for different points on the target to preliminary estimate the relevance of this contribution to the total noise of a velocity measurement. In order to eliminate the random fast fluctuation effect described in section 7.1.3, the finesse data recorded at each point of the disc correspond to 100 averaged scans. Table 33 shows the results for 3 independent tests. In each one of them, the standard deviation of both the Doppler finesse fluctuation and the corresponding calculated velocity fluctuation are presented.

Test	I	II	III
Number of points on the target	21	35	40
Doppler finesse (Mean)	48.06	45.44	46.87
Doppler finesse (Standard deviation)	1.18	0.80	1.07
Velocity fluctuation (Standard deviation)	0.50 m/s	0.38 m/s	0.48 m/s

Table 33. *Statistics of the point-of-impact dependence of the averaged measured finesse for the Doppler channel.*

7.1.6 Differences between the frequency response in the reference and the Doppler channel

As seen in section 7.1.5, when the target is rotating, the spectral response of the interferometer in the Doppler channel is affected by fluctuations that introduce noise in the velocity determination. This noise can be eliminated by averaging single measurements but, if the mean response corresponding to of all the points of the target does not coincide with the response for the reference channel, a bias error will remain in the velocity measurement. In the three tests presented section 7.1.5, this error has been calculated using the results shown in Fig. 69.

Test	I	II	III
Number of points on the target	21	35	40
Doppler finesse (Mean)	48.06	45.44	46.87
Reference finesse (Mean)	48.56	46.80	46.25
Velocity error (Mean)	0.21 m/s	0.62 m/s	-0.28 m/s

Table 34. *Bias error in the velocity determination due to differences between the mean frequency response in the Reference and the Doppler channel.*

This error depends on our capability during the set-up of the system to assure identical frequency response in both channels.

The effect of both statistical (section 7.1.5) and bias (section 7.1.6) errors due to differences in the frequency response produced by variations of the speckle at the input of the optical fiber would nevertheless be negligible in an atmospheric application of this technique. Indeed, the spatial coherence area in the surface of the telescope, that is, the typical size of the speckle, is expected to be very small when compared to the receiving area (see Eq. (30) in section 3.2.1). This results in a big amount of little speckles (for the typical values used in section 3.2.1, more than 2×10^6) that do not change significantly the illumination of the optical fiber as the atmospheric scatterers move.

7.2 BS3 splitting-ratio. Normalization constant

For recovering the value of the normalized frequency response from the detected voltages (V_{1m}, V_{2m} in the reference channel and V'_{1m}, V'_{2m} in the Doppler channel), the acquisition routine uses a normalization factor (k) that has to be measured during the calibration phase. Following (Eqs. (105) and (106)).

- Reference channel: $\overline{F}(\nu_0) = k\,\frac{V_{2m}}{V_{1m}}; \quad k = \frac{V_{1c}}{V_{2cM\,\mathrm{ax}}}$ (115)

- Doppler channel: $\overline{F}(\nu_0 + f_D) = k\,\frac{V'_{2m}}{V'_{1m}}; \quad k = \frac{V_{1c}}{V_{2cMax}},$ (116)

where V_{1c}, is the non-variant output voltage at detector 1 during the calibration stage and V_{2cMax} is the maximum output voltage at detector 2 during the response scanning.

In an ideal case, with non-variant and identical system performance in both channels, the normalization factor should not undergo variations. Nevertheless, similarly to what occurs with the spectral response of the filter, fluctuations of this factor can be observed in the Doppler channel when the point-of-impact of the beam on the disc changes. Of course, in part, these fluctuations are due to the variations of the cavity frequency response analyzed in section 7.1.5. However, there is a component of this noise that is due to small variations of the splitting-ratio of the beamsplitter that is used, placed immediately before the interferometer, to separate the incident beam in two (BS3 in Fig. 40). This dependence on the point-of-impact, which has been verified removing the mirrors from the optical path, is probably due to both angular and polarization factors. When the wheel rotates, this

phenomenon induces certain noise in the velocity determination. It has been calculated which is the error in the velocity measurement corresponding to variations of k with respect to the one used by the routine to perform the calculations. Fig. 74 shows the results of these calculations for different measured velocities within a range of ± 10 m/s, in a system with a recorded finesse F = 47.62, a cavity length d = 4 cm and a factor in the reference channel k = 0.8, operating at 1064 nm.

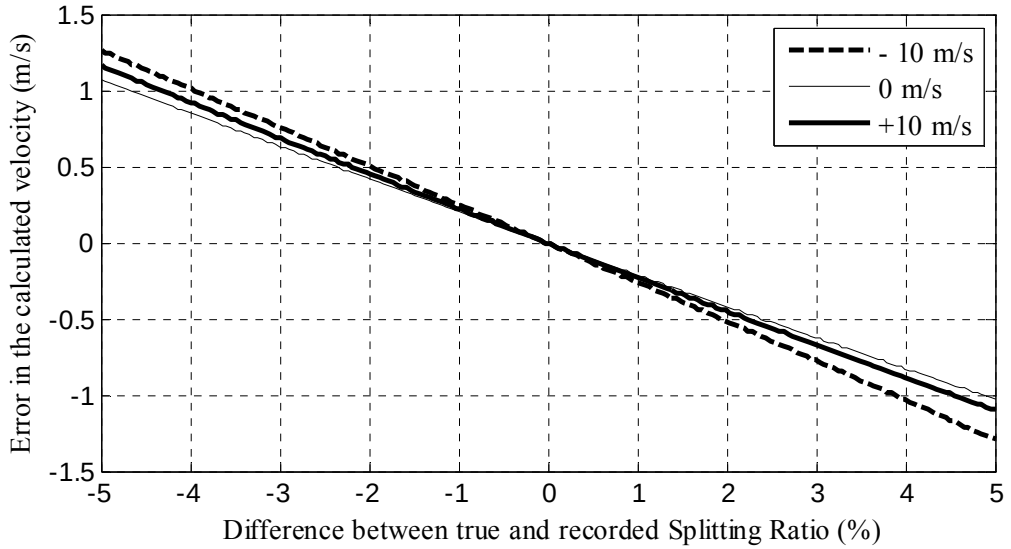

Fig. 74. *Velocity error due to variations of the normalization factor in the Doppler channel. k = 0.8, F = 47.62, cavity length d = 4 cm, operation wavelength λ_0 = 1064 nm.*

Table 35 shows, for the three tests performed in section 7.1.5, the statistics of the variations of the normalization constant in the Doppler channel and the corresponding velocity error when the zero-speed is measured in different points on the reflecting surface.

Test	I	II
Number of points on the target	35	40
k_D (Mean)	1.13	1.07
k_D (Standard deviation)	0.046 (4.07%)	0.041 (3.83%)
Velocity fluctuation (Standard deviation)	0.84 m/s	0.80 m/s

Table 35. *Statistics of the point-of-impact dependence of the normalization factor for the Doppler channel*

7.3 Tuning control system

7.3.1 Estimation of the frequency drifts compensated by the system

As it has been already reported in section 6.5, the objective of this subsystem is to compensate the relative frequency drifts between the laser and the filter. In our prototype, any displacement of the emitted frequency with respect to the filter slope produces a change in a control signal that, after being amplified by the interferometer controller, is applied to the piezoelectric cells to readjust the cavity length and, hence, compensate the drift (see Fig. 60).

If the control voltage used to tune the cavity length is monitored, the frequency drifts that the system is compensating in each moment can be estimated. Fig. 75 and Fig. 76 display this voltage in two different tests. In both cases the duration of the observation was two minutes.

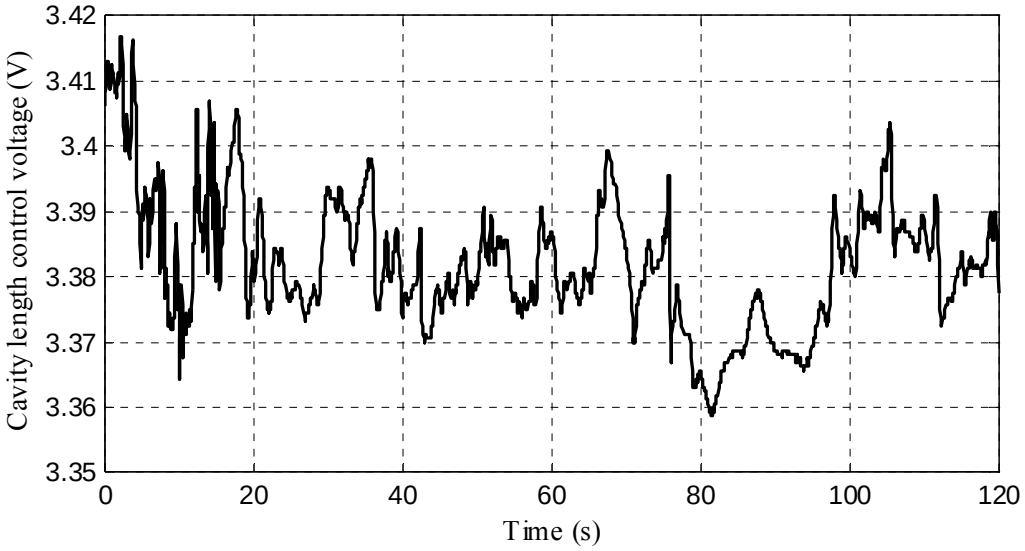

Fig. 75. *2 minutes monitoring of the voltage that controls the cavity length with 'sensitivity' equal to 1 % and 'interval' 50 ms (see section 6.6.3).*

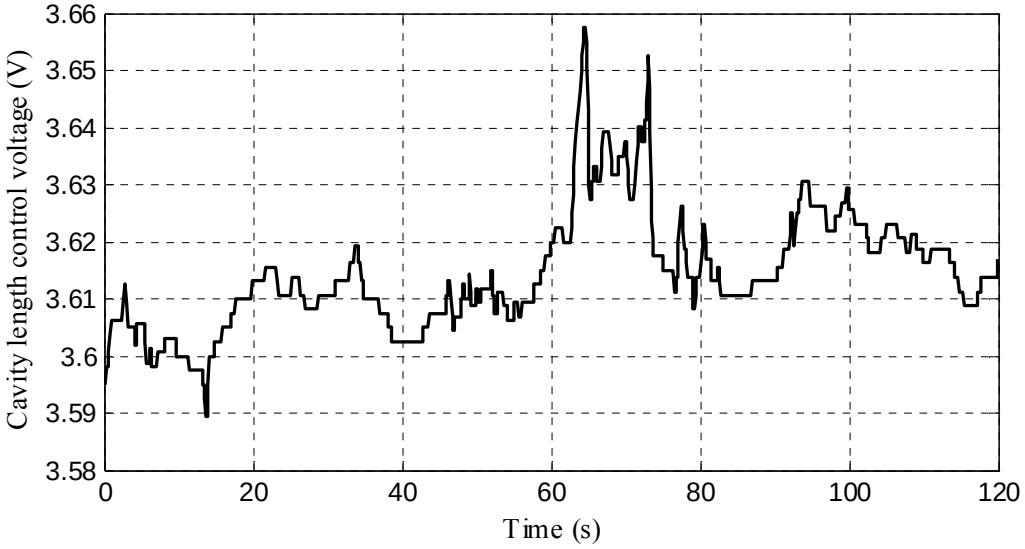

Fig. 76. *2 minutes monitoring of the voltage that controls the cavity length with 'sensitivity' equal to 4 % and 'interval' 100 ms (see section 6.6.3).*

The maximum variation of the control voltage during the two minutes observation has been 60 mV in the first case and 70 mV in the second one. If these variations are translated to frequency shifts of the response, they result respectively in 101 MHz and 86 MHz (it has been measured that, in these tests, the ratio of the resulting frequency shift to the control voltage that is been applied is 1.44 GHz/V). Considering that the bandwidth of the filter was about 80 MHz, it can be stated that, if these frequency drifts had not been compensated, part of the measurements would have been displaced completely out of the sensitive zone of the response. The fact that these results are obtained in observations of only two minutes

duration, confirms that the tuning control subsystem is indispensable in a velocimeter using an interferometer like the one considered here.

7.3.2 Effect of 'sensitivity' and 'interval' parameters

Regarding the measurements displayed in Fig. 75 and Fig. 76, the configuration of the tuning control system changed from one test to the other. In the first one, the system was programmed to act, if it was necessary, every 50 ms ('interval' parameter; see section *6.6.3*) and to react only when the change of the response to the emitted frequency with respect to its optimal value is bigger than 1 % ('sensitivity' parameter; see section *6.6.3*). In the second test these parameters where set respectively to 100 ms and 4 %. It can be observed that, as it can be expected, in the first case the voltage changes more frequently.

The effect of increasing these parameters is that the frequency drifts grow bigger before they are compensated. Bigger displacements of the measurements from their optimal location on the response produce a loss of sensitivity and, as a consequence, a bigger uncertainty in the detected velocity. The frequency drifts that, during two minutes of continuous acquisitions, are not compensated by the tuning control system have been monitored for different values of 'sensitivity' and 'interval' parameters. The standard deviation of these drifts has been in turn translated into the corresponding increase in the calculated uncertainty, averaged over the whole velocity dynamic range. As examples, results obtained, first when 'sensitivity' is fixed to 1 % and secondly, when 'interval' is set to 50 ms, are displayed in Table 36 and Table 37, and in Fig. 77 and Fig. 78.

Sensitivity (%)	1.0									
Interval (ms)	20	50	100	200	300	400	500	600	700	800
Frequency drift (MHz) (standard deviation)	1.06	1.20	0.96	2.45	2.63	3.20	4.51	5.76	6.29	8.86
Increase in uncertainty (%)	1.96	2.16	1.77	5.56	6.17	8.19	15.09	25.42	31.95	-

Table 36. *Increase in mean uncertainty due to non-compensated frequency drifts as a function of the parameter 'interval'.*

Interval (ms)	100									
Sensitivity (%)	1.0	2.0	3.0	4.0	5.0	6.0	7.0	8.0	9.0	10.0
Frequency drift (MHz) (standard deviation)	0.96	1.48	1.76	2.29	2.74	3.07	3.78	3.89	4.48	4.78
Increase in uncertainty (%)	1.77	2.78	3.70	4.99	6.48	7.83	11.03	11.49	15.09	16.90

Table 37. *Increase in mean uncertainty due to non-compensated frequency drifts as a function of the parameter 'sensitivity'.*

In both cases it is clear that the higher are 'sensitivity' and 'interval' the more important is the increase in the uncertainty of the velocity measurements. These results can be used to establish constraints on these parameters. For instance, if 'interval' (i.e. the time between corrections) is set to 100 ms and a loss of precision above 2 % is not allowed, the 'sensitivity' parameter has to be set below 1 %. These have been indeed the values used in the velocity measurements presented in section 7.4.5.

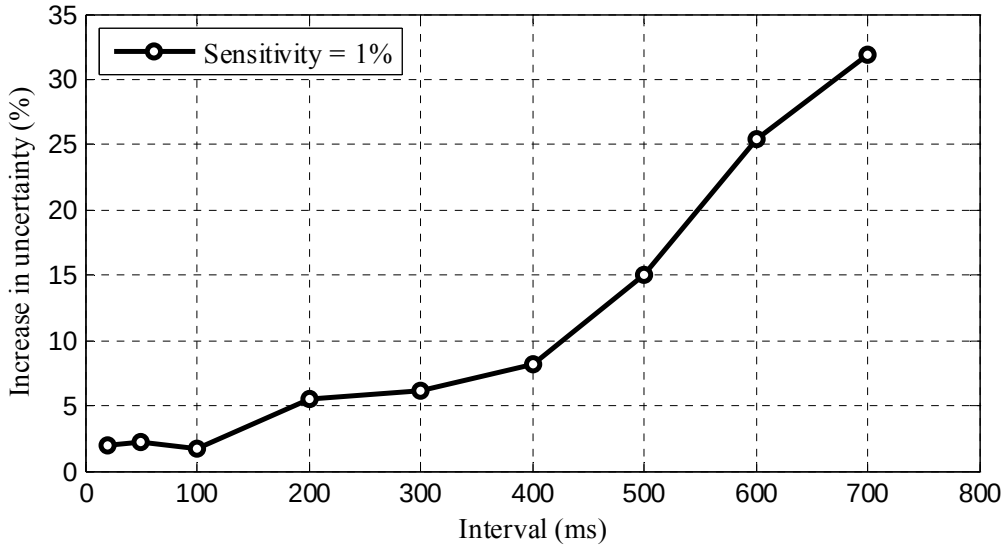

Fig. 77. *Increase in mean uncertainty due to non-compensated frequency drifts as a function of the parameter 'interval'.*

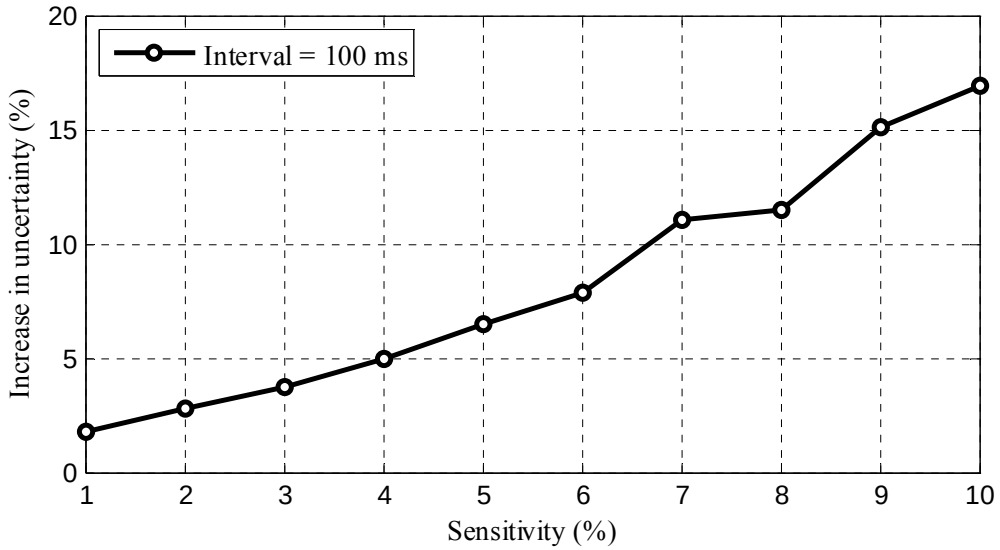

Fig. 78. *Increase in mean uncertainty due to non-compensated frequency drifts as a function of the parameter 'interval'.*

Due to the differential nature of the technique, as long as the drifts of the emitted frequency do not oblige the set of measurable frequencies to get off the slope of the response, going over the resonance peak, velocity measurements are possible in the whole velocity dynamic range. The effects of the displacements are in such cases limited to an increase in the velocity uncertainty. Limits for 'interval' and 'sensitivity' have been also determined; 'interval' above 800 ms (if 'sensitivity' is set to 1%) and 'sensitivity' above 15 % (if 'interval' is set to 100 ms) would impede measurements in the whole dynamic range (see Fig. 79).

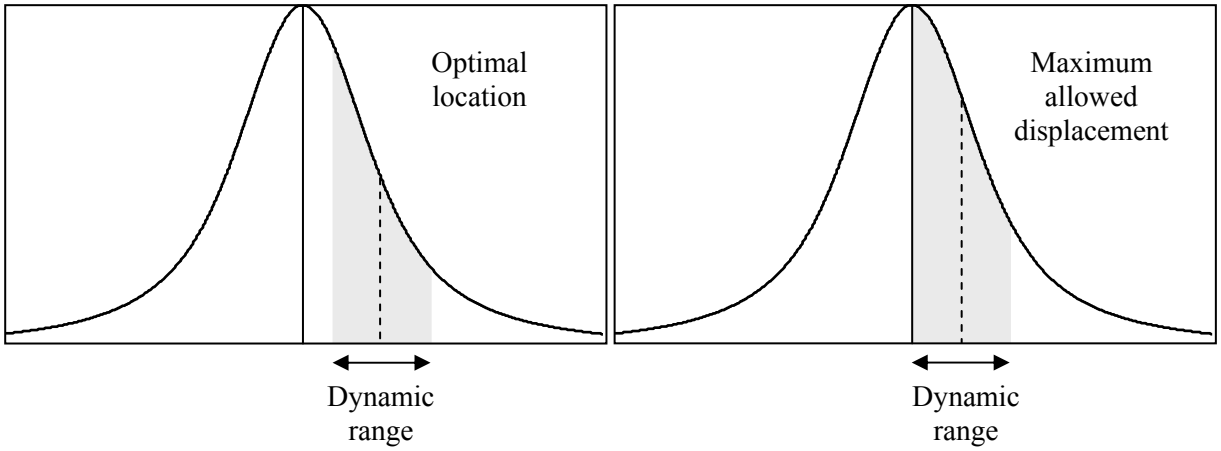

Fig. 79. *Location of the emitted frequency and the frequency dynamic range of the measurements. Optimal location (left) and maximum allowed displacement (right).*

7.4 Velocity measurements

7.4.1 Description of the tests

Several sets of velocity measurements have been carried out with the continuous-wave solid-target velocimeter described in section 6. As described in section 6.2.5, the target used to asses the measurement technique is a rotating disc whose linear speed on the edge is measured by the velocimeter (see Fig. 43). The angular speed of the disc is controlled by a DC regulator (Ref. IED Electronics VT-30).

The speed of the disc is monitored by an independent *ad-hoc* opto-electronic system [64], which is indispensable for estimating the quality of the Doppler measurements. An optical transmitter-receiver device illuminates one side of the disc and detects the radiation scattered by a collection of uniformly distributed reflecting patches attached to it. Then, a LabVIEW® routine measures the frequency of the resulting pulsed signal detected by the receiver and calculates the linear speed of the target.

In an ideal noiseless system that is not affected by systematic errors, each single measurement would provide the true velocity of the target. Measurements, nevertheless, are affected both by noise and systematic errors. The effect of noise is the presence of random variations in the detected velocity when the same true velocity is repeatedly measured (uncertainty) and it can be reduced averaging individual measurements. If there were not systematic errors, the mean of the detected values would coincide with the true velocity of the target. However, systematic errors exist in the measuring process and their effect is a bias error in the measured velocity, i.e. a difference between the true and the mean detected speed. For calculating both the effect of noise and the bias error and in such way characterize the quality of the results, in each velocity measurement, the same true velocity has been repeatedly measured.

Both noise and bias error are in general different for different measured velocities. The velocity tests have thus been run for a set of different speeds within a given velocity range. As seen in section 5.2, once the velocity range and the finesse of the interferometer are fixed, the optimal cavity length can be calculated. In the tests presented here, the main parameters of the measurements configuration are the ones shown in Table 38.

Radial velocity bandwidth	± 10 m/s
Disc Diameter (D)	50 cm
Angle of incidence (θ_i)	45º
Angular velocity range	± 540 rpm
Finesse	45
Cavity length	4 cm
Number of measured velocities	10

Table 38. *Velocity tests configuration parameters.*

7.4.2 Power conditions

For assessing the performance of the velocimeter, the quality parameters of the measurements (uncertainty and bias error) have to be compared with the theoretical expected values assuming the conditions present during the tests. As seen in section 5.2.2.4, the uncertainty depends strongly on the optical intensity incident on the frequency discriminator. Consequently, the optical power has had to be measured or estimated in different points of the prototype set-up.

Fig. 80 shows a scheme of the optical section of the prototype where the measuring points are indicated. Table 39 presents the optical power obtained in each of these points. From points 1 to 9 (non-shaded rows), the optical power has been directly measured with a commercial power meter (Ref.: Edmund Optics NT54-018). From these measurements, the true values of some parameters have been calculated and are also shown in Table 39. The optical power in points 10 to 12 (shaded rows) has been estimated from the incident power (optical power in point 9) and the parameters of the optical fiber, the collimating lens, the diaphragm and the beamsplitter. The values used for these calculations are also shown in Table 39.

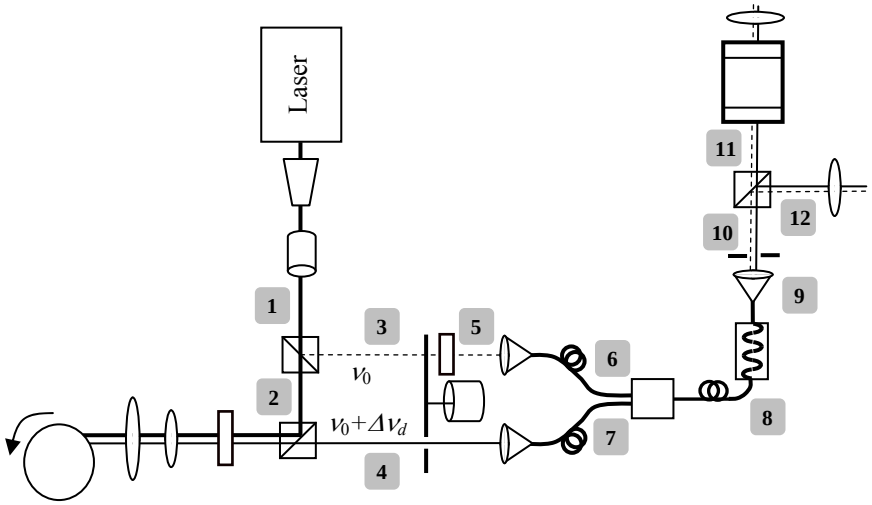

Fig. 80. *Measurement points listed in Table 39.*

The attenuator located in the reference channel before the optical fiber coupler is adjustable, and it is used to equal the incident power in both channels. Nevertheless, the optical power collected in the Doppler channel changes significantly when the point-of-impact of the beam on the target changes and this balance is not possible in all the acquisitions when the target is rotating. The values presented in Table 39 are therefore necessarily a particular instance, yet typical, in which the optical power in both channels is balanced at the measuring points from 6 to 12.

Point	Optical power	Related parameters
1	1.33 mW	
2	1.15 mW	Beamsampler transmistance: 86.5 %
3	118 μW	Beamsampler reflectance: 8.8 %
4	15.7 μW	Transmitting-receiving loss: 18.6 dB
5	7.8 μW	Attenuator: 11.8 dB
6	6.2 μW	Coupling efficiency (Ref. channel): 79 %
7	6.2 μW	Coupling efficiency (Doppler. channel): 39 %
8	2.7 μW	2×1 Coupling efficiency: 44 %
9	2.3 μW	Mode scrambler transmission: 85 %
10	1.58 nW	Numerical aperture of the optical fiber: 0.275 Collimating lens focal length: 10 mm Diaphragm diameter: 1.5 mm
11	0.76 nW	Beamsplitter transmittance: 50 %
12	0.76 nW	Beamsplitter reflectance: 50 %

Table 39. *Optical power measured (non-shaded) and estimated (shaded) at different points of the prototype set-up.*

7.4.3 Expected uncertainty in the velocity determination

The uncertainty in the measurements due to the noise will be characterized by the standard deviation of the measured values. In section 5.2.2.4, the uncertainty due to the photoreceiver noise has been estimated for a system like the one implemented and tested in this section, considering an incident power equal to the one estimated in section 7.4.2 (see Table 39). Also, in sections 7.1 and 7.2, other sources of noise have been identified and characterized, and they have to be also considered in the analysis of the system performance. If the different contributions to the error are uncorrelated, the overall uncertainty σ_O can be calculated as follows,

$$\sigma_O = \sqrt{\sum_i \sigma_i^2}\ , \tag{117}$$

where σ_i is the standard deviation associated to each noise source. In the case of the system assessed in this section, the overall uncertainty for an individual acquisition is

$$\sigma_O = \sqrt{\sigma_{PR}^2 + \sigma_{FR}^2 + \sigma_{PI}^2 + \sigma_{SR}^2}\ , \tag{118}$$

where σ_{PR} is the uncertainty due to the photoreceiver noise (sections 4.4.2 and 5.2.2.4), σ_{FR} is the one associated to random variations of the frequency response (section 7.1.3), and σ_{PI} and σ_{SR} are related to the point-of-impact dependence of the frequency response and the splitting ratio of BS3 in the Doppler channel (sections 7.1.5 and 7.2).

In the velocity measurements, averaging is used to reduce the uncertainty in the velocity determination. When sample averaging is performed, the variance of each one of the uncorrelated sources of noise is divided by an 'averaging factor' (*AF*) that is equal to the

number of accumulated samples. The uncertainty of the measurements in this case (σ_{AV}) can be written thus as follows.

$$\sigma_{AV} = \sqrt{\frac{\sigma_{PR}^2}{AF} + \frac{\sigma_{FR}^2}{AF} + \frac{\sigma_{PI}^2}{AF} + \frac{\sigma_{SR}^2}{AF}} = \frac{\sigma_O}{\sqrt{AF}} \tag{119}$$

The expected uncertainty associated to the noise of the photoreceiver σ_{PR} has been calculated as in section 5.2, for a set of velocities within the velocity range, using the system configuration parameters shown in Table 38 and the incident optical power from Table 39. Fig. 81 displays these results.

The expected uncertainty due respectively to the observed random variations of the frequency response (σ_{FR}) and to the point-of-impact dependence in the Doppler channel of both the frequency response (σ_{PI}) and the splitting ratio in BS3 (σ_{SR}) has been also calculated for the range of measurable velocities. The results are shown in Fig. 82.

It can be observed that for this low level of incident power (1.58 nW), the photoreceiver noise is clearly dominant and the effect of the rest of sources of noise could be neglected. However, this would not be the case if the incident power was bigger. As example, if the incident power is 10 nW, the mean value of the photoreceiver uncertainty within the velocity range is 0.88 m/s (see Table 4 in section 5.2.3.1), comparable to the values obtained for the rest of sources of noise, which do not depend on the incident power. On the other hand, for an optical power of 100 nW the mean photoreceiver uncertainty would go down to 0.15 m/s and would start to become irrelevant compared with the rest of contributions.

Since a veloctity measurement can be only performed when both the reference and the Doppler channels have been processed, the maximum temporal resolution of the measuring system is equal to the chopper period. The samples that are acquired during that time interval are therefore always averaged in order to reduce the noise of the measurement. The different velocity tests presented in this section have been carried out using a chopper frequency of 100 Hz and a sampling rate of 40000 samples/s. These figures correspond to 200 available samples within each chopper half-period. In order to avoid the transition zones between the half-periods, only the 100 central samples of each half-period are averaged to obtain each single velocity measurement. Applying thus Eq. (119) with an averaging factor AF_1 = 100, the overall expected uncertainty of the measurements can be computed. Results for the partial and the overall uncertainties for the set of velocities within a range of ± 10 m/s are shown in Table 40.

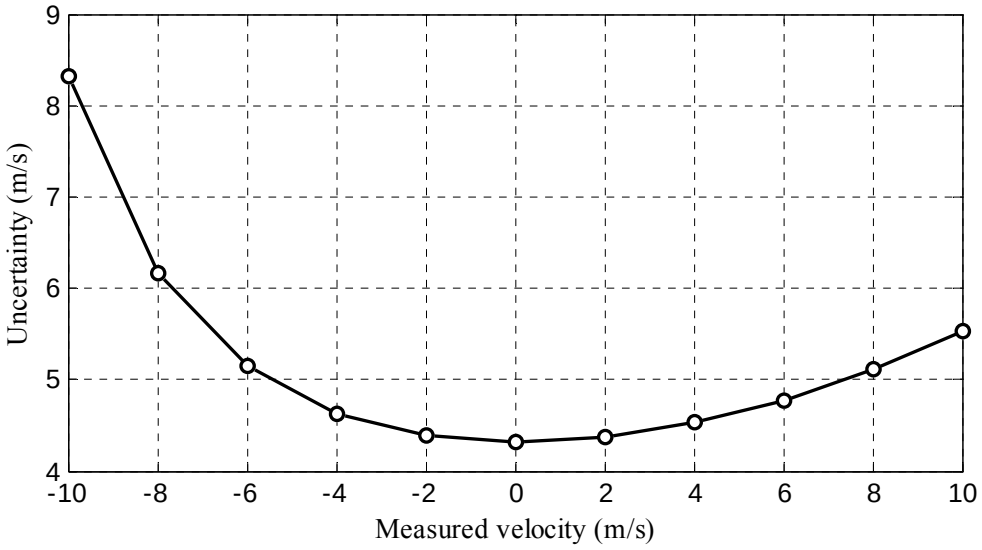

Fig. 81. *Expected velocity uncertainty due to the photoreceiver noise as a function of the measured velocity, when no averaging is performed.*

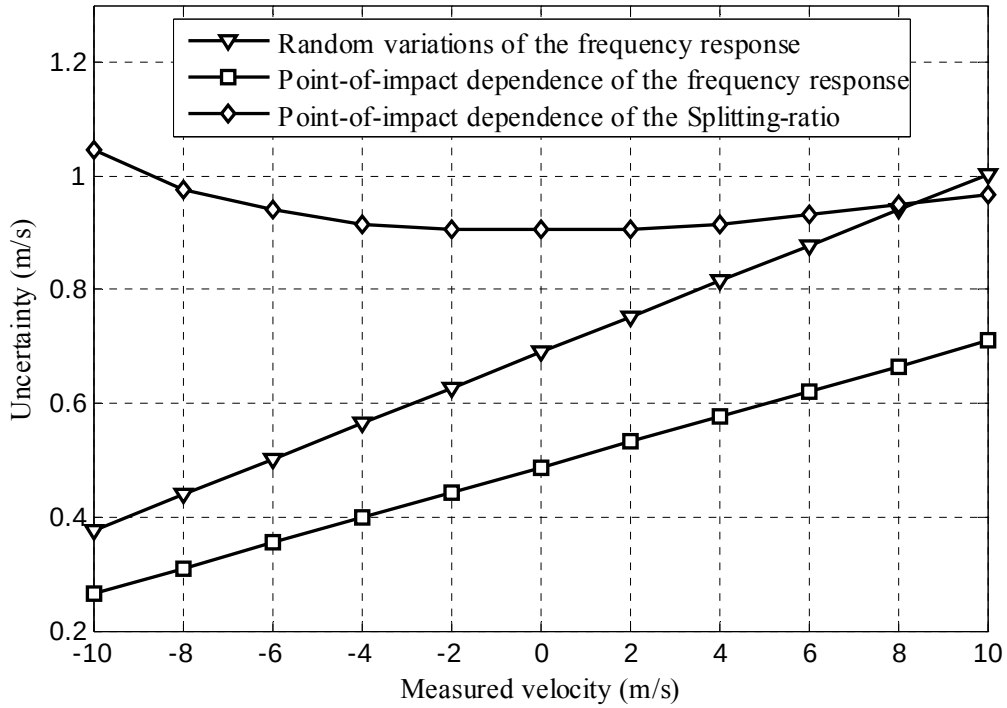

Fig. 82. *Expected velocity uncertainty according to the measured fluctuations of the frequency response and point-of-impact dependence of the frequency response and the splitting ratio in the Doppler channel.*

Measured velocity (m/s)	σ_{PR} (m/s)	σ_{FR} (m/s)	σ_{PI} (m/s)	σ_{SR} (m/s)	σ_{O} (m/s)	σ_{AV} (m/s) $AF_1 = 100$
-10	8.32	0.38	0.27	1.06	8.40	0.84
-8	6.17	0.44	0.31	0.98	6.27	0.63
-6	5.14	0.50	0.35	0.92	5.27	0.53
-4	4.63	0.56	0.40	0.90	4.77	0.48
-2	4.38	0.63	0.44	0.88	4.54	0.45
0	4.31	0.69	0.49	0.88	4.49	0.45
2	4.37	0.75	0.53	0.88	4.56	0.46
4	4.53	0.82	0.58	0.89	4.73	0.47
6	4.78	0.88	0.62	0.90	4.99	0.50
8	5.11	0.94	0.66	0.91	5.33	0.53
10	5.53	1.00	0.71	0.93	5.74	0.57

Table 40. *Partial and overall expected uncertainty*

7.4.4 Bias error in the velocity determination

The bias error, i.e., the difference between the true and the mean measured speed, is the consequence of systematic errors in the measuring process. Contrary to what happens with the random errors due to noise, which can be reduced by applying sample averaging, the bias error cannot be eliminated unless the different systematic errors are either eliminated or characterized, determined and removed from the results. Some of these errors have been already identified.

As seen in section 7.1.6, when the frequency response in the Doppler channel does not match exactly that of the reference channel, an error in the velocity determination appears. This is a systematic error that, in the case of the tested prototype, although small, is difficult to control. The response in the Doppler channel depends on the point of impact of the radiation, and it undergoes random fluctuations when the target is rotating. The 'average response' is the one that should be the same as in the reference channel and it is not possible to adjust it in static conditions. The different tests presented in section 7.1.6 show velocity errors induced by this cause ranging from – 0.28 to 0.62 m/s.

The bias error is calculated as the difference between the "true" and the mean measured speed. An error monitoring the target velocity taken as reference will, therefore, also contribute to the calculated bias error. In the case of the tests presented here, errors in the velocity of the target used as reference arise from both the measurement of the angular speed of the disc and the estimation of the angle of incidence. In both cases, the aim is to reduce their importance as much as possible, but certain non-determined component of the bias error will be actually induced necessarily by the errors in the determination of the "true" radial speed.

7.4.5 Velocity measurements

In this section, four sets of velocity measurements, spanning the velocity range of the system, will be presented. In all the tests, for each velocity value, the duration of the measurements is

two minutes. The mean and the standard deviation of the detected velocity have been calculated for determining the bias error and the uncertainty of the measurement.

Also, the effectiveness of averaging acquisitions has been tested. In each two-minutes velocity measurement, an additional averaging factor $AF_2 = 200$, which corresponds to a data integration of 8 seconds, has been applied to the individual measurements and the effects of the sample averaging in the uncertainty of the resulting data have been analyzed.

The main configuration parameters of these velocity tests are summarized in Table 41.

Frequency discriminator	
Finesse	45
Cavity length	4 cm
Power	
Incident power	2 nW
Target	
Disc diameter	50 cm
Angle of incidence	45º
Acquisition	
Chopper frequency	100 Hz
Sampling rate	40000 samples/s
AF for one single measurement	100
Measured velocities	
Radial velocity range	± 10 m/s
Range of angular speeds	± 540 rpm
Number of measured velocities	10
Velocity measurement duration	2 min

Table 41. *Main settings and parameters of the velocity tests*

7.4.5.1 Results

Table 42 to Table 45 show, for each of the tests presented here, the results of the radial (line-of-sight component) velocity measurements. For each measured velocity, the displayed data are: the 'true' velocity (as determined from the optolectronic system measuring the angular velocity (see section 7.4.1)), the mean detected velocity, the bias error and the uncertainty, first, when no averaging is applied (besaides the one intrinsically applied to obtain each single measurement (see section 7.4.3)) and secondly, with 8 seconds integration. Figs. Fig. 83 to Fig. 86 display, also for each of the tests, the mean measured values and the single measurement uncertainty versus the true velocity. In each figure the line corresponding to an ideal detector (measured velocity equal to 'true' velocity) is also displayed. No graphic representation of the uncertainty of averaged measurements is made in the plots.

Test I

Angular speed (rpm)	'True' radial Velocity (m/s)	Mean measured velocity (m/s)	Uncertainty (m/s) (Single meas.)	Uncertainty (m/s) (8 s integration)	Bias error (m/s)
-630.8	-11.68	-11.72	2.01	0.19	-0.04
-480.0	-8.89	-8.83	1.85	0.13	0.06
-384.8	-7.12	-6.95	1.57	0.07	0.17
-241.5	-4.47	-4.48	1.32	0.05	-0.01
-118.5	-2.19	-2.45	0.94	0.06	-0.26
131.7	2.44	2.43	0.92	0.08	0.00
253.2	4.69	4.53	1.08	0.09	-0.16
367.5	6.80	6.62	1.32	0.12	-0.19
468.8	8.68	8.48	1.59	0.09	-0.20
616.5	11.41	11.08	1.56	0.08	-0.34

Table 42. *Results for test I*

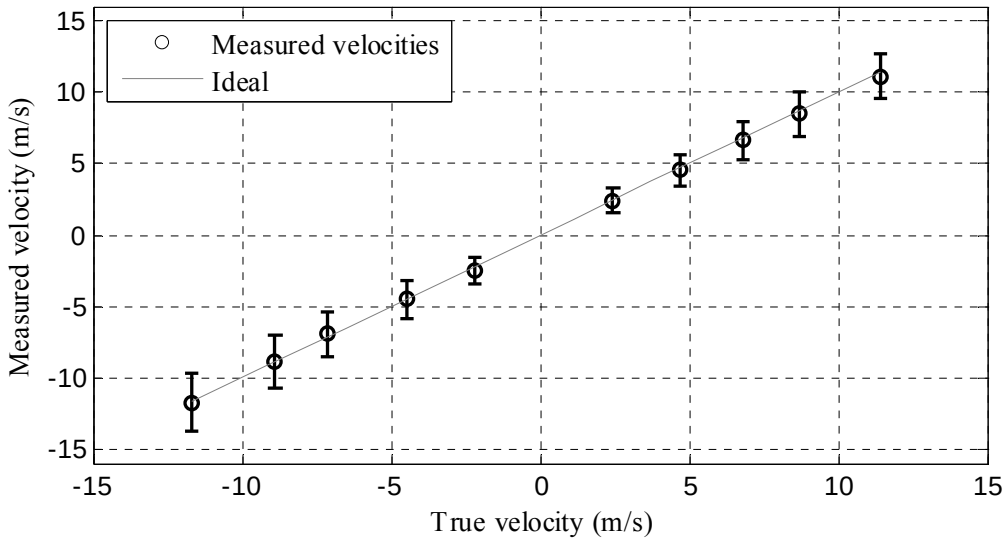

Fig. 83. *Measured velocities and uncertainty vs. 'true' radial velocity with no averaging (Test I)*

The linear least square fitting of the results leads to a relation between the measured velocity (v_m) and the "true" radial velocity (v_t)

$$v_m = 0.9856\, v_t - 0.0965 \tag{120}$$

Similar presentation of results are shown in for the tests II, II and IV

Test II

Angular speed (rpm)	'True' radial Velocity (m/s)	Mean measured velocity (m/s)	Uncertainty (m/s) (Single meas.)	Uncertainty (m/s) (8 s integration)	Bias error (m/s)
-519.6	-9.62	-8.91	1.60	0.14	0.71
-412.2	-7.63	-7.25	1.50	0.17	0.38
-303.0	-5.61	-5.58	1.50	0.28	0.03
-183.0	-3.39	-3.73	1.14	0.23	-0.34
-96.0	-1.78	-1.90	0.75	0.07	-0.12
93.6	1.73	1.93	0.91	0.10	0.20
194.4	3.60	4.18	1.15	0.16	0.58
295.8	5.48	6.17	1.41	0.26	0.69
435.0	8.05	8.60	1.48	0.25	0.55
541.2	10.02	10.38	1.54	0.20	0.36

Table 43. *Results for test II*

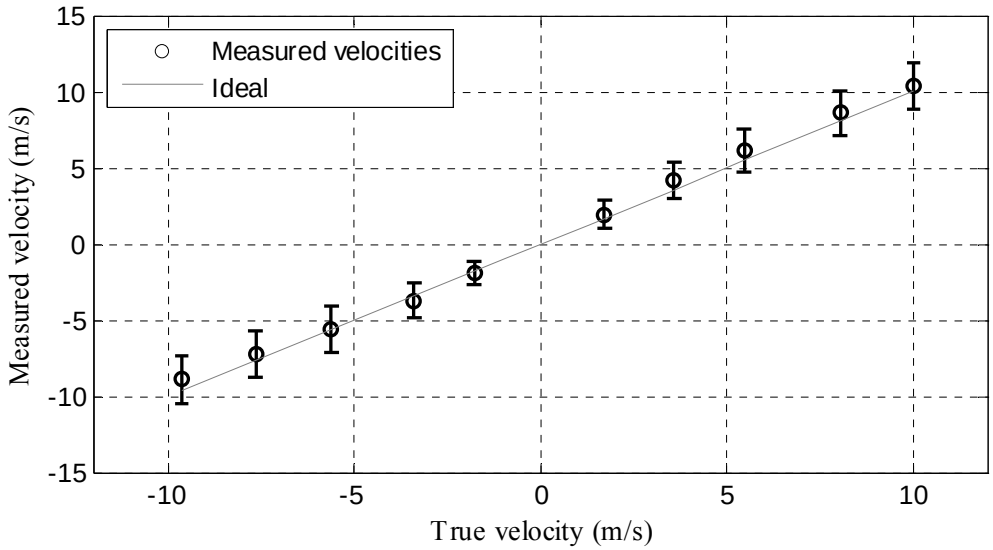

Fig. 84. *Measured velocities and uncertainty vs. 'true' radial velocity with no averaging (Test II)*

The linear least square fitting of the results:

$$v_m = 1.0135\, v_t + 0.3023 \tag{121}$$

Test III

Angular speed (rpm)	'True' radial Velocity (m/s)	Mean measured velocity (m/s)	Uncertainty (m/s) (Single meas.)	Uncertainty (m/s) (8 s integration)	Bias error (m/s)
536.1	9.92	9.69	1.62	0.12	-0.23
425.3	7.87	7.89	1.59	0.12	0.02
330.1	6.11	6.38	1.40	0.12	0.27
243.8	4.51	4.74	1.22	0.07	0.23
143.6	2.66	2.96	0.96	0.11	0.30
82.9	1.54	1.48	0.65	0.07	-0.05
-96.9	-1.79	-2.33	0.84	0.16	-0.54
-183.7	-3.40	-3.87	0.93	0.10	-0.47
-271.7	-5.03	-5.44	1.12	0.10	-0.41
-373.5	-6.91	-7.19	1.30	0.14	-0.28
-487.1	-9.02	-8.65	1.38	0.15	0.36
-584.5	-10.82	-10.29	1.47	0.12	0.53

Table 44. *Results for test III*

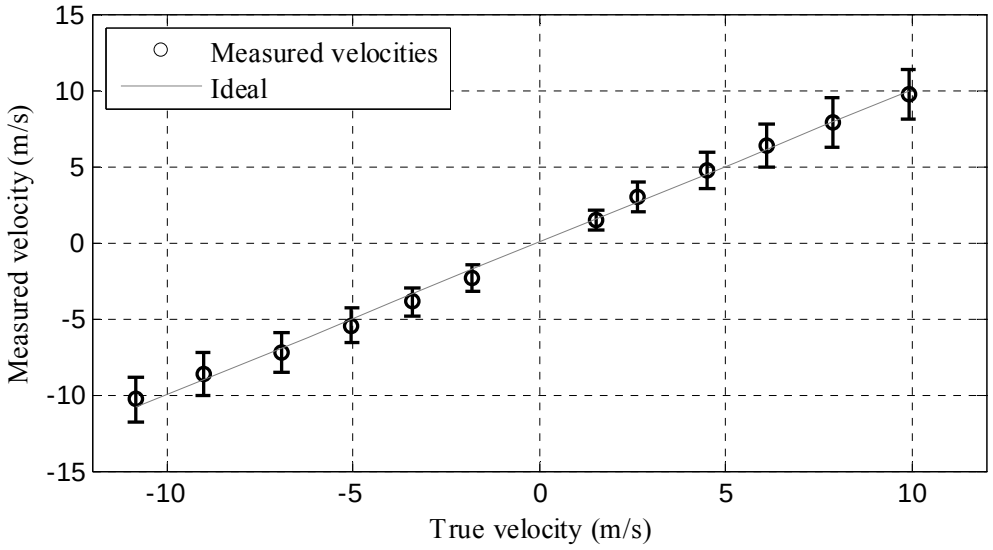

Fig. 85. *Measured velocities and uncertainty vs. 'true' radial velocity with no averaging (Test III)*

The linear least square fitting of the results:

$$v_m = 0.9974\, v_t - 0.0235 \qquad (122)$$

Test IV

Angular speed (rpm)	'True' radial Velocity (m/s)	Mean measured velocity (m/s)	Uncertainty (m/s) (Single meas.)	Uncertainty (m/s) (8 s integration)	Bias error (m/s)
-523.7	-9.69	-9.22	2.31	0.13	0.48
-448.9	-8.31	-8.11	2.14	0.15	0.20
-396.5	-7.34	-7.03	2.17	0.11	0.31
-317.3	-5.87	-6.12	1.71	0.14	-0.25
-229.4	-4.25	-4.25	1.69	0.13	0.00
-154.6	-2.86	-3.16	1.40	0.15	-0.30
-79.8	-1.48	-1.44	0.75	0.07	0.03
79.8	1.48	1.62	0.84	0.14	0.14
154.0	2.85	2.82	1.14	0.11	-0.03
224.4	4.15	4.16	1.41	0.23	0.00
299.3	5.54	6.22	1.49	0.11	0.68
381.5	7.06	7.39	1.44	0.15	0.33
455.1	8.43	8.29	1.57	0.19	-0.13
526.8	9.75	9.79	1.49	0.07	0.04

Table 45. *Results for test IV*

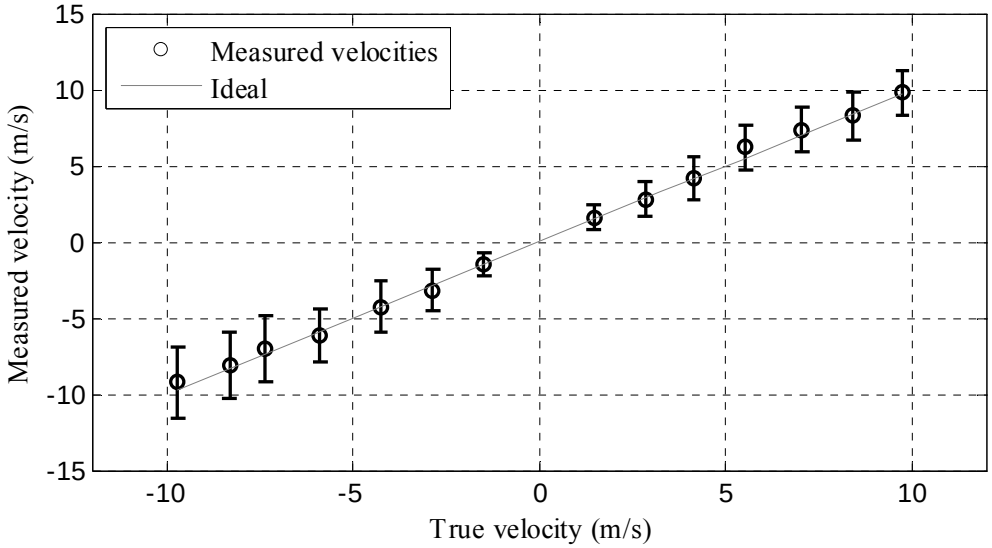

Fig. 86. *Measured velocities and uncertainty vs. "true" radial velocity with no averaging (Test IV)*

The linear least square fitting of the results:

$$v_m = 0.9987\, v_t + 0.1071 \tag{123}$$

In general, results permit to say that the velocimeter is correctly measuring the velocity of the target. In the next section, the results are analyzed in connection with the quality parameters defined in section 7.4.1.

7.4.5.2 Analysis of the bias error

The bias error observed during the tests does not show a predictable behavior. This can be partly explained by the fact that, as shown in section 7.1.3, the frequency response of the filter, besides being affected by fast random variations that can be reduced by sample averaging, undergoes slower fluctuations that can produce differences in the response from one two-minutes-duration averaged acquisition to another. The system has also had to be re-adjusted and re-calibrated during the tests to prevent the filter response to suffer degradation like the one described in section 7.1.4. Cavity re-adjustments can produce a change in the bias error that is due to differences in the response between the reference and the Doppler channels (see section 7.1.6). Finally, it has been observed that the angular speed of the rotating disc is not ideally constant during the two minutes acquisition corresponding to each measurement. These fluctuations can introduce an error in the estimated true speed that would affect the calculation of the bias error.

However, the value of the bias error is always low (mean absolute value in each test: 0.14, 0.39, 0.31 and 0.21 m/s respectively) and, according to what has been said above, could be reduced first by enhancing the stability of the filter response: that would reduce the slow fluctuations of the response and would avoid the need for re-adjusting the system during tests. This could be achieved by improving the isolation, both thermal and mechanical, of the assembly. Also, a better equalization of the measuring channels (reference and Doppler) would prevent differences in the response that contribute to the bias error (see section 7.1.6).

Finally, it is also worth to mention that, although it is an external factor that does not modify the quality of the Doppler measurements, it could be expected that a more stable velocity regulator improved the figures obtained during the tests.

7.4.5.3 Analysis of the uncertainty

Regarding the uncertainty, a comparison with the expected values calculated in section 7.4.3 is presented in Fig. 87.

It can be observed that the measured values are of the same order of magnitude of the expected uncertainty. The agreement is very good for low measured velocities. When the speed increases, the measured uncertainty tends to be bigger than the expected values, almost doubling them in both ends of the velocity measurable range. Independently of the numerical values, in all the tests the general trend is the expected one, namely less uncertainty for lower measured velocities. Also –except in Test III– the uncertainty, as it happens with the calculated values, grows faster for negative velocities (closer to the interferometer resonance peak) than for positive velocities.

These uncertainty figures are obtained with a time resolution corresponding to one chopper period, without applying any additional velocity measurement averaging. The uncertainty should be reduced by a factor equal to the square root of the number of the averaged measurements (see section 7.4.3). The results when an integration of 8 seconds ($AF_2 = 200$) is applied in the two-minutes-duration measurements are shown in Table 42 to Table 45. In all the cases the obtained noise reduction is approximately the same than the expected one according to Eq. (119).

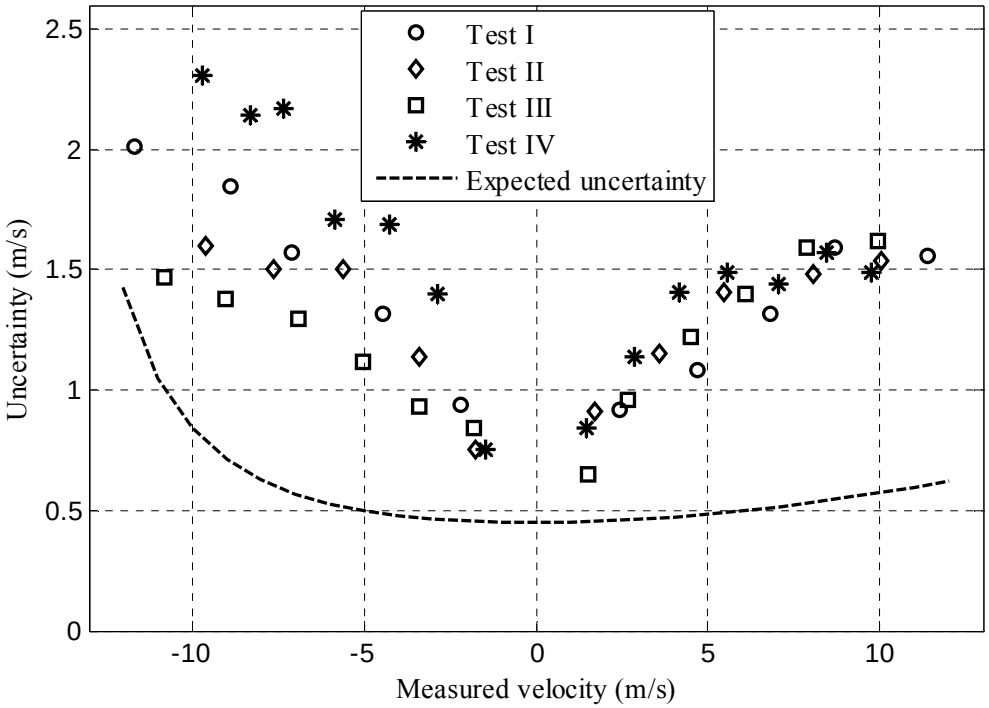

Fig. 87. *Comparison between the uncertainty obtained in each test and the expected uncertainty for a single velocity measurement.*

8 Conclusions and further work

8.1 Conclusions

This work has been devoted to the study, analysis, implementation and evaluation of Doppler wind lidar systems based on the so-called edge-technique.

The first part of the dissertation is dedicated to the analysis of these systems. After some general issues related to Doppler wind lidars (chapter 2), the lidar signal (chapter 3) and the edge-technique (chapter 4), a detailed performance analysis of an edge-technique-based Doppler wind lidar is presented in chapter 5. The study has been carried out evaluating the quality of the velocity measurements and it has been used both to optimize the configuration of two different edge-technique-based Doppler lidars (the continuous-wave hard-target prototype and the planned *UPC* atmospheric aerosol-based system) and to estimate their performance.

In the first place, a systematic method has been defined for calculating the best configuration of the frequency discriminator (in this case, a Fabry-Perot interferometer) (sections 5.2 and 5.3). The method is based on maximizing the precision of the velocity measurements, taking into account the constraint imposed by the minimum range of measurable velocities, which is one of the measurement requirements. This method has been applied to the systems under analysis and has served to optimize, in each case, the frequency response and the cavity length of the interferometer. Further analyses of the performance of the systems have been carried out using the configuration first calculated with this method.

In the case of the continuous-wave velocimeter (section 5.2), the expected uncertainty, calculated for different measuring conditions, has been used in the second part of the thesis for evaluating the performance of the laboratory prototype and hence for validating the

effectiveness, in an edge-technique-based Doppler lidar, of some of the main components and subsystems that will eventually be part of the *UPC* atmospheric system.

The estimation of the performance of a Doppler wind lidar like the one planned in the *UPC* project, also under different measuring conditions (defined basically by standard aerosol atmospheric profiles), has permitted to anticipate some of its characteristics as wind measuring system (section 5.3). First, as expected, the lidar under analysis provides precise measurements only in zones with high aerosol content. Under these conditions, the estimated performance is comparable to other aerosol-based instruments using direct detection and, also as expected, worse than the one provided by coherent systems. In all the cases, uncertainty can be enhanced by means of sample averaging, hence by reducing time and range resolution. All three parameters –uncertainty, time resolution and range resolution– have been therefore considered when analyzing the results and comparing with the performance of other systems.

The effect of Rayleigh (molecular) contamination on aerosol-based wind velocity measurements has been studied in detail too. Two different effects can be identified and have been considered. In the first place, in an edge-technique-based system relying on aerosol return the Rayleigh component acts as background noise that impairs the precision of the measurements. This effect, however, has been shown not to be significant in a system like the one proposed here in most of typical measuring conditions (section 5.3.3.4). Secondly, the molecular component induces a bias error in the velocity determination that reduces the accuracy of the measurements. This happens because the filter frequency response to this component is not the same than the one to the aerosol component, which is the one taken as reference to measure the Doppler shift. This effect has been calculated for different measurement scenarios and, as a conclusion, it has been stated that it should be removed or reduced even in atmospheric regions with high aerosol content (section 0). A possible solution to this problem including a second filter to discriminate the Rayleigh component in the return signal has been presented (section 4.4.3) and its performance estimated (section 5.3.5) also in the first part of this dissertation.

The second part of the thesis (chapters 6 and 7) deals with the practical assessment of an edge-technique-based laboratory prototype using continuous-wave radiation. Many of the elements that will also be part of the atmospheric system have been used in the prototype, their operation has been tested and their effectiveness demonstrated: in the optical set-up, those devoted to guide, combine and condition the light beams and, in the electrical part, the detectors, the receivers and the acquisition board. The Fabry-Perot interferometer that will eventually be used in the atmospheric wind lidar has been characterized in detail and, although the processed signals are not exactly the same –the atmospheric signals will be pulsed–, its capability to discriminate frequencies has been assessed (section 7.1). The tuning control loop to compensate the relative frequency drifts between the response of the interferometer and the laser has been also successfully implemented, its need has been confirmed and its behavior has been carefully characterized (section 7.3). Finally, the routines for the system calibration, the acquisition and processing of the signals and the filter tuning control (section 6.6) have been programmed and applied to obtain valid velocity measurements.

The velocity measurements performed with the laboratory velocimeter have been analyzed in detail (section 7.4). The obtained precision shows very good agreement with the expected performance calculated in the first part of this work. Accuracy is more difficult to characterize than precision because most of systematic errors are due to tolerances in the implementation of the technique or during the realization of the measurements and in most of cases do not depend on system parameters. However, it can be said that the accuracy of the

velocity measurements provided by the prototype is good as well (in general, under 0.5 m/s). Possible sources of error and possible solutions have also been identified.

Besides the confirmed capability of the elements and subsystems used in the prototype, some practical conclusions that will be useful when implementing the Doppler wind lidar can be derived from these results. It has been observed that mechanical vibrations affect the stability of the mirrors and produce fast fluctuations of the frequency response. These fluctuations produce noise in the measuring process and a loss of precision in the velocity determination even in high SNR conditions. Thermal instability, in both the laser and the interferometer, provoke, in turn, displacements of the location of the laser frequency on the filter slope that reduce the precision and can make impossible velocity measurements. These displacements, however, are compensated by the tuning control loop. Furthermore, combined thermal and mechanical instabilities produce a progressive degradation of the interferometer mirror parallelism and, as a result, a decrease of the resolving power of the filter response. This degradation obliges to readjust and calibrate the laboratory prototype every ten minutes. This would result clearly impractical in an operative instrument dedicated to monitor the speed of wind and must be corrected. The first approach should be achieving a better thermal and mechanical isolation of the interferometer. Also, the use of less flexible, more stable cavities such as optically-contacted, piezo-tunable Fabry-Perot etalons [27] or, fixed-gap resonators, tunable by controlling the temperature [8] or the pressure [26] within the cavity, should be considered in the future.

8.2 Further work

8.2.1 Implementation of an edge-technique-based Doppler wind lidar

Further activities related to this thesis are mainly linked to the implementation of the planned edge-technique-based *UPC* Doppler wind lidar, whose analysis and design has been carried out in the first part of this work and whose feasibility has been tested with the continuous-wave laboratory prototype.

The main differences and challenges associated to a first approach of such a system can be identified:

- The transmitter will be the single-mode injection-seeded Nd:YAG pulsed-laser whose seeder has been used as the continuous-wave source in the laboratory prototype.
- A telescope, with a diameter typically between 20 and 40 cm, should be used as reception optics.
- Enabling both measuring channels –reference (at the emitted frequency) and Doppler (at the received frequency)– will require also a different solution. In the laboratory prototype, with continuous-wave radiation, an optical chopper is used to alternate them, while in the atmospheric, pulsed system, a sample of the emitted pulse has to be reintroduced in the telescope (Fig. 11, in section 4). The separation between this sample and the return signal when processing the detected signals will be performed with a proper temporal analysis.
- The receiving electronics and the acquisition board have to be adapted to the sampling rate needed for acquiring atmospheric signals with the required range resolution.
- Although the Fabry-Perot interferometer will be the same than the one used in the continuous-wave velocimeter, its configuration has to be different to have in account the

pulsed nature of the signals and the consequent different resulting frequency response (section 4.3).

- The calibration, processing and control routines have also to be adapted to the characteristics of the atmospheric signals. A special challenge is the design of the calibration procedures. The frequency response that must be recorded and used during this phase to perform the intensity-to-frequency conversion is the one corresponding to pulsed light, and its calibration is more complicated than in the continuous-wave case. The calibration usually starts in edge-technique Doppler wind lidars by sampling a portion of the emitted pulses to illuminate the interferometer. Then, some type of scanning procedure between the laser spectrum and the transmission curve of the filter has to be done in order to sample, usually with low resolution, the frequency response. Finally, fitting techniques have to be used to obtain the complete calibration curve [2].

- As seen in section 0, some kind of solution must also be implemented for avoiding the bias error induced by the background Rayleigh contamination on aerosol-based measurements. The approach described and analyzed in section 0 requires another filter – that could be also a Fabry-Perot– to be used for discriminating the molecular and aerosol components in the return signal.

8.2.2 Implementation of a double-edge-technique-based Doppler wind lidar

Another approach that is worth to consider, analyze and probably implement in the future is a more sophisticated and sensitive variation of the edge-technique: the double-edge-technique [5], which permits, using an iterative scheme in the retrieval of the velocity, to avoid as well the bias error produced by the molecular return. In this technique two filters are also necessary, which must be tuned to locate their opposite slopes symmetrically with respect to the emitted frequency (Fig. 2 (right)).

Using this scheme, Doppler shifts produce an increase of transmitted intensity in one filter and simultaneously a decrease in the second one, so improving the sensitivity of the measuring system. In most of operative applications of this method the two required filters are implemented using a mirror divided in two semicircular areas with slightly different cavity lengths.

This approach has been considered, since the beginning of the project, as a further, enhanced approach that would eventually be taken in account after implementing a simpler, cheaper and technologically less demanding edge-technique-based instrument. One of the key points that leads to consider the double-edge-technique more demanding and costly than the edge-technique is the need of a second filter. However, as it has been shown in section 0, edge-technique Doppler wind lidars require as well a second filter for removing the effect of molecular contamination. It could be therefore reasonable to use directly the double-edge approach to build the atmospheric system. This issue has to be analyzed and discussed in detail before making the choice.

8.2.3 Rayleigh-based measurements

Although direct-detection Doppler wind lidars are less sensitive than coherent systems when performing aerosol-based measurements, they have some advantages; one of them is the flexibility to adapt their configuration to molecular measurements. The main modifications that should be introduced respect to an aerosol-based system are summarized bellow.

- Because the λ^{-4} dependence of the atmospheric Rayleigh scattering, systems relying on molecular return operate advantageously at shorter wavelengths. Double (532 nm) or triple (355 nm) harmonics of the Nd:YAG laser have to be employed therefore for efficient molecular-based operation.
- The atmosphere constituents are subject to random motion and collisions resulting in a significant broadening of the spectrum of the Rayleigh scattering. The filters used in edge-technique or double-edge-technique have to be adapted to this feature, requiring significantly wider responses and greater free spectral range. The free spectral range can be easily configured in our Fabry-Perot interferometer by adjusting the cavity length, while increasing the band-pass width would require using less reflective mirrors for reducing the finesse.
- At 532 nm and 355 nm, photo-multiplier-tubes (PMT), with higher quantum efficiency, can be used as photo-detectors.
- Calibration in molecular systems is more complicated than in aerosol ones because, [3]besides measuring the response to pulsed signals, an accurate estimation of the thermal-motion-induced broadening is required to calculate the frequency response of the filter to the Rayleigh return. The shape of this spectrum depends on the temperature and the pressure within the sensing volume and therefore, estimations of these atmospheric parameters must be made. The accuracy requirements in the estimation of the pressure are not very strict and standard profiles can satisfactorily be used; this is not the case of the temperature, which may be needed with an accuracy of 1 or 2 K for typical measurement specifications. This makes it indispensable to use numerical weather prediction systems in the calibration procedures [38].
- The presence of an aerosol component on the return signal would produce also a bias error on the velocity determination in edge-technique or double-edge-technique systems relying on molecular return [50], [65]. The standard solution used in Double-Edge-Technique-based molecular systems to desensitize measurements from Mie contamination is based on minimizing its effect by accurately designing the spectral features of the filters (the spectral gap between filters and their bandwidth). This approach is not possible with the edge-technique, which is only applicable for molecular-based measurements in aerosol-free conditions. A prospective development to perform Rayleigh-based measurements should therefore use the double-edge solution.

List of symbols, acronyms and abbreviations

Latin symbols

a	Radius of the receiving telescope $[\mathrm{m}]$.
A_c, A_r, A_s	Coherence area over the telescope, receiving area of the telescope and illuminated area at a distance R $[\mathrm{m}^2]$.
B	Equivalent noise bandwidth of the receiver [Hz].
B_τ	Spectral width of the return $[\mathrm{Hz}]$.
c	Speed of light in the vacuum $[\mathrm{m\,s^{-1}}]$.
$\tilde{c}(x,y,t)$	Circular random process.
d	Cavity length of a Fabry-Perot interferometer $[\mathrm{m}]$.
D_1, D_2	Diameter of the lenses of the reducer – collimator $[\mathrm{m}]$.
E_T	Energy of the emitted pulse $[\mathrm{J}]$.
F	Finesse of a Fabry-Perot interferometer.
F_{en}	Excess noise factor of a photo-detector
F_R, F_{eff}	Reflectivity finesse and Effective finesse of a Fabry-Perot interferometer.
$f(\nu)$	Continuous-wave transmission function of the optical filter.
f_0	Frequency distance between the resonance peak of the filter and the location of the emitted frequency $[\mathrm{Hz}]$.
f_1, f_2	Focal length of the lenses of the reducer – collimator $[\mathrm{m}]$.
f_D	Doppler frequency shift $[\mathrm{Hz}]$.
f_S	Sampling rate $[\mathrm{s^{-1}}]$.
$F(\nu)$	Frequency response of the optical filter.
$F_{\max}$	Maximum transmission of the filter.
$F_M(\nu)$, $F_R(\nu)$	Frequency response of the filter for Mie and Rayleigh signals.
$F_\mathrm{v}(v_r)$	Filter response of the filter as a function of the measured radial velocity.
h	Altitude $[\mathrm{m}]$.
$h(\nu)$	Energy-normalized spectrum of the incident signal.

h_0	Reference altitude: 8000 m.
$h_L(\nu)$, $h_R(\nu)$	Energy-normalized energy spectrum of the laser emitted pulse and the Rayleigh return.
$h_{R-CW}(\nu)$	Spectrum of the Rayleigh return for continuous-wave illumination.
i_{DK}	Bulk dark current of a photo-detector before multiplication $[\mathrm{A}]$.
i_{IEN}	Input-referred equivalent noise current generated in the receiver circuitry $[\mathrm{A\,Hz^{-1/2}}]$.
i_{PD}	Signal photocurrent in the photo-detector $[\mathrm{A}]$.
$\tilde{I}(x,y,0,t)$	Optical intensity over the received area $[\mathrm{W\,m^{-2}}]$
$J_{\lambda/4}$, J_{RS}	Jones matrix of a quarter-wave plate and of an ideal non-polarizing reflecting surface.
J_T, J_{BL}, J_R	Jones vector of the transmitted, backscattered and received light in the transmitting – receiving assembly.
k	Boltzmann's constant: $k = 1.38\times10^{-23}\ \mathrm{J\,K^{-1}}$; wave number [rad/m] (Chapter 3); Splitting ratio of the beam-splitter *BS3* (Chapter 7).
L	Distance between lenses in the reducer – collimator $[\mathrm{m}]$.
L_1, L_2, L_3	Distance between elements in the transmitting – receiving assembly $[\mathrm{m}]$.
$L_R(R)$, $L_M(R)$	Rayleigh and Mie lidar ratio $[\mathrm{sr}]$.
m_{am}	Air molecule mass (4.8×10^{-26} kg).
M	Multiplication factor of a photo-detector.
$n(R)$	Scatterers number concentration $[\mathrm{m^{-3}}]$.
N_{V_R}	Number of scatterers in the volume V_R.
$P(R)$	Instant incident optical power onto the telescope $[\mathrm{W}]$.
P_{BG}	Background optical power $[\mathrm{W}]$.
P_{in}	Incident optical power $[\mathrm{W}]$.
P_M, P_R	Mie and Rayleigh components of the collected power $[\mathrm{W}]$.
P_S	Incident optical power onto the photo-detector $[\mathrm{W}]$.
P_{ref}, P_{Dop}	Incident optical power from the reference and the Doppler channels $[\mathrm{W}]$.
P_T	Average power of the transmitted pulse $[\mathrm{W}]$.
q	Electron charge (1.6021765×10^{-19} $[\mathrm{C}]$).

R	Distance from the lidar to the atmospheric layer contributing to the received field at instant time t $[\mathrm{m}]$.
R_0	Responsivity of a photo-detector without multiplication $[\mathrm{A\,W^{-1}}]$.
$\vec{R}_{Ri}$	Vector between each point at the entrance pupil of the telescope to the scatterer position $[\mathrm{m}]$.
$\vec{R}_{Ti}$	Position vector of an individual scatterer $[\mathrm{m}]$.
$s\,(t)$	Function describing the temporal envelope of the transmitted field.
S_1, S_2	Detected signals in detectors 1 and 2 $[\mathrm{V}]$.
t	Time elapsed since pulse emission $[\mathrm{s}]$.
T	Temperature $[\mathrm{K}]$.
$\tilde{U}(x,y,0,t)$	Total normalized incident field on every point of the telescope receiving area $[\mathrm{W^{1/2}\,m^{-1}}]$.
$U_i(x,y,0,t)$	Normalized incident field on each point of the telescope receiving area from the scatterer 'i' $[\mathrm{W^{1/2}\,m^{-1}}]$.
$U_T(x,y,z,t)$	Normalized transmitted electric field $[\mathrm{W^{1/2}\,m^{-1}}]$
V_1, V_2	Detected voltages $[\mathrm{V}]$
V_{ch}	Synchronization voltage of the optical chopper $[\mathrm{V}]$.
V_R	Illuminated volume at a distance R $[\mathrm{m^3}]$.
$\vec{v}_i$	Velocity of the scatterer 'i' with respect the position of the lidar $[\mathrm{m\,s^{-1}}]$.
v_l	Linear velocity of the rotating disc $[\mathrm{m\,s^{-1}}]$.
v_m	Radial velocity measured with the laboratory velocimeter $[\mathrm{m\,s^{-1}}]$.
v_r	Radial velocity: Velocity in the line-of-sight direction $[\mathrm{m\,s^{-1}}]$.
v_{Ri}	Velocity component of the scatterer 'i' in the direction between each point on the receiving area and the position of the scatterer $[\mathrm{m\,s^{-1}}]$.
v_{ri}	Radial component of the velocity of the scatterer 'i' $[\mathrm{m\,s^{-1}}]$.
v_{Ti}	Velocity component of the scatterer 'i' in the direction given by its position vector $[\mathrm{m\,s^{-1}}]$.

W_1, W_2	Diameter of the spot on lenses 1 and 2 in the transmitting – receiving assembly $[\mathrm{m}]$.
x, y, z	Position coordinates $[\mathrm{m}]$.

Greek Symbols

$\alpha(z)$	Extinction coefficient along the propagation path $[\mathrm{m^{-1}}]$.
α_1, α_2, α_3	System constants $[\mathrm{V\,W^{-1}}]$.
$\alpha_M(z)$, $\alpha_R(z)$	Mie and Rayleigh extinction coefficients $[\mathrm{m^{-1}}]$.
$\beta(R)$	Atmospheric volume backscatter coefficient at a distance R $[\mathrm{m^{-1}\,sr^{-1}}]$.
$\beta_R(\lambda, h)$	Rayleigh volume backscatter coefficient $[\mathrm{m^{-1}\,sr^{-1}}]$.
$\beta_M(\lambda, h)$	Mie volume backscatter coefficient $[\mathrm{m^{-1}\,sr^{-1}}]$.
$\delta F_M(\nu)$	Bias in the measurement of the frequency response.
$\delta\nu$	Bias in the determination of the received frequency $[\mathrm{Hz}]$.
Δf	Frequency interval corresponding to one sampling period during the acquisition of the frequency response $[\mathrm{Hz}]$.
ΔF	Change in the filter transmission.
ΔR, Δh	Range and altitude resolution $[\mathrm{m}]$.
ΔT	Time resolution $[\mathrm{s}]$.
Δz	Thickness of the atmospheric layer contributing to the received field at instant time t $[\mathrm{m}]$.
$\Delta\nu_\mathrm{L}$, $\Delta\nu_\mathrm{M}$, $\Delta\nu_\mathrm{R}$	Spectral width of the emitted pulse, the Mie and the Rayleigh returns $[\mathrm{Hz}]$
$\Delta\nu_\theta$	Frequency variation associated to incident angular variation to the Fabry-Perot interferometer $[\mathrm{Hz}]$.
$\Delta\nu_\mathrm{U}$	Uncertainty-based velocity range $[\mathrm{m\,s^{-1}}]$.
$\Delta\Omega$	Solid angle from the scatterers to the receiving area $[\mathrm{sr}]$.
$\varepsilon\left[F_\mathrm{v}(v_r)\right]$	Uncertainty in the measurement of the frequency response for a detected radial velocity v_r.

$\varepsilon(v_r)$	Uncertainty in the velocity determination for a detected velocity v_r $\left[\mathrm{m\,s^{-1}}\right]$.
$\langle\varepsilon\rangle_{2\Delta v_U}$	Uncertainty averaged along the velocity range $\left[\mathrm{m\,s^{-1}}\right]$.
ϕ_i	Phase of the field reflection coefficient of the scatterer 'i' $\left[\mathrm{rad}\right]$.
$\tilde{\eta}(x,y,t)$	Exponential random process: Square of the Rayleigh random process $\tilde{\mu}(x,y,t)$.
φ	Round trip phase shift in a resonant cavity $\left[\mathrm{rad}\right]$
λ	Wavelength $\left[\mathrm{m}\right]$.
λ_0	Emitted wavelength $\left[\mathrm{m}\right]$.
$\tilde{\mu}(x,y,t)$	Rayleigh random process: Magnitude of the circular random process $\tilde{c}(x,y,t)$.
ν	Optical frequency $\left[\mathrm{Hz}\right]$
ν_0	Emitted frequency $\left[\mathrm{Hz}\right]$.
ν_{in}	Frequency of the incident radiation $\left[\mathrm{Hz}\right]$.
ν_{LO}	Local oscillator frequency in the coherent receiver $\left[\mathrm{Hz}\right]$.
θ	Incidence angle on the etalon [rad].
$\theta(\nu)$	Sensitivity to velocity changes as a function of the received frequency $\left[\mathrm{m^{-1}\,s}\right]$.
$\tilde{\theta}(x,y,t)$	Uniformly-distributed random process: Angle of the circular random process $\tilde{c}(x,y,t)$.
θ_{e}	Elevation angle $\left[\mathrm{rad}\right]$.
θ_{D}	Half divergence angle of the emitted beam $\left[\mathrm{rad}\right]$.
θ_{I}	Incidence angle onto the rotating disc $\left[\mathrm{rad}\right]$.
$\theta_{\mathrm{V}}(v_r)$	Sensitivity to velocity changes as a function of the detected velocity $\left[\mathrm{m^{-1}\,s}\right]$.
ρ	Reflectivity of the mirrors in a Fabry-Perot interferometer.
$\vec{\rho}$	Position vector of a point on the entrance pupil of the receiving telescope $\left[\mathrm{m}\right]$
σ_{bi}	Cross-section per solid angle of the scatterer 'i' in the direction of the telescope (backscatter direction) $\left[\mathrm{m^2\,sr^{-1}}\right]$

σ_{PD}	Standard deviation of the signal photocurrent in the photodetector $[\mathrm{A}]$.
σ_{FR}	Uncertainty in the velocity determination due to random fluctuations of the Frequency response $[\mathrm{m\,s^{-1}}]$.
σ_{PI}, σ_{SR}	Uncertainty in the velocity determination due to the point-of-impact dependence of the frequency response and the splitting ratio of *BS3* $[\mathrm{m\,s^{-1}}]$.
σ_{PR}	Uncertainty in the velocity determination due to the photoreceiver noise $[\mathrm{m\,s^{-1}}]$.
σ_{O}	Overall uncertainty in the velocity determination $[\mathrm{m\,s^{-1}}]$.
σ_{F}	Standard deviation of the measured finesse.
$\sigma_{F(\Delta f)}$, $\sigma_{F(FR)}$	Standard deviation of the measured finesse due to frequency sampling noise and to random fluctuations of the frequency response.
τ_{p}	Nominal pulse duration $[\mathrm{s}]$.
ω	Angular speed of the rotating disc $[\mathrm{rad\ s^{-1}}]$.

Acronyms and abbreviations

ADM	Atmospheric Dynamics Mission.
AF	Averaging factor: number of accumulated samples.
ASR	Aerosol scattering ratio.
APD	Avalanche photo-diode.
BS1, BS2, BS3	Beam-splitters 1, 2 and 3 in the laboratory prototype.
CO_2	Carbon dioxide.
CW	Continuous-wave.
FS	Frequency shifter.
FSR	Free Spectral Range $[\mathrm{Hz}]$.
FWHM	Full-width half-maximum $[\mathrm{Hz}]$.
GTWS-SDT	Global Tropospheric Wind Sounder Science Definition Team.
HDWL	Hybrid Doppler Wind Lidar.
HWHM	Half-width half-maximum $[\mathrm{Hz}]$.
lidar	Light detection and ranging.

LIWAS	Lidar Windshear Alerting System.
MOPA	Master oscillator / power amplifier architecture.
NASA	National Aeronautics and Space Administration.
Nd:Yag	Neodymium-doped Yttrium Aluminum Garnet.
NOAA	National Oceanic and Atmospheric Administration.
N_2	Nitrogen.
O_2	Oxigen.
PRF	Pulse repetition frequency $[\mathrm{Hz}]$.
radar	Radio detection and ranging.
SNR	Signal-to-noise ratio in the measurement of the response.
TEA	Transverse excited atmospheric technology.
Tm:YAG	Thulium-doped Yttrium Aluminium Garnet.
Tm,Ho:YAG	Thulium-Holmium-doped Yttrium Aluminium Garnet.
UPC	Universtitat Politècnica de Catalunya – BARCELONA**TECH.**
US	United States.

References

[1] R. T. Menzies and R. M. Hardesty, "Coherent Doppler lidar for measurements of wind fields," *Proceedings of the IEEE,* vol. 77, pp. 449-462, 1989.

[2] C. L. Korb, B. M. Gentry and C. Y. Weng, "Edge technique: theory and application to the lidar measurement of atmospheric wind," *Appl. Opt.,* vol. 31, pp. 4202-4213, 1992.

[3] M. L. Chanin, A. Garnier, A. Hauchecorne and J. Porteneuve, "A Doppler lidar for measuring winds in the middle atmosphere," *Geophysical Research Letters,* vol. 16, pp. 1273-1276, 1989.

[4] V. J. Abreu, "Wind measurements from an orbital platform using a lidar system with incoherent detection: an analysis," *Appl. Opt.,* vol. 18, pp. 2992-2997, 1979.

[5] C. L. Korb, B. M. Gentry, S. X. Li and C. Flesia, "Theory of the Double-Edge Technique for Doppler Lidar Wind Measurement," *Appl. Opt.,* vol. 37, pp. 3097-3104, 1998.

[6] S. F. Clifford, J. C. Kaimal, R. J. Lataitis and R. G. Strauch, "Ground-based remote profiling in atmospheric studies: an overview," *Proceedings of the IEEE,* vol. 82, pp. 313-355, 1994.

[7] P. Hays, M. Dehring, L. Fisk, P. Tchoryk, I. Dors, J. Ryan, J. Wang, M. Hardesty and B. Gentry. Space-based doppler winds LIDAR: A vital national need. 2005.

[8] P. Ingmann, E. Anderson, A. Dabas, M. Endemann, E. Kallen, D. Offiler and A. Stoffelen, "SP-1311, 'ADM-aeolus' april 2008," ESA Communication Production Office, 2200 AG Noordwijk. The Netherlands, Tech. Rep. SP-1311, 2008.

[9] R. Atlas and G. D. Emitt, "Review of Observing System Simulation Experiments to Evaluate the Potential Impact of Lidar Winds on Numerical Weather Prediction," *Reviewed and Revised Papers Presented at the 24th International Laser Radar Conference,* vol. II, pp. 726-729, 2008.

[10] S. Rahm, "Precursor experiment for an active true airspeed sensor," *Opt. Lett.,* vol. 26, pp. 319-321, 03/15, 2001.

[11] A. Dolfi-Bouteyre, G. Canat, M. Valla, B. Augere, C. Besson, D. Goular, L. Lombard, J. -. Cariou, A. Durecu, D. Fleury, L. Bricteux, S. Brousmiche, S. Lugan and B. Macq, "Pulsed 1.5-µm LIDAR for Axial Aircraft Wake Vortex Detection Based on High-Brightness Large-Core Fiber Amplifier," *IEEE Journal of Selected Topics in Quantum Electronics,* vol. 15, pp. 441-450, 2009.

[12] A. Peña, C. B. Hasager, S. Gryning, M. Courtney, I. Antoniou and T. Mikkelsen, "Offshore wind profiling using light detection and ranging measurements," *Wind Energy,* vol. 12, pp. 105-124, 2009.

[13] F. Bingöl, J. Mann and G. C. Larsen, "Light detection and ranging measurements of wake dynamics part I: one-dimensional scanning," *Wind Energy,* vol. 13, pp. 51-61, 2010.

[14] Y. Yeh and H. Z. Cummins, "Localized fluid flow measurements with an HeNe laser spectrometer," *Appl. Phys. Lett.,* vol. 4, pp. 176-178, 1964.

[15] J. Foreman J.W., E. W. George and R. D. Lewis, "Measurement of localized flow velocities in gases with a laser doppler flowmeter," *Appl. Phys. Lett.,* vol. 7, pp. 77-78, 1965.

[16] W. Foreman and R. M. Huffaker, "Development of a laser Doppler flowmeter for gas velocity measurement," *Aero-Astrodynamics Research Review no. 3. NASA T M X-53389,* pp. 66-71, 1965.

[17] A. V. Jelalian and R. M. Huffaker, "Application of Laser Doppler Techniques to Turbulent Velocity Measurements. Part II. Laser Doppler Techniques for Remote Wind Velocity Measurements," *Specialits Conference on Molecular Radiation and its Application to Diagnostic Techniques, NASA TM X-53711,* pp. 345-356, 1967.

[18] R. M. Huffaker and R. M. Hardesty, "Remote sensing of atmospheric wind velocities using solid-state and CO_2 coherent laser systems," *Proceedings of the IEEE,* vol. 84, pp. 181-204, 1996.

[19] J. W. Bilbro, C. DiMarzio, D. Fitzjarrald, S. Johnson and W. Jones, "Airborne Doppler lidar measurements," *Appl. Opt.,* vol. 25, pp. 3952-3960, 1986.

[20] T. J. Kane, W. J. Kozlovsky, R. L. Byer and C. E. Byvik, "Coherent laser radar at 1.06 μm using Nd:YAG lasers," *Opt. Lett.,* vol. 12, pp. 239-241, 1987.

[21] S. W. Henderson, C. P. Hale, J. R. Magee, M. J. Kavaya and A. V. Huffaker, "Eye-safe coherent laser radar system at 2.1 μm using Tm,Ho:YAG lasers," *Opt. Lett.,* vol. 16, pp. 773-775, 1991.

[22] R. Targ, B. C. Steakley, J. G. Hawley, L. L. Ames, P. Forney, D. Swanson, R. Stone, R. G. Otto, V. Zarifis, P. Brockman, R. S. Calloway, S. H. Klein and P. A. Robinson, "Coherent lidar airborne wind sensor II: flight-test results at 2 and 10 μm," *Appl. Opt.,* vol. 35, pp. 7117-7127, 1996.

[23] J. Cariou, M. Valla and G. Canat, "Fiber lasers: new effective sources for coherent lidars," *Lidar Technologies, Techniques, and Measurements for Atmospheric Remote Sensing III. Proc.SPIE,* vol. 6750, pp. 675007-1-675007-12, 2007.

[24] G. Benedetti-Michelangeli, F. Congeduti and G. Fiocco, "Measurement of Aerosol Motion and Wind Velocity in the Lower Troposphere by Doppler Optical Radar," *J. Atmos. Sci.,* vol. 29, pp. 906-910, 1972.

[25] M. J. McGill, W. R. Skinner and T. D. Irgang, "Analysis techniques for the recovery of winds and backscatter coefficients from a multiple-channel incoherent Doppler lidar," *Appl. Opt.,* vol. 36, pp. 1253-1268, 1997.

[26] C. Souprayen, A. Garnier, A. Hertzog, A. Hauchecorne and J. Porteneuve, "Rayleigh-Mie Doppler wind lidar for atmospheric measurements. I. Instrumental setup, validation, and first climatological results," *Appl. Opt.,* vol. 38, pp. 2410-2421, 1999.

[27] B. M. Gentry, H. Chen and S. X. Li, "Wind measurements with 355-nm molecular Doppler lidar," *Opt. Lett.,* vol. 25, pp. 1231-1233, 2000.

[28] M. T. Dehring, C. A. Nardell, J. C. Pavlich, P. B. Hays and I. Dors, "Performance and comparison of 532-nm and 355-nm groundwinds lidars," *Lidar Remote Sensing for Industry and Environment Monitoring III. Proc.SPIE,* vol. 4893, pp. 337-347, 2003.

[29] D. Morancais, F. Fabre, M. Endemann and A. Culoma, "ALADIN doppler wind lidar: recent advances," *Lidar Technologies, Techniques, and Measurements for Atmospheric Remote Sensing III. Proc.SPIE,* vol. 6750, pp. 675014-1-675014-12, 2007.

[30] W. Baker, M. Hardesty, R. Atlas, A. Clement, G. D. Emmitt, R. Fulton, B. Gentry, R. Katar, M. Kavaya, S. Mango, K. Miller, D. Pawlak, J. Pereira and J. Yoe, "Wind profiles – the missing link in the global observing system," August, 17, 2006. 2006.

[31] A. V. Jelalian, *Laser Radar Systems.* Norwood MA (USA): Artech House, 1992.

[32] M. J. Post, "Development of coherent laser radar," *International Geoscience and Remote Sensing Symposium, 1994. IGARSS '94. Surface and Atmospheric Remote Sensing: Technologies, Data Analysis and Interpretation,* vol. 2, pp. 923-925, 1994.

[33] A. Rodríguez-Gómez, "Sistemas lidar coherentes e incoherentes de baja potencia para la detección de velocidad de blancos sólidos," Octubre, 1998, 1998.

[34] Z. S. Liu, W. B. Chen, T. L. Zhang, J. W. Hair and C. Y. She, "An incoherent Doppler lidar for ground-based atmospheric wind profiling," *Appl. Phy. B,* vol. 64, pp. 561-566, 1997.

[35] J. M. Vaughan, *The Fabry-Perot Interferometer. History, Theory, Practice and Applications.* Taylor & Francis, 1989.

[36] F. Congeduti, G. Fiocco, A. Adriani and C. Guarrella, "Vertical wind velocity measurements by a Doppler lidar and comparisons with a Doppler sodar," *Appl. Opt.,* vol. 20, pp. 2048-2054, 1981.

[37] C. Weitkamp, *Lidar :Range-Resolved Optical Remote Sensing of the Atmosphere.* New York: Springer, 2005.

[38] A. Dabas, M. L. Denneulin, P. Flamant, C. Loth, A. Garnier and A. Dolfi-Bouteyre, "Correcting winds measured with a Rayleigh Doppler lidar from pressure and temperature effects," *Tellus Series A,* vol. 60, pp. 206-215, 2008.

[39] J. Mendrok, "The SARTre Model for Radiative Transfer in Spherical Atmospheres and its Application to the Derivation of Cirrus Cloud Properties," pp. 1-147, 2006.

[40] M. Nelkin and S. Yip, "Brillouin Scattering by Gases as a Test of the Boltzmann Equation," *Phys. Fluids,* vol. 9, pp. 380-381, 1966.

[41] G. Tenti, C. D. Boley and R. C. Desai, "On the Kinetic Model Description of Rayleigh-Brillouin Scattering from Molecular Gases," *Can. J. Phys.,* vol. 52, pp. 285-290, 1974.

[42] X. Pan, M. N. Shneider and R. B. Miles, "Coherent Rayleigh-Brillouin scattering in molecular gases," *Phys. Rev. A,* vol. 69, pp. 033814, 2004.

[43] A. Comerón Tejero, C. Muñoz Porcar, F. Rocadenbosch Burillo, A. Rodríguez Gómez, M. Sicard and S. Tomás Martínez, "Lidar measurements of wind velocity fields," in *Recent Advances in Atmospheric Lidar*Anonymous Bucharest-Magurele: Editura INOE, pp. 239-334.

[44] J. M. Vaughan, "Scattering in the atmosphere," in , P. C. Sabatier and E. R. Pike, Eds. San Diego CA: Academic Press, 2002, pp. 937-957.

[45] M. E. Thomas and D. D. Duncan, "Atmospheric transmission," in *The Infrared and Electro-Optical Systems Handbook Vol 2. Atmospheric Propagation of Radiation*, F. G. Smith, Ed. Bellingham, Washington 98227-0010: SPIE Optical Engineering Press, 1993, pp. 3-156.

[46] V. Srivastava, J. Rothermel, A. D. Clarke, J. D. Spinhirne, R. T. Menzies, D. R. Cutten, M. A. Jarzembski, D. A. Bowdle and E. W. McCaul, "Wavelength Dependence of Backscatter by use of Aerosol Microphysics and Lidar Data Sets: Application to 2.1- ?m Wavelength for Space-Based and Airborne Lidars," *Appl. Opt.,* vol. 40, pp. 4759-4769, 09/20, 2001.

[47] J. W. Goodman, *Statistical Optics.* New York: Wiley, 1985.

[48] B. J. Rye, "The spectral correlation of atmospheric lidar returns with range-dependent backscatter," *J. Opt. Soc. Am. A,* vol. 7, pp. 2199-2207, 1990.

[49] M. Imaki and T. Kobayashi, "Ultraviolet high-spectral-resolution Doppler lidar for measuring wind field and aerosol optical properties," *Appl. Opt.,* vol. 44, pp. 6023-6030, 2005.

[50] C. Flesia and C. L. Korb, "Theory of the Double-Edge Molecular Technique for Doppler Lidar Wind Measurement," *Appl. Opt.,* vol. 38, pp. 432-440, 1999.

[51] H. Xia, D. Sun, Y. Yang, F. Shen, J. Dong and T. Kobayashi, "Fabry-Perot interferometer based Mie Doppler lidar for low tropospheric wind observation," *Appl. Opt.,* vol. 46, pp. 7120-7131, 2007.

[52] C. L. Korb, B. M. Gentry and S. X. Li, "Edge technique Doppler lidar wind measurements with high vertical resolution," *Appl. Opt.,* vol. 36, pp. 5976-5983, 1997.

[53] Z. Liu, D. Wu, J. Liu, K. Zhang, W. Chen, X. Song, J. W. Hair and C. She, "Low-Altitude Atmospheric Wind Measurement from the Combined Mie and Rayleigh Backscattering by Doppler Lidar with an Iodine Filter," *Appl. Opt.,* vol. 41, pp. 7079-7086, 2002.

[54] D. Bruneau, A. Garnier, A. Hertzog and J. Porteneuve, "Wind-Velocity Lidar Measurements by Use of a Mach-Zehnder Interferometer, Comparison with a Fabry-Perot Interferometer," *Appl. Opt.,* vol. 43, pp. 173-182, 01/01, 2004.

[55] S. D., Z. Z., Z. J., H. H. and K. T., "Accuracy Analysis of the Fabry Perot Etalon Based Doppler Wind Lidar," *Optical Review,* vol. 12, pp. 409-414, 2005.

[56] S. M. Sze and K. K. Ng, *Physics of Semiconductor Devices.* Wiley-Interscience, 2006.

[57] Z. S. Liu, B. Y. Liu, Z. G. Li, Z. A. Yan, S. H. Wu and Z. B. Sun, "Wind measurements with incoherent Doppler lidar based on iodine filters at night and day," *Appl. Phy. B,* vol. 88, pp. 327-335, 2007.

[58] A. Ansmann and D. Müller, "Lidar and atmospheric aerosol particles," in *Lidar :Range-Resolved Optical Remote Sensing of the atmosphereLidar and Atmospheric Aerosol Particles*, C. Weitkamp, Ed. New York: Springer, 2005, pp. 104-141.

[59] S. W. Henderson, P. Gatt, D. Rees and R. M. Huffaker, "Wind lidar," in *Laser Remote Sensing*, T. Fujii and T. Fukuchi, Eds. Boca Raton, FL 33487-2742: CRC Press. Taylor & Francis Group, 2005, pp. 469-722.

[60] Z. Liu, B. Liu, S. Wu, Z. Li and Z. Wang, "High spatial and temporal resolution mobile incoherent Doppler lidar for sea surface wind measurements," *Opt. Lett.,* vol. 33, pp. 1485-1487, 2008.

[61] Z. Wang, Z. Liu, L. Liu, S. Wu, B. Liu, Z. Li and X. Chu, "Iodine-filter-based mobile Doppler lidar to make continuous and full-azimuth-scanned wind measurements: data acquisition and analysis system, data retrieval methods, and error analysis," *Appl. Opt.,* vol. 49, pp. 6960-6978, 12/20, 2010.

[62] C. M. Shun and P. W. Chan, "Applications of an Infrared Doppler Lidar in Detection of Wind Shear," *Journal of Atmospheric and Oceanic Technology,* vol. 25, pp. 637, 2008.

[63] B. M. Gentry and C. L. Korb, "Edge technique for high-accuracy Doppler velocimetry," *Appl. Opt.,* vol. 33, pp. 5770-5777, 1994.

[64] M. T. Herranz Barbed and A. Rodríguez Gómez, *Sistema De Monitorización De Velocidades.* 1998.

[65] C. Souprayen, A. Garnier and A. Hertzog, "Rayleigh?Mie Doppler wind lidar for atmospheric measurements. II. Mie scattering effect, theory, and calibration," *Appl. Opt.,* vol. 38, pp. 2422-2431, 1999.

List of publications

Journals

M Sicard, M Mallet, D García-Vizcaíno, A Comerón, F Rocadenbosch, P Dubuisson and **C Muñoz-Porcar** "Intense dust and extremely fresh biomass burning outbreak in Barcelona, Spain: Characterization of their optical properties and estimation of their direct radiative forcing". *Environmental Research Letters* Vol. 7 Number 3 pp 2-7 (2012) doi:10.1088/1748-9326/7/3/034016

Michaël Sicard; Mohd Nadzri Md. Reba; Sergio Tomas Martinez; Adolfo Comerón Tejero; Oscar Batet Torrell; **Constantino Muñoz Porcar**; Alejandro Antonio Rodriguez Gomez; Francisco Rocadenbosch Burillo; Casiana Muñoz Tuñón; Jesús Jiménez Fuensalida. "Results of site testing using an aerosol, backscatter lidar at the Roque de los Muchachos Observatory". *Monthly notices of the Royal Astronomical Society*. 405-1, pp 129-142 (2010).

Michaël Sicard, Adolfo Comerón, Francisco Rocadenbosch, Alejandro Rodríguez, **Constantino Muñoz**. "Quasi-analytical determination of noise-induced error limits in lidar retrieval of aerosol backscatter coefficient by the elastic two-component algorithm". *Applied Optics* vol. 48. pp 176-182 (2009).

Adolfo Comerón, Francesc Rocadenbosch, Miguel Angel López, Alejandro Rodríguez, **Constantino Muñoz**, David García-Vizcaíno, Michaël Sicard. "Effects of noise on lidar data inversion with the backward algorithm". *Applied Optics* vol. 43. pp 2572-2577 (2004).

Francisco Rocadenbosch Burillo; Michaël Sicard; Adolfo Comerón Tejero; Alejandro Antonio Rodriguez Gomez; **Constantino Muñoz Porcar**; MA López; David Garcia Vizcaino; R Agishev. "Remote sensing mediante LIDAR en la UPC". *Buran*, vol. 10, pp 21-27 (2003)

Book chapters

Adolfo Comerón Tejero; **Constantino Muñoz Porcar**; Francisco Rocadenbosch Burillo; Alejandro Antonio Rodriguez Gomez; Michaël Sicard; Sergio Tomas Martinez. "Lidar measurements of wind velocity fields". *Recent advances in atmospheric lidars*. pp. 239 - 334.(Romania): Editura INOE (2010). ISBN 978-973-88109-6-9.

International congresses

Sergio Tomas Martinez; **Constantino Muñoz Porcar**; Michaël Sicard; Francisco Rocadenbosch Burillo; Alejandro Antonio Rodriguez Gomez; Adolfo Comerón Tejero. "Overview of wind lidar techniques and current related developments at the Technical University of Catalonia". *Proceedings IEEE International Geoscience & Remote Sensing Symposium* 2008. pp 1120-1123 (2008).

Constantino Muñoz, Alejandro Rodríguez, Adolfo Comerón, Oscar Batet, David Garcia, Francesc Rocadenbosch, Michaël Sicard. "Speed measurements with a continuous wave lidar prototype". *IGARSS 2007 Conference Proceedings*, vol. 1-12, pp. 2775- 2778 (2007).

Constantino Muñoz Porcar; Alejandro Antonio Rodriguez Gomez; Adolfo Comerón Tejero; David Garcia Vizcaino; Francisco Rocadenbosch Burillo; Carles Diaz Peris."Continuous-wave solid target Doppler lidar prototype". *Proceedings of ODIMAP V - 5th Topical Meeting on Optoelectronic Distance/Displacement Measurements and Applications*. pp 204-209 (2006).

Constantino Muñoz, Alejandro Rodríguez, Adolfo Comeron, Gilbert Bourdet, Francesc Rocadenbosch. "Doppler lidar prototype for speed measurements". *Proceedings of SPIE Vol.* 5240. Laser Radar Technology for Remote Sensing. pp 174-182 (2004).

Michaël Sicard; Sergio Tomas Martinez; Mohd Nadzri Md. Reba; Adolfo Comerón Tejero; Oscar Batet Torrell; **Constantino Muñoz Porcar**; Alejandro Antonio Rodriguez Gomez; Francisco Rocadenbosch Burillo; Casiana Muñoz Tuñón; Jesús Jiménez Fuensalida. "Aerosol stratification characterization of an astronomical site by means of a backscatter lidar at the Roque de los Muchachos Observatory". *Proceedings of SPIE* vol. 7475, art. no.: 74750P (2009)

Michaël Sicard; Sergio Tomas Martinez; Adolfo Comerón Tejero; Francisco Rocadenbosch Burillo; Alejandro Antonio Rodriguez Gomez; **Constantino Muñoz Porcar**; Oscar Batet Torrell "Planetary boundary layer height and wind field characterization by means of a lidar at the Teide Observatory in the Canary Islands" *Proceedings IEEE International Geoscience & Remote Sensing Symposium* 2008. pp 915-918 (2008)

Francisco Rocadenbosch Burillo; I Mattis; Christine Böckmann; G Pappalardo; Jens Bösenberg; L Alados; Aldo Amodeo; Albert Ansmann; A Apituley; Dimitrios Balis; A Chaikovsky; Adolfo Comerón Tejero; V [et al] Freudenthaler; **Constantino Muñoz Porcar**; Michaël Sicard "The European aerosol research lidar network (EARLINET): an overview" *Proceedings IEEE International Geoscience & Remote Sensing Symposium* 2008. pp 410-413 (2008)

M Frontoso; Michaël Sicard; Adolfo Comerón Tejero; C Pérez; Jose M. Baldasano Recio; **Constantino Muñoz Porcar** "The vertical distribution of Saharan dust over the western and central Mediterranean through dust modelling and lidar observations" *Proceedings IEEE International Geoscience & Remote Sensing Symposium* 2007. pp 1059-1062 (2007)

S Tomás; Michaël Sicard; J Masjuan; Mohd Nadzri Md. Reba; **Constantino Muñoz Porcar**; Francisco Rocadenbosch Burillo "A wind speed and fluctuation simulator for characterizing the wind lidar correlation method" *Proceedings IEEE International Geoscience & Remote Sensing Symposium* 2007. pp 2779-2782 (2007)

Adolfo Comerón Tejero; Francisco Rocadenbosch Burillo; Alejandro Antonio Rodriguez Gomez; **Constantino Muñoz Porcar**; David Garcia Vizcaino; MA López; Michaël Sicard "Range-resolved atmospheric remote sensing using lidar" *Proceedings of ODIMAP V - 5th Topical Meeting on Optoelectronic Distance/Displacement Measurements and Applications*. pp. 57-66 (2006)

Michaël Sicard; Francisco Rocadenbosch Burillo; A Hénon; C Pérez; Alejandro Antonio Rodriguez Gomez; **Constantino Muñoz Porcar**; David Garcia Vizcaino; Adolfo Comerón Tejero; JM Baldasno "Evidence of discrepancies between columnar-averaged lidar ratios measured by sun photometer and lidar by means of a Raman lidar in Barcelona" *Reviewed and Revised Papers Presented at the 23rd International Laser Radar Conference*. pp. 437 – 440 (2006)

Dhiraj Kumar; Michaël Sicard; Sergio Tomas Martinez; **Constantino Muñoz Porcar**; Francisco Rocadenbosch Burillo; Adolfo Comerón Tejero "Engineering of a water-vapour, Raman, elastic-backscatter Lidar at the Technical University of Catalonia (Spain)" *Proceedings of SPIE*, Vol. 6367. art. no. 63670U (2006)

Adolfo Comerón Tejero; Francisco Rocadenbosch Burillo; Alejandro Antonio Rodriguez Gomez; MA López; **Constantino Muñoz Porcar**; David Garcia Vizcaino; Michaël Sicard "Lidar techniques for remote sensing of the atmosphere" *Proceedings of SPIE*, Vol. 5830. pp. 296-306 (2004)

Francisco Rocadenbosch Burillo; Michaël Sicard; Albert Ansmann; U Wandinger; W Matthias; G Pappalardo; Christine Böckmann; Adolfo Comerón Tejero; Alejandro Antonio Rodriguez Gomez; **Constantino Muñoz Porcar**; MA López; David Garcia Vizcaino "Statistical considerations on the Raman inversion algorithm: data inversion and error assessment" *Proceedings of SPIE*, Vol. 5240. pp. 116-126. (2003)

Francisco Rocadenbosch Burillo; Michaël Sicard; Adolfo Comerón Tejero; Jose M. Baldasano Recio; Alejandro Antonio Rodriguez Gomez; R Agishev; **Constantino Muñoz Porcar**; MA López; David Garcia Vizcaino "The UPC Scanning Raman Lidar: an engineering overview" *Abstracts of the 1st EARLINET Symposium*. pp. 2 – 2 (2003)

Francisco Rocadenbosch Burillo; Cecilia Soriano Ortiz; Adolfo Comerón Tejero; Jose M. Baldasano Recio; Alejandro Antonio Rodriguez Gomez; **Constantino Muñoz Porcar**; David Garcia Vizcaino. "3D scanning portable backscatter lidar platform for atmospheric remote sensing: performance and architecture overview" *Proceedings of the SPIE*, Vol.4168. pp 158-169 (2001)

Cecilia Soriano Ortiz; Francisco Rocadenbosch Burillo; Alejandro Antonio Rodriguez Gomez; **Constantino Muñoz Porcar**; David Garcia Vizcaino; Jose M. Baldasano Recio; Adolfo Comerón Tejero "Barcelona atmospheric monitoring with lidar: first measurements with the UPC's scanning portable lidar" *Proceedings of the SPIE*, Vol. 4168. pp 170-181 (2001)

National Congresses

Adolfo Comerón Tejero; Michaël Sicard; Francisco Rocadenbosch Burillo; Alejandro Antonio Rodriguez Gomez; MA López; **Constantino Muñoz Porcar**; David Garcia Vizcaino "Red europea de lidares avanzados: EARLINET" *Grupos de Trabajo y Ponencias del VIII Congreso Nacional del Medio Ambiente. Grupo de trabajo 27: Teledetección y sensores ambientales*. pp. 1-5 (2006)

Michaël Sicard; Francisco Rocadenbosch Burillo; Adolfo Comerón Tejero; Alejandro Antonio Rodriguez Gomez; **Constantino Muñoz Porcar**; David Garcia Vizcaino "Determinación de la altura de la capa de mezcla con un lidar de aerosoles" *Actas electrónicas del VII Congreso Nacional del Medio Ambiente*. pp. 9 – 23 (2004)

David Garcia Vizcaino; Victor Federico Dios Otin; Alejandro Antonio Rodriguez Gomez; Adolfo Comerón Tejero; Francisco Rocadenbosch Burillo; **Constantino Muñoz Porcar** "Anemómetro laser doppler para la medida de dos componentes de velocidad para aplicaciones hidrodinamicas (2d-lda)" *XVI Simposium Nacional de la Unión Científica Internacional de Radio. URSI 2001*. pp. 25 – 26 (2001)

Adolfo Comerón Tejero; Francisco Rocadenbosch Burillo; Alejandro Antonio Rodriguez Gomez; **Constantino Muñoz Porcar**; David Garcia Vizcaino "Lidar: principios y aplicaciones" *Grupos de Trabajo y Ponencias del V Congreso Nacional del Medio Ambiente. Grupo de trabajo 24: Sensores de datos medioambientales y sistemas de teledetección* (2000)

David Garcia Vizcaino; Alejandro Antonio Rodriguez Gomez; JA Eslava; Adolfo Comerón Tejero; Victor Federico Dios Otin; Francisco Rocadenbosch Burillo; **Constantino Muñoz Porcar** "Sistema Lidar Heterodino para medida de desplazamiento de superficies" *XV Simposium Nacional de la Unión Científica Internacional de Radio*. Libro de actas. pp. 29 – 30 (2000)